A STUDY ON RESPONSE AND CAPACITY OF MONOPOD BUCKET FOUNDATIONS SUPPORTING OFFSHORE WIND TURBINES IN SANDY SOILS

A Thesis

Submitted in Partial Fulfilment of the Requirements

for the Degree of

DOCTOR OF PHILOSOPHY

by

Tanmoy Kumar Deb

DEPARTMENT OF CIVIL ENGINEERING
INDIAN INSTITUTE OF TECHNOLOGY GUWAHATI
GUWAHATI-781039, INDIA

October 2018

CERTIFICATE

This is to certify that the thesis entitled "***A Study on Response and Capacity of Monopod Bucket Foundations Supporting Offshore Wind Turbines in Sandy Soils***" submitted by Tanmoy Kumar Deb (Registration No. 126104004) to Indian Institute of Technology Guwahati, for the award of degree of Doctor of Philosophy in Civil Engineering, is a record of bonafide research work carried out by him under my supervisor and guidance. The thesis work, in my opinion, has reached the requisite standard fulfilling the requirement for the degree of Doctor of Philosophy. This results contained in this thesis have not been submitted in part or full to any other University or Institute for award of any degree or diploma.

Date:

Place:

Dr. Baleshwar Singh
Professor
Department of Civil Engineering
Indian Institute of Technology Guwahati
Guwahati-781039
India

Dedicated to Mother Nature

ACKNOWLEDGEMENTS

I would like to express my deep and sincere gratitude to my supervisor, Prof. Baleshwar Singh for his constructive advices, insightful guidance and support throughout the PhD work. His valuable suggestions and encouraging interactions acted as a driving force for me to carry out the research work.

I would also like to thank my doctoral committee members: Prof. Arbind Kr. Singh, Dr. T.V. Bharat and Dr. Karuna Kalita for their valuable suggestions throughout the study. I would also like to thank Prof. Anjan Dutta, Prof. Gautam Barua, Dr. A. Narayana Reddy, Dr. Sachin Singh Gautam, Mr. Jens-Erik Jepsen and Mr. Abhimanyu Kumar for their valuable suggestions. I am grateful to the Central Library for offering a vast resource of research materials and making them easily accessible.

I am also thankful to my juniors, friends, batch mates and colleagues for their support during my research work. Finally, I am thankful to my parents, my wife and the remaining family members for their encouragement and support during the research period.

Tanmoy Kumar Deb

ABSTRACT

With the increasing demand for renewable and environment friendly energy, wind turbine farms are moving seaward due to several reasons: unavailability of suitable land locations, noise pollution produced by wind turbines during operation, visual impact on the natural environment, and availability of stronger and stable wind speeds. Offshore wind turbine foundations are subjected to large lateral forces arising from wind forces and water currents and the vertical self-weight loading is substantially lesser. The most commonly used monopile foundation system is expensive due to the necessary pile-driving equipment, and is also not recyclable after installation. The bucket foundation system has emerged as a practical alternative due to its cost-effective installation and retrieval method.

In order to develop design expressions, it is necessary to understand the response of the bucket foundations under typical offshore loading conditions. This thesis presents the results of three-dimensional finite element analyses of bucket foundations embedded in medium dense and very dense sandy seabeds, considering the non-linear behaviour of the soil.

Under vertical compressive loading, the response of bucket foundation was investigated for three diameters (12, 15 and 18 m), each having three aspect ratios (0.5, 0.75 and 1.0). The effects of skirt length and soil plug of the bucket foundation were investigated by comparing the vertical response with that of surface circular foundation and embedded solid foundation, respectively. For a given diameter, the ultimate vertical capacity of surface circular foundation is noted to be the minimum followed by bucket foundation and embedded solid foundation. The ultimate vertical capacity of bucket foundation is noted to increase in near linear manner with aspect ratio and bucket diameter. As compared to skirt length, increasing bucket diameter has higher influence on the ultimate vertical capacity.

For the bucket foundation, along the embedment length, both the shear stress and earth pressure are noted to increase parabolically to attain a peak value and reduce to a minimum value at the skirt end. The magnitudes of peak shear stress and earth pressure are noted to increase with bucket diameter and skirt length. For the bucket and embedded solid foundations, at failure condition, outward movement or lateral expulsion of the soil mass is noted below mid-depth of the embedment length. In the case of bucket foundation, the magnitude of lateral expulsion is noted to decrease with higher aspect ratio. However, in the case of embedded solid foundation, the magnitude of lateral expulsion is noted to increase with aspect ratio. Both bucket and embedded solid foundations fail under punching shear, and a confined deep flow mechanism is observed along with the formation of an elastic zone in the shape of a wedge. The soil plug located inside the bucket foundation is observed to act as an integral part of the foundation.

The displacement vector diagram beneath the bucket foundation resembles the shape of an inverted parabola, in which the minimum and maximum displacements of the soil are noted at the centre and at the edges, respectively. In contrast, the displacement vector diagram at the base of embedded solid foundation resembles the shape of an upright parabola, with the maximum and minimum vertical displacements of the soil, respectively at the centre and at the edges. The difference in the displacement vector diagrams shows that the soil plug inside bucket foundation provides a cushion effect while transferring the end-bearing load from the superstructure to the soil mass underneath.

In order to determine the effect of soil plug on the vertical bearing capacity of bucket foundations, numerical simulations were also carried out by considering zero shaft resistance around the skirt perimeter. For all the bucket geometries, the reduction in the end-bearing capacity is found to be in the range between 18-25% in medium dense sand and between 17-23% in very dense sand. The ultimate vertical capacities of bucket and surface circular

foundations of the same diameter were utilized to determine vertical capacity depth factor. Based on the results, predictive equations have been proposed for the bucket foundation to determine the ultimate vertical bearing capacity and settlement under superstructure load.

Under lateral loading, the response of bucket foundation was analysed by considering the same three diameters (12, 15 and 18 m) and aspect ratios (0.5, 0.75 and 1). The superstructure load ranged from 5 to 15 MN. The hub height was taken as 100 m and the lateral loading height was varied from 0 to 100 m. For a given loading height and superstructure load, the ultimate lateral capacity is observed to increase with increasing value of either bucket diameter or skirt length. Increasing bucket diameter shows greater influence on the ultimate lateral capacity as compared to skirt length. The ultimate lateral capacity is noted to increase marginally with superstructure load. The influence of superstructure load on ultimate lateral capacity keeps on decreasing with an increase in bucket skirt length.

For a given bucket geometry and loading height, the lid rotation at failure is noted to decrease with superstructure load. The lid rotation at failure is noted to be generally higher for a bucket foundation embedded in very dense sand as compared to medium dense sand. The initial stiffness is noted to be lesser with a smaller aspect ratio. For the same bucket geometry, the initial stiffness is noted to be greater under higher superstructure load, reduces nonlinearly with increasing loading height, and is always greater in the denser sand. Interaction diagrams of lateral load and overturning moment capacity at various loading heights have been represented graphically for serviceability limit state, fatigue limit state, worst expected transient load limit state, and ultimate limit state. Finally, predictive expressions have been proposed for the depth of point of rotation, initial stiffness, ultimate lateral capacity and allowable capacity of bucket foundations in medium and very dense sands.

TABLE OF CONTENTS

LIST OF FIGURES

LIST OF TABLES

LIST OF SYMBOLS

Symbol	Parameter
a	Constant exponent
A	Dimensionless constant
b	Constant exponent
$[B]$	Strain-displacement matrix
c'	Effective cohesion (N/m^2)
c_a	Displacement correction factor
c_b	Updated displacement correction factor
D	Diameter of bucket foundation (m)
D_{Em}	Diameter of embedded solid foundation (m)
$[D]$	Constitutive matrix
$[D^{ep}]$	Elasto-plastic constitutive matrix
D_{Sc}	Diameter of surface circular foundation (m)
$\{\Delta d\}_n$	Nodal displacements of an element (m)
E_{steel}	Modulus of elasticity of steel (N/m^2)
E_{soil}	Modulus of elasticity of soil (N/m^2)
F	External force (N)
ΔF	Load increment (N)
$F'(\{\sigma\}\{k\})$	Yield function
G	Shear modulus (N/m^2)
H	Lateral load (N)
$H_{Ultimate}$	Ultimate lateral capacity (N)
$H_{Allowable}$	Allowable lateral capacity (N)
h	Loading height (m)
I	Internal nodal force (N)
I_a	Updated internal nodal forces (N)
J	Deviatoric stress (N/m^2)
j	Number of repeating variable
K_E	Element stiffness matrix
K_{ini}	Initial stiffness (N/m)
K_0	Structural stiffness (N/m)
K_a	New structural stiffness (N/m)

k	State parameter
L	Embedment length (m)
L_{ref}	Reference embedment length (m)
L^*	Dimensional length (m)
L/D	Aspect ratio of bucket foundation
LE	Left exterior side of bucket foundation
LI	Left interior side of bucket foundation
M*	Dimensional mass (kg)
M	Moment (N-m)
m	State parameter
N_q, N_γ	Bearing capacity factors
N	Pressure exponent
$P(\{\sigma\}\{m\})$	Plastic potential function
p_a	Atmospheric pressure (N/m^2)
p'	Mean effective stress (N/m^2)
R_a	Residual force (N)
R_b	Updated residual force (N)
RP_1	Reference point 1
RP_2	Reference point 2
RE	Right exterior side of bucket foundation
RI	Right interior side of bucket foundation
SDV1, SDV2	Solution dependent state variables
SP	Principal stress (N/m^2)
SP1	Minimum principal stress (N/m^2)
SP2	Intermediate principal stress (N/m^2)
SP3	Maximum principal stress (N/m^2)
T	Dimensional time (s)
Δu_a	Incremental displacement (m)
V	Superstructure load (N)
V_{load}	Vertical capacity of bucket foundation (N)
V_m	Mean vertical load (N)
$V_{Bucket,Ultimate}$	Ultimate vertical capacity of bucket foundation (N)
$V_{Embedded\ Solid,\ Ultimate}$	Ultimate vertical capacity of embedded solid foundation (N)

$V_{Surface,Ultimate}$	Ultimate vertical capacity of surface circular foundation (N)
w'	Lateral displacement (m)
w	Vertical displacement of bucket (m)
Z	Depth of point of rotation (m)
$1P$	Rotor frequency or first excitation frequency (Hz)
$2P/3P$	Blade passing frequency or second excitation frequency (Hz)
γ'	Unit weight of soil (N/m^3)
γ'_{steel}	Unit weight of steel (N/m^3)
$\{\Delta\varepsilon\}$	Incremental total strain
$\{\Delta\varepsilon^e\}$	Elastic strain components
$\{\varepsilon^p\}$	Plastic strain components
$\{\Delta\varepsilon_i^p\}$	Plastic strain increment
δ	Interface friction angle
ε	Strain
θ	Lode's angle
Θ	Rotation at the bucket lid centre
κ	Empirical parameter
λ	Empirical parameter
μ	Poisson's ratio of soil mass
μ_{steel}	Poisson's ratio of steel
σ_{at}	Atmospheric pressure (N/m^2)
σ, σ'	Stress state (N/m^2)
$\{\Delta\ \sigma'\}$	Incremental stress (N/m^2)
σ_{at}	Atmospheric pressure (N/m^2)
σ'_1	Major effective principal stress (N/m^2)
σ'_3	Minor effective principal stress (N/m^2)
σ_n	Stress normal to plane of failure (N/m^2)
τ_f	Shear stress at failure (N/m^2)
ϕ'	Effective angle of internal friction
ψ	Dilation angle

Chapter 1

INTRODUCTION

1.1 INTRODUCTION

Excessive worldwide usage of fossil fuels over last few decades has aggravated the climate change problem. To meet the increasing global energy demand, emphasis is necessary to decrease the dependence on fossil fuels and to focus on renewable sources of energy. Amongst all available sources of green energy, wind energy can meet several goals such as bringing down air pollution problem and greenhouse gas emission. Wind power can be converted into electricity by means of wind turbines located onshore and offshore. Wind energy farms are moving seaward due to several reasons: unavailability of suitable land locations, noise pollution produced by wind turbines during operation, visual impact on the natural environment, and availability of stronger and stable wind speeds offshore.

Europe is leading the offshore wind energy sector, with its first small-scale offshore farm constructed in 1991 in Vindeby in Denmark, which consisted of eleven 450 kW turbines that provided a total capacity of 4.95 MW (Kurian et al. 2014). Later in 2003, the first large-scale offshore wind farm was also installed in Denmark at Horns Rev, with 80 wind turbines having a total capacity of 160 MW.

At the end of 2016, nearly 88% of all offshore wind turbine installations were located in waters off the coast of ten European countries. The remaining 12% was located largely in

China, followed by Japan, South Korea and the United States (GWEC 2017). At that time, the first four leading countries in terms of installed cumulative offshore wind farm capacity were the United Kingdom (5,156 MW), Germany (4,108 MW), China (1,627 MW) and Denmark (1,271 MW), as highlighted in Figure 1.1.

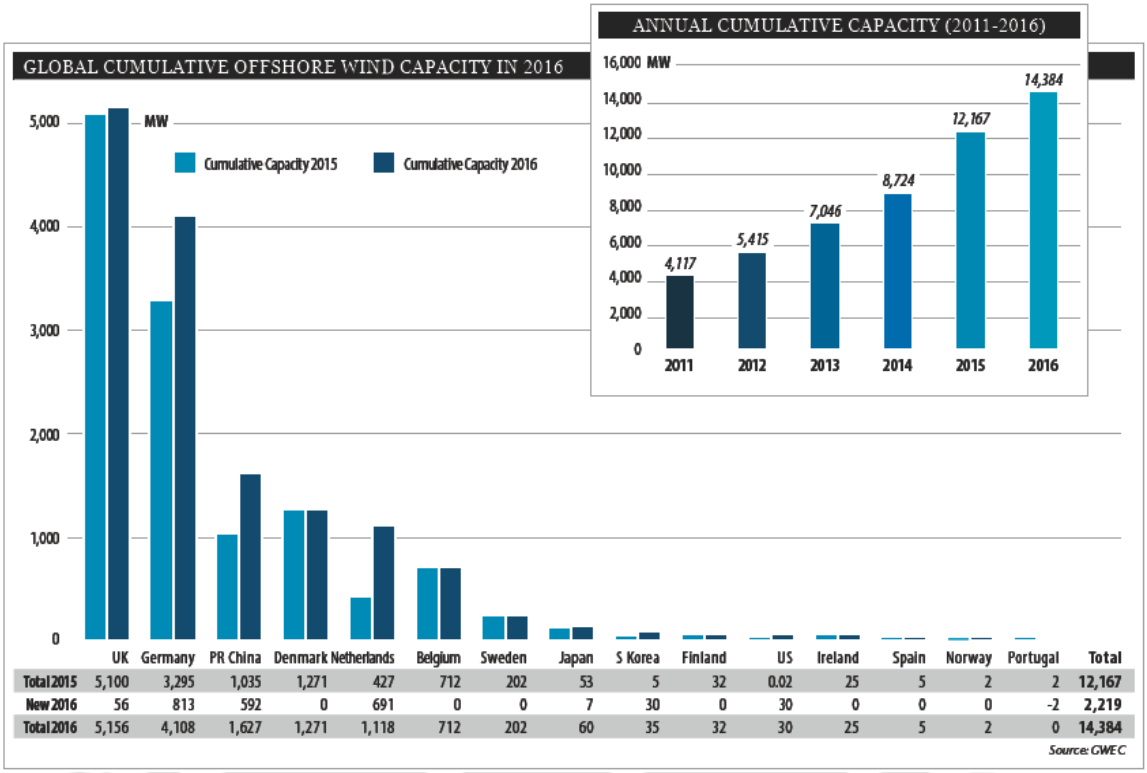

	UK	Germany	PR China	Denmark	Netherlands	Belgium	Sweden	Japan	S Korea	Finland	US	Ireland	Spain	Norway	Portugal	Total
Total 2015	5,100	3,295	1,035	1,271	427	712	202	53	5	32	0.02	25	5	2	2	12,167
New 2016	56	813	592	0	691	0	0	7	30	0	30	0	0	0	-2	2,219
Total 2016	5,156	4,108	1,627	1,271	1,118	712	202	60	35	32	30	25	5	2	0	14,384

Figure 1.1. Cumulative offshore wind capacity by country (GWEC 2017)

The spread of the offshore wind industry to North America, East Asia, India and elsewhere has already begun. In India, the first offshore wind farm project is being planned (developed) in an area of about 70 sq. km, with a tentative capacity of 1000 MW near the Gulf of Khambat, approximately 25 km off the coast of Gujarat in water depth ranging from 10 to 18 m.

Offshore wind turbine development is continuing its upscaling trend, and the industry continues to push toward larger turbines, seeking rated capacities greater than 8 MW in deeper waters. Large turbine sizes are generally preferred in offshore applications because of fewer installations and lower maintenance, and many developers are anticipating continued

turbine growth, with the expectation that the benefits of increased turbine size will continue to lower energy costs. The turbine height is related to turbine capacity, water depth and mean wind speed. Constant development efforts are also underway to reduce the turbine self-weight which also influences the choice of foundation type and size.

1.2 FOUNDATION TYPES FOR OFFSHORE WIND TURBINE STRUCTURES

In offshore conditions, several foundation types can be employed to support the wind turbine structures. The choice of foundation type mainly depends upon the load coming from self-weight in addition to the environmental loads, the seabed soil properties and the water depth at which the installation is desired. The various foundation types for supporting offshore wind turbines are shown in Figure 1.2 and are mentioned below:

1. Gravity-based foundation
2. Suction bucket foundation
3. Monopile foundation
4. Tripod foundation
5. Jacket foundation

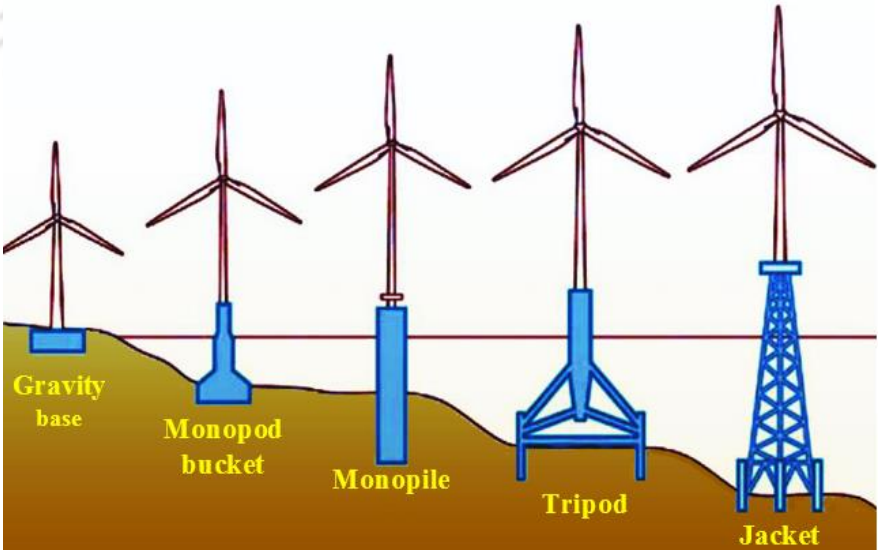

Figure 1.2 Foundation types for offshore wind turbine structures

Gravity-based and monopile foundations are generally installed in shallow waters (with a maximum depth of about 30 m), while tripod and jacket foundations are more appropriate for intermediate and deeper waters up to a depth of about 90 m.

1. Gravity-based foundation: Gravity foundation is typically a concrete shell structure employed to resist overturning load through the bearing resistance of the soil underneath and the self-weight of the concrete. For such foundation type, the soft top soil layer is removed to ensure that the subsoil has sufficient bearing capacity. For deeper water depths, higher hydrodynamic loads are encountered as a result of which the total cost increases substantially.

2. Suction bucket foundation: Suction bucket foundations are also referred to as suction anchors, suction piles, suction cans and bucket foundations. This foundation type was previously used for supporting offshore oil and gas platforms. Recent studies have established that these foundations can also serve as a viable and economically attractive alternative foundation type for offshore wind turbine structures. A bucket foundation comprises of a large diameter steel cylinder with a closed top. The foundation is fabricated onshore and then floated to desired site for installation. The installation is carried out in two stages, namely, self-weight installation and installation by suction.The bucket foundation gets partially embedded into the sea-bed from its self-weight. Remaining penetration is completed by reducing the pressure below the bucket lid by pumping the water out until the base of the lid comes in contact with the seabed.

3. Monopile foundation: Monopile is the most popular foundation type for offshore wind turbine structures. The monopile is a welded steel pile with its diameter the same as that of the lower section of the wind turbine tower. A transition piece is first grouted to the monopile prior to connection with the wind turbine tower. Typical diameter and length of monopile foundation can be as high as 6 m and 40 m, respectively with thickness of 150 mm (Malhotra 2011). The monopile foundation is installed by hydraulic or vibratory hammer.

4. Tripod foundation: Tripod foundation is pre-fabricated steel structure which is generally preferred for water depth more than 30 m approximately. The load coming from the wind turbine tower is transferred to three steel piles or suction buckets installed in the seabed at each leg location of the tripod.

5. Jacket foundation: Jacket foundation is a modified form of the tripod foundation. The jacket is a 3-4 legged structure made up of interconnected steel pipes, and is attached to the seabed through piles or bucket foundations.

1.3 LOADS ON OFFSHORE WIND TURBINE FOUNDATIONS

The loads acting on the offshore wind turbine are principally due to the aerodynamic load induced by wind and the hydrodynamic load generated due to crashing of water waves against the structure. The resultant of these loads acts laterally at an eccentric location above the sea bed, giving rise to large overturning moment at the foundation lid level. The vertical load arising due to self-weight of the wind turbine and its foundation system is lesser in magnitude compared to the lateral load arising from the combined action of wind and water waves.

The frequency of ocean waves varies between 0.04 and 0.1 Hz, whereas frequency range of energy-rich wind waves is typically between 0.05 and 0.5 Hz. The rotational speed of the modern offshore wind turbine typically ranges between 10-20 revolutions per minute which corresponds to an operational frequency between 0.17-0.33 Hz (Bisoi and Haldar 2014). For any particular wind turbine, the actual operational frequency is known as the first excitation frequency or the rotor frequency and is denoted by 1*P*. In this frequency range, minor excitations can take place due to aerodynamic imbalances in the distribution of mass. Further, during operating condition, the blades of the wind turbine, when passing in front of the tower, cause a shadowing effect and produce a reduction of wind load on the tower. This is a dynamic load having frequency equal to two times (2*P*) the rotational frequency of the

turbine for a two-bladed turbine and three times the rotational frequency of the turbine (3*P*) for a three-bladed wind turbine. In this frequency range, large impulse like excitation takes place as blades pass the tower.

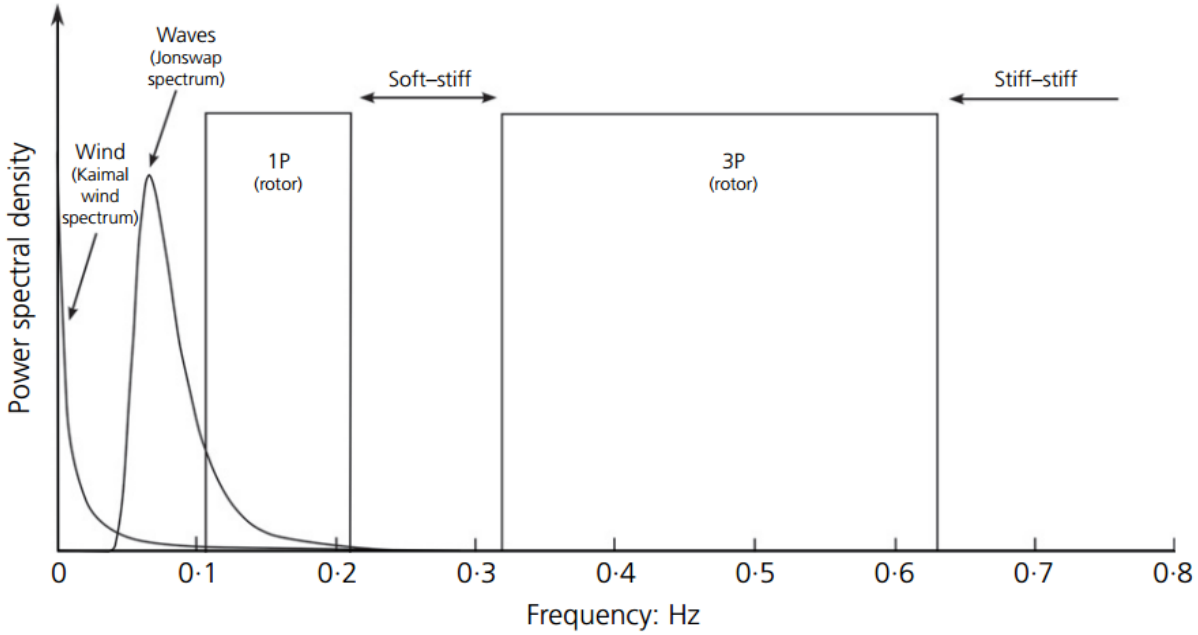

Figure 1.3 Typical frequency ranges for a three-bladed standard 5 MW wind turbine (Cox and Bhattacharya 2016)

Figure 1.3 shows the typical frequency range for a three-bladed wind turbine system with a rated capacity of 5 MW. For design, the first natural frequency of the wind turbine foundation system must be separated from the excitation frequencies generated as result of wind and wave loading. These days, the foundations are designed so that the first natural frequency lies within 1*P* and 3*P* frequency range. For a wind turbine foundation system, the natural frequency below 1*P* frequency is termed as soft-soft design. When the natural frequency is kept between 1*P* and 3*P* frequency range, it is referred as soft-stiff design. When the natural frequency of the wind turbine foundation system exceeds the 3*P* frequency band, it is termed as stiff-stiff design (Bhattacharya et al. 2014).

Apart from load from wind and waves, the foundation for offshore wind turbines is also loaded from currents. As compared to the wind and wave loads, current-induced load has

minimal effect. However, both waves and currents induce shear stress on the seabed and cause erosion of soil in the vicinity of the foundation. In cold regions, these foundations also experience heavy load arising from drifting ice which should be accounted in the design.

1.4 BUCKET FOUNDATION AS A SUPPORTING BASE

Depending on the foundation type, the foundation cost can be up to 40% of the overall cost of the offshore wind turbine. In recent times, bucket foundation has become an increasingly popular supporting base for offshore wind turbine due to its cost effectiveness, rapid installation with lower noise and feasibility of easy removal. A clearer understanding of the response of bucket foundation under offshore loading conditions and its load transfer mechanisms to the seabed would lead to increased confidence in designing such foundations. The thesis focuses on the response and capacity of monopod bucket foundations as the supporting base for offshore wind turbine structures.

1.5 OBJECTIVES OF THE STUDY

The main purpose of the present study is to understand the load-displacement response and capacity of monopod bucket foundations installed in sandy soils, under both vertical and lateral loading conditions, by conducting three-dimensional finite element analysis. The objectives of the study can be summarized as follows:

1. To investigate the response of monopod bucket foundation under vertical loading, and to evaluate the effect of foundation geometry, aspect ratio and sand type.
2. To compare the vertical response of bucket foundation with those of surface circular foundation and solid embedded foundation, and
    - To correlate the vertical bearing capacity of bucket foundation with that of surface circular foundation.

- To study the influence of soil plug on the vertical bearing capacity of the bucket foundation by comparing with that of embedded solid foundation.

3. To study the failure mechanism of bucket foundation and compare with that of embedded solid foundation.
4. To develop expressions for determination of ultimate vertical capacity and settlement of bucket foundations.
5. To investigate the response of monopod bucket foundation under lateral loading at different heights above seabed, and to evaluate the effect of foundation geometry, aspect ratio and sand type.
6. To study the lateral load transfer mechanism and to predict the depth of point of rotation.
7. To develop design expressions for initial stiffness, ultimate and allowable capacities of monopod bucket foundation for different combinations of geometry, superstructure load, loading height and sand type.

1.6 STRUCTURE OF THE THESIS

The thesis is organized into six chapters as follows:

Chapter 1 presents an introduction of offshore wind energy, available foundation types of offshore wind turbines, loads acting on the foundation, along with the objectives and organization of the thesis.

Chapter 2 presents a comprehensive literature review of the behaviour of bucket foundations under vertical load, lateral load, both vertical and lateral loads, and combined vertical, lateral and moment loads in sandy and clayey soils.

Chapter 3 outlines finite element modelling aspects of surface circular foundation, embedded solid foundation and bucket foundation under vertical loading, followed by modelling aspects of bucket foundation under lateral loading, in which the lateral load acts at any loading height.

Chapter 4 presents results of response of bucket foundation under vertical compressive loading in medium dense and very dense sandy soils. The variation of ultimate vertical capacity of bucket foundation with aspect ratio has been reported. Furthermore, the failure mechanisms of surface circular foundation, embedded solid foundation and bucket foundation are explored. The effect of skirt length on the vertical response is investigated by comparing with the results of surface circular foundation. The effect of soil plug on the vertical response is explored by comparing the end bearing capacity with that of embedded solid foundation. The finite element results are utilized to propose predictive equations for determining the vertical bearing capacity of bucket foundation.

Chapter 5 presents results of response of bucket foundation under lateral loading in medium dense and very dense sandy soils. The effect of aspect ratio, superstructure load and loading height on the ultimate lateral capacity have been investigated. The variations of lateral stress, depth of point of rotation and initial stiffness of bucket foundation with aspect ratio and loading height have been investigated. The development of failure mechanism of bucket foundation has been studied in various loading stages up to ultimate condition, and the variations with loading height and superstructure load have been reported. Based on the numerical results, both failure and allowable envelopes have been developed, and expressions are proposed for the preliminary design of monopod bucket foundations.

Chapter 6 lists the summary of the present study and the scope for future work.

Chapter 2

LITERATURE REVIEW

2.1 INTRODUCTION

The aspects of bucket foundation response under offshore loading conditions that are of relevance for the study are reviewed in this chapter. The available literature is categorized in four groups, namely, studies on the behaviour of bucket foundations under vertical loading, studies under lateral and moment loading, studies under vertical and lateral loading, and studies under combined lateral, vertical and moment loading. Each category is further sub-divided based on soil types. At the end, a summary of the literature is made, based on which the scope of the present study is defined.

2.2 BEHAVIOUR UNDER VERTICAL LOADING

2.2.1 Response in Sandy Soils

Houlsby and Byrne (2000) highlighted the possibilities of a novel form of foundation for offshore wind turbines, and discussed the loadings on this foundation system which were different from those previously encountered by the offshore oil and gas industry.

Later, Byrne and Houlsby (2002) reported the results of experimental investigations on the vertical loading response of suction caisson foundations. The experiments were carried out using a sophisticated three-degree-of-freedom loading rig. The caissons were embedded

in sand saturated with viscous silicon oil so that modelled drainage times were representative of typical offshore conditions. The experiments involved cyclic loading about different mean loads, including cycling into tension and the monotonic loading at different rates. The relationship between the cyclic loading and monotonic loading was explored. It was found that the rate of loading had little effect on the response. One of the key conclusions was that the serviceability requirement would dictate design rather than capacity.

Villalobos (2007) conducted laboratory experiments on scaled skirted foundations having aspect ratio between 0.26 to 2.0 in two dry sandy soils of different relative densities under pure vertical load, in order to investigate the behaviour during different stages of loading until failure, and compared the experimental results with theoretical results. The results were compared with theoretical bearing capacity methods from literature, which considering a constant angle of friction, to observe the mobilized friction angle. From the experiments in loose sand, the yield point due to application of vertical monotonic load was not observed, whereas the peak was prominent in case of dense sand. From a comparison of experimental and theoretical bearing capacity results, usage of peak angle of internal friction was observed to overestimate the bearing capacity. Later, the experimental results were utilized to determine the bearing capacity factors (N_q and N_γ).

Eid (2013) investigated the behaviour of vertically loaded skirted foundation in dry sand using numerical simulations and laboratory experiments considering surface, skirted and pier foundations. The effect of aspect ratio ranging from 0.5 to 2.0 and varying sand strength were studied. Inclusion of skirt enhanced the bearing capacity of foundation by a factor of 1.4 for an aspect ratio of 0.5 to slightly higher value for aspect ratio value of 2.0, regardless of the foundation width and sand friction angle. The ratios of bearing capacities of skirted foundation models to pier foundation models were almost constant and equal to 0.93, regardless of the foundation size and sand conditions. Correlations were then introduced to

determine the minimum bearing capacity and the maximum settlement of the skirted foundation of any aspect ratio from the corresponding magnitudes of the surface foundation, which were applicable for any shear strength and relative density of the sand.

Wakil (2013) performed laboratory tests on bucket foundations embedded in sandy bed in order to investigate the effect of skirt length and relative density on the vertical bearing capacity. The bucket skirt was noted to improve the vertical capacity appreciably by up to 6.25 times for the maximum aspect ratio of 1.5, and the enhancement of vertical bearing capacity was found to be more effective in the case of loose sand as compared to that in medium dense and dense sands.

Barari et al. (2016) conducted model tests as well as three-dimensional finite element analyses on bucket foundations and equivalent embedded solid foundations to examine the uniaxial vertical capacity. The experiments were carried out in quartz sand and involved monotonic application of vertical load. It was found that the drained capacity of the bucket foundation was dependent on embedment ratio. The analyses showed that the embedded foundations had significantly higher capacity than the equivalent surface ones. However, the skirted foundation capacity was slightly lower than that of the solid foundation with a proportional larger difference for a lower embedment ratio. On the basis of the tests and analyses, new expressions for the depth factor of shallow foundations were validated for embedment ratios up to unity.

Park et al. (2016) performed a series of two-dimensional axisymmetric finite element analyses to study the unique load transfer characteristics of bucket foundations in sands, using the Mohr-Coulomb model following non-associated flow rule. A pronounced increase in the soil lateral stress and a corresponding increase in the shaft resistance along the bucket length were observed. A higher level of arching was seen to occur in the soil due to the much lower depth-to-diameter ratio of the bucket foundation compared with that of a pile. The

arching also caused the failure surface to widen due to additional vertical stress imposed on the soil. Based on the numerical results, predictive equations for shaft resistance and a combined shape and depth factor for the base capacity were proposed.

Haddad et al. (2018) conducted experiments on small scale surface and bucket foundations to determine their difference in load-settlement behaviour in loose saturated sand under uniaxial vertical loading. The results showed that the skirt around foundation significantly enhanced vertical bearing capacity. The surface footing failed under vertical load at a settlement equal to 6–11% of foundation diameter, while the bucket foundation failed at a larger settlement. All the bucket geometries failed in punching shear mode and no bulging of the soil around the foundation was noted around the foundation. An expression for depth factor was proposed to approximate the bearing capacity of bucket foundation in terms of that of the surface footing and embedment ratio.

2.2.2 Response in Clayey Soils

Yun and Bransby (2007) utilized finite element analysis and centrifuge modelling to investigate the vertical bearing capacity of foundations with different geometries (surface, embedded and skirted) and embedment ratios on normally consolidated clayey soil. They also carried out upper bound plasticity analysis, which highlighted the mechanistic reasons for the varying response and allowed examination of the effect of changing skirt interface friction. The analyses indicated that the vertical capacity of bucket foundation can be considered normally as if the foundation was rigid with an embedment depth equal to the skirt depth. Based on the numerical analysis, a design method was proposed to determine the vertical bearing capacity of the skirted foundation. Further, a good agreement with the centrifuge test results partially validated the design method.

Mana et al. (2010) utilized finite element analyses to investigate the vertical capacity of bucket foundation embedded in clayey soil. Shallow foundations with embedment

provided either by a peripheral skirt or a rigid plug were considered in axi-symmetry and plane strain. The effect of idealizing the bucket foundation as embedded solid foundation and idealizing the geometry to conditions of plane strain were addressed by comparing the bearing capacity factor and kinematic mechanism leading to failure. Based on the results of numerical analyses, a closed-form expression was presented for the calculation of bearing capacity factors for circular skirted foundations over a practical range of embedment ratio, skirt-soil interface roughness and soil strength heterogeneity, to within ±2.5% of the finite element calculations.

Mana et al. (2012) investigated the kinematic soil failure mechanism around skirted foundations, embedded in lightly overconsolidated clay and subjected to undrained compression and tension, through digital image analysis in drum centrifuge tests, and compared them with predictions from finite element analyses. Analysis of images captured in the centrifuge tests showed some difference in the kinematic mechanisms governing failure of the skirted foundation in tension and compression. In tension, a reverse end bearing mechanism involving a bulb of soil beneath the foundation was mobilised even for a skirt depth to foundation diameter ratio as low as 0.1. Despite the difference in associated failure mechanism observed from centrifuge tests, bearing capacity factors for a selected embedment ratio were similar in compression and uplift. A comparison of the failure mechanisms observed in the centrifuge tests with those predicted by finite-element analyses showed some marked differences, though there was a close agreement of bearing capacity factors.

2.2.3 Response in Layered Soils

Park et al. (2015) performed three-dimensional finite element analyses to determine vertical bearing capacity of bucket foundations in two-layered soil profiles consisting of alternating layers of sand and clay. The embedment depth of the foundation was within the upper layer only. It was observed that the location of the clay layer had an important

influence on the bearing capacity. For the case of sand layer overlying clay layer, the effect of the clay layer becomes negligible if the depth of the clay layer from the skirt tip is higher than 3 times the diameter of the foundation. For the case of clay layer overlying sand layer, the capacity becomes almost identical to uniform clay case if the depth of the sand layer is higher than diameter of the foundation. For the limited ranges of the foundation size and the shear strength of sand and clay used, predictive equations and design charts were proposed.

2.3 BEHAVIOUR UNDER LATERAL LOADING

2.3.1 Response in Sandy Soils

Ibsen et al. (2005) presented a status report outlining the nature of laboratory model tests, field trials and full-scale field installation as the necessary diverse techniques for the development of a reliable design procedure of bucket foundations. Further, they reported the full-scale field installation of a prototype bucket foundation and its performance under static loading, where the in-service performance was measured for a period of approximately three years. An evaluation of the in-service performance showed the adequacy of the design specifications of that prototype bucket foundation.

Abdel-Rahman and Achmus (2006) carried out finite element analyses to investigate the behaviour and bearing capacity of large bucket foundations resting on medium dense sand, for offshore wind energy converters under lateral and moment loading. For specific deformation states (rotation angles) and especially for the ultimate limit state of the foundation structure, lateral load-moment load interaction diagrams were presented.

Wakil (2010) performed twelve loading tests on small scale circular skirted footings to shed some light on their performance when subjected to lateral loads. The effects of skirt length and the relative density of sand were investigated. The experimental study also included comparison between ultimate horizontal loads attained by skirted and unskirted

footings with the same soil properties. From the laboratory test results, it was found that the skirts changed the failure mode of circular shallow footings from sliding mechanism into rotational mechanism. In addition, the skirts attached to the footings increased the ultimate horizontal capacity of shallow footings appreciably.

Zhang et al. (2010) presented a three-dimensional limit method based on upper bound theory for checking the stability of suction bucket foundations supporting offshore platforms. The bucket embedded in sand was subjected to a lateral load applied above the mud line. In order to simulate the lateral load, a fictitious soil layer was assumed, having a thickness equal to the vertical distance from the load point to the surface of the foundation. The unit weight and shear strength of the fictitious soil layer were set to be zero. The three-dimensional slip surface was modelled using a generalized pattern and the soil-bucket failure mechanism was approximated by a series of rectangular prisms. Results of the limit method were verified with centrifuge test results, which indicated that the proposed method could very well predict the ultimate lateral capacity of bucket foundations with reasonable accuracy.

Zhu et al. (2011) carried out large-scale model tests on suction installation and lateral loading of caisson foundations in saturated silt in a large soil tank. Test results of installation resistance during suction installation showed that the seepage effect was limited in silt, and the suction required to penetrate the caisson could be well predicted based on the sleeve friction and cone resistance of cone penetration tests. The deformation mechanism and soil-structure interaction of the caisson subjected to lateral loads were investigated. The instantaneous rotation centre of the model caisson at failure was noted to be at a depth of about four-fifths of the skirt length, almost directly below the lid centre. Based on the assumption of a common position of the instantaneous rotation centre and dominating resistance forces on the caisson, an analytical expression for the ultimate moment capacity was presented.

Zhu et al. (2013) presented cyclic load tests in which approximately 10,000 cycles, with different loading characteristics, were applied to a model caisson foundation in loose sand. On the basis of these tests, a framework for assessing the accumulated angular rotation was developed. The settlement and cyclic stiffness response of the caisson were also assessed. It was found that the accumulated settlement of the caisson increased with the number of cycles and cyclic amplitude. Also, cyclic loading regime between one-way and full two-way cycling produced the largest rotations. The cyclic stiffness was relatively unaffected by the number of cycles. Using an appropriate scaling technique, the proposed framework was used to predict the long-term accumulated angular rotation of a field-scale monocaisson structure.

Achmus et al. (2013) investigated the bearing behaviour of monopod buckets under drained monotonic loading in very dense and medium dense sands, by means of numerical simulation with the finite element method. The numerical model was validated by comparison with reported field test results. It was shown that the bucket experienced a heave during horizontal loading, which led to the formation of a gap between the bucket lid and the internal soil plug with increasing load. At large loads and rotations close to failure of the system, there was no contact between the lid and soil, and the whole load was transferred to the soil via the bucket skirt. A parametric study showed as to how the ultimate capacity and initial stiffness of the system were dependent on the bucket dimensions and the load eccentricity. Normalized equations for ultimate capacity and initial stiffness were derived from the numerical simulation results.

Li, Feng and Zhang (2014) presented a modified suction caisson, consisting of an internal longer caisson within an external short-skirted structure, and conducted model tests to investigate its lateral bearing capacity in saturated marine fine sand. The results showed that the modification significantly increased the lateral bearing capacity and reduced the

lateral deflection, compared to its corresponding conventional suction caisson. Parametric studies indicated that the lateral capacity of the modified suction caisson increased with the increase of both the external skirted structure dimensions and the internal caisson aspect ratio, and decreased with the increase of the load eccentricity. The lateral deflection decreased for the increased size of the external skirted structure. In the limit state, the rotation centre was found at a depth of about 0.5–0.7 times the length of the internal caisson and around 0.15 diameter of the internal caisson away from its centre line.

Li, Zhang, Feng and Guo (2014) carried out model tests on the modified suction caisson subjected to monotonic lateral load, embedded in saturated medium sand, to study the bearing capacity. A three-dimensional continuum finite element model was also to developed investigate the soil deformation and earth pressures. The outer skirt of modified suction caisson was noted to increase the lateral capacity significantly and limit the deflection at a given rotation angle. From the numerical results, the rotation centre of the foundation moved upward with the increase of skirt width and length, whereas it moved downward with the increase of lateral load.

Zhu et al. (2014) carried out model tests on suction caissons of different sizes in sandy silt to investigate the effects of diameter, aspect ratio, and load eccentricity on normalized moment capacity. The instantaneous rotation centre of model caissons were found to be at the depth of about four-fifths of the skirt length, almost directly below the lid centre. A new calculation approach of deflection-based bearing capacity was proposed based on the mechanisms of soil-structure interaction and deflection of the caisson. This analytical approach could predict the moment-rotation curves of the model tests in sandy silt and of a field test in sand. This deflection-based approach made it possible to calculate bearing capacity at any allowable angular rotation. Finally, design charts of monocaisson foundations in silt and sand for offshore wind turbines were provided.

Li et al. (2015) conducted experimental and finite element analyses on the bearing capacity of modified suction caissons in saturated marine fine sand under static horizontal loading. Several equations were proposed to calculate the maximum moment bearing capacity, by taking into account the external skirt width, the internal compartment aspect ratio and the loading eccentricity into account. Deflection and net earth pressure distribution methods were used to determine the rotation centre position, and these two methods were proved to be satisfactory. It was found that the rotation centre moved downward and forward with increasing horizontal load, and then tended to be stable when the maximum load was approached. The distance between the rotation centre and the caisson lid at failure decreased with increasing external skirt dimensions, the internal compartment aspect ratio and the loading eccentricity. Based on the simulation results, an expression to estimate the combined capacity of the modified suction caisson was proposed.

Zhang, Gao, Li and Mahfouz (2016) investigated the bearing capacity of modified suction caissons in saturated marine fine sand through monotonic lateral load tests, in which load was applied under both displacement-controlled and load-controlled methods. In the displacement-controlled tests, softening behaviour of lateral load-deflection curves was observed, and the softening degree of the load-deflection response increased with increasing external skirt length or decreasing loading eccentricity. It was found that the rotation centre of the modified suction caisson at failure determined by the load-controlled method was slightly lower than that by the displacement-controlled method. The calculated capacity based on the position of centre of rotation in serviceability limit state was relatively conservative, compared with the calculated capacity based on the position of centre of rotation in the ultimate limit state.

Cox and Bhattacharya (2016) summarised the findings from a series of tests conducted using representative caisson models in loose sand under 1g conditions, replicating

a fully drained prototype state, and identified key factors which influenced the serviceability performance of an offshore structure founded on a single caisson. These experiments recorded the rotational foundation stiffness, the evolution of foundation stiffness under cyclic loading and the accumulation of structural rotation with loading cycles. It was discovered that the caisson stiffness was dependent on the local soil strain, and would increase under cyclic loading in a logarithmic manner. Further, caisson system was noted to retain and accumulate structural rotation under cyclic load, following a power relationship. From these observations, it was possible to produce an analytical model describing the changing serviceability state of a prototype suction caisson structure with loading cycles. Based on the tests, an analytical model was proposed to describe the changing serviceability state of a prototype suction caisson structure with loading cycles.

Tang et al. (2016) utilized limit analysis method to determine the updated rotation centre position and horizontal bearing capacity of bucket foundations, and to evaluate their failure mechanisms. A set of formulas was suggested to calculate the rotation centre position and horizontal bearing capacity. The calculated results were compared with numerical simulation, experiments and with other theoretical methods. The proposed method was accurate in determining the rotation centre and horizontal bearing capacity.

Zhang, Li and Gao (2016) described a series of model tests and numerical simulations to understand the earth pressure mobilization of modified suction caisson and that of the corresponding regular suction caisson in sand under monotonic lateral loading. Results showed that the yield envelopes for the both the suction caisson types, in the horizontal load-moment space could be represented by a linear relationship. Numerical results indicated that in the ultimate limit state, the maximum net earth pressure acting on the external skirt wall in the loading direction was larger than that on the internal compartment wall. However, the

maximum net earth pressure along the caisson embedded depth was obtained at the modified suction caisson base opposite the loading direction.

Bagheri et al. (2017) presented the results of three-dimensional finite element analyses of suction bucket foundation used for offshore wind turbines in medium dense and dense sandy soils subjected to static horizontal load. Dimensionless horizontal load-displacement and overturning moment-rotation relationships were derived utilizing the Power law and Buckingham's theorem. There was good agreement between the numerical analysis results and the straight lines obtained from the Power law until specific values of horizontal load and overturning moment. Numerical results showed that the bucket rotation and displacement were highly dependent on the bucket geometry and soil properties in addition to loading conditions. Finally, normalized equations and interaction diagrams for the ultimate horizontal load and overturning-moment capacities were presented.

Wang et al. (2017) performed force-controlled lateral static and cyclic centrifuge tests at 50g to investigate the lateral bearing capacity of bucket foundations with three aspect ratios, embedded in sandy soil. Four different soil conditions were considered, namely, loose-dry, loose-saturated, dense-dry, dense-saturated sands. The lateral load carrying capacity was determined by three methods using load-displacement curve, displacement rate-load curve and simplified analytical calculation. From the first method, it was concluded that the ultimate lateral capacity was obtained when the normalized lateral displacement (displacement divided by the bucket diameter) reached 3%. Displacement rates were plotted against the lateral load to give the second method for defining the ultimate lateral capacity. In cyclic tests, the lateral displacement and stiffness were found to be related to the cycle number in the first 5 cycles, but the change was less apparent in the rest. The results demonstrated the behaviour of bucket foundation in service conditions. Finally, a simplified calculation method was used as the third method which was checked with test results.

Yang et al. (2017) created finite element models of bucket foundations with two aspect ratios of 0.5 and 1.33, and also conducted centrifuge tests on the two models. The load-displacement curves of the numerical analysis and test results had good agreement. In addition, several other three-dimensional numerical models, with aspect ratio varying from 0.2 to 2.0, were numerically modelled to evaluate the effect of the aspect ratio on the lateral loading capacity. The development and distribution of stress and plastic strain were used to study the failure mechanism of bucket foundation for the different aspect ratios. The influence of the position of lateral load applied was also analysed. Sensitivity analysis for the parameters of material properties such as internal friction angle, Young's Modulus, and friction coefficient between the bucket and soil were performed using non-linear analysis with the Mohr-Coulomb soil model. The lateral bearing capacity increased with increasing aspect ratio values. Sensitivity analysis showed that the internal friction angle and the friction coefficient strongly affected the bearing capacity, while the Young's modulus and the dilation angle had little influence on the capacity.

2.3.2 Response in Clayey Soils

Aubeny et al. (2003) carried out plastic limit analysis of the lateral load capacity of suction caissons in an anisotropic, purely cohesive soil assuming conditions of rotational symmetry about the vertical or gravity axis. The formulation utilized a form of the Hill yield criterion that was modified to allow for different soil strengths in triaxial compression and extension. Using this yield criterion, energy dissipation relationships were formulated for continuous and discontinuous deformation fields. These dissipation relationships were then applied to a postulated caisson failure mechanism comprising a wedge near the free soil surface (mudline), a two-dimensional flow around failure at depth, and a hemispherical slip surface at the base of the rotating caisson. The plastic limit analysis predictions compared favourably to predictions obtained from finite-element simulations, which employed a Hill

yield criterion. Parametric studies indicated that the horizontal load capacities of suction caisson predicted using a conventional approach (a von Mises yield surface fitted to the soil simple shear strength) differed from anisotropic predictions by less than 10%.

Sun et al. (2010) explored the lateral load carrying capacity of bucket foundations resting on soft clayey ground, based on three-dimensional finite element method and limit equilibrium method. From the numerical analyses, the bucket foundation was noted to fail under rotation, where the point of rotation lied at a certain depth below the mudline and above the base of the foundation. Based on limit equilibrium method, an expression was proposed to evaluate the lateral load carrying capacity to serve as a design guideline for engineering practice.

Kumar and Rao (2010) carried out an experimental study on earth pressure mobilization in caissons embedded in marine clay. Based on the results, a contiguous wall made up of embedded caissons in soft clay was proposed to serve as a coastal protection wall. The tests were carried out on models with embedment depth ratio up to 4 at different load eccentricity ratios. The test results showed that the caissons could be loaded to produce lateral deflection up to 30-35% of diameter. The lateral capacity was estimated corresponding to deflection ratio of 20%, and it was noted to be a function of undrained strength, embedment depth ratio and load eccentricity ratio. A unique relation was established between lateral load and deflection in the normalized form, which matched very well with published field lateral load deflection curves.

Barari and Ibsen (2012) carried out experimental tests and numerical simulations on small scaled bucket foundation of 30 cm diameter, installed in Yoldia clay. The aspect ratio of ranged from 0.25 to 1. Moment load was applied in terms of the lateral force through a lever arm with lengths of 261, 174, and 11 cm. The numerical simulations were carried out by varying elastic modulus and undrained shear strength of the soil. The results obtained

from the laboratory experiments were compared with that of the numerical simulations. Finally, a yield surface describing combined loading combinations at failure, in the lateral, vertical, and moment loading coordinate system, was presented.

Kumar and Rao (2012) carried out laboratory tests on model caissons embedded in marine clay, to study the response of lateral load-ground level deflection under static and cyclic lateral loading by varying embedment depth ratio, load eccentricity ratio, and soil undrained strength. The results showed that with the lateral load required to cause a specified ground level deflection increased with higher embedment depth ratio. At a given lateral load, the deflection level has increased with higher magnitude of load eccentricity ratio. From the cyclic load test results, deflections mobilized at the cyclic load ratio of 0.6 were found to be small in magnitude (equal to 1% to 2% of the caisson diameter). A marked increase in the ground level deflection up to about 900 cycles was observed, and thereafter the deflection remained almost the same.

Ding et al. (2015) presented a new type of wide-shallow composite bucket foundation (WSCBF), which could be adapted to the development needs of offshore wind turbines due its special structural form. Several field tests on WSCBF were carried out in saturated clay off the coast of Jiangsu, to determine the deformation mechanism, the soil–structure interaction and the ultimate lateral capacity. Based on the position of the rotation centre, analytical expressions of soil pressure and ultimate bearing capacity for the WSCBF were presented. The accuracy of the test results and analytical expressions was validated and supplemented by numerical simulation using finite element method. From the numerical simulation, the envelope of ultimate bearing capacity of the WSCBF was described in *H–M* load space, clarifying the load-bearing characteristics of the WSCBF under combined loads.

2.4 BEHAVIOUR UNDER VERTICAL AND LATERAL LOADING

2.4.1 Response in Sandy Soils

Byrne et al. (2001) carried out laboratory tests on shallow bucket foundations embedded in sandy bed to investigate the monotonic loading response. Experiments were carried out by varying the embedment length of the bucket foundation as well as varying mineralogy and density of the soil. The results from the vertical bearing capacity tests were presented and compared with conventional bearing capacity expressions. Cyclic lateral and moment loading tests were also carried on different geometries bucket foundation under very low vertical loads of constant magnitude to determine the limiting moment capacity. From the test results obtained by combined loading, expression of moment capacity of bucket foundation was developed.

Byrne and Houlsby (2003) explored the problems encountered in the design of offshore wind turbine foundations, embedded in sandy soil. Previous research works dealing with the design of offshore foundations were reviewed, and design calculations for the sizing of foundations and structures appropriate for the offshore foundations were presented.

Byrne and Houlsby (2004) performed laboratory experiments on model suction caisson foundations, where typical cyclic loads were applied. In order to simulate typical offshore soil conditions, the foundation was embedded in oil-saturated sand. Most of the tests were carried out with constant vertical load, while realistic moment and lateral cyclic loads were applied. Some experiments were also carried out by varying the vertical load during the test, which showed that the response depended on the vertical load level. From the laboratory tests, it was found that the rate of loading had little influence on the load-displacement behaviour of bucket foundations. Earlier, they had reported the results of only vertical loading on model suction caissons (Byrne and Houlsby 2002).

Nguyen-Sy and Houlsby (2005) presented a theoretical model for the analysis of suction caisson foundations, based on a thermodynamic framework and macro-element concept. The main goal of this work was to model the cyclic behaviour of a caisson foundation correctly, and this necessitated extension of previous modelling concepts to use of multiple yield surfaces. Firstly, the elastic-plastic response was first described in terms of a single yield-surface model, using a non-associated flow rule. Later, the same was extended to a multiple yield surface model, to capture hysteresis phenomena. The installation of the caisson using suction was also analysed as a part of the theoretical model.

Kelly et al. (2006) conducted laboratory tests on suction caissons founded in both sand and clay by applying cyclic vertical and moment loads to simulate an equivalent series of field tests. The caissons used in the laboratory were 0.15, 0.2 and 0.3 m in diameter, whereas those for the field tests were 1.5 and 3.0 min diameter. The loads applied in the laboratory tests were scaled from those in the field tests, and the models were loaded in a near-identical manner to the field trials. The test results were presented in non-dimensional form for comparison in terms of both stiffness and capacity. The non-dimensional laboratory data from moment loading tests were similar to the field data in most cases. However, the non-dimensional data from vertically loaded caisson tests in the laboratory and in the field showed significant differences, and possible reasons for these were discussed.

Houlsby et al. (2006) described a programme of field testing on suction caisson foundations in an artificially prepared sand test bed near Luce Bay, in Scotland. The tests were applicable to the design of either monopod or quadruped foundations for offshore wind turbines. Records were presented for suction installation of the caisson, cyclic moment loading under both quasi-static and dynamic conditions to simulate the behaviour of a monopod foundation, and cyclic vertical loading and pullout to simulate one footing in a quadruped foundation. Variations of stiffness with load level of the foundation were

observed, with high initial stiffness followed by hysteretic behaviour at moderate loads and degradation of response at high loads.

Foglia et al. (2015) investigated the response of bucket foundations on sand subjected to planar monotonic and cyclic loading. Thirteen monotonic and cyclic laboratory tests were conducted on a skirted footing model having a 0.3 m diameter and embedment ratio equal to 1. The loading regime reproduced typical conditions of offshore wind turbines such as very large cyclic overturning moment, large cyclic horizontal load and comparatively little, self-weight induced, vertical load. The experimental soil-foundation response was interpreted within a macro-element approach, using an existing analytical model, suitably modified to accommodate the footing embedment and the application of cyclic load. The proposed model provided evidences of its ability to reproduce the essential features of the experimentally observed behaviour. The results of the study increased confidence in the use of the macro-element approach to predict the response of bucket foundations for offshore wind turbines, particularly the long-term accumulated displacements.

Ghaseminejad et al. (2018) carried out three-dimensional numerical analyses of bucket foundations founded in loose, medium and dense sands under pure horizontal, vertical and moment loadings. The influence of variations in the geometry of the bucket (diameter and aspect ratio) and soil properties on respective load and moment capacities were evaluated and discussed. The effect of embedment was also examined and depth factor relationships were developed for a range of soil properties. Normalized expressions of pure horizontal and vertical bearing capacities were found to be linearly proportional to aspect ratio, while a quadratic relationship was observed between pure moment capacity depth factor and aspect ratio. It was observed that failures under pure horizontal and moment loads were governed by a combination of horizontal and rotational translations.

2.4.2 Response in Clayey Soils

Houlsby et al. (2005) described a programme of field testing of caisson foundations in a clay test bed at Bothkennar, in United Kingdom. The tests were relevant to the design of foundations for offshore wind turbines, in the form of either monopod or tetrapod foundations. Records were presented for installation of the caisson, cyclic moment loading under both dynamic and quasi-static conditions, cyclic inclined vertical loading, and pullout loading of the caisson. The stiffness of the foundation was noted to vary, where high initial stiffness followed by hysteretic behaviour at moderate loads and degradation of response at high loads were observed.

Barari and Ibsen (2011) performed experimental studies on small scale bucket foundations placed on Yoldia clay to investigate the effect of embedment on the undrained bearing capacity under vertical loading. The tests were accompanied by finite element numerical simulations for a better understanding of influential parameters. The obtained results for circular surface and bucket foundations were also compared with the plasticity solutions in order to verify the accuracy of the simulations. From a comparison of the variation of normalized vertical limit state, a quadratic relationship between ultimate vertical load and embedment ratio was proposed.

Fu et al. (2017) presented the results of finite element analyses calculating the undrained capacities of skirted circular foundations under using both the Tresca failure criterion and the Modified Cam Clay (MCC) model. To account for the complexity in the results, a novel method of separating the contributions of soil above and beneath the skirt tip, and for the constant and linearly varying components of undrained shear strength profile was outlined. This method could be used to estimate the undrained ultimate uniaxial vertical, horizontal, and rotational capacity factors of skirted circular foundations in clay for any given

embedment ratio and strength heterogeneity. The adaptability of the proposed method was shown through validation against previously published embedded strip footing data.

2.5 BEHAVIOUR UNDER COMBINED LOADING

2.5.1 Response in Sandy Soils

Byrne and Houlsby (1999) presented the results of a series of loading tests of model footings on very dense dry sand to determine their behaviour with different skirt depths, under a variety of conditions. The results represented the long-term (drained) response to general loading regimes. The tests were specifically designed to allow derivation of models of foundation behaviour based on work-hardening plasticity theory. The study showed that the response of a skirted footing could be successfully described within a plasticity context. The yield surfaces in {*V*:(*M/D)*: *H*} space were shown to be well described by parabolic ellipsoids. The study indicated that the shape of these yield surfaces, during pre-peak bearing capacity behaviour, was a function of the preload ratio (vertical load/peak vertical load). The study also indicated the change in shape of the yield surface with increasing embedment ratio. In all cases, the use of an associated flow rule in the deviatoric (*M/D*: *H*) plane was supported by the tests.

Villalobos et al. (2009) presented data from combined loading experiments on suction caissons in loose and dry sand, consisting of a comprehensive set of drained monotonic rotational and translational loading under a constant vertical load. The caisson geometry and the loading conditions were chosen to reflect typical designs for offshore wind turbines. The results were interpreted within the framework of work-hardening plasticity theory, which allowed the evaluation of the yield surface and flow rule. A key result from the work was that the caisson could mobilise a moment and/or horizontal resistance under tensile loads. This aspect of response had been ignored in previous works, but was clearly important in

applications where the vertical load was low when compared to the bearing capacity of the foundation. It was found that associated flow rule described incremental rotational and horizontal displacements, and in contrast to previous works, an associated flow rule was necessary for the appropriate description of the plastic vertical displacement increments.

Ibsen, Barari and Larsen (2013) conducted laboratory experiments on bucket models with different embedment ratios to study the behaviour of these foundations in dense saturated sand subjected to combined loads at different eccentricities and vertical loads. Based on the model tests, strain-hardening criterion was developed by calibrating failure criteria for buckets subjected to combined static loads. The shape of the yield surface, potential surface and failure surface were noted to depend on the embedment ratio and load path. For the model bucket foundations tested in dense sand, associated flow was observed to be plausible in the radial planes, whereas non-associated flow was observed in the planes along the vertical axis.

Ibsen, Larsen and Barari (2013) and Larsen et al. (2013) carried out an extensive number of loading tests with small-scale bucket foundations subjected to combined loading. The tests were performed on buckets of various sizes, embedment ratios and load paths on saturated dense sand. The experimental results were used to evaluate the behaviour of the bucket foundations in accordance with the macro-model approach. Although previous authors had proposed a linear relationship between the moment capacity and the vertical load, this relationship did not fit the observed capacities in the present study. Therefore, a modified expression was proposed to describe the combined capacity as a function of the tensile capacity and the inclination factor.

Liu et al. (2014) presented the results from elasto-plastic analyses of three-dimensional finite element models of wide-shallow bucket foundation, with the aim of defining the shape of the yield envelope in the *V-H*, *V-M*, *H-M* and *V-H-M* spaces and the

failure mode. The compressive bearing capacity of the foundation was determined by the displacement. The corresponding load under a vertical displacement of 6% of the diameter of the foundation was the vertical ultimate bearing capacity. The vertical loading had an amplification effect on the horizontal load bearing and moment capacity, and the application of horizontal loading in the opposite direction to the moment load increased the moment capacity by 20-40%. New simplified calculation methods were proposed for the vertical load-bearing capacity and the overturning stability. In the proposed method, the vertical capacity consisted of the top plate resistance of the bucket and the side frictional resistance. The overturning stability was determined by the safety factor method, and depended on the location of the rotation point. A comparison between the results of the finite element analysis and the simplified calculation methods showed that the proposed equations properly predicted the capacities of the wide-shallow bucket foundations.

Ibsen et al. (2015) reported results of multiple loading tests on shallow bucket foundations under combined vertical, horizontal and moment loading, addressing the effect of embedment on the strain-hardening behaviour. The kinematic mechanisms accompanying pre-failure were presented. It was argued that the drained capacity of offshore bucket foundations and the ratio of plastic increments were largely influenced by embedment depth and the preload ratio (vertical load/peak vertical load*)*

Vahdatirad et al. (2016) introduced a load-displacement based approach to assess the bearing capacity as well as the deformation of a mono-bucket foundation subjected to combined vertical, lateral and moment loading. A *p-y* curve developed for the bucket foundation was used to quantify the lateral soil response around the foundation. A numerical routine was proposed to set up the model and run the calculations. The model was validated and its accuracy was analyzed by comparison with field test results for a bucket foundation installed in silty sand.

2.5.2 Response in Clayey Soils

Bransby and Randolph (1999) investigated the response of skirted foundation under combined vertical, lateral and moment undrained loading using finite element method. The study focussed on the effect of foundation embedment depth on the size and shape of the combined vertical (*V*)-lateral (*H*)-moment (*M*) yield locus. The yield locus was found to be of similar shape as that of a surface foundation but the size was increased. Upper bound plasticity analysis was carried out to calculate the load bearing capacities for a range of embedment depths and undrained soil shear strength profiles, and design charts were presented for their determination. Normalisation of the yield locus by the load bearing capacities allowed the yield locus to be generalised for varying soil profiles and embedment depths.

Taiebat and Carter (2000) presented the results of three-dimensional finite element analyses of circular foundations on the surface of homogeneous, purely cohesive soil. The foundations were assumed to adhere fully to the soil, to allow the development of compressive, tensile and shear stresses at the interface between the footing and the soil. The predicted ultimate response of the foundations to combined vertical, horizontal and moment loading was compared with other available theoretical predictions. A three-dimensional failure locus was presented for these foundations, based on the numerical predictions. An equation that approximated the shape of the failure locus was also suggested, and this provided a convenient means of calculating the bearing capacity of circular foundations on a uniform clay and subjected to combined loading.

Gourvenec and Randolph (2002) presented the results of two and three-dimensional finite element analyses of combined loading of strip and circular skirted foundations resting on homogeneous and non-homogeneous clay. The results were presented in terms of the shape of the failure envelopes in vertical, moment and horizontal loading space, and then

compared with data from similar studies where either soil non-homogeneity or three-dimensional geometry was investigated.

Doherty et al. (2004) investigated the effect of skirt flexibility on the overall load-displacement response of a caisson foundation embedded in clayey soil and subjected to vertical, horizontal and moment loads. The study was carried out numerically using the scaled boundary finite element method, to represent an elastic half-space, combined with shell finite elements to represent the caisson's skirt. The flexibility of the caisson's skirt was observed to have a significant influence on the load-displacement response, and charts were presented relating the dimensionless stiffness of the foundation to the relative stiffness of the skirt.

Later, Doherty et al. (2005) presented solutions for stiffness coefficients to represent the elastic behaviour of the caisson. The stiffness coefficients took into account the possibility of non-homogeneity in the soil (stiffness varying with depth), the geometry of the foundation, and the contribution to the stiffness from the skirt of the caisson foundation. Tabulated values allowed a simple curve fit to the stiffness values to be employed for particular cases. The accuracy of the method was tested against previous solutions for particular cases.

Cassidy et al. (2006) introduced a strain-hardening plasticity model that described the behaviour of caisson foundations when subjected to combined vertical, horizontal and moment loads in clay. The development and calibration of the model was based on centrifuge experimental results, theoretical knowledge (bearing capacity and upper bound plasticity theory) and numerical finite element studies. It was applicable to integrated wave-structure-soil analysis. This was demonstrated with example dynamic analyses of a proposed three legged jack-up in over 140 m water depth. The presented results showed how the caisson model could be used to study (a) optimum caisson geometries, (b) penetration and relative

movement of the foundations, including permanent deformation in extreme events, and (c) comparative behaviour between different footing types.

Bransby and Yun (2009) conducted plane-strain finite element analyses to investigate directly how the skirt geometry affected the undrained strip foundation capacity under combined horizontal-moment loading as well as the mechanisms occurring at failure. Conditions of both uniform and non-uniform undrained strength of the clay soil were considered. The results showed that deformation of the soil between external skirts could lead to significantly less foundation capacity than that of an equivalent embedded solid foundation. In addition, the failure envelopes for skirted foundations with different embedment ratios differed significantly. This made general recommendations for failure envelope shapes problematical. Finally, significant increase in foundation bearing capacity could be achieved by adding an intermediate skirt to the foundation, which resulted in a foundation capacity that was nearly equal to an embedded solid foundation.

Gourvenec and Barnett (2011) proposed closed-form expressions for undrained bearing capacity of skirted foundations under general in-plane loading, which was valid for a range of embedment ratios and soil shear strength heterogeneities. The expressions enabled the prediction of the ultimate limit states (V_{ult}, H_{ult} and M_{ult}) that provided the apex points of the failure envelope, and the shape of the normalised failure envelope. The results showed that the size and shape of failure envelopes of the skirted foundations under general loading were dependent on load combination, embedment ratio and degree of soil strength heterogeneity. However, the shape of the failure envelope in the (H, M/D) plane was most dependent on embedment ratio, while the level of vertical load and the degree of soil strength heterogeneity had a secondary effect.

Hung and Kim (2012) conducted three-dimensional finite element analyses to investigate the effects of embedment depth, non-homogeneity of clay and combined loads on

the undrained bearing capacities of bucket foundations. The undrained shear strength and Young's modulus of clay were assumed to vary linearly with depth, and the stress-strain response was simulated using the Tresca criterion. The bearing capacities were calculated and found to be largely dependent on the aspect ratio of the bucket foundation. Based on the results of the finite element analyses, new equations were proposed to calculate the vertical, horizontal, and moment bearing capacities as well as to define the capacity envelopes under general combined loads. In the proposed equations, the vertical capacity consisted of an end-bearing resistance and a skin friction resistance, whereas the horizontal capacity consisted of a normal resistance, a radial shear resistance, and a base shear resistance.

Mehravar et al. (2016) discussed the results of a three-dimensional finite element study addressing the effect of embedment ratio of caisson foundations on the undrained bearing capacity under uniaxial vertical (*V*), horizontal (*H*) and moment (*M*) loading. A series of equations was proposed to predict the ultimate vertical, maximum horizontal and moment bearing capacity factors. The undrained response of caisson foundations under combined *V*-*H* and *V*-*M* load space was studied and presented using failure envelopes generated with side-swipe method. The kinematic mechanism accompanying failure under uniaxial loading was addressed and presented for different embedment ratios. Predictions of the uniaxial bearing capacities were compared with other models, and it was confirmed that the proposed equations appropriately described the capacity of caisson foundations under uniaxial vertical, horizontal and moment loading in homogenous undrained soils.

2.6 SUMMARY OF LITERATURE REVIEW AND SCOPE OF THE STUDY

This section summarizes the literature on the response of bucket foundations under vertical loading, lateral loading and combined loading. The experimental investigations included laboratory 1g model tests, centrifuge tests and small scale field tests. Numerical analyses involved finite element analyses using commercial software packages and upper

bound plasticity methods to simulate the offshore loading regime and to analyze the response of bucket foundations.

Based on the literature review, the following are the key points:

Under vertical loading

- The numerical analyses and experimental results have indicated that the ratio of ultimate vertical bearing capacity of skirted foundation to pier foundation corresponds to a value close to of 0.93.
- The vertical bearing capacity increases appreciably with higher skirt length. The enhancement in the vertical capacity is observed to be greater in the case of sand with lower relative density.
- Under the application of vertical load, the soil mass entrapped within the bucket foundation is displaced with the foundation as a rigid body. Arching phenomenon is noted in the soil mass surrounding the bucket foundation. The arching phenomenon leads to an increase of earth pressure along the embedment length of the bucket foundation.
- In a two-layered soil profile consisting of sand and clay, the vertical depth of the second layer from the base of the bucket foundation significantly affects the vertical bearing capacity.

Under lateral loading

- The inclusion of skirt increases the lateral capacity noticeably as compared to the unskirted surface foundation. Under the applied lateral load, the skirted foundation fails by rotational translation as compared to sliding translation of the unskirted foundation.
- Under the action of monotonic load on bucket foundation embedded in sandy bed, the instantaneous centre of rotation of the foundation is obtained right under the bucket lid. Under cyclic load, the centre of rotation lies at greater depths.

- From numerical investigation in sand, gradual formation of gap at the top of soil plug is noted. Under large lateral load or near failure, no contact between the soil plug and bucket lid is observed, which indicates that the total load is transferred to the surrounding soil by the bucket skirt. At large rotations, the moment resistance is almost entirely produced by horizontal and skin friction stresses acting on the skirt perimeter.
- In laboratory tests on modified suction caissons in sand, load-deflection curves show softening behaviour in displacement-controlled method and not in load-controlled method. The softening behaviour decreases with higher load eccentricity value. At failure, the rotation centre is found to lie at a shallower depth in case of displacement-controlled method compared to load-controlled method.
- From laboratory cyclic lateral tests conducted in sand, the lateral displacement is observed to increase with increasing number of cycles. The lateral stiffness decreases initially during the first cycle and the decrease rate is lower for increasing number of cycles.
- In both sandy and clayey soils, under moment loading, the comparison of laboratory and field cyclic load test results in non-dimensional form shows similar response. However, under vertical loading, considerable difference in the response is seen.

Most of the numerical studies considered two-dimensional models, either two-dimensional plane strain condition or axisymmetric geometries. Hence, investigation is necessary by considering three-dimensional models and non-linear soil behaviour to capture a more realistic response. Based on the literature review, the scope of the study is outlined below. It is necessary to consider prototype sizes which would provide a better insight for the design of monopod bucket foundations, specifically related to:

- effect of soil plug on vertical bearing capacity,
- depth factor under vertical loading,

- lateral response for a wide range of loading heights of the resultant of wind, current and water waves acting along the wind turbine tower,
- variation of depth of point of rotation of the bucket foundation with loading height,
- effect of superstructure load and lateral loading height on the failure mechanism,
- effect of initial stiffness in order to avoid resonance condition of the wind turbine foundation system, and
- long-term lateral response of bucket foundation under cyclic lateral loads resembling offshore loading conditions.

Chapter 3

THREE-DIMENSIONAL FE MODEL

3.1 INTRODUCTION

This chapter focuses on the theory of finite element method used for computer implementation in order to simulate the response of monopod bucket foundation under vertical and lateral loading conditions. The numerical simulation was carried out using finite element software Abaqus (Dassault Systèmes 2010).

Finite element method is suitable for problems with complex geometries. In this method, the domain is discretized into a finite number of elements and variational approach is used to form an approximation of the solution over the discretized elements in the domain. The elements are connected to each other by nodes and the arrangement of the discretized elements is commonly known as mesh. The element matrix formulation, the convergence criteria and the numerical modelling aspects are described below.

3.2 FINITE ELEMENT FORMULATION

3.2.1 Formulation of Element Matrix

The element formulation of finite element analysis is derived from the principle of virtual work. The principle states that the externally applied forces (F) are equal and opposite to the internal stresses, and is expressed as:

$$F = \int_{Vol} [B]^T \sigma \, dV \tag{3.1}$$

where σ is the vector of current stress state of the body and $[B]$ is the strain-displacement matrix.

The strain matrix $\{\Delta\varepsilon\}$is given as:

$$\{\Delta\varepsilon\} = [B]\{\Delta d\}_n \tag{3.2}$$

where matrix $[B]$ contains only derivatives of the shape functions N, while $\{\Delta d\}_n$ contains the list of nodal displacements of a single element.

The above equation can also be in terms of applied nodal force and the corresponding nodal displacement.

$$\{F\} = [K_E]\{\Delta d\}_n \tag{3.3}$$

The $[K_E]$ is the element stiffness matrix and can be expressed as:

$$[K_E] = \int_{Vol} [B^T][D][B]dV \tag{3.4}$$

where $[D]$ is the constitutive matrix which represents the stress-strain relationship. The constitutive matrix considered in the numerical simulation is presented in the next section.

3.2.2 Formulation of Elasto-Plastic Constitutive Material Model

In this study, the responses of medium dense and very dense sandy soils are simulated using Mohr-Coulomb elasto-plastic material model. Under the application of load on the soil mass, the soil mass starts deforming elastically and beyond a certain point of load application, it begins to yield. Yield condition in general, can be defined as the limit of elasticity and the beginning of plastic deformation under any possible combination of stresses. In other words, yield criteria for frictional materials would be a function of the first stress invariant or the mean pressure.

Coulomb's yield criterion is given by Equation (3.5).

$$\tau_f = c' + \sigma_n' \tan \phi' \tag{3.5}$$

where τ_f and σ_n' are the shear and effective normal stresses on the failure plane, and the cohesion, c', and angle of shearing resistance, ϕ', are material parameters.

Coulomb's law of friction can be extended to the general state of stress in soils. Using the Mohr's circle of stress, Equation (3.5) can be rewritten as:

$$\sigma_{1f}' - \sigma_{3f}' = 2c' \cos \phi' + (\sigma_{1f}' + \sigma_{3f}') \sin \phi' \tag{3.6}$$

Equation (3.6) is called the Mohr-Coulomb failure criterion, where σ'_{1f} and σ'_{3f} are the major and minor effective principal stresses at failure. This is adopted as the yield function in the present model as follows:

$$F'(\{\sigma'\}, \{k\}) = \sigma_{1f}' - \sigma_{3f}' - 2c' \cos \phi' - (\sigma_{1f}' + \sigma_{3f}') \sin \phi' \tag{3.7}$$

The yield function, F', is a scalar function of stress (expressed in terms of either the stress components or stress invariants) and state parameters, $\{k\}$. In principal effective stress space, the yield function plots as an irregular hexagonal cone as shown in Figure 3.1. The six-fold symmetry again arises from the possible permutations of principal stresses (Potts and Zdravkovic 1999).

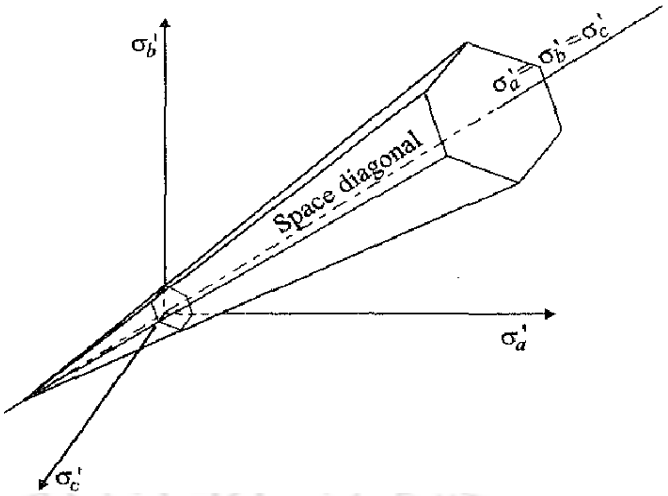

Figure 3.1 Representation of Mohr-Coulomb yield surface in three-dimensional principal stress space

The incremental total strain generated in the material, $\{\Delta\varepsilon\}$, is divided into two components as in Equation (3.8).

$$\{\Delta\varepsilon\} = \{\Delta\varepsilon^e\} + \{\Delta\varepsilon^p\} \tag{3.8}$$

where $\{\Delta\varepsilon^e\}$ and $\{\Delta\varepsilon^p\}$ are elastic and plastic strain components. Within elastic range, elastic deformation can easily be determined using Hooke's law.

Moreover, with further application of load, the combination of stresses reaches the yield surface and the material begins to deform plastically. In order to determine the magnitude of plastic deformation once the stress state is on yield surface, plastic strain increment or plastic strain rate is determined by flow rule given by Equation (3.9).

$$\Delta\varepsilon_i^p = \Lambda \frac{\partial P(\{\sigma\},\{m\})}{\partial \sigma_i} \tag{3.9}$$

where $\Delta\varepsilon_i^p$ represents six components of plastic strain rate (or increment). P and Λ are the plastic potential function and the scalar multiplier. The plastic potential function can be expressed by Equation (3.10).

$$P = (\{\sigma'\},\{m\}) \tag{3.10}$$

where {m} is a state parameter vector.

The relationship between the yield and plastic potential functions is shown in the Figure 3.2. As the soil is in plastic deformation stage, the plastic potential function passes through the current stress state (point A), which is on the yield surface.

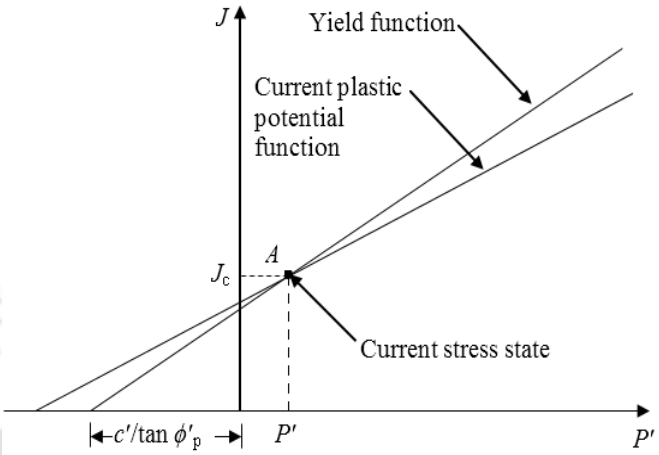

Figure 3.2 Relationship between the yield and plastic potential function

The incremental stress generated due to the application of load can be obtained from Equation (3.11).

$$\{\Delta\sigma'\} = \left[D^{ep}\right]\{\Delta\varepsilon\} \tag{3.11}$$

Based on substitution, the elasto-plastic constitutive matrix, $[D^{ep}]$ is given by Equation (3.12).

$$\left[D^{ep}\right] = [D] - \frac{[D]\left\{\frac{\partial P(\{\sigma'\},\{k\})}{\partial\sigma'}\right\}\left\{\frac{\partial F(\{\sigma'\},\{k\})}{\partial\sigma'}\right\}^T[D]}{\left\{\frac{\partial F(\{\sigma'\},\{k\})}{\partial\sigma'}\right\}^T[D]\left\{\frac{\partial P(\{\sigma'\},\{m\})}{\partial\sigma'}\right\} - \frac{1}{\Lambda}\left\{\frac{\partial F(\{\sigma'\},\{k\})}{\partial k}\right\}^T\{\Delta k\}} \tag{3.12}$$

To summarise, the elastic behaviour of the medium dense and very dense sandy soils is defined by Young's modulus of elasticity (E_{soil}) and Poisson's ratio (μ), whereas plasticity behaviour is defined by cohesion (c'), effective angle of internal friction (ϕ') and dilation angle (δ).

3.2.3 Modelling of Contact Interface

The interface between soil and foundation i.e. the contact between the respective interacting surfaces can be established using two types of contact discretization options,

namely node-to-surface discretization and surface-to-surface discretization. These approaches use master-slave concept in which master surface is stiffer as compared to slave surface. The master surface is generally more refined as compared to the slave surface and can penetrate into the slave surface depending on the type of discretization used for the analysis.

In node-to-surface discretization method, the node of the slave surface interacts with the point of projection of nearby nodes of the master surface as shown in Figure 3.3. In this discretization method, the penetration of slave nodes into the master surface is constrained. The master nodes however, can penetrate the slave surface, as shown in Figure 3.4.

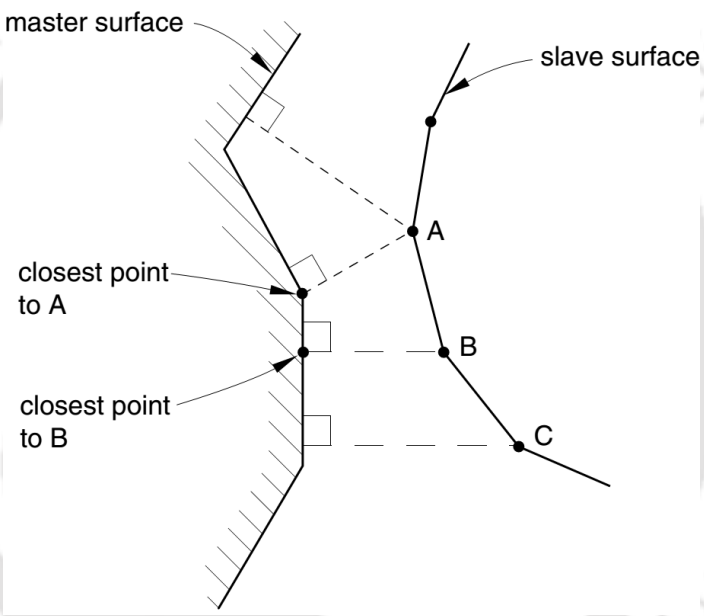

Figure 3.3 Node-to-surface contact discretization approach

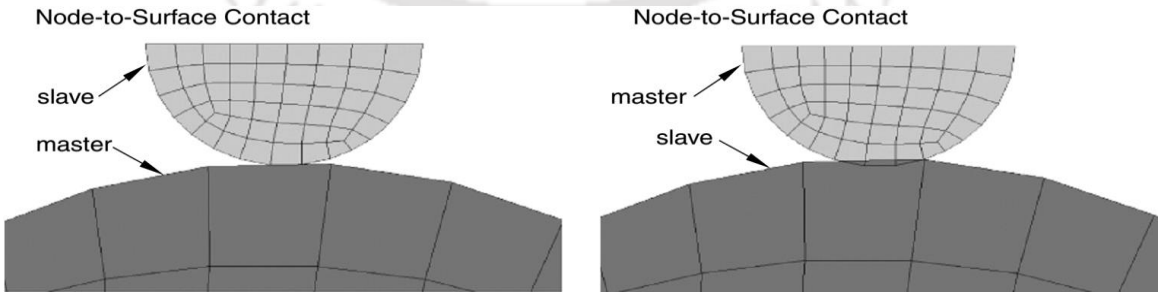

Figure 3.4 Contact enforcement for node-to-surface discretization approach (Dassault Systèmes 2010)

The surface-to-surface formulation enforces contact conditions in an average sense over regions nearby adjacent to slave nodes rather than only at individual slave nodes (Figure 3.5). The averaging regions are approximately centered on slave nodes, so that each contact constraint will predominantly consider one slave node but will also consider adjacent slave nodes. Some penetration may be observed at individual nodes; however, large undetected penetrations of master nodes into the slave surface do not occur with this discretization. The contact direction is based on an average normal of the slave surface in the region surrounding a slave node.

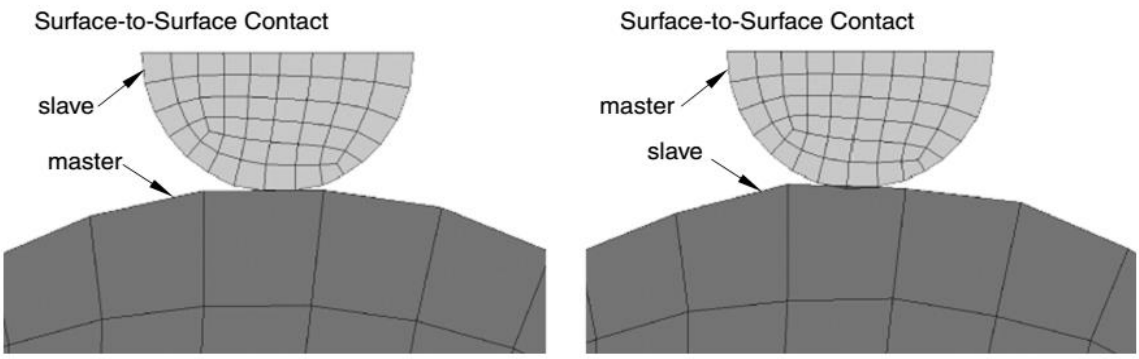

Figure 3.5 Contact enforcement for surface-to-surface discretization approach (Dassault Systèmes 2010)

In contact simulation, it becomes necessary to specify in advance about the tracking approach which accounts for relative motion of two interacting surfaces in the simulation. There are two tracking approaches available in Abaqus/Standard, namely, finite sliding tracking approach and small sliding tracking approach. Finite sliding tracking approach allows arbitrary relative separation, sliding and rotation of the surfaces in contact. For finite sliding contact, the connectivity of currently active contact constraints changes upon relative tangential motion of contacting surfaces. The small sliding tracking approach assumes that there is relatively little sliding of one surface along the other and is based on linearized approximations of the master surface per constraint. The group of nodes involved with

individual contact constraints are fixed throughout the analysis for small sliding nodes, although the active/inactive status of these constraints typically changes during the analysis

3.2.4 Convergence Criteria in Solving Nonlinear Problems

In nonlinear analysis, the solution cannot be calculated by solving a single system of equations, as would be done in a linear problem. Instead, the solution is found by specifying the loading as a function of time and incrementing the time to obtain the nonlinear response. Therefore, Abaqus/Standard breaks the simulation into a number of time increments and finds the approximate equilibrium configuration at the end of each time increment. Using the Newton method, it often takes several iterations to determine an acceptable solution to each time increment.

Consider the external forces, F, and the internal (nodal) forces, I, acting on a body (Figure 3.6). The internal loads acting on a node are caused by the stress elements that are attached to that node. For the body to be in equilibrium, the external and internal forces must balance each other and can be expressed as:

$$F - I = 0 \tag{3.13}$$

The nonlinear response of a structure to a small load increment, ΔF, is shown in Figure 3.7. Abaqus/standard uses the structure's stiffness, K_0, which is based on its configuration at u_o and ΔF to calculate a displacement correction, c_a, for the structure. Using c_a, the structure's configuration is updated to u_a.

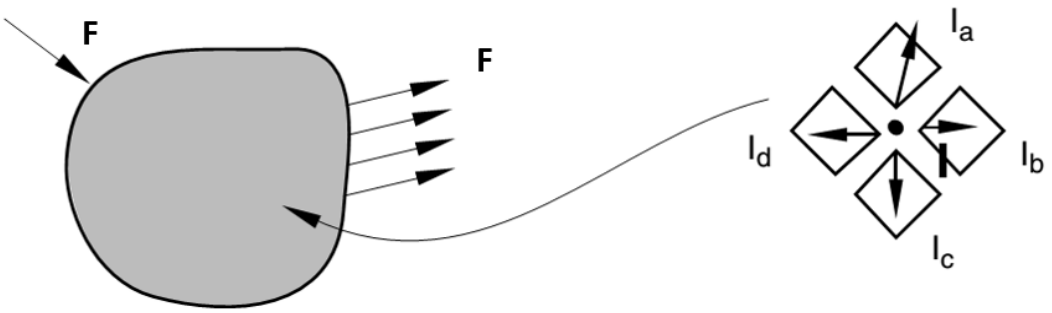

Figure 3.6 Externally applied force on a body and internal forces acting in one of the nodes of the body (Dassault Systèmes 2010)

Abaqus/Standard then calculates the structure's internal forces, I_a in this updated configuration. The difference between the total applied load (F) and I_a can be calculated as

$$R_a = F - I_a \tag{3.14}$$

where, R_a is the force residual for the iteration.

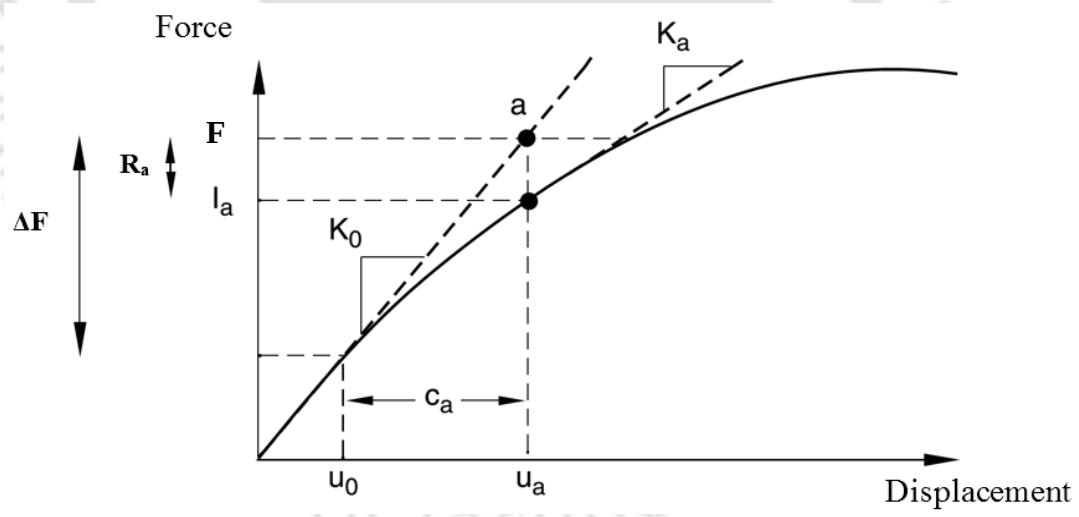

Figure 3.7 First iteration in an increment

If R_a is zero at every degree of freedom in the model, point *a* in Figure 3.7 would lie on the force-displacement curve and the structure would be in equilibrium. In a nonlinear problem, as R_a will never be exactly zero, so Abaqus/Standard compares it to a tolerance value. If R_a is less than this force residual tolerance at all nodes, Abaqus/Standard accepts the solution as being in equilibrium. By default, this tolerance value is set to 0.5% of an average

force in the structure, averaged over time. Abaqus/Standard automatically calculates this spatially and time-averaged force throughout the simulation.

If R_a is less than the current tolerance value, F and R_a are considered to be in equilibrium and u_a is a valid equilibrium configuration for the structure under the applied load. However, before Abaqus/Standard accepts the solution, it also checks that the last displacement correction, c_a, is small relative to the total incremental displacement, $\Delta u_a = u_a - u_0$. If c_a is greater than a fraction (1% by default) of the incremental displacement, Abaqus/Standard performs another iteration. Both convergence checks must be satisfied before a solution is said to have converged for that time increment.

If the solution from an iteration is not converged, Abaqus/Standard performs another iteration to try to bring the internal and external forces into balance. First, Abaqus/Standard forms the new stiffness, K_a, for the structure based on the updated configuration, u_a. This stiffness, together with the residual R_a, determines another displacement correction, c_b, that brings the system closer to equilibrium (point b), shown in Figure 3.8.

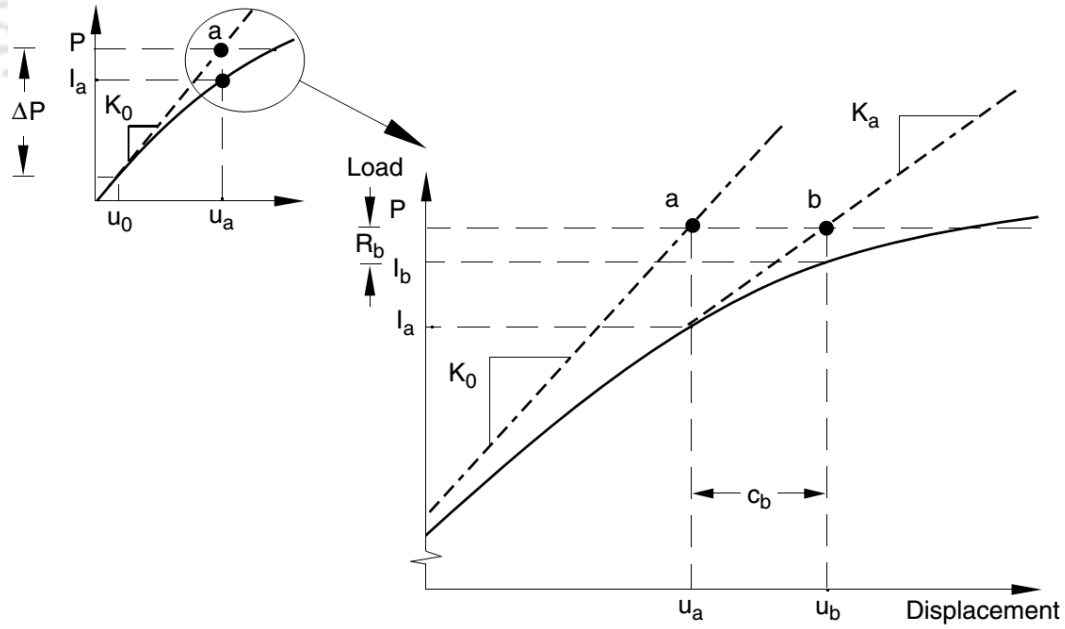

Figure 3.8 Convergence criteria in Abaqus/Standard (Dassault Systèmes 2010)

Abaqus/Standard calculates a new force residual, R_b, using the internal forces from the structure's new configuration, u_b. Again, the largest force residual at any degree of freedom, R_b, is compared against the force residual tolerance, and the displacement correction for the second iteration, c_b, is compared to the increment of displacement, Δu_b. If necessary, Abaqus/Standard performs further iterations.

For each iteration in a nonlinear analysis Abaqus/Standard forms the model's stiffness matrix and solves a system of equations. Therefore, the computational cost of each iteration is close to the cost of conducting a complete linear analysis, making the computational expense of a nonlinear analysis potentially many times greater than the cost of a linear analysis. Since it is possible with Abaqus/Standard to save results at each converged increment, the amount of output data available from a nonlinear simulation can also be much greater than that available from a linear analysis of the same geometry.

3.2.5 Numerical Modelling Using Abaqus

The three-dimensional finite element modelling of the behaviour of bucket foundation, embedded in sandy seabed and subjected to offshore loading conditions, have been carried out using Abaqus V6.10. Due to the geometric and loading symmetry, only half of the bucket foundation embedded in the soil domain is modelled. Three-dimensional finite element model of monopod bucket foundation embedded in the soil domain is shown in Figure 3.9. The boundary conditions were applied in the soil domain by constraining displacements in every direction at the base. In addition, normal displacements were constrained in the symmetric plane, and lateral displacements were restrained along the curved periphery of the soil domain.

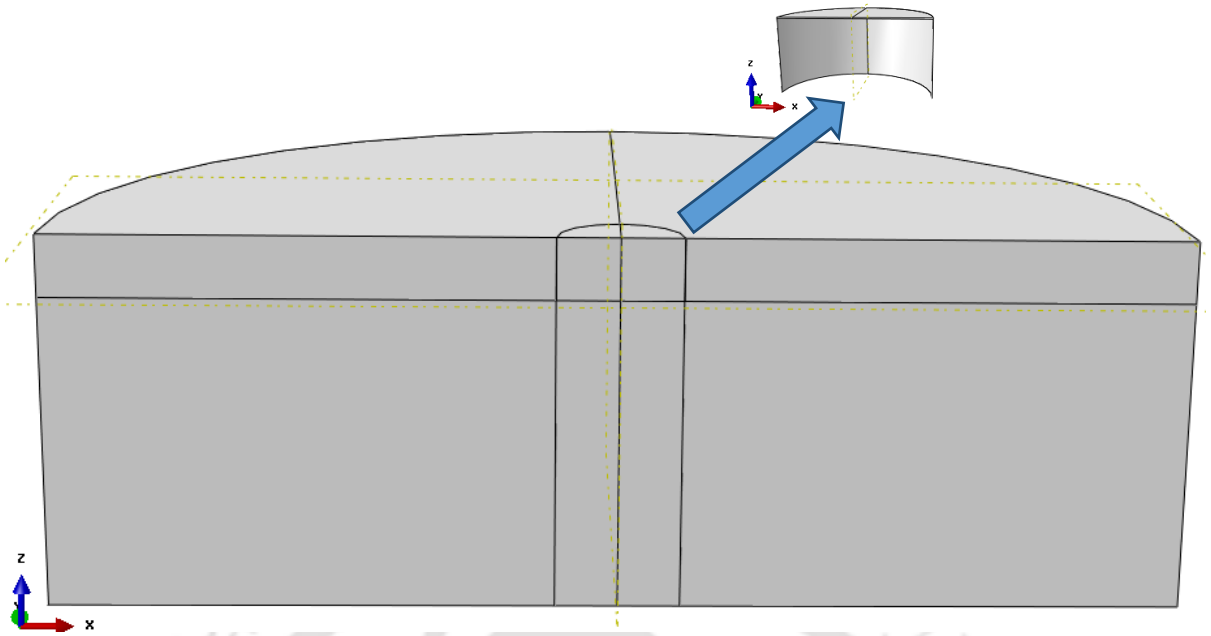

Figure 3.9 Three-dimensional finite element model of bucket foundation and soil domain

3.2.6 Material Properties

The properties of the steel material used to model the linear elastic behaviour of the bucket foundation are listed in Table 3.1.

Table 3.1 Material properties of bucket foundation considered in the numerical study

Steel parameter	Value
Buoyant unit weight (γ'_{steel}), kN/m^3	68.5
Modulus of elasticity (E_{steel}), kPa	210 × 10^6
Poisson's ratio (μ_{steel})	0.15

The study considers that the bucket foundation is embedded in sandy seabed. Both medium dense and very dense sands have been considered to model the vertical and lateral response of bucket foundation. The nonlinearity of the sandy soil constituting the seabed is modelled using Mohr-Coulomb elasto-plastic material model obeying non-associative flow rule. In finite element analyses, even for sandy soil, a very small cohesion value needs to be specified to avoid the convergence issues.

The modulus of elasticity (E_{soil}) of the soil mass varies with the mean stress, as expressed in Equation (3.15).

$$E_{soil} = \kappa.\sigma_{at}.\left(\frac{\sigma_m}{\sigma_{at}}\right)^{\lambda} \tag{3.15}$$

where, σ_{at} = 100 kN/m^2 is reference stress, κ determines the soil stiffness at the reference stress state, λ rules the stress dependency of the soil stiffness and σ_m is the mean principal stress. The procedure for experimental determination of the parameters κ and λ is elaborated in Appendix-A. The values of these parameters utilized to simulate the non-linearity of the medium and very dense sand have been taken from EAU (2004) and are reported in Table 3.2.

Table 3.2 Soil parameters used for the numerical study

Soil parameter	Medium dense sand	Very dense sand
Effective unit weight (γ'_{soil}), kN/m^3	9.0	11.0
Oedometric stiffness modulus, κ	400	600
Oedometric stiffness modulus, λ	0.60	0.55
Poisson's ratio, μ	0.25	0.25
Internal friction angle, ϕ'	35°	40°
Dilation angle, δ'	5°	10°
Cohesion (c'), kN/m^2	0.1	0.1

3.2.7 Numerical Simulation

The vertical and lateral extents of the soil domain have been determined based on several trials. The soil domain is fixed such that the domain boundary does not impart any boundary effects to the response of the foundation. Once, the vertical and lateral extents of soil domain are fixed, mesh convergence study is conducted. The results of domain size and mesh convergence analyses are reported in Appendix-B. Once the extents of soil domain and the number of elements required to obtain reasonably accurate results are known, further analyses have been carried out for a wide range of bucket geometries, superstructure loads and load cases.

3.2.8 Modelling Vertical Response of Foundation

3.2.8.1 Numerical modelling steps of vertical bearing capacity

The vertical response of the bucket foundation was also compared with that of two other foundation types made of the same steel material, namely, surface circular foundation and embedded solid foundation.

The numerical simulation of vertical bearing capacity is carried out in several steps. Firstly, the geostatic step is invoked and gravity load is applied to establish the initial stress state in the soil domain. Ideally, in this step, the applied loads and generated initial stresses should exactly equilibrate to produce zero deformations. However, in complex and nonlinear problems, Abaqus/Standard iterates during the geostatic step in order to obtain a stress state that equilibrates the prescribed boundary conditions and loads. In the second step, contact between the foundation and soil is established. The foundation being stiffer is considered as master surface and soil as slave surface. The contact discretization approach has been discussed in the earlier section. In the third step, displacement-controlled vertical load is applied at the centre of the foundation top. The details of interface modelling aspects and load application procedures are discussed in the following sections.

3.2.8.2 Modelling of interfaces

The bucket foundation is a hollow cylindrical steel structure, capped at the top with vents. As the foundation is installed with the vents kept open, the skirt entraps the soil inside. After the installation, the vents are closed and the entrapped soil mass acts as an integral part of the foundation and contributes to the vertical bearing capacity.

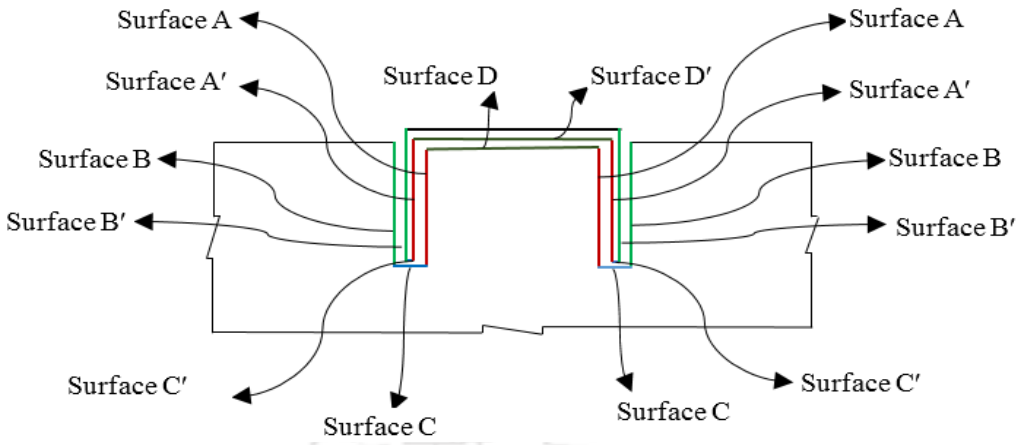

Figure 3.10 Schematic diagram showing the interaction between the various surfaces of bucket foundation and soil mass

Under vertical load, during the downward movement of the foundation, no relative movement of the inside soil mass is allowed with respect to the internal bucket surface. Numerically, the interface between the internal bucket skirt surface (surface A′) and the corresponding soil surface (surface A), shown in Figure 3.10, is defined by the normal component of frictional force and no sliding or no relative movement of one surface relative to the other is allowed. Similar interface behaviour is assigned between the underside of the bucket lid (surface D′) and the soil surface underneath (surface D), as well as the skirt tip (surface C′) and the soil below the skirt (surface C).

The interface between the external bucket skirt surface (surface B′) and the surrounding soil surface (surface B) are modelled by prescribing the normal and tangential components of frictional force. As a result, the bucket moves downward relative to the adjacent exterior soil mass. The above mentioned interaction steps have enabled the simulation of the response of bucket foundation under vertical load.

In a similar manner, the interface behaviour of surface circular foundation and embedded solid foundation have also been modelled. The schematic diagram of a surface circular foundation of 0.3 m thickness, resting on the surface of the sand bed, is shown in Figure 3.11.

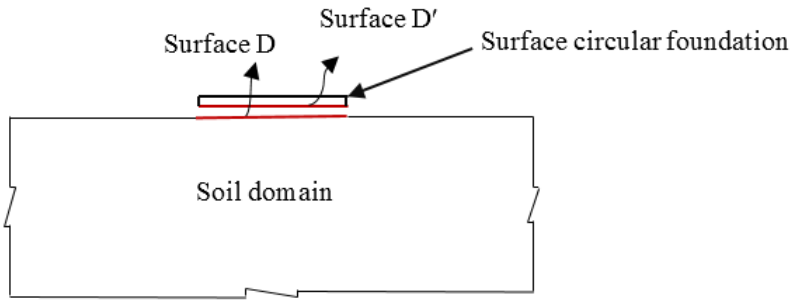

Figure 3.11 Schematic diagram showing the interaction between surface circular foundation and soil surface

The surface D′ represents the bottom surface of the circular foundation, which interacts with the top soil surface D. This interaction is modelled as rough, and the relative movement of the nodes between the nodes of the two surfaces are restrained from moving relative to each other. Under the application of vertical load, normal interaction is prescribed between the surfaces D′ and D, and the nodes are constrained to move together only in the downward direction.

Figure 3.12 shows the schematic diagram of the surfaces of the embedded solid foundation interacting with the soil surfaces. The embedded solid foundation has two surfaces, namely, a vertical surface (Surface A′) and a horizontal surface at the base (surface B′). The corresponding soil surfaces interacting with these two foundation surfaces are surface A and surface B. Under the action of vertical load, the vertical surface (surface A′) of embedded solid foundation moves downwards into the soil domain, with respect to the respective interacting soil surfaces. Hence, the interface behaviour is modelled with both tangential and normal components of frictional force. No separation or gap formation is allowed to take place between the interacting surfaces. The base of the foundation (surface B′) is modelled to behave similar to a rough foundation and only the normal component of frictional force is prescribed. Thus, the nodes constituting the foundation surface (surface B′) and soil surface (surface B) are constrained to move vertically and restrained against any lateral movement.

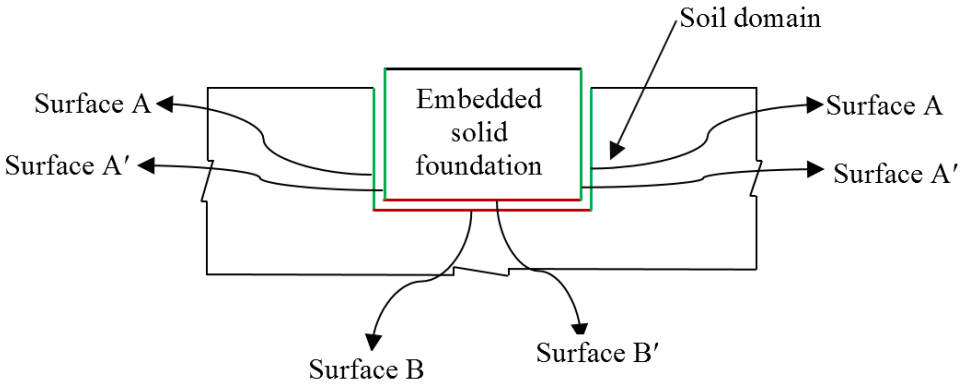

Figure 3.12 Schematic diagram showing the interaction between soil surfaces and corresponding embedded solid foundation surfaces

3.2.8.3 Loading details

The discretized models of bucket foundation, surface circular foundation and embedded solid foundation are shown in Figures 3.13-3.15. In each of the foundation types, the top centre node is assigned as the reference point. As the foundations are assumed to behave in a rigid manner, rigid body constraint is then used to tie all other nodes (shown in red colour) to the respective reference point. Thereafter, displacement-controlled vertical load is applied at the reference point of the respective foundation, till failure.

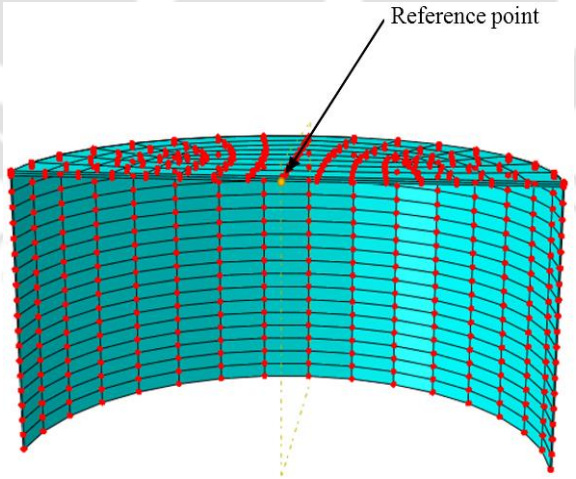

Figure 3.13 Reference point connecting the nodes of discretized bucket foundation (D = 12 m & L = 12 m)

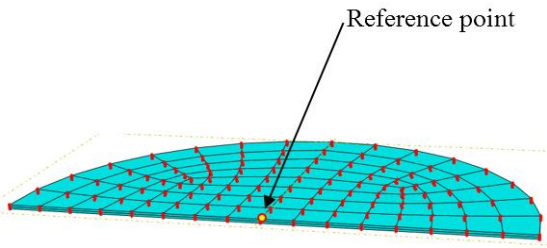

Figure 3.14 Reference point connecting the nodes of discretized surface circular foundation (D = 12 m)

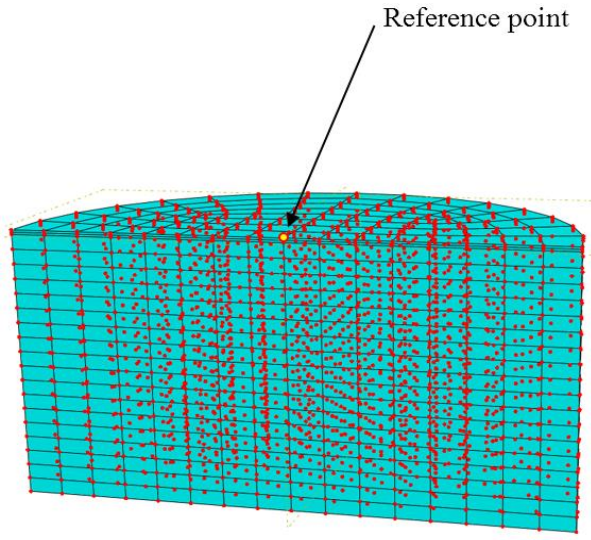

Figure 3.15 Reference point connecting the nodes of discretized embedded solid foundation (D = 12 m & L = 12 m)

3.2.9 Modelling Lateral Response of Foundation

3.2.9.1 Numerical modelling steps of lateral capacity of bucket foundation

The numerical simulation of lateral bearing capacity bucket foundations is carried out in four steps. In the first geostatic step, gravity load is applied within the soil domain. In the second step, contact between the foundation and soil is established. The interfaces between the foundation and the soil are discussed in the following section. In the third step, vertical load equal to the dead weight of the superstructure is applied at the lid centre of the bucket foundation. In the fourth step, lateral load is applied as displacement at the desired loading height above the bucket foundation. The details of the interface modelling and load application procedure are discussed below.

3.2.9.2 Modelling of interfaces

The interaction between the bucket foundation and soil is represented by a schematic diagram as shown in Figure 3.16.

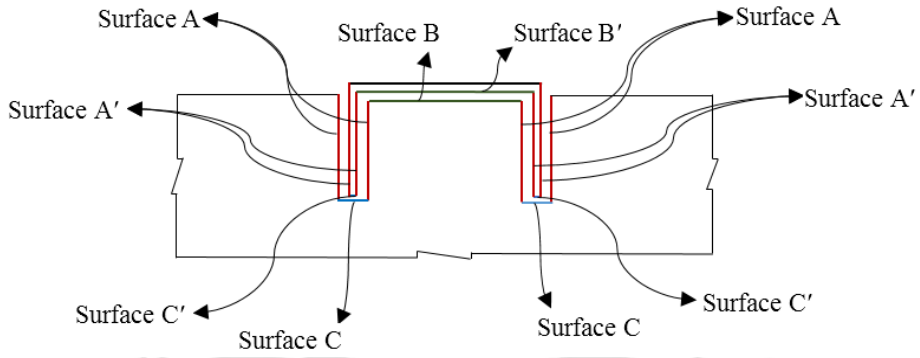

Figure 3.16 Schematic diagram of surfaces of soil mass interacting with surfaces of bucket foundation

The interior and exterior bucket surfaces along the bucket length are represented by surface A′. At rest, the bucket foundation surface A′ is in complete contact with adjacent soil surface (represented by A here). Similarly, the surface under bucket lid and skirt tip (surface B′ and surface C′) are in complete contact with the respective underlying soil surfaces (Surface B and Surface C). The interacting surfaces have been represented with the same colour code (as shown in Figure 3.16).

Node-to-surface interaction is used to establish contact along interfaces between the bucket and soil. The interaction between surfaces A and A′ is prescribed by specifying both the tangential and normal components of frictional force. Under the application of lateral load, the bucket skirt can slide upward or downward but no separation or gap formation is allowed in due course of movement. The interfaces between the bucket lid and the underlying soil mass (i.e. between surfaces B′ and B) and between the skirt tip and the soil below (i.e. between surfaces C′ and C) have been established by prescribing only the normal component of frictional force, and separations between the corresponding interacting surfaces are activated.

3.2.9.3 Loading details

In the offshore environment, resultant lateral load arising from the action of wind currents and water waves act above the foundation lid. The application of the resultant load is simulated by defining two reference points. Firstly, all underside lid nodes of the bucket foundation are tied to the central underside node (reference point 1), as shown in Figure 3.17. In order to apply the eccentric lateral load above the bucket lid, another point (reference point 2) is created at that particular loading height (Figure 3.18). Reference point 1 is then tied to reference point 2 using rigid body constraint. Thus, the distance between reference points 1 and 2 can be varied depending upon the loading height of the resultant lateral load.

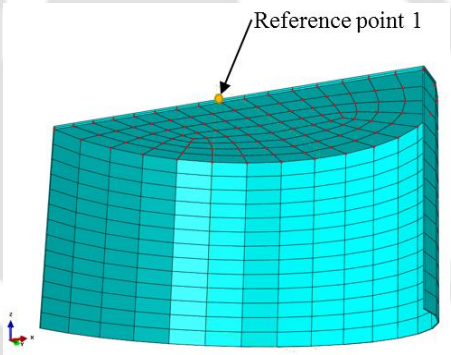

Figure 3.17 Reference point 1 connecting the nodes of discretized bucket foundation

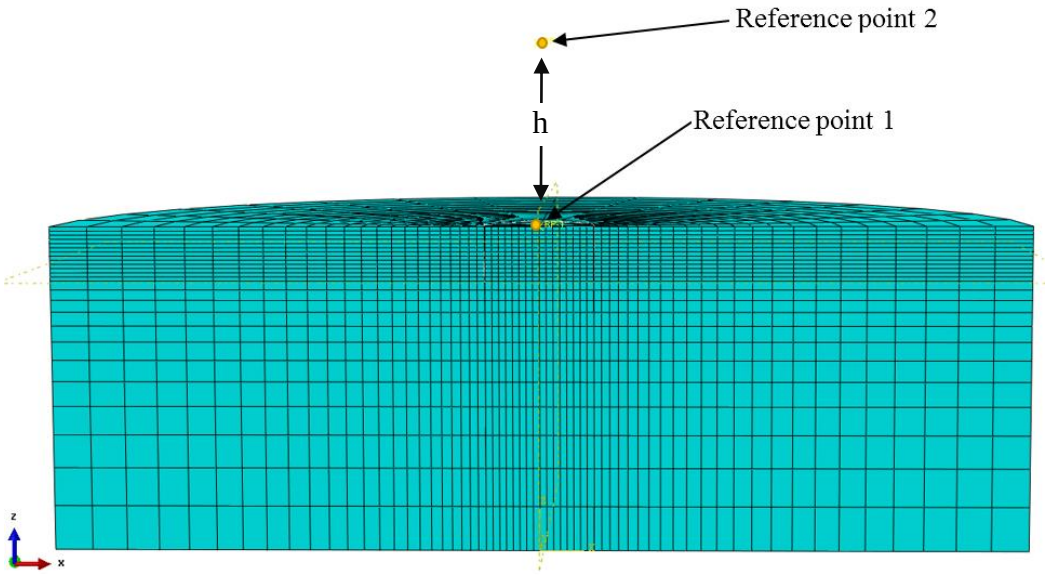

Figure 3.18 Reference points indicating the eccentric location above the foundation lid for lateral load application

Chapter 4

VERTICAL LOAD-RESPONSE OF MONOPOD BUCKET FOUNDATIONS

4.1 INTRODUCTION

Studies on the behaviour of bucket foundations resting on granular soils under vertical compressive vertical loading are relatively limited in the literature (Eid 2012; Kim et al. 2014; Park et al. 2016). In most of the other previous studies, the bucket foundation was analyzed numerically as a skirted strip foundation using two-dimensional finite element analyses (FEA) or as a surface circular foundation using three-dimensional FEA without considering the skirt length (Mehravar et al. 2016). However, the three-dimensional geometry of the foundation should be modelled to consider the shape effect and the soil-bucket interaction (Hung and Kim 2012). An understanding of the mechanism by which the vertical superstructure load is transferred by the foundation to the seabed will ensure safe operation of the wind turbine foundation system.

This chapter deals with the three-dimensional numerical investigation of vertical bearing capacity and response of bucket foundations embedded in medium and very dense sandy seabeds. The roles of embedded length of bucket foundation and the entrapped soil plug on the vertical bearing capacity have been investigated by simulating and comparing the results with that of surface circular foundation and embedded solid foundation, respectively.

The results obtained from the analyses of numerical simulations are discussed in the following sections.

4.2 NUMERICAL RESULTS

Figure 4.1 shows the schematic diagrams of the surface circular foundation, bucket foundation and embedded solid foundation considered in this study. The foundation material properties and the soil properties have been listed in Table 3.1 and Table 3.2. The details of the foundation geometries are presented in Table 4.1. The thickness of the surface circular foundation, the bucket lid and its skirt were chosen as 0.1 m, 0.1 m and 0.03 m, respectively. The foundation diameters (D) were taken as 12, 15 and 18 m, with aspect ratio varying from 0.5 to 1 in the case of bucket and embedded solid foundations.

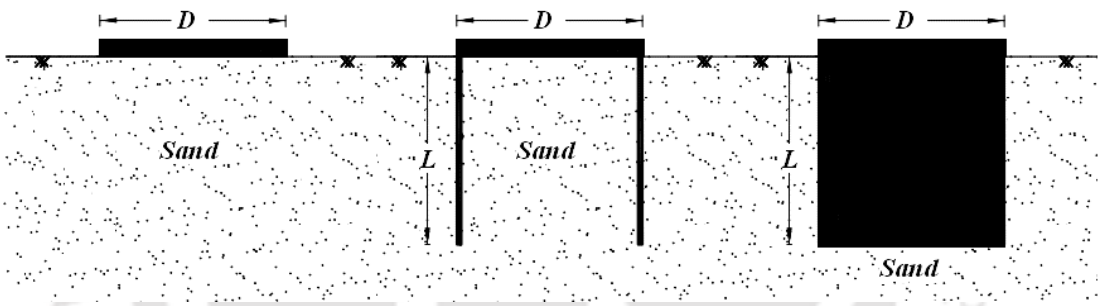

Figure 4.1 Foundations used for numerical analysis: (a) Surface circular foundation; (b) Bucket foundation; (c) Embedded solid foundation

The numerical simulation of vertical bearing capacity of the foundations was carried out by following the modelling steps as mentioned in Chapter 3. In order to eliminate the effect of foundation self-weight on the vertical response, the unit weight of the foundation was taken equal to that of the surrounding soil (Gourvenec and Mana 2011; Mana et al. 2010; Mana et al. 2013). When using the results in practice, the submerged weight of the foundation minus the submerged weight of displaced soil should be subtracted from the computed vertical load capacity of the foundation. The remainder capacity is the maximum superstructure load that the foundation can carry.

Table 4.1 Geometric details of the foundations under vertical loading

Diameter, *D* (m)	**Skirt length, *L* (m)**			**Aspect ratio (*L/D*)**
	Surface circular foundation	**Bucket foundation**	**Embedded solid foundation**	
12	-	6	6	0.5
	-	9	9	0.75
	-	12	12	1
15	-	7.5	7.5	0.5
	-	11.25	11.25	0.75
	-	15	15	1
18	-	9	9	0.5
	-	13.5	13.5	0.75
	-	18	18	1

The vertical load-settlement response of the surface circular, bucket and embedded solid foundations, lateral and shear stress variation along the embedded length of bucket foundation at failure, and their variation with increased embedment depth have been investigated for several aspect ratios. The extents of lateral and vertical movement of soil mass at failure, under the base or tip of the three foundation types, have been examined. Then, the failure mechanisms have been identified for the three foundation types.

In general, the ultimate or failure state of the foundation can be assumed to have reached when there is a continuous increase in settlement with no further increase in the load carrying capacity. But in certain cases, even though a large settlement has been reached, the vertical load capacity continues to increase incrementally. For such cases, the ultimate capacity can be defined corresponding to a settlement, which is sufficiently high to cause collapse of the structure. In the present study, the ultimate vertical capacity of the considered foundations is taken as the vertical load applied at the top centre of the foundation, which causes a vertical settlement equal to 10% of the respective foundation diameter, measured at the top centre (Eid 2012; Park et al. 2015).

4.2.1 Settlement of All Foundation Types under Vertical Loading

The variations of vertical load-settlement plots of surface circular, bucket and embedded solid foundations are depicted in Figure 4.2(a)-(c) and Figure 4.3(a)-(c), respectively for medium dense and very dense sandy seabeds. For all the foundation types, the settlement is noted to vary non-linearly with applied vertical load. The surface circular foundation is noted to yield the least vertical capacity as compared to the other two foundation types. The maximum vertical capacity is obtained for embedded solid foundation. The ultimate vertical capacities obtained for all three foundation types are presented in Table 4.2.

As compared to surface circular foundation with same diameter, the vertical capacity of bucket foundation is noted to improve due to the inclusion of skirt. For example, in case of surface circular foundation having 12 m diameter, the ultimate vertical bearing capacity is obtained as 117.07 MN in medium dense sand bed. For the bucket foundation of same diameter and skirt length of 6 m, the ultimate vertical capacity is noted to improve to 126.98 MN. For the solid foundation of same diameter and embedment length, the maximum ultimate vertical capacity of 151.08 MN is obtained, which is 1.19 times that of the bucket foundation.

In very dense sand, the ultimate vertical bearing capacity of the 12 m surface circular foundation is found to be 388.58 MN. For the same diameter of 12 m, the ultimate capacity of bucket foundation is noted to increase from 421.73 to 422.59 and 431.35 MN, as the aspect ratio is increased from 0.5 to 0.75 and 1.0. Similarly, for aspect ratios of 0.5, 0.75 and 1, the ultimate vertical capacities of the embedded solid foundations are 498.07, 510.07 and 538.68 MN, which are 1.18, 1.21 and 1.25 times that of the bucket foundation.

Similar trends of vertical load capacity vs. settlement are observed for the other foundation diameters in both sand types.

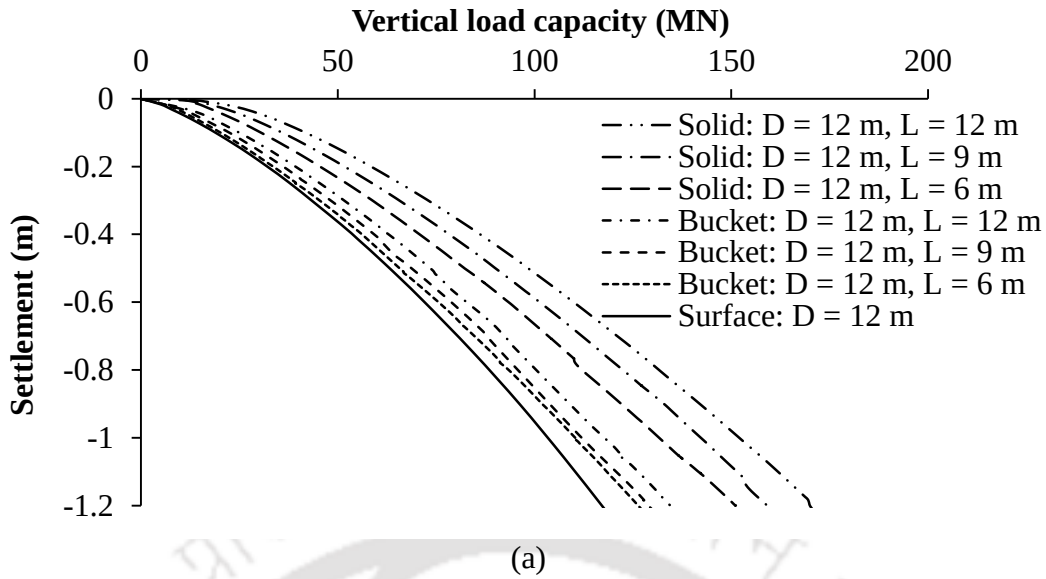
Vertical load capacity (MN)
0
50
100
150
200
Settlement (m)
0
-0.2
-0.4
-0.6
-0.8
-1
-1.2
Solid: D = 12 m, L = 12 m
Solid: D = 12 m, L = 9 m
Solid: D = 12 m, L = 6 m
Bucket: D = 12 m, L = 12 m
Bucket: D = 12 m, L = 9 m
Bucket: D = 12 m, L = 6 m
Surface: D = 12 m

(a)

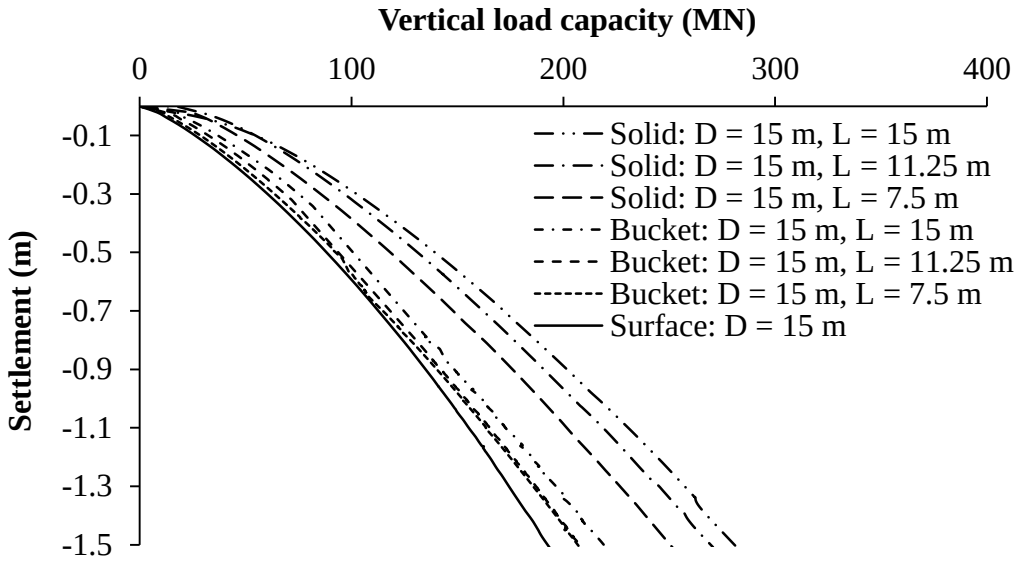
Vertical load capacity (MN)
0
100
200
300
400
Settlement (m)
-0.1
-0.3
-0.5
-0.7
-0.9
-1.1
-1.3
-1.5
Solid: D = 15 m, L = 15 m
Solid: D = 15 m, L = 11.25 m
Solid: D = 15 m, L = 7.5 m
Bucket: D = 15 m, L = 15 m
Bucket: D = 15 m, L = 11.25 m
Bucket: D = 15 m, L = 7.5 m
Surface: D = 15 m

(b)

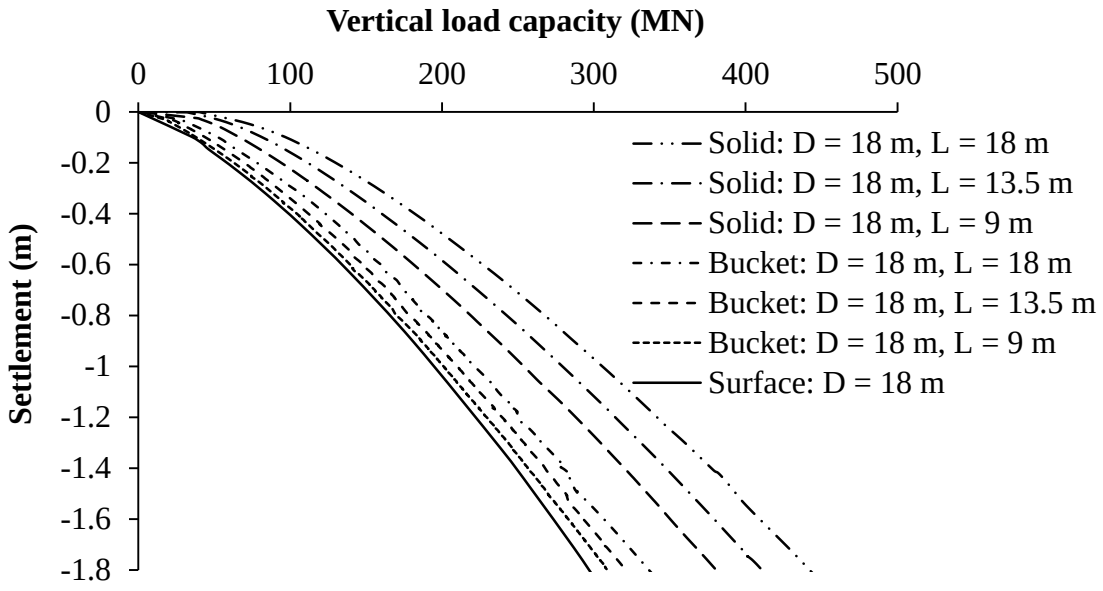

(c)

Figure 4.2 Vertical load vs. settlement response of the three foundation types in medium dense sand: (a) *D* = 12 m; (b) *D* = 15 m; (c) *D* = 18 m

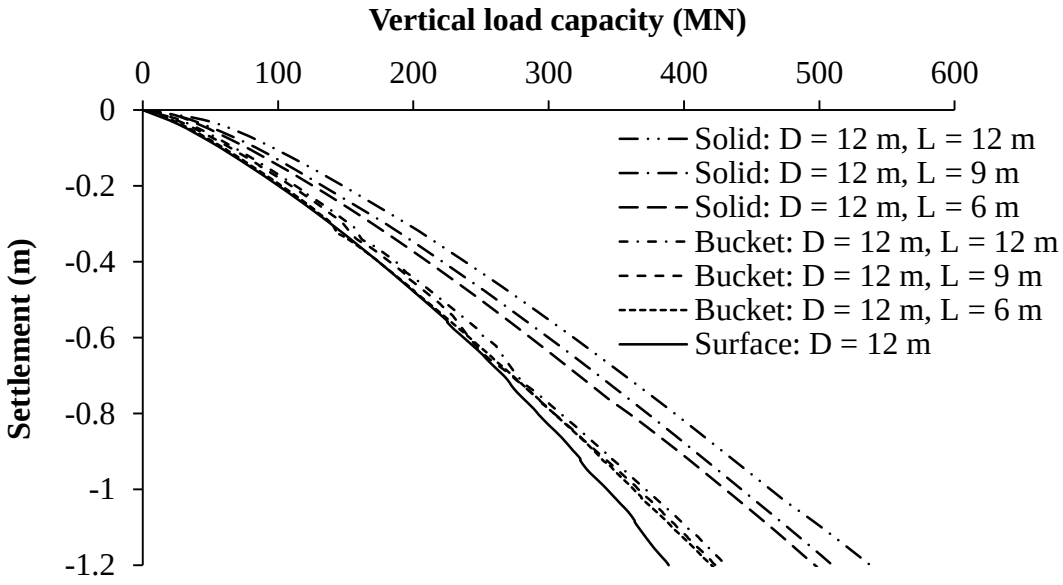

(a)

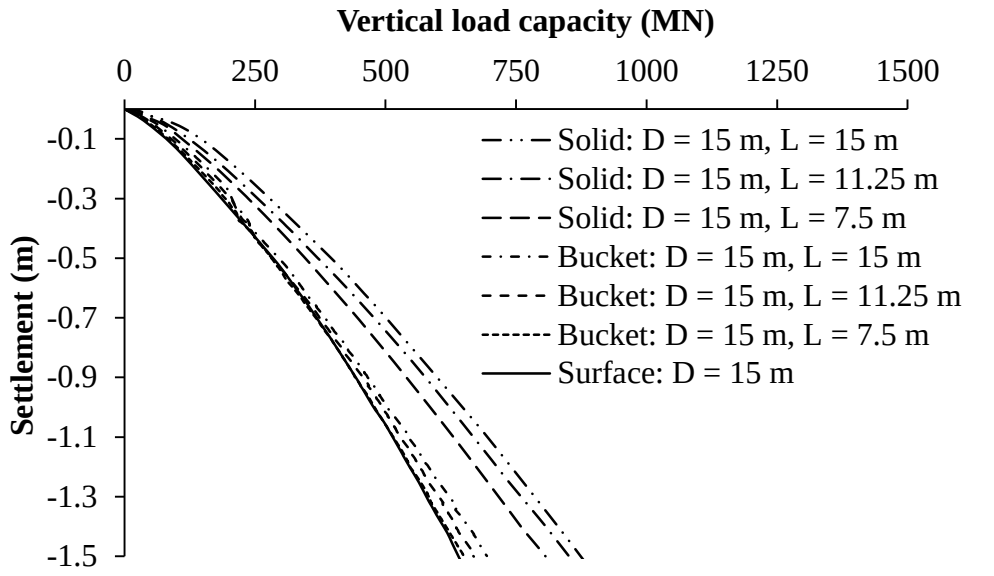

(b)

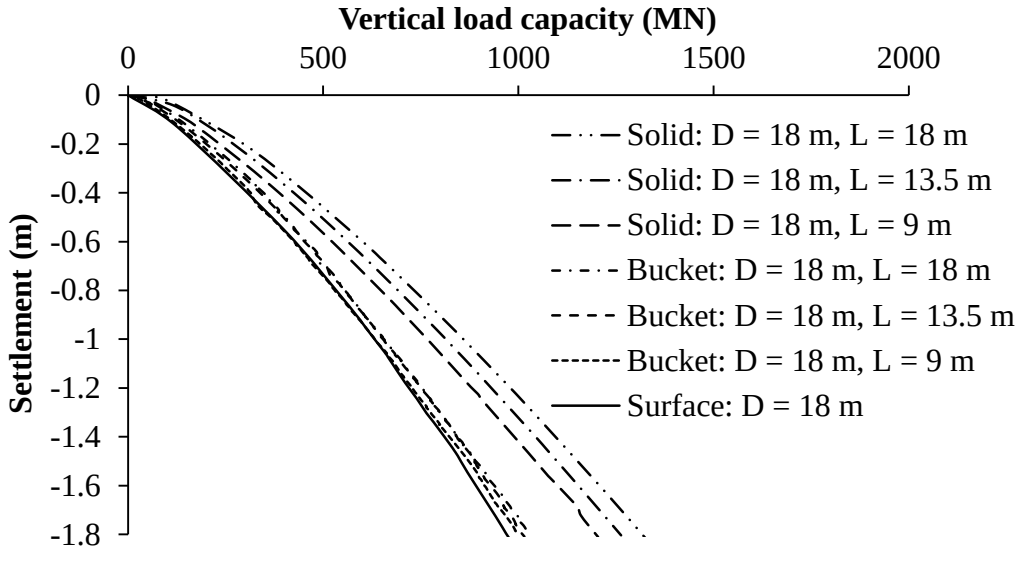

(c)

Figure 4.3 Vertical load vs. settlement response of the three foundation types in very dense sand: (a) *D* = 12 m; (b) *D* = 15 m; (c) *D* = 18 m

Table 4.2 Ultimate vertical capacity of surface circular, bucket and embedded solid foundations

Sand type	Foundation type	Aspect ratio (L/D)	Ultimate vertical capacity (MN)			$V_{Embedded\ Solid,\ Ultimate}/V_{Bucket,\ Ultimate}$		
			D = 12 m	D = 15 m	D = 18 m	D = 12 m	D = 15 m	D = 18 m
Medium dense sand	Surface	0	117.07	193.51	296.90	--	--	--
	Bucket	0.5	126.98	206.56	308.40	1.19	1.21	1.23
		0.75	128.61	207.20	320.20	1.24	1.31	1.29
		1	134.36	218.76	335.48	1.27	1.31	1.32
	Solid	0.5	151.08	250.42	380.56	--	--	--
		0.75	159.39	270.59	411.49	--	--	--
		1	170.59	287.56	442.14	--	--	--
Very dense sand	Surface	0	388.58	639.33	969.81	--	--	--
	Bucket	0.5	421.73	651.17	996.23	1.18	1.24	1.20
		0.75	422.59	669.14	1010.26	1.21	1.27	1.25
		1	431.35	694.14	1028.07	1.25	1.26	1.28
	Solid	0.5	498.07	806.63	1198.65	--	--	--
		0.75	510.07	852.23	1263.11	--	--	--
		1	538.68	873.82	1317.41	--	--	--

4.2.2 Shear Stress along Embedment Length of Bucket Foundation

Under the application of vertical load, the bucket foundation moves down relative to the adjacent soil mass, giving rise to shear stress along the bucket length. The variations of shear stress along the embedment length of the bucket foundations at failure are presented in Figure 4.4(a)-(c).

At failure load, the shear stress is noted to increase parabolically along the along the embedment length, attains a peak and then reduces gradually. For example, in case of the bucket foundation of 12 m diameter and aspect ratio of 0.5 embedded in medium dense sand, the shear stress increases gradually from bed level and attains peak stress of 24.38 kN/m^2 at a depth of 2.15 m [Figure 4.4(a)]. As the aspect ratio is increased to 0.75 and 1, the peak stresses increase to 33.53 and 39.50 kN/m^2 at depths of 2.63 and 2.67 m, respectively. For the same bucket foundation, when embedded in very dense sand, higher peak stress values of 53.48, 42.99 and 42.34 kN/m^2 have been obtained at 2.08 m, 2.82 m and 3.34 m for the three aspect ratios, respectively.

Similarly, in medium dense sand, for the bucket diameter of 15 m and aspect ratios of 0.5, 0.75 and 1.0, peak shear stresses of 37.75, 42.99 and 42.34 kN/m^2 have been obtained at depths of 2.80, 3.26 and 3.54 m, respectively [Figure 4.4(b)]. The peak shear stress increases to 59.66, 97.63 and 104.69 kN/m^2 at 3.18, 3.52 and 3.54 m depths, for aspect ratios of 0.5, 0.75 and 1.0 in very dense sand.

In case of bucket foundation of 18 m diameter, embedded in medium dense sand, maximum shear stresses of 41.50, 52.30, and 55.0 kN/m^2 have been found at 3.71, 3.79 and 5.01 m depths, respectively for aspect ratios of 0.5, 0.75 and 1.0 [Figure 4.4(c)]. In very dense sand, the corresponding maximum shear stresses are 44.76, 134.79 and 120.88 kN/m^2 at depths of 5.24, 4.57 and 4 m, respectively.

For a given sand type, the magnitude of maximum shear stress obtained is noted to increase with bucket geometry size (i.e. with embedment length for the same diameter and also with diameter for the same aspect ratio). The depth, where the maximum shear stress is encountered, increases with increasing aspect ratio value. For a given bucket geometry and aspect ratio, the magnitude of shear stress is higher when embedded in very dense sand. The increase in the shear stress is due to the increase of earth pressure acting at that point along the embedment length and is discussed in the following section.

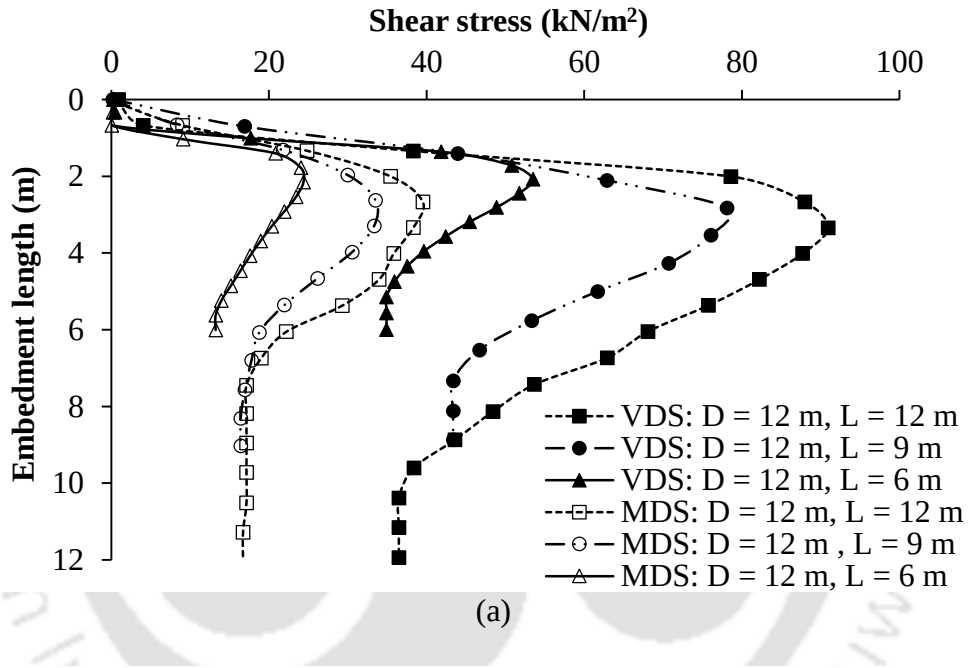

(a)

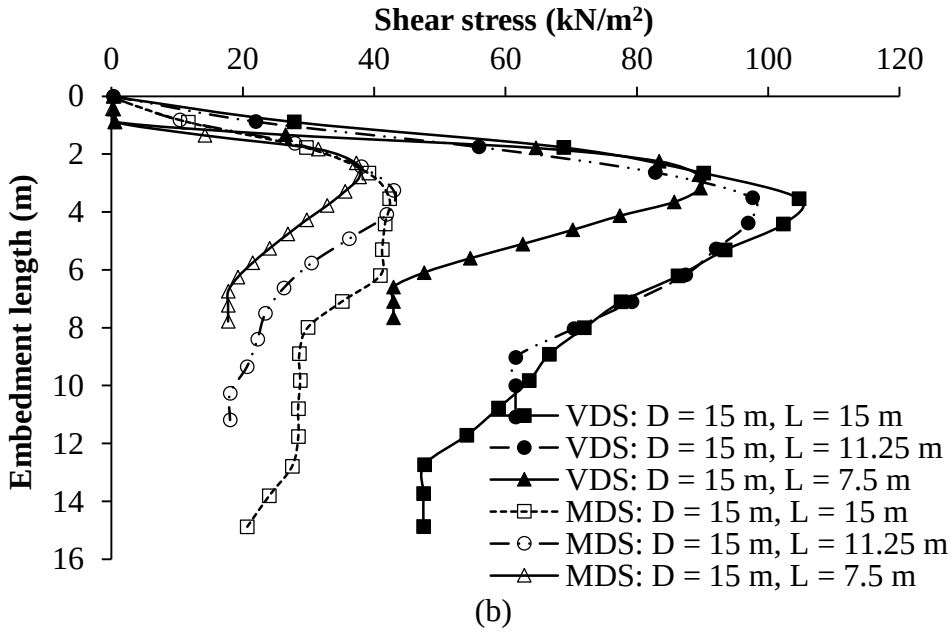

(b)

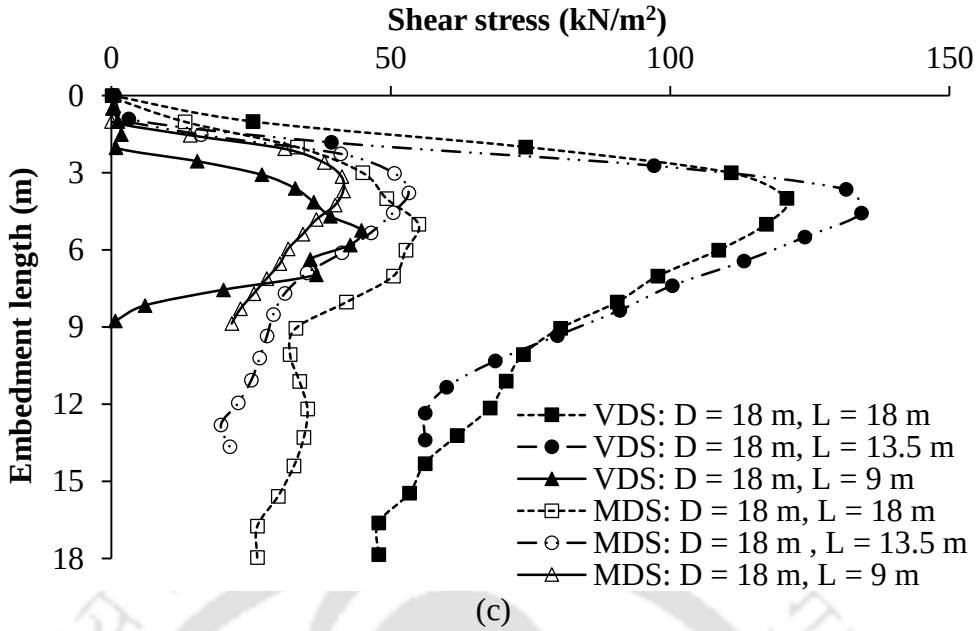

(c)

Figure 4.4 Variation of shear stress along embedded length of bucket foundation at failure: (a) *D* = 12 m; (b) *D* = 15 m; and (c) *D* = 18 m

4.2.3 Earth Pressure along Embedded Length of Bucket Foundation

Under the application of vertical load till failure, the soil mass located near the embedment length is also dragged along with the foundation. Figure 4.5(a)-(c) shows the variation of earth pressure along the embedment length for all bucket geometries at failure. For a given bucket geometry embedded in either sand type, the earth pressure is noted to increase parabolically, reaches a maximum value and gradually reduces along the embedment length. The maximum lateral earth pressure, not being noted at the bottom portion of the embedment length, is due to the lateral expulsion of soil away from the skirt surface at the bottom, as observed from the lateral displacement vector diagrams in Figure 4.6(a)-(c) and Figure 4.7(a)-(c).

For the bucket of 12 m diameter and aspect ratios of 0.5, 0.75 and 1, embedded in medium dense sand, maximum earth pressures of 54.03, 75.25 and 90.39 kN/m^2 have been obtained at depths of 1.78, 2.63 and 2.67 m [Figure 4.5(a)]. When embedded in very dense

sand, the maximum earth pressure increases to 104.49, 155.34 and 180.19 kN/m^2 at depths of 1.72, 2.82 and 3.34 m, respectively for aspect ratios of 0.5, 0.75 and 1.0.

In case of 15 m diameter bucket foundation having aspect ratios of 0.5, 0.75 and 1, embedded in medium dense sand, the peak lateral stresses of 84.25, 98.04 and 97.92 kN/m^2 have been obtained at depths of 2.31, 3.26 and 3.54 m [Figure 4.5(b)]. The peak lateral stresses increase to 180.40, 198.74 and 215.40 kN/m^2 at 2.71, 3.52 and 3.54 m depths for the same diameter and aspect ratios of 0.5, 0.75 and 1, respectively embedded in very dense sand.

Similarly, in case of bucket foundation with 18 m diameter and aspect ratios of 0.5, 0.75 and 1, embedded in medium dense sand, the peak earth pressure values of 94.90, 120.34 and 108.09 kN/m^2 are obtained at 3.15, 3.79 and 5.01 m depths, respectively [Figure 4.5(c)]. For the same diameter and aspect ratios of 0.5, 0.75 and 1, embedded in very dense sand, the peak earth pressure magnitude increases to 111.86, 231.02 and 276.87 kN/m^2 at depths of 5.24, 5.50 and 3.64 m, respectively.

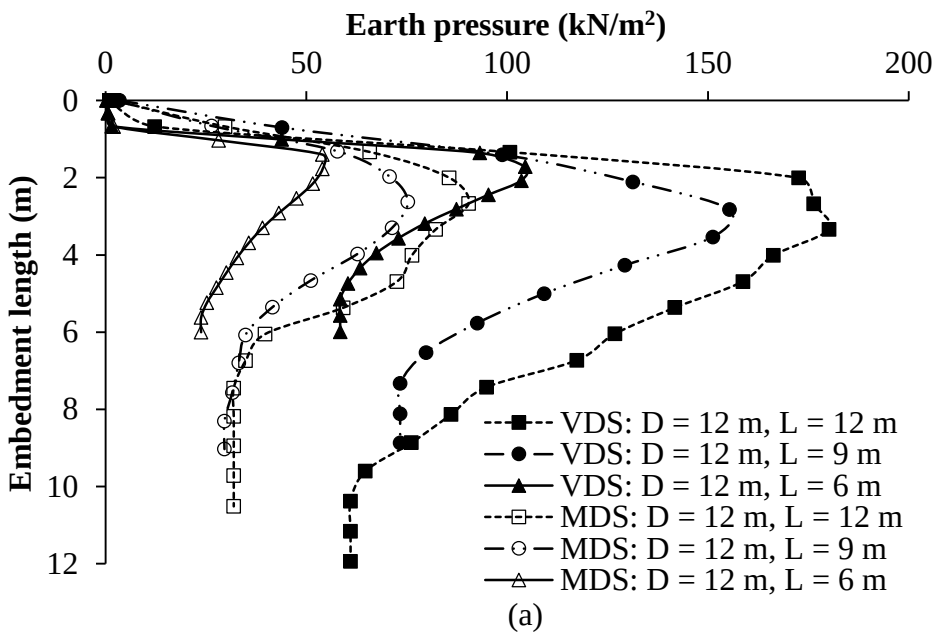

(a)

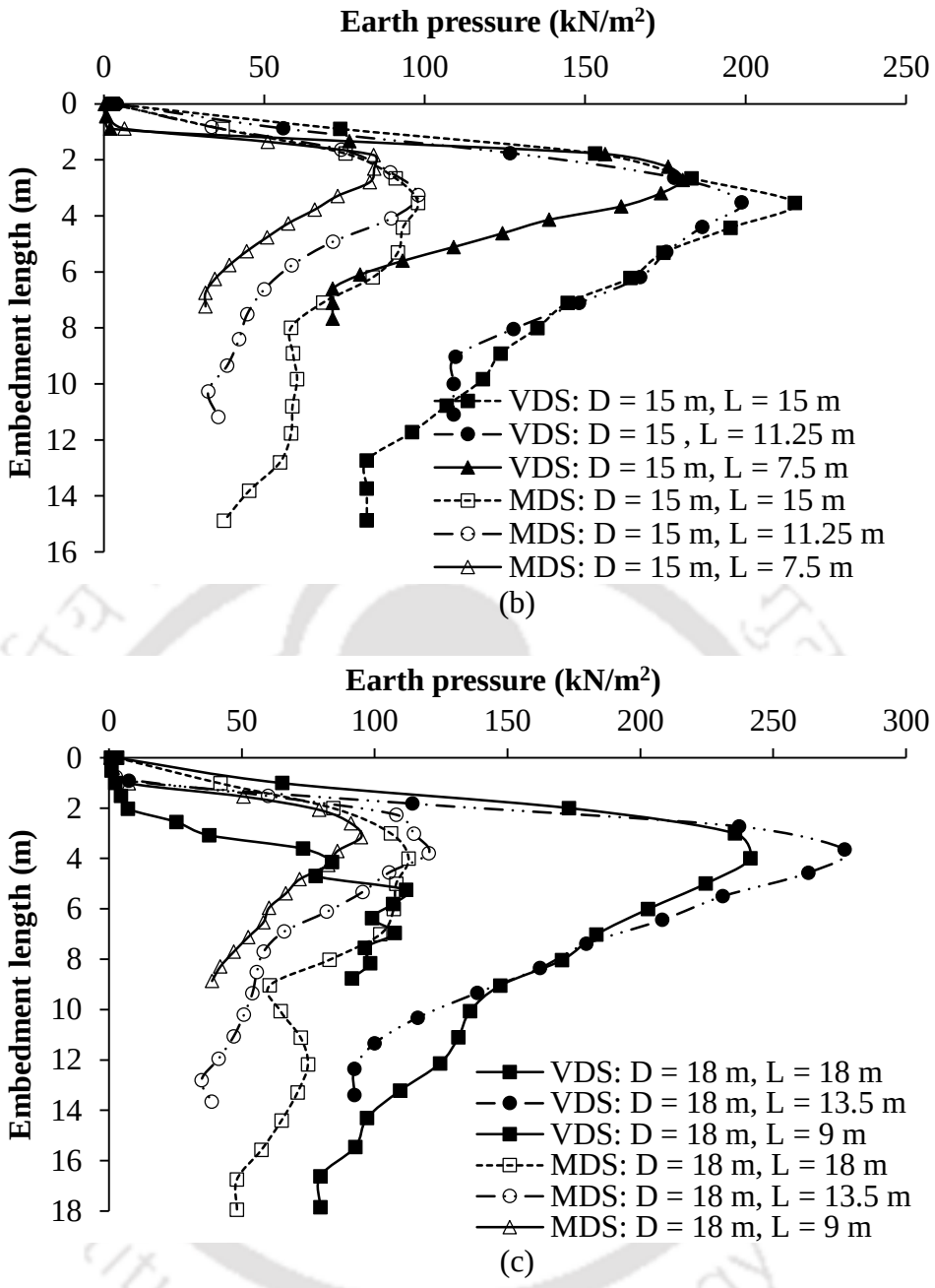

Figure 4.5 Variation of earth pressure along embedded length of bucket foundation at failure: (a) D = 12 m; (b) D = 15 m; and (c) D = 18 m

For a given foundation, the embedment length location where the maximum earth pressure is noted, increases with the aspect ratio of bucket foundation. The magnitude of peak or maximum earth pressure is greater in very dense sand as compared to medium dense sand for all the bucket diameters and aspect ratios considered in the study. The increase of lateral

stress along the entire embedment length for increasing aspect ratio value leads to increased interface strength mobilization at failure, which results in higher vertical capacity.

4.2.4 Lateral Displacement Vectors of Soil Mass near the Foundation Tips at Failure

Under the application of vertical load at the foundation centre, noticeable soil movement is observed along the foundation embedment length in medium dense and very dense sandy seabeds, as shown respectively in Figure 4.6(a)-(c) and Figure 4.7(a)-(c). At failure condition, corresponding to a settlement value equal to 10% of foundation diameter, below mid-depth of the embedment length, outward movement or lateral expulsion of the soil mass is noted for bucket and embedded solid foundations. In the case of bucket foundation, the expulsion of the soil mass increases considerably at depths below the embedment length of the foundation. The extent of lateral movement of soil mass at the tip or edge of foundation for the three foundation types embedded in medium dense and very dense sands are listed in Table 4.3.

From the table, at the edge of surface circular foundation (D = 12 m) embedded in medium dense sand, the soil movement or lateral expulsion is noted as 0.192 m. For the bucket foundation of same diameter, the lateral expulsion of the soil mass is found to be 0.314 m away from the bucket tip for an aspect ratio of 0.5 m [Figure 4.6(a)]. The magnitude of lateral expulsion at the bucket tip is noted to decrease to 0.284 and 0.257 m as the aspect ratio is increased to 0.75 and 1, as shown in Figure 4.6(b)-(c). The lateral expulsion extents for the 12 m diameter embedded solid foundation have been found as 0.127, 0.137 and 0.139 m for aspect ratios of 0.5, 0.75 and 1, respectively [Figure 4.7(a)-(c)]. The magnitude of lateral expulsion of soil mass is noted to be the least in case of embedded solid foundation.

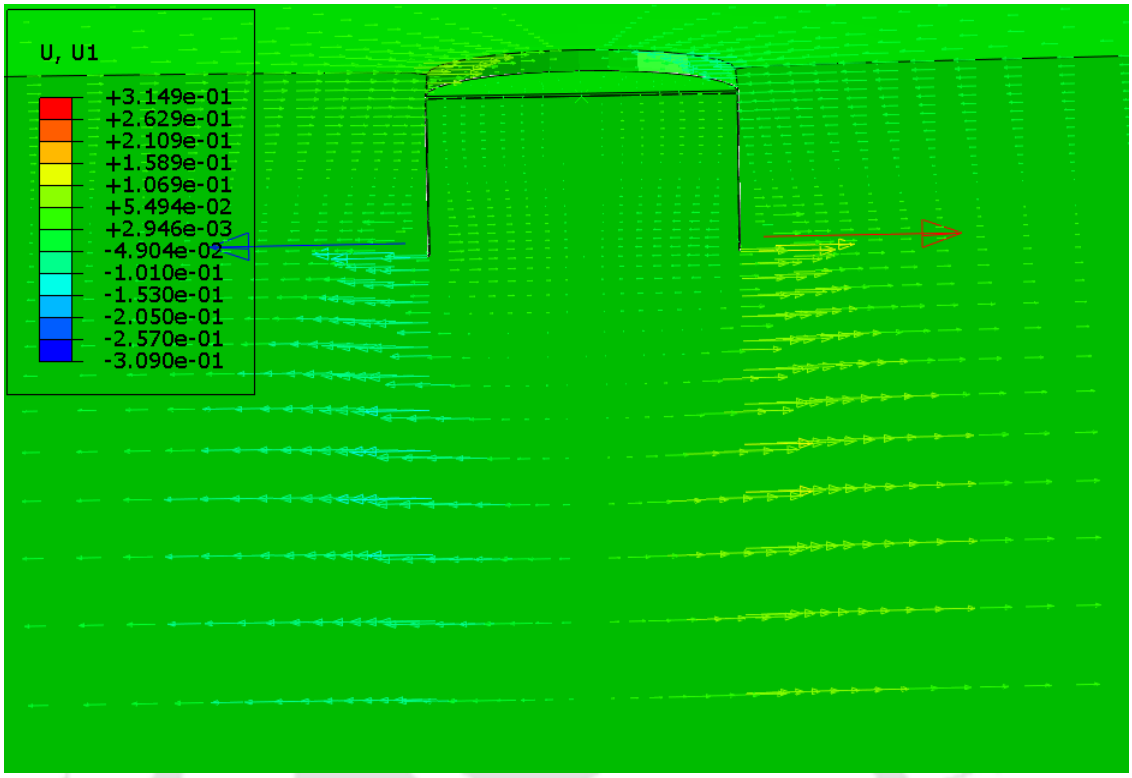

(a)

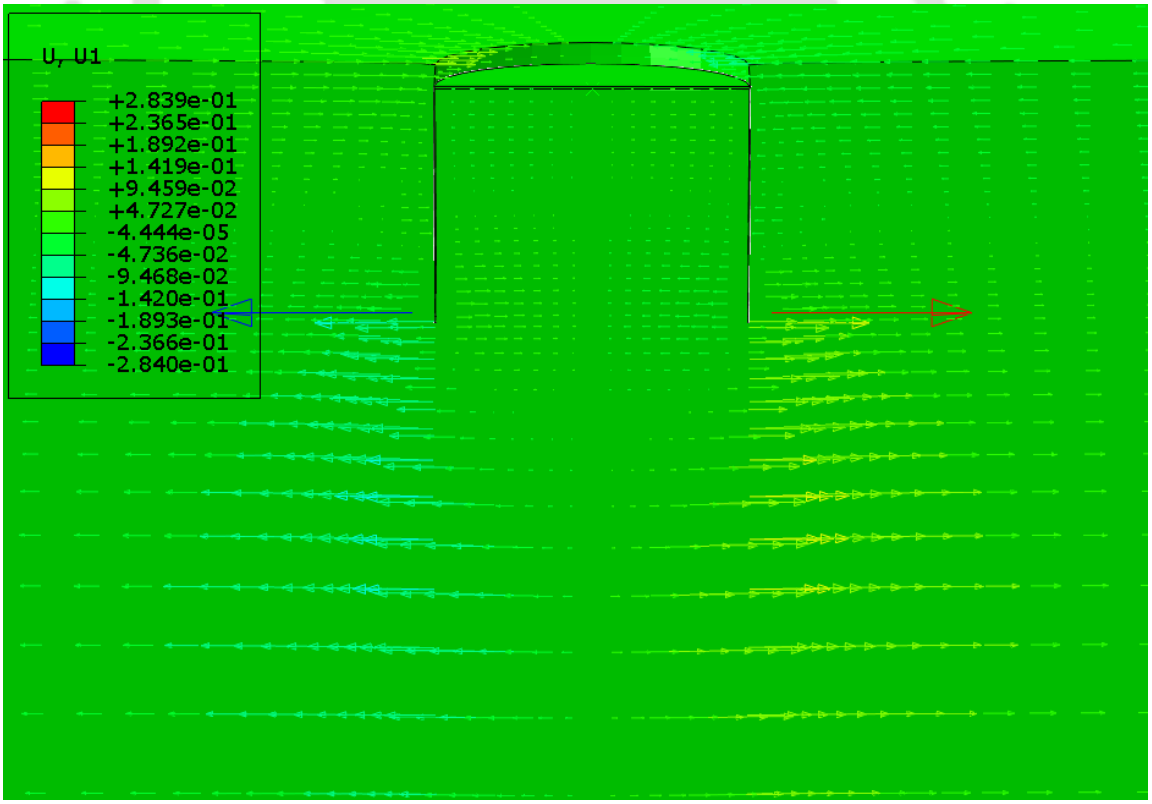

(b)

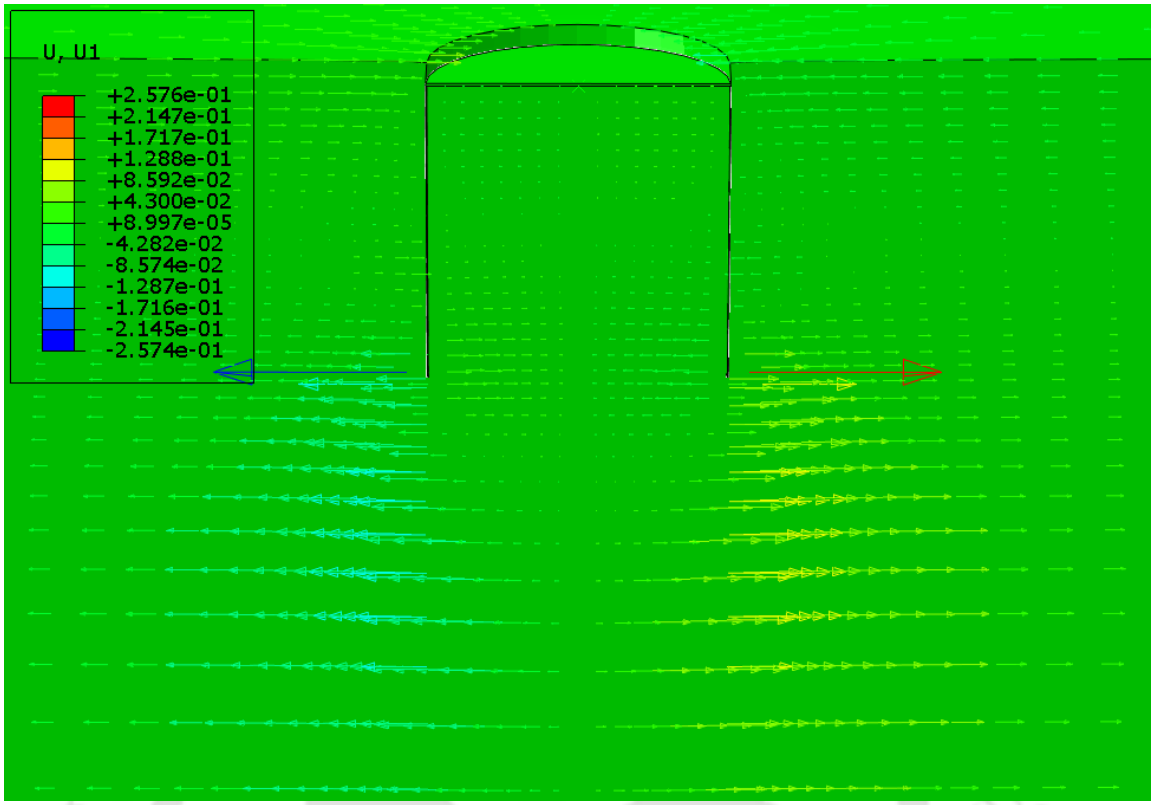

(c)

Figure 4.6 Lateral displacement vector diagrams of bucket foundations in medium dense sand: (a) D = 12 m & L = 6 m; (b) D = 12 m & L = 9 m; (b) D = 12 m & L = 12 m

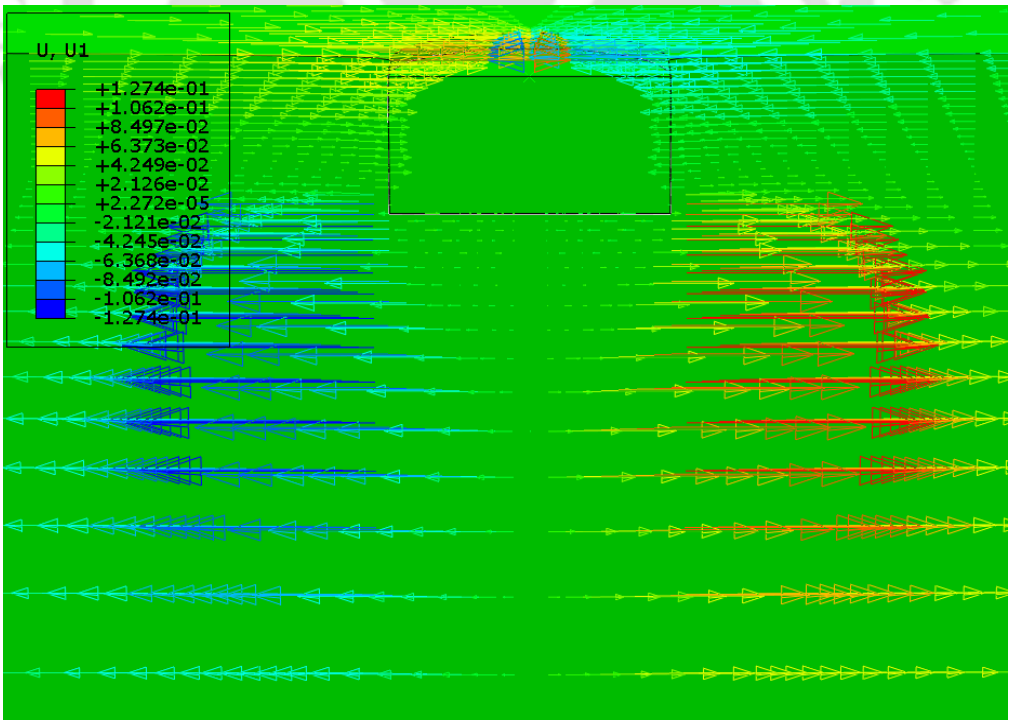

(a)

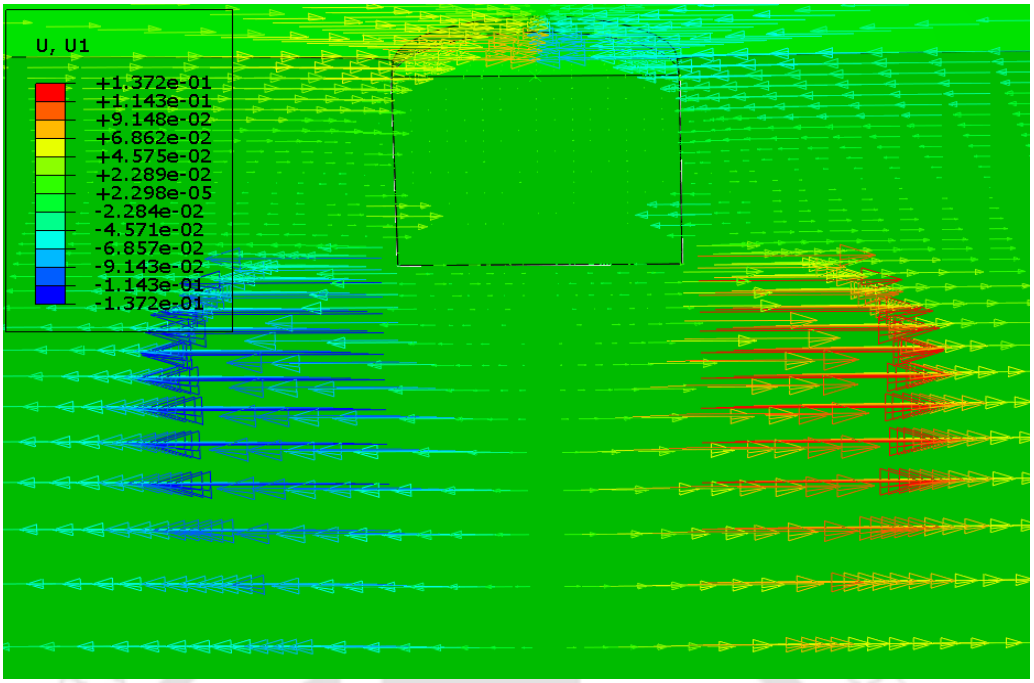

(b)

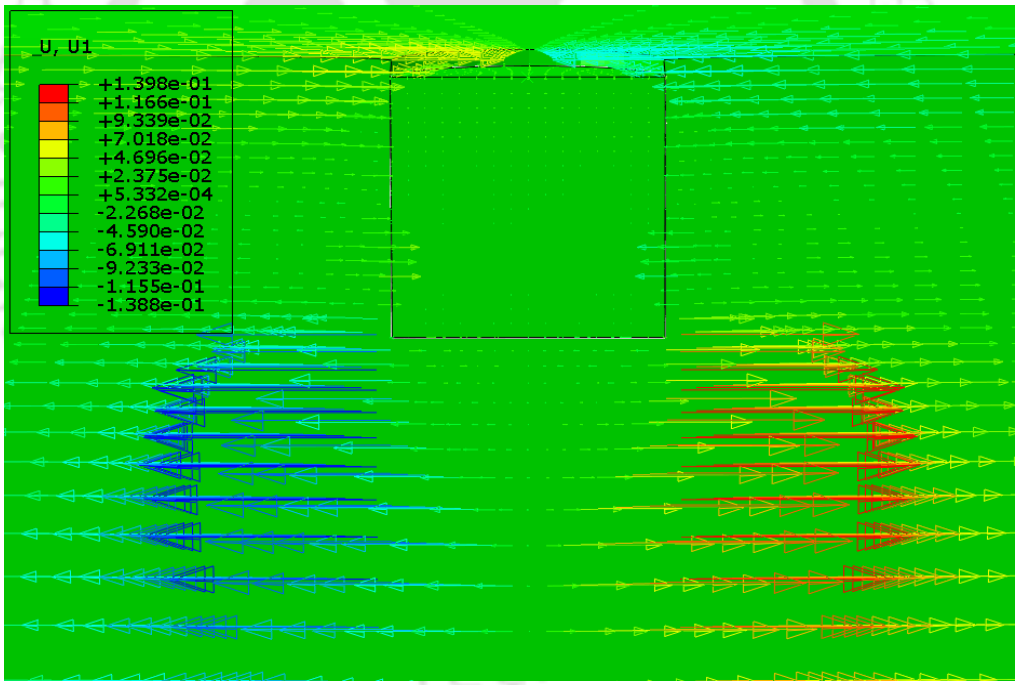

(c)

Figure 4.7 Lateral displacement vectors of embedded solid foundations in medium dense sand: (a) D = 12 m & L = 6 m; (b) D = 12 m & L = 9 m; (b) D = 12 m & L = 12 m

For the considered soil types, for any given foundation type, the magnitude of soil movement at the tip of foundation is noted to be greater in case of very dense sand as compared to medium dense sand. The magnitude of lateral expulsion is noted to decrease

with higher aspect ratio in the case of bucket foundation. However, in the case of embedded solid foundation, the magnitude of lateral expulsion is noted to increase with aspect ratio.

Table 4.3 Lateral displacement of soil mass near the tip of the foundations at failure

Foundation type	Foundation geometry	Lateral displacement of soil near the foundation tip (in m)	
		Medium dense sand	Very dense sand
Surface circular foundation	D = 12 m	0.192	0.283
	D = 15 m	0.204	0.360
	D = 18 m	0.293	0.397
Bucket foundation	D = 12 m, L = 6 m	0.314	0.341
	D = 12 m, L = 9 m	0.284	0.309
	D = 12 m, L = 12 m	0.257	0.279
	D = 15 m, L = 7.5 m	0.345	0.373
	D = 15 m, L = 11.25 m	0.253	0.265
	D = 15 m, L = 15 m	0.193	0.231
	D = 18 m, L = 9 m	0.279	0.308
	D = 18 m, L = 13.5 m	0.315	0.326
	D = 18 m, L = 18 m	0.239	0.305
Embedded solid foundation	D = 12 m, L = 6 m	0.127	0.137
	D = 12 m, L = 9 m	0.137	0.142
	D = 12 m, L = 12 m	0.139	0.141
	D = 15 m, L = 7.5 m	0.154	0.167
	D = 15 m, L = 11.25 m	0.168	0.168
	D = 15 m, L = 15 m	0.171	0.192
	D = 18 m, L = 9 m	0.196	0.198
	D = 18 m, L = 13.5 m	0.199	0.204
	D = 18 m, L = 18 m	0.204	0.209

4.2.5 Variation of Ultimate Vertical Bearing Capacity of Bucket Foundation with Skirt Length and Diameter

The variation of ultimate vertical capacity with skirt length for different bucket foundation diameters in both sand types are presented in Figures 4.8-4.9, and with diameter for different skirt lengths are shown in Figures 4.10-4.11. From the figures, the ultimate vertical capacity of bucket foundation is noted to increase with both skirt length and with diameter. The magnitude of ultimate vertical capacity of bucket foundation embedded in very dense sand is found to substantially higher compared to that of the foundation embedded in

medium dense sand. Though the plots of Figure 4.8 to Figure 4.11 have been made based on the ultimate vertical capacity values of only the nine bucket geometries that have been studied, the vertical capacity value for any other geometry within the considered diameter range (12 to 18 m) and skirt length range (6 to 18 m) can be estimated approximately through linear interpolation.

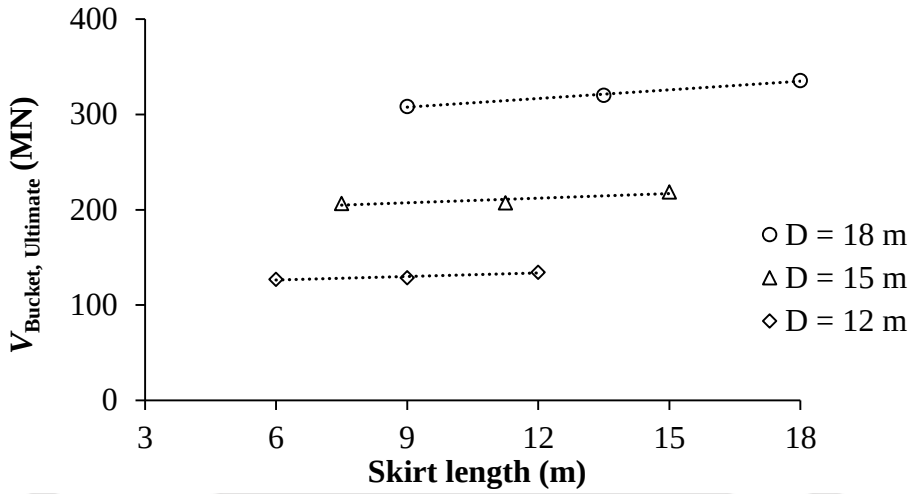

Figure 4.8 Variation of ultimate vertical capacity with skirt length of bucket foundations in medium dense sand

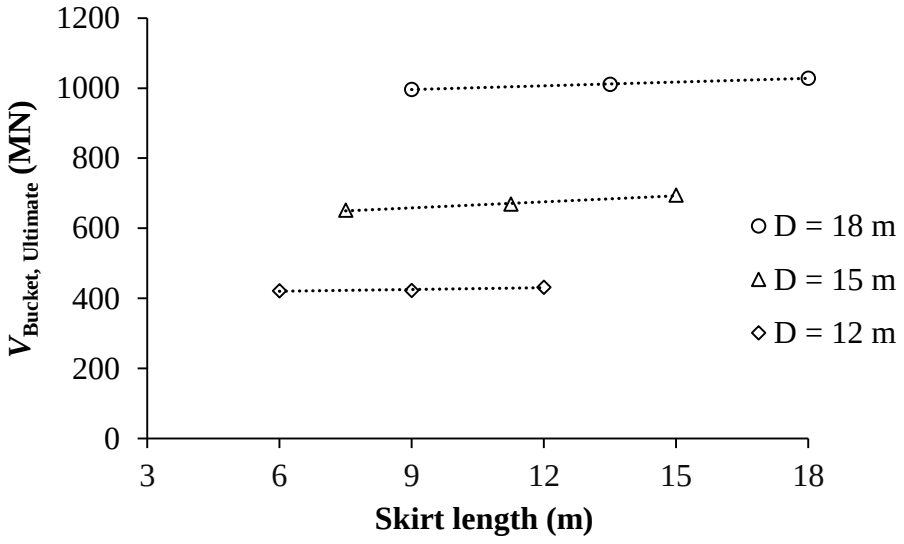

Figure 4.9 Variation of ultimate vertical capacity with skirt length of bucket foundations in very dense sand

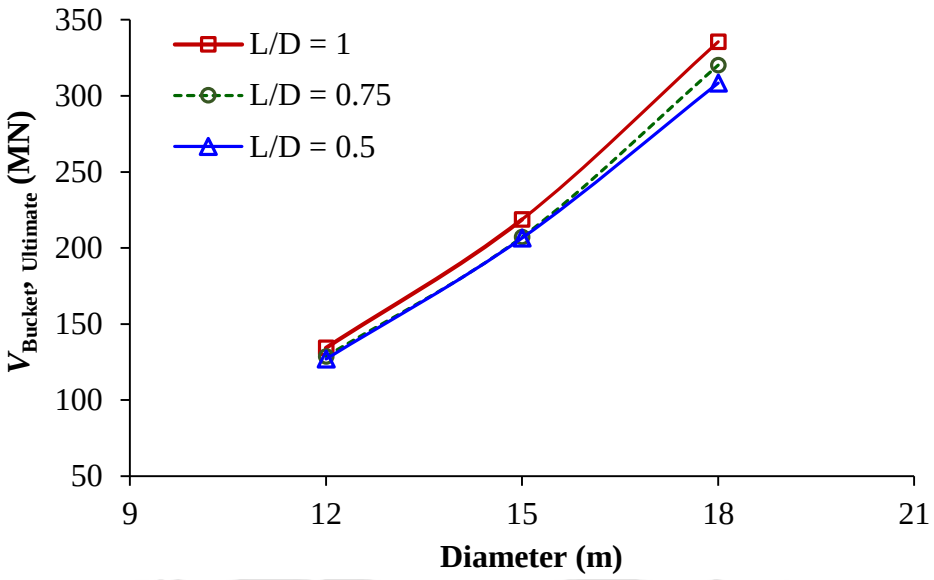

Figure 4.10 Variation of ultimate vertical capacity with diameter of bucket foundations in medium dense sand

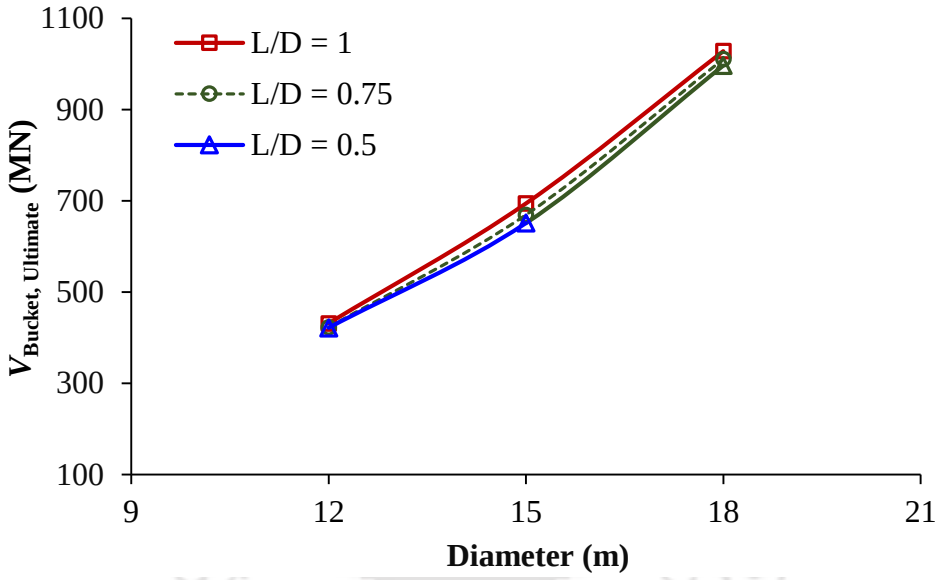

Figure 4.11 Variation of ultimate vertical capacity with diameter of bucket foundations in very dense sand

From Figure 4.8, for a fixed skirt length of 12 m for the bucket foundation in medium dense sand, the ultimate vertical capacity increases from 134.36 MN to an interpolated value of 317.43 MN (a difference of 183.07 MN) as the diameter is varied by 6 m magnitude from 12 to 18 m. Similarly, from Figure 4.10, for a fixed diameter of 12 m, it is noted that the ultimate vertical capacity decreases from 134.36 MN to 126.98 MN (a difference of 7.38

MN) as the skirt length is varied by 6 m magnitude from 12 to 6 m. It is evident that as compared to diameter, increasing skirt length has lesser influence on the ultimate vertical capacity.

4.2.6 Failure Mechanisms all Foundation Types under Vertical Load

Under the application of vertical load till failure, any given foundation settles giving rise to plastic strains. The movement of soil under vertical load is illustrated in terms of displacement vectors. The variation of the generated plastic strains for surface circular, embedded solid and bucket foundations at failure is illustrated in Figures 4.12-4.17.

In case of surface circular foundation in both medium dense sand [Figure 4.12(a)] and very dense sand [Figure 4.15(a)], a surface flow mechanism is observed under the foundation with a distinct elastic zone of downward moving soil wedge, which is a characteristic feature of a Prandtl-type failure mechanism. Plastic strains are generated from the edges of the foundation and as they are extended radially outward and downward, the strain magnitude is found to decrease. Higher extent of the spread of the plastic strain zone is noted with increased values of surface circular foundation diameter.

The plastic zone surrounding the elastic wedge represents punching failure mechanism. The vertical soil movement beneath the foundation at failure, depicted in Figure 4.12(b) and Figure 4.15(b) in terms of displacement vectors, resembles a parabolic shape in both the sand types. This indicates that in case of surface circular foundation, the maximum vertical displacement of the soil mass is noted to take place beneath the centre of the foundation base.

The response of soil plug inside the bucket foundation and the load transfer mechanism are highlighted by comparing the plastic strain and displacement vector diagrams with those of the embedded solid foundation. In case of bucket foundation, the surrounding soil mass along the exterior interface of the skirt is noted to yield plastically throughout the

embedment length [Figure 4.13(a)]. The soil mass also yields plastically along the interior interface of the skirt near the base of the foundation. From the skirt tip, this region of plastically yielded soil extends up to a considerable depth in the soil mass by surrounding an elastic wedge. The displacement vector diagram beneath the bucket foundation resembles the shape of an inverted parabola [Figure 4.14(a)], in which the minimum and maximum displacements of the soil are noted at the centre and at the edges, respectively.

While comparing the failure mechanisms, similar elastic wedge formation is noted in case of embedded solid foundation [Figure 4.13(b)]. Plastic strain generation is noted along the embedment length at the vertical interface. The displacement vector diagram at the foundation base resembles the shape of an upright parabola [Figure 4.14(b)], with the maximum and minimum vertical displacements of the soil at the centre and at the edges, respectively. This shows that the end-bearing capacity of the embedded solid foundation is greater than that of the bucket foundation with the same dimensions.

The comparison of plastic strain magnitude of bucket foundation with solid foundation shows similar failure mechanism. It indicates that the soil plug located inside the bucket foundation acts as an integral part of the foundation bucket foundation. The displacement magnitude vectors, however, indicates that the end-bearing load transferred by the soil plug shows some softening or cushion effect. Similar behaviour is noted for bucket and solid foundations embedded in very dense sandy seabed [Figures 4.16-4.17].

Both bucket and embedded solid foundations in medium and very dense sandy soil fail under punching shear, and a confined deep flow mechanism is observed along with the formation of an elastic zone in the shape of a wedge.

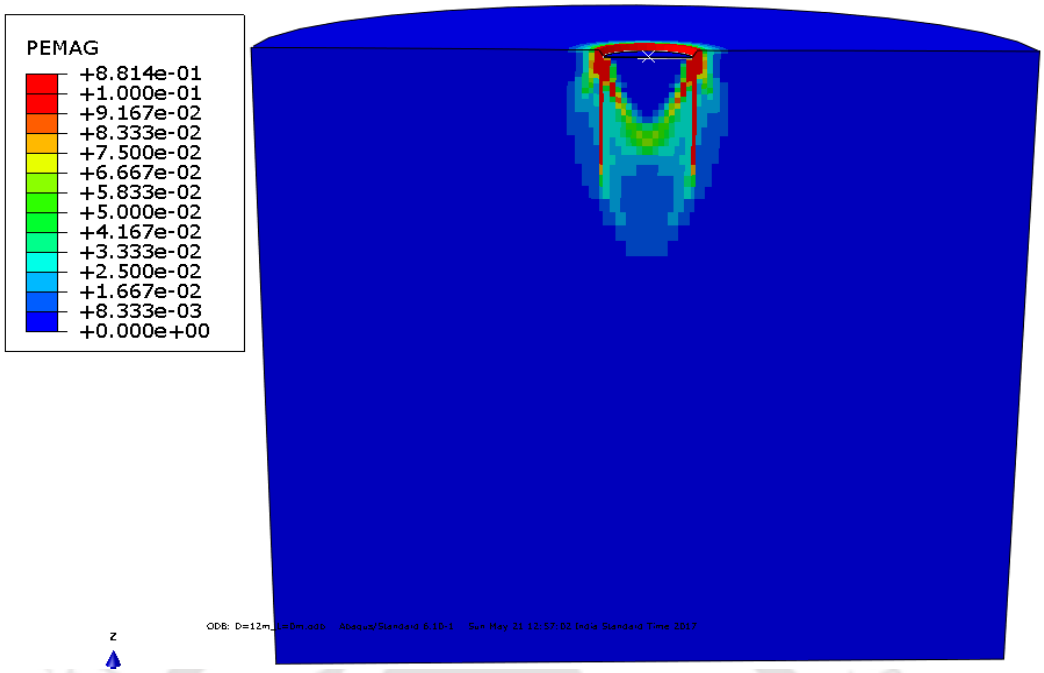

(a)

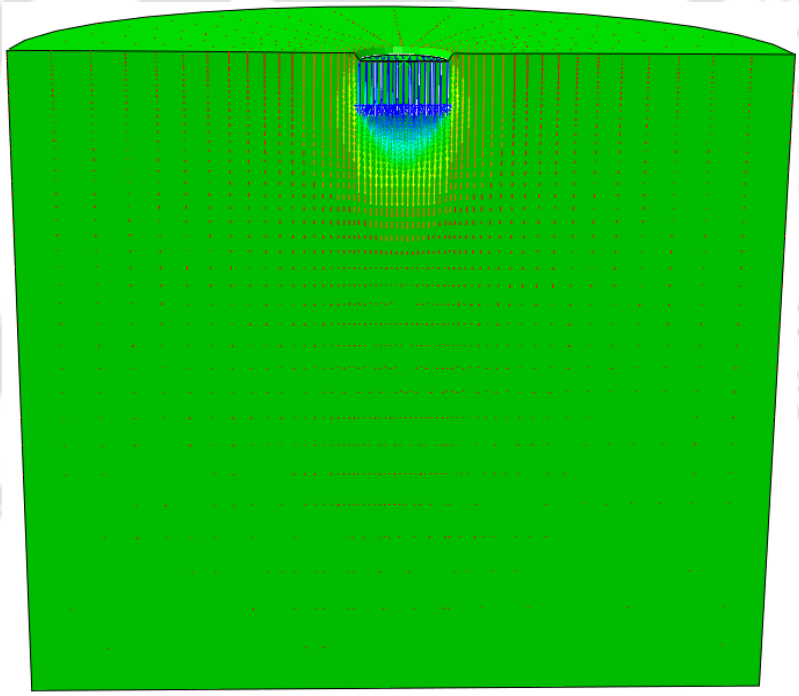

(b)

Figure 4.12 Failure of surface circular foundation (D = 12 m) in medium dense sand shown in terms of: (a) generated plastic strain; and (b) displacement vectors

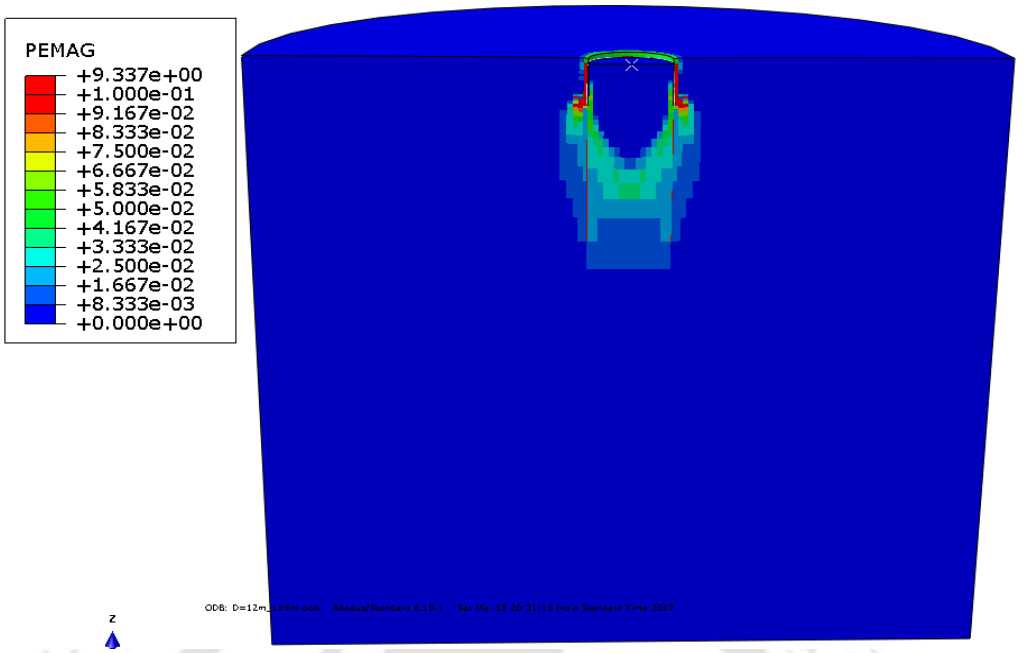

(a)

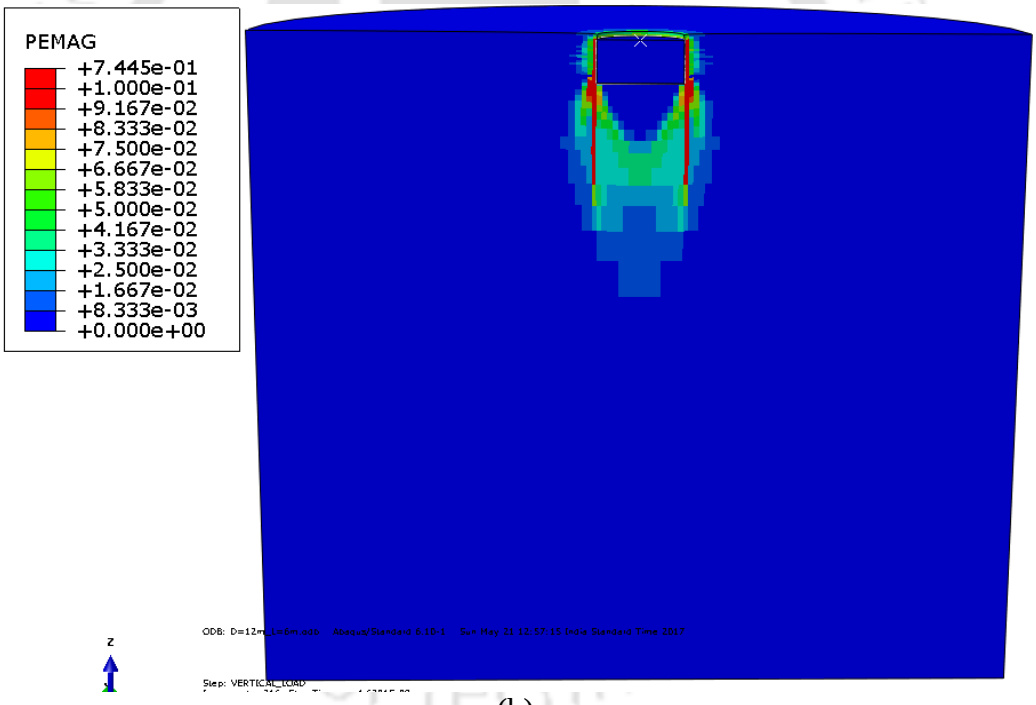

(b)

Figure 4.13 Plastic deformation in medium dense sand at failure of: (a) bucket (D = 12 m & L = 6 m); and (b) embedded solid foundation (D = 12 m & L = 6 m)

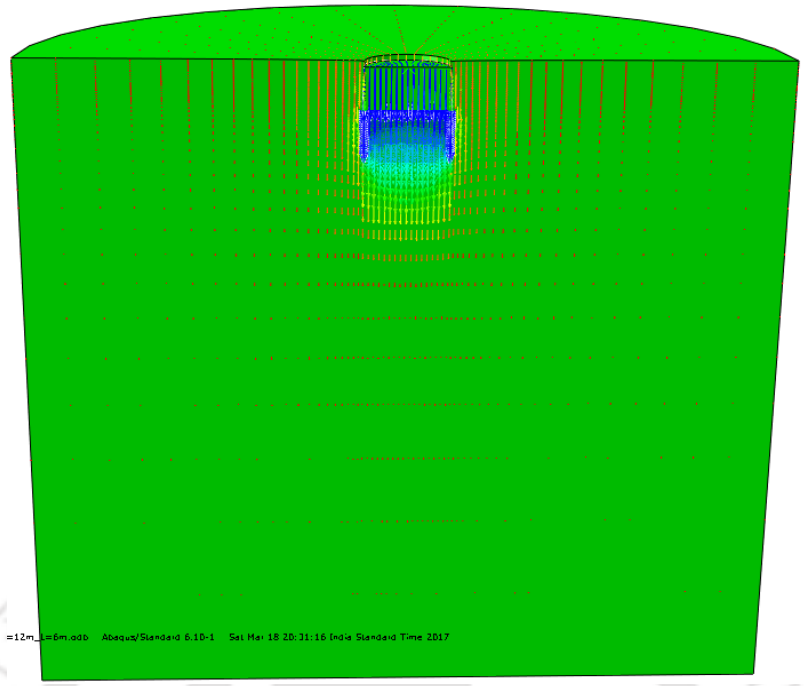

(a)

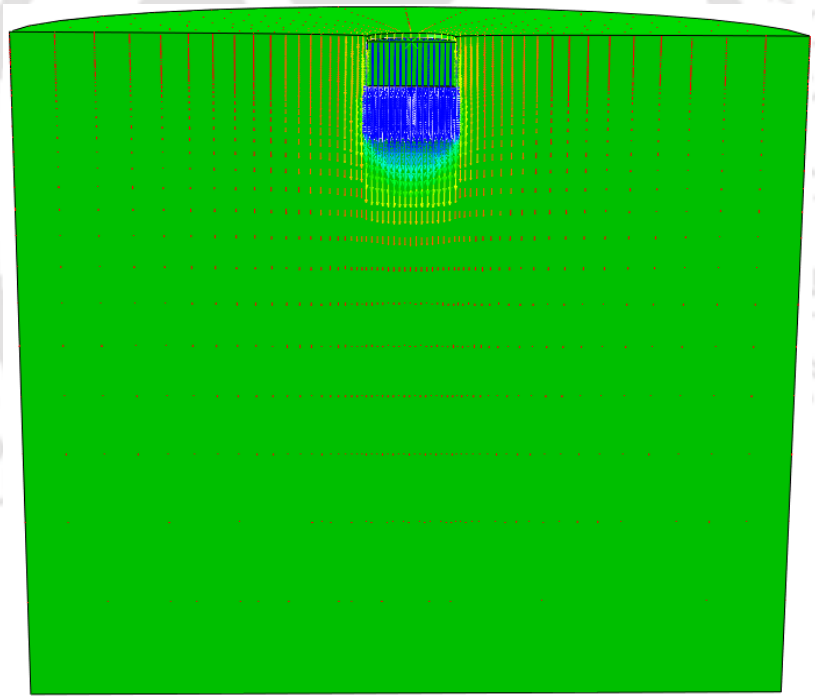

(b)

Figure 4.14 Vertical displacement vector diagram in medium dense sand at failure of: (a) bucket (D = 12 m & L = 6 m); and (b) embedded solid foundation (D = 12 m & L = 6 m)

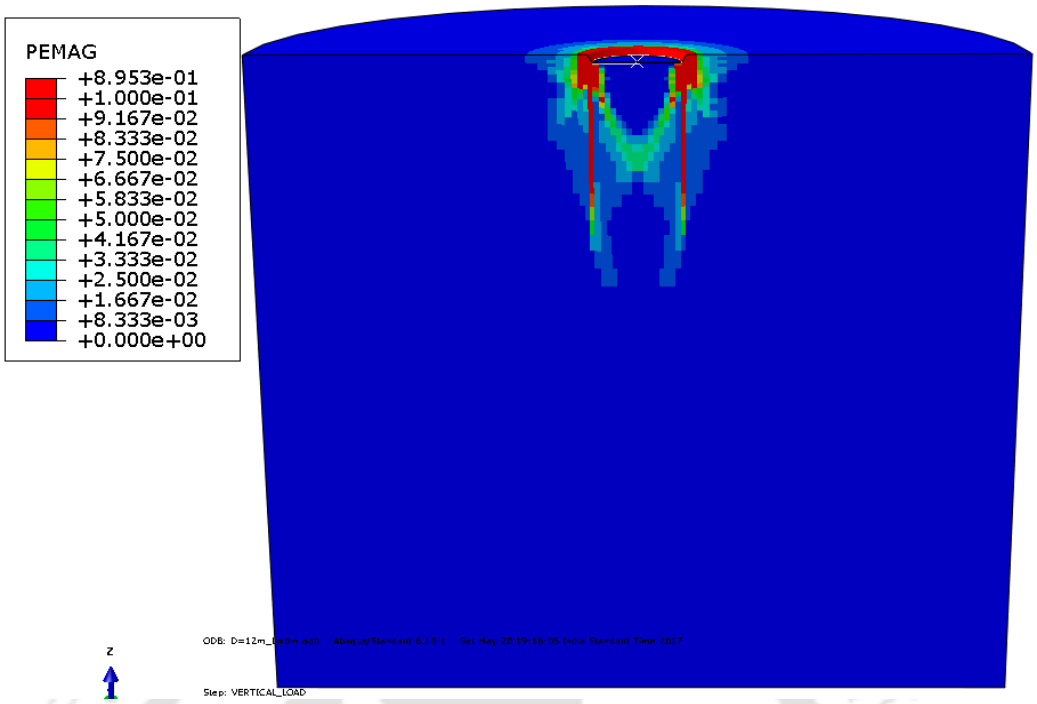

(a)

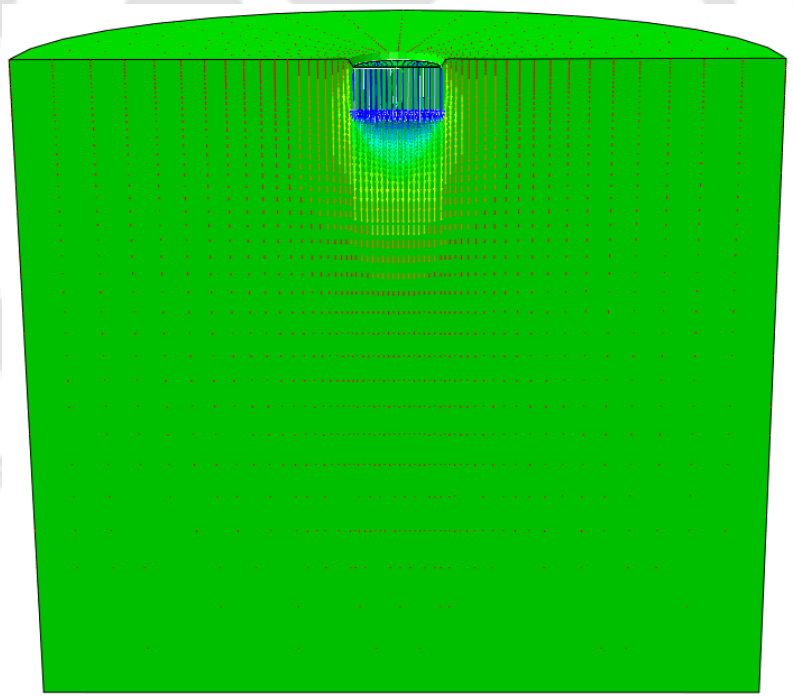

(b)

Figure 4.15 Failure of surface circular foundation (D = 12 m) in very dense sand shown in terms of: (a) generated plastic strain; and (b) displacement vectors

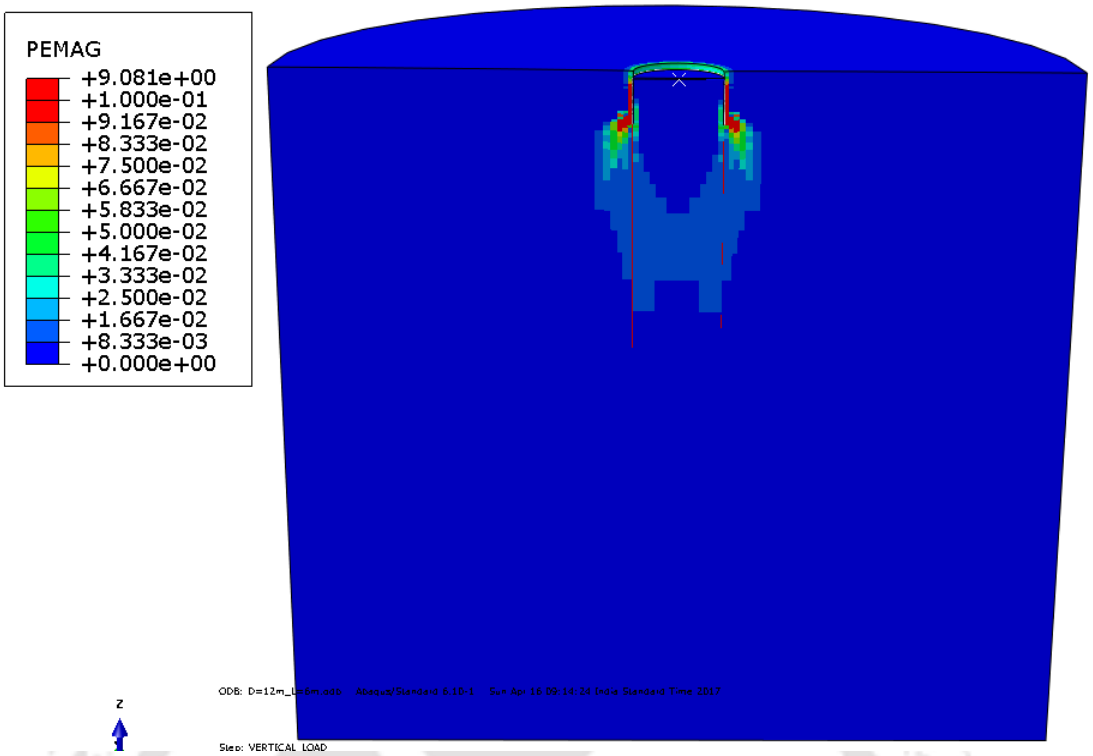

(a)

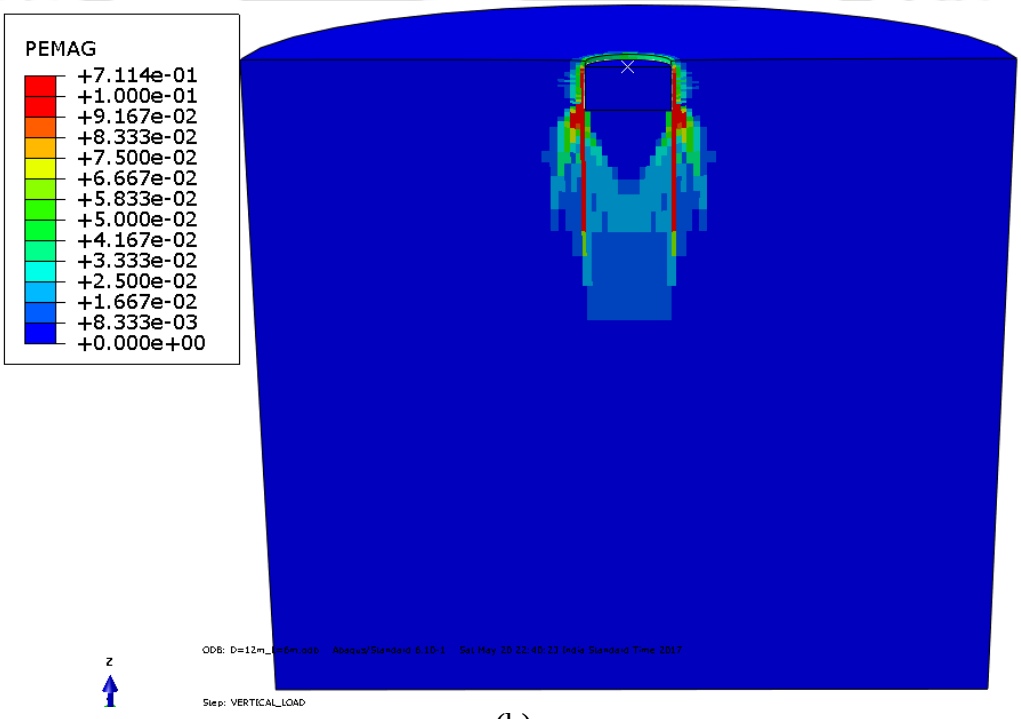

(b)

Figure 4.16 Plastic deformation in very dense sand at failure of: (a) bucket (D = 12 m & L = 6 m); and (b) embedded solid foundation (D = 12 m & L = 6 m)

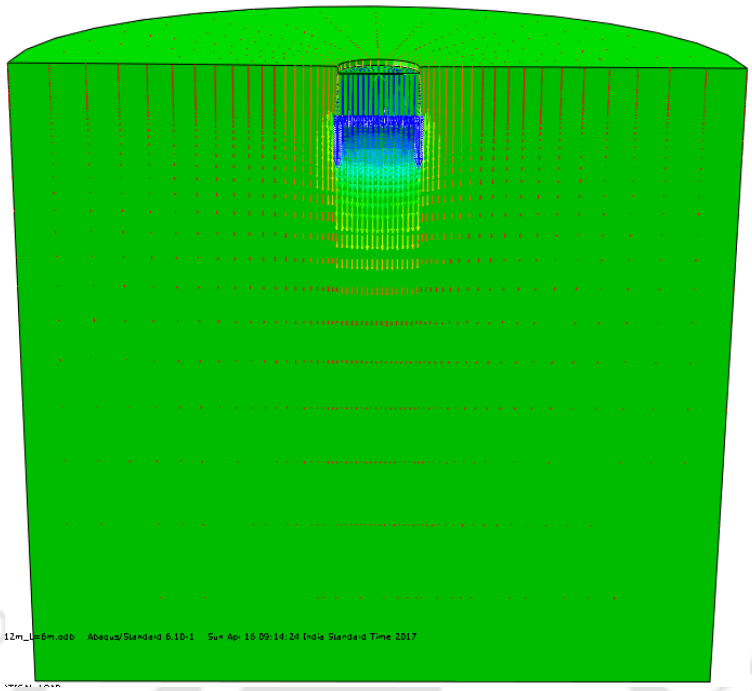

(a)

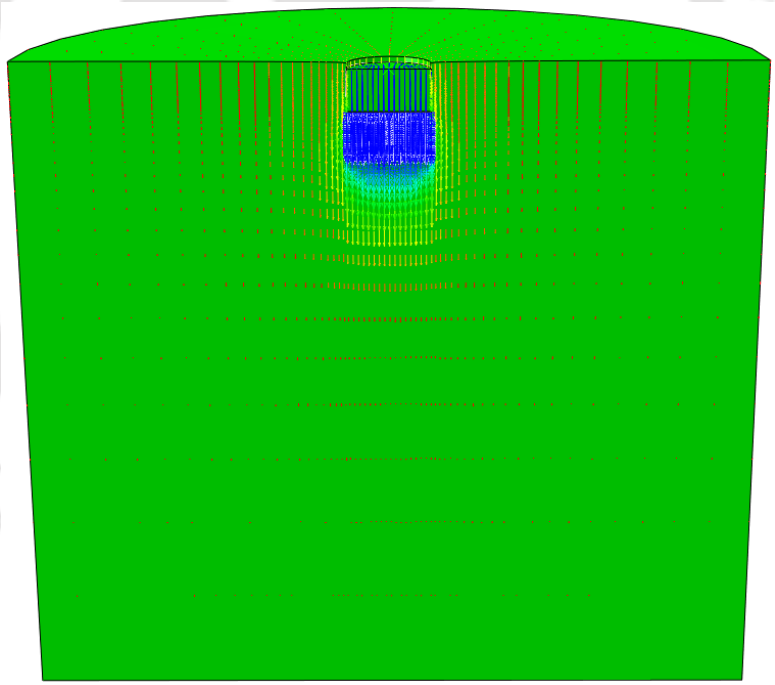

(b)

Figure 4.17 Vertical displacement vector diagram in very dense sand at failure of: (a) bucket (D = 12 m & L = 6 m); and (b) embedded solid foundation (D = 12 m & L = 6 m)

4.3 COMPARISON OF ULTIMATE VERTICAL CAPACITY

4.3.1 Relationship Between Vertical Capacity Depth Factor and Aspect Ratio

The ultimate vertical capacities from Table 4.2 have been utilized to determine vertical capacity depth factor (D_{vc}), being defined as the ratio between the ultimate vertical bearing capacity of bucket foundation of a particular skirt depth to that of surface circular foundation of the same diameter.

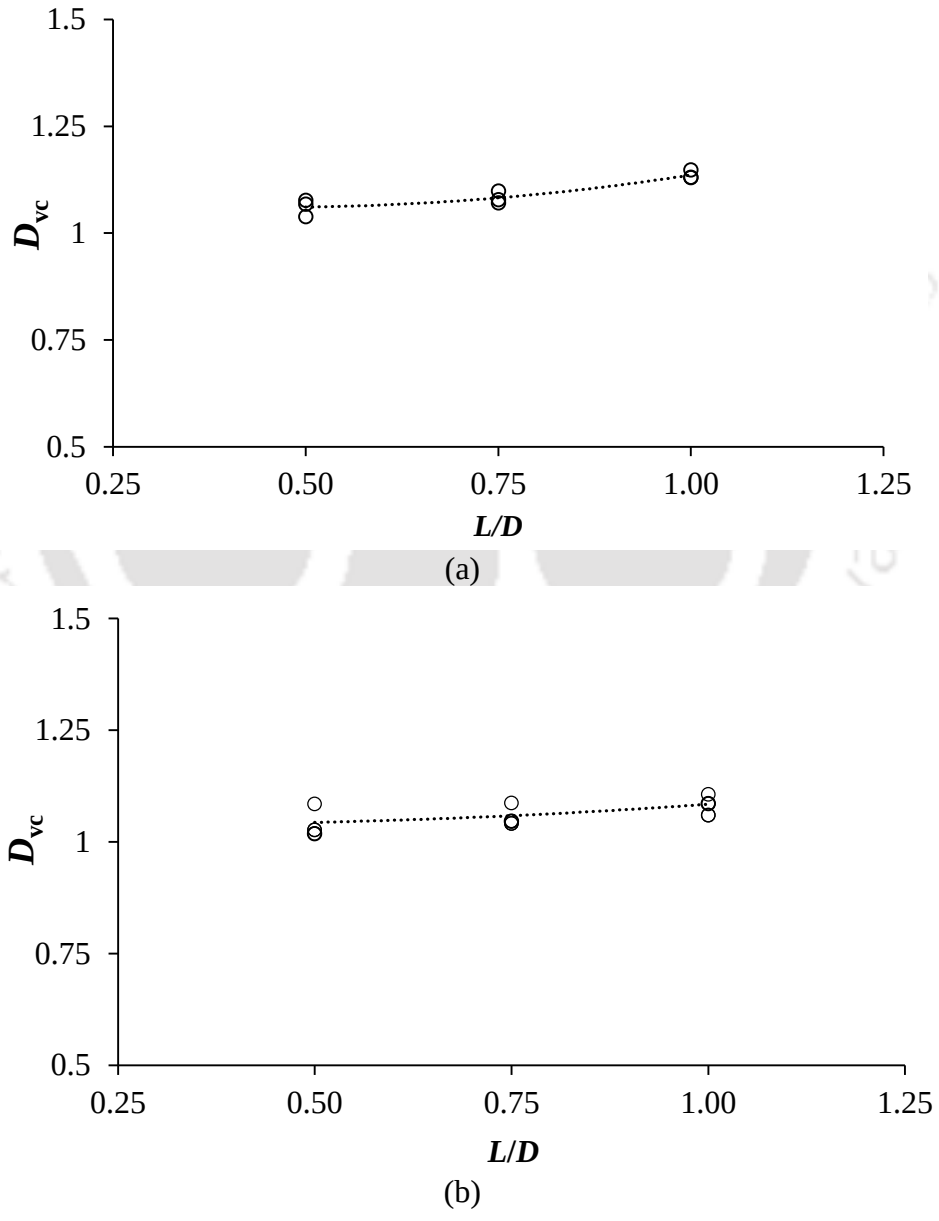

Figure 4.18 Variation of vertical capacity depth factor with aspect ratio: (a) in medium dense sand; (b) in very dense sand

Figure 4.18(a)-(b) shows the variation of vertical capacity depth factor with aspect ratio of the foundations. The depth factor is noted to increase non-linearly with aspect ratio.

In these figures, the data points have been utilized to obtain best-fit curves represented by the general form of expression, as given in Equation (4.1). From the curve fitting analysis, the values of the coefficients for the predictive expressions for the ultimate vertical capacity of bucket foundations in both sand types are presented in Table 4.4.

$$D_{VC} = \frac{V_{Bucket,Ultimate}}{V_{Surface,Ultimate}} = a\left(\frac{L}{D}\right)^2 + b\left(\frac{L}{D}\right) + c \tag{4.1}$$

Table 4.4 Values of coefficients to determine vertical capacity depth factor for both sand types

Coefficient	Soil type	
	Medium dense sand	Very dense sand
a	0.2549	0.0852
b	-0.2324	-0.4680
c	1.1135	1.0458

The above expression can be utilized to estimate the ultimate capacity bucket foundation of any other diameter and skirt length within the range of the parametric study, if the vertical ultimate capacity of the corresponding surface foundation with the same diameter is known.

4.3.2 Effect of Soil Plug on End-Bearing Capacity

In order to determine the effect of soil plug on the ultimate vertical bearing capacity of bucket foundations, numerical simulations were carried out by considering zero shaft resistance or zero interface friction angle. As a result of which, the vertical capacities obtained for both the bucket foundations and embedded solid foundations are only due to the end-bearing resistance. The end-bearing capacities obtained from the numerical analyses are presented in Table 4.5.

The effect of soil plug on the vertical bearing capacity of bucket foundation is reported as the difference in the end-bearing capacity in medium dense sand (Table 4.6) and in very dense sand (Table 4.7). The difference in the end-bearing capacities can be attributed to the cushioning effect of the soil plug inside the bucket foundation, as already observed from the displacement vector diagrams [Figures 4.14(a) and 4.17(a)]. The percentage differences between the two foundation types for each geometry are presented in Tables 4.6 and 4.7.

From the tables, for a constant diameter, the difference of the end-bearing capacities between embedded solid and bucket foundation i.e. the magnitude of reduction in the end-bearing capacity is noted to increase with aspect ratio. For example, in medium dense sand, the end-bearing capacity reduces by 33.07 MN for a bucket foundation with diameter and aspect ratio of 12 m and 0.5, respectively. Further, for the same diameter, the difference of end-bearing capacity is noted to increase to 33.40 MN and 35.78 MN, respectively, for increased aspect ratio values of 0.75 and 1.

For a bucket foundation of 12 m diameter and aspect ratio of 0.5, embedded in very dense sand, the reduction in the end-bearing capacity is noted to be 88.58 MN. The difference in the end-bearing capacities increases to 94.51 and 92.11 MN, respectively for aspect ratios of 0.75 and 1.0.

For a 15 m diameter foundation aspect ratios of 0.5, 0.75 and 1, the reductions in the end-bearing capacities of embedded solid and bucket foundations are found to be 49.70, 62.54 and 59.75 MN in medium dense sands and 130.84, 149.21 and 163.71 MN for foundations embedded in very dense sands. For higher diameter of 18 m and aspect ratios of 0.5, 0.75 and 1, the reduction in the end-bearing capacities are found to be 68.89, 93.25 and 106.51 MN in medium dense sand and 212.67, 238.16 and 283.79 MN for foundations embedded in very dense sands.

From the above mentioned details, a clear increase in the magnitude of reduction in the end-bearing capacity foundation with aspect ratio is observed for foundations in nearly all the cases in medium dense and very dense sands. With increasing bucket diameter, the reduction in end-bearing capacity is greater. The reduction in the end-bearing capacity, expressed as percentage, is also presented in Table 4.6 and Table 4.7.

The magnitude of reduction of the end-bearing capacity of foundation is noted to be higher in case foundation embedded in very dense sand as compared to that of the one founded in medium dense sands. Contrastingly, the percentage by which the end-bearing capacity reduces, is noted to be higher in case of medium dense sand.

Table 4.5 End-bearing capacities of bucket and embedded solid foundations (with zero shaft resistance)

Soil type	**Foundation type**	**Aspect ratio (*L*/*D*)**	**Ultimate vertical capacity (MN)**		
			***D* = 12 m**	***D* = 15 m**	***D* = 18 m**
Medium dense sand	Bucket	0.5	114.48	192.84	297.43
		0.75	121.32	193.18	296.21
		1	124.46	211.66	310.22
	Solid	0.5	147.55	242.54	366.32
		0.75	154.72	255.72	389.46
		1	160.24	271.41	416.73
Very dense sand	Bucket	0.5	387.58	647.91	960.04
		0.75	391.95	661.43	966.34
		1	396.72	670.02	968.24
	Solid	0.5	476.16	784.75	1172.71
		0.75	486.46	810.64	1204.50
		1	488. 83	833.73	1252.03

Table 4.6 Difference in end-bearing capacities of bucket and embedded solid foundations (with zero shaft resistance) in medium dense sand

Diameter	Aspect ratio (*L*/*D*)	Difference in end-bearing capacity (MN)	Difference in end-bearing capacity (%)
D = 12 m	0.5	33.07	22.41
	0.75	33.40	21.59
	1	35.78	22.33
D = 15 m	0.5	49.70	20.49
	0.75	62.54	24.46
	1	59.75	22.01
D = 18 m	0.5	68.89	18.81
	0.75	93.25	23.94
	1	106.51	25.56

Table 4.7 Difference in end-bearing capacities of bucket and embedded solid foundations (with zero shaft resistance) in very dense sand

Diameter	Aspect ratio (*L*/*D*)	Difference in end-bearing capacity (MN)	Difference in end-bearing capacity (%)
D = 12 m	0.5	88.58	18.60
	0.75	94.51	19.43
	1	92.11	18.84
D = 15 m	0.5	136.84	17.44
	0.75	149.21	18.41
	1	163.71	19.64
D = 18 m	0.5	212.67	18.13
	0.75	238.16	19.77
	1	283.79	22.67

4.4 PREDICTIVE EXPRESSIONS

4.4.1 Prediction of Ultimate Vertical Capacity

The results of ultimate vertical bearing capacities of bucket foundations in medium dense sand and very dense sand are normalized against effective unit weight (γ'), diameter (D) and length (L) of bucket foundation and plotted against aspect ratio, as shown in Figure 4.19(a)-(b).

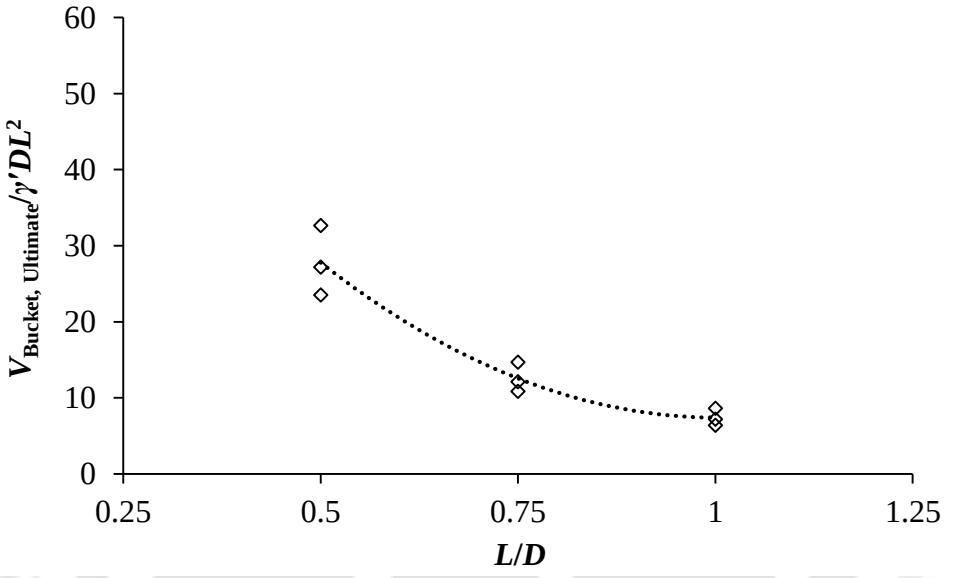

(a)

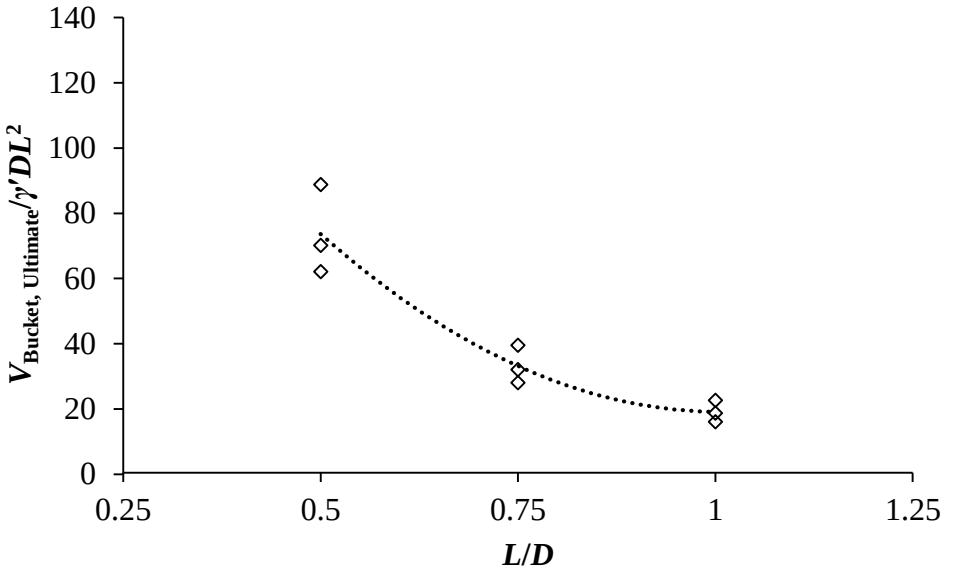

(b)

Figure 4.19 Variation of normalized ultimate vertical capacity with aspect ratio of bucket foundation: (a) in medium dense sand; (b) in very dense sand

$$V_{Bucket,Ultimate} = \gamma' L^2 \left[a^{**} \frac{L^2}{D} + b^{**} L + c^{**} D \right] \quad (4.2)$$

Based on the data points, expression has been developed to determine the ultimate vertical bearing capacity of bucket foundation, given by Equation (4.2). The values of the coefficients in the equation for the two sand types are presented in Table 4.8.

Table 4.8 Values of coefficients to determine the ultimate vertical capacity of bucket foundation

Sl. No.	Coefficient	Ultimate vertical bearing capacity (MN)	
		Medium dense sand	Very dense sand
1.	a^{**}	80.66	211.50
2.	b^{**}	-161.74	-426.33
3.	c^{**}	88.49	233.96

4.4.2 Prediction of Settlement under Superstructure Load

Typical self-weight of a 5 MW offshore wind turbine is 10 MN (Achmus et al. 2013; Ahmed and Hawlader 2016; LeBlanc et al. 2010; Malhotra 2011). With increasing capacity and size of the wind turbine, the self-weight increases. The settlement values of all the bucket foundation geometries under three superstructure loads (5, 10 & 15 MN) are presented in Table 4.9. Under the application of vertical superstructure load (self-weight) of the wind turbine structure, the bucket foundation settles downward. For a given bucket geometry, the settlement is noted to increase with superstructure load. However, the settlement is noted to reduce with increasing aspect ratio. The settlement is seen to be higher in the case of foundation embedded in very dense sand.

Table 4.9 Settlement of bucket foundation under the superstructure load

Soil type	Bucket geometry	Settlement under superstructure load (mm)		
		***V* = 5 MN**	***V* = 10 MN**	***V* = 15 MN**
Medium dense sand	*D* = 12 m, *L* = 6 m	15.5	31	46.5
	D = 12 m, *L* = 9 m	14.6	29.2	43.8
	D = 12 m, *L* = 12 m	13.9	27.7	41.6
	D = 15 m, *L* = 7.5 m	9.8	19.6	29.4
	D = 15 m, *L* = 11.25 m	8.8	17.6	26.3
	D = 15 m, *L* = 15 m	6.6	13.1	19.7
	D = 18 m, *L* = 9 m	8.5	17.0	25.5
	D = 18 m, *L* = 13.5 m	7.0	14.0	20.9
	D = 18 m, *L* = 18 m	5.7	11.3	17.0
Very dense sand	*D* = 12 m, *L* = 6 m	5.0	10.1	16.3
	D = 12 m, *L* = 9 m	4.6	9.1	13.7
	D = 12 m, *L* = 12 m	4.6	9.1	13.7
	D = 15 m, *L* = 7.5 m	3.9	7.9	11.8
	D = 15 m, *L* = 11.25 m	3.9	7.7	11.6
	D = 15 m, *L* = 15 m	3.9	7.7	11.6
	D = 18 m, *L* = 9 m	2.9	5.9	8.8
	D = 18 m, *L* = 13.5 m	2.8	5.7	8.5
	D = 18 m, *L* = 18 m	2.5	4.9	7.4

The settlement values of bucket foundation under the superstructure loads of 5, 10 and 15 MN are presented in the normalized form and plotted against the normalized superstructure loads. The normalized settlement versus normalized superstructure loads for bucket foundations embedded in medium dense sand and very dense sand are presented in Figure 4.20(a)-(c) and Figure 4.21(a)-(c), respectively. From the plots, the data points of normalized settlement versus normalized superstructure loads are utilized to fit curves and the expression has been arrived at, to predict the allowable settlement for wind turbine superstructure load ranging from 5 MN to 15 MN. The expression is given by Equation (4.3). The coefficients of the equation are presented in Table 4.10.

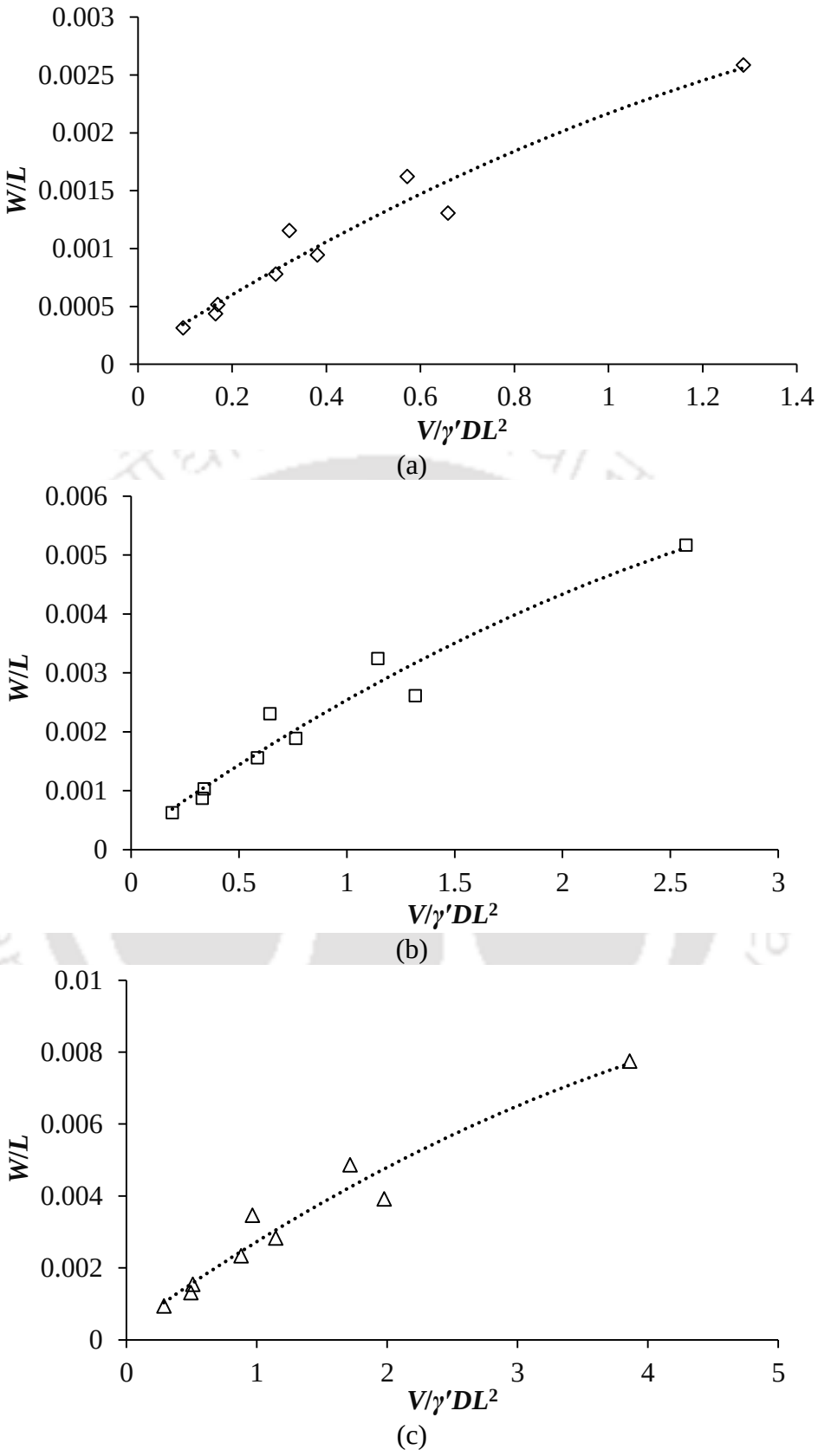

Figure 4.20 Variation of normalized settlement with bucket foundation geometry in medium dense sand under different superstructure loads: (a) 5 MN; (b) 10 MN; and (c) 15 MN

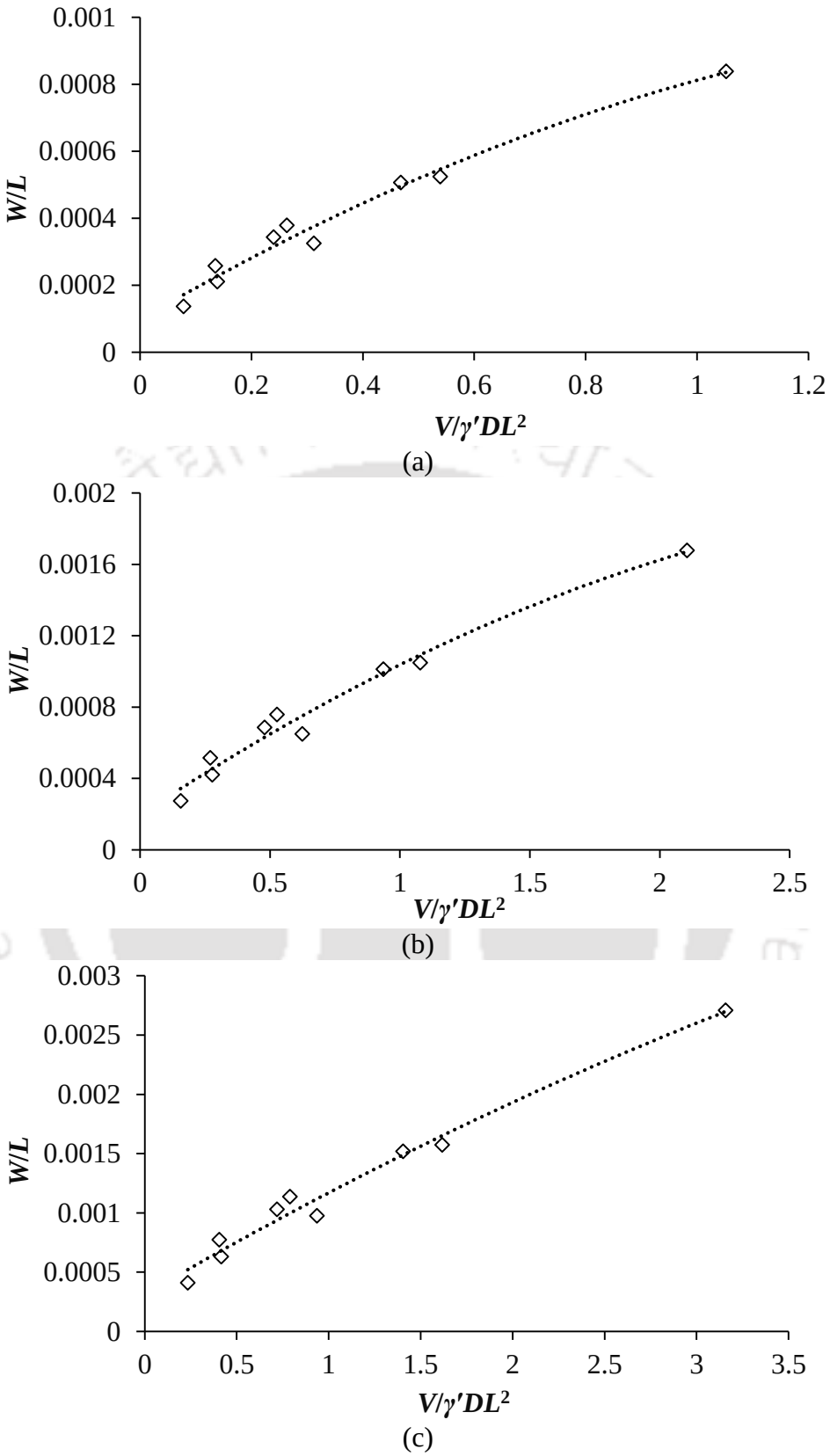

Figure 4.21 Variation of normalized settlement with bucket foundation geometry in very dense sand under different superstructure loads: (a) 5 MN; (b) 10 MN; and (c) 15 MN

$$W = L\left[a''' + b'''\left(\frac{V}{\gamma' DL^2}\right) + c'''\left(\frac{V}{\gamma' DL^2}\right)^2\right] \quad (4.3)$$

Table 4.10 Values of coefficients to determine the settlement under superstructure load

Soil type	Coefficient	Settlement under superstructure load (m)		
		***V* = 5 MN**	***V* = 10 MN**	***V* = 15 MN**
Medium dense sand	a‴	0.0001	0.0002	0.0003
	b‴	0.0026	0.0026	0.0026
	c‴	-0.0005	-0.0003	-0.0002
Very dense sand	a‴	0.0001	0.0002	0.0003
	b‴	0.001	0.001	0.0009
	c‴	-0.0003	-0.0001	-0.00005

4.5 SUMMARY

Based on the numerical study, the following main conclusions have been drawn:

1. Under the action of externally applied vertical load, the vertical bearing capacity of bucket foundation for a given diameter is greater than that of surface circular foundation and is lower than that of solid foundation with the same skirt length. The ultimate vertical capacity increases with aspect ratio and is also higher in very dense sand.
2. The magnitude of maximum shear stress along embedment length obtained is noted to increase with bucket geometry size. The depth, where the maximum lateral stress is encountered, increases with aspect ratio. The magnitude of shear stress is higher when embedded in very dense sand.
3. For a given diameter, greater lateral displacement of the soil mass away from the base tip is noted in the case of bucket foundation compared to that of the embedded solid foundation.
4. At failure, surface flow mechanism is observed for surface circular foundations, whereas confined deep flow mechanism is observed for both bucket and embedded solid foundations. Beneath all the foundation types, formation of an elastic zone in the shape of wedge is noted. The surface circular foundation is observed to fail showing Prandtl-type

failure mechanism whereas both bucket and solid embedded foundations fail under punching type failure mechanism.

5. A non-linear relationship has been obtained between the depth factor (ratio of ultimate vertical capacities of bucket foundation to surface foundation) and aspect ratio of bucket foundations. If the ultimate capacity of the surface circular foundation is known, the ultimate vertical bearing capacity of the bucket foundation can be determined.
6. Based on further analyses of solid and bucket foundation with zero shaft resistance, the reduction of end-bearing capacity of bucket foundation due to the presence of soil plug is found to be between 18-25% in medium dense sand and between 17-23% in very dense sand.
7. Predictive equations have been proposed to determine the ultimate bearing capacity of the bucket foundation of any geometry and its settlement under superstructure load.

Chapter 5

LATERAL LOAD-RESPONSE OF MONOPOD BUCKET FOUNDATIONS

5.1 INTRODUCTION

Globally, the average capacity of turbines for offshore wind power projects has increased from 3.4 MW in 2015 to 4.7 MW in 2016. This trend is expected to continue, with average turbine capacity expected to reach 7.0 MW for projects installed in 2020 (Walter et al. 2016). With the increase of average turbine capacity, the hub height and rotor diameter also increase considerably. Offshore wind turbines in 2015 averaged a hub height of 90 m and rotor diameter of 119 m, while 2030's offshore wind turbines will measure around 125 m and 190 m in hub height and rotor diameter, respectively (Geuss 2016). The schematic diagram of an offshore wind turbine is shown in Figure 5.1 and its evolution over time is presented in Figure 5.2.

The increasing capacity and size lead to increased self-weight of the wind turbine. Typical self-weight of a 5 MW offshore wind turbine is 10 MN (Achmus et al. 2013; Ahmed and Hawlader 2016; LeBlanc et al. 2010; Malhotra 2011).

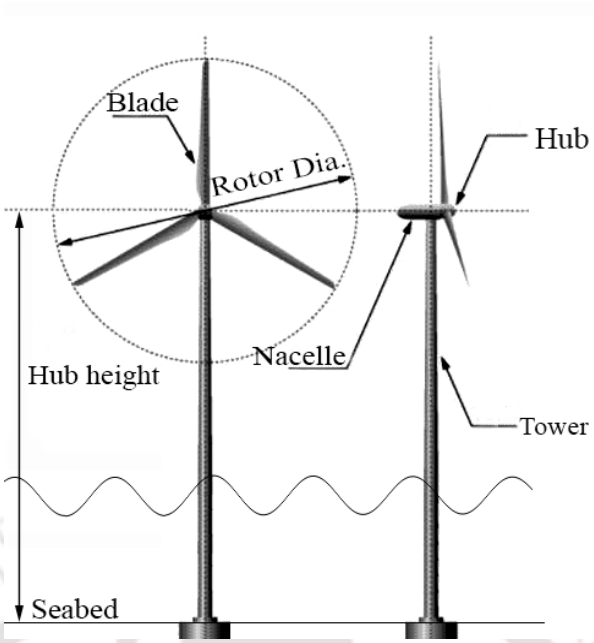

Figure 5.1 Schematic diagram of an offshore wind turbine

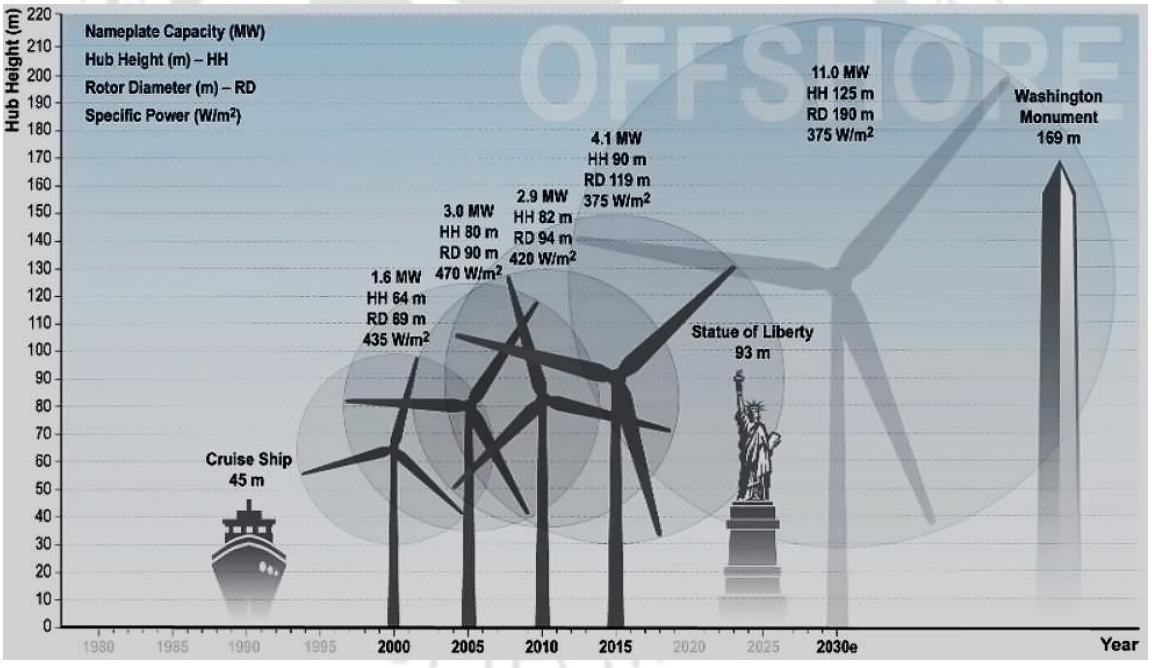

Figure 5.2 Evolution of offshore wind turbines over the years (Geuss 2016)

The overturning moment generated due to water waves and wind force is a crucial aspect in the design of monopod bucket foundations. The response of the foundation under the resultant lateral load acting at different loading heights up to hub height, when embedded in medium dense and very dense sandy soils, is discussed in this chapter.

5.2 GEOMETRIC AND LOADING DETAILS

The bucket geometries considered in the study are presented Table 5.1. Three bucket diameters of 12, 15 and 18 m were chosen, and the aspect ratio of the bucket foundations was varied from 0.5 to 1 for each diameter. The thickness of bucket lid and skirt were taken as 0.1 m and 0.03 m. The loading details are presented in Table 5.2. The superstructure load ranged from 5 to 15 MN. The hub height was taken as 100 m and the lateral loading height was varied from 0 to 100 m. A parametric study was then performed on nine geometries of the monopod bucket foundation subjected to pure lateral loading, lateral load acting at seven loading heights and pure moment loading. The schematic diagram of a discretized bucket foundation embedded in the seabed is shown in Figure 5.3.

Table 5.1 Geometric details of bucket foundations under lateral loading

Diameter, *D* (m)	**Skirt length, *L* (m)**	**Aspect ratio (*L*/*D*)**
12	6	0.5
	9	0.75
	12	1
15	7.5	0.5
	11.25	0.75
	15	1
18	9	0.5
	13.5	0.75
	18	1

Table 5.2 Loading details considered in the present study

Superstructure load (MN)	**Lateral loading cases**
5, 10, 15	0 m, 2.5 m, 5 m, 10 m, 20 m, 30 m, 40 m, 100 m and pure moment

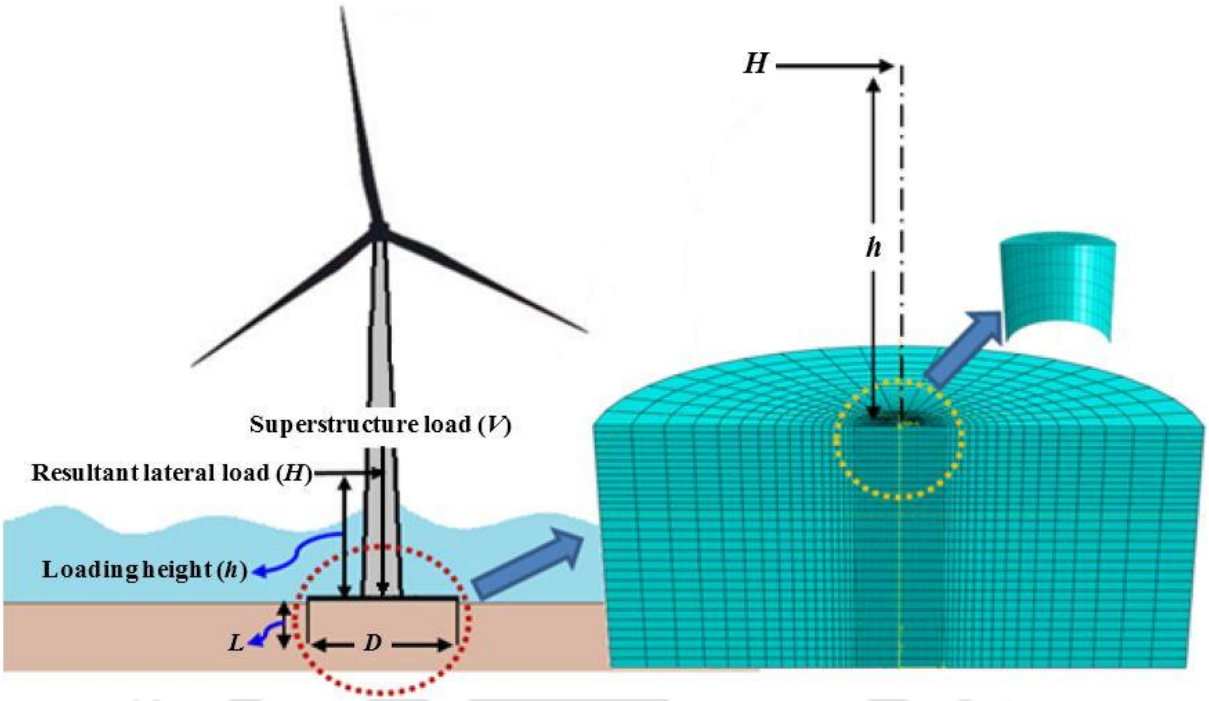

Figure 5.3 Schematic diagram of bucket foundation embedded in soil domain

5.3 NUMERICAL RESULTS

In general, the ultimate or failure state of the foundation can be assumed to have been reached when there is a continuous increase in lateral displacement with no further increase in lateral load capacity. But in certain cases, even though a large displacement has been reached, the lateral load capacity continues to increase incrementally. For such cases, the ultimate capacity can be defined corresponding to a displacement, which is sufficiently high to cause collapse of the structure. In the present study, the ultimate lateral capacity (H_{Ultimate}) of the bucket foundation for any loading height is the applied load, which causes a lateral displacement equal to 10% of bucket diameter, measured at the lid centre level. At such a large value of displacement, full mobilization of passive earth pressure along the entire skirt perimeter surface can be assumed to have taken place.

In a few cases, before reaching the prescribed maximum lid displacement equal to 10% of bucket diameter, the simulation failed to converge due to numerical instability. For such cases, hyperbolic method was used to estimate the ultimate lateral load capacity

(Haiderali et al. 2013). A field test on bucket foundation at Frederikshavn in Denmark (Ibsen et al. 2005) and a numerical study (Abdel-Rahman and Achmus 2006) were initially used to validate the numerical modelling process adopted in this study, as elaborated in Appendix-C.

The variation of the lateral response of the bucket foundation with loading height, superstructure load and aspect ratio in medium dense and very dense sands is discussed in the subsequent sections.

5.3.1 Load-Displacement, Load-Rotation and Overturning Moment-Rotation Response in Medium Dense Sands

Figure 5.4(a) illustrates typical lateral load capacity versus lid displacement response of a monopod bucket foundation of 12 m diameter and 6 m skirt length, under superstructure load of 5 MN, loaded up to ultimate condition. Before reaching ultimate condition, for a given displacement level at bucket lid, as the loading height is increased from 0 to 100 m, there is a significant reduction in lateral load capacity of the bucket foundation. For any lateral load level, observed displacement increases as the loading height is increased from 0 to 100 m. This increase in bucket lid displacement with loading height can be attributed to increased thrust on the bucket at the seabed level (Kumar and Rao 2012).

From Figure 5.4(a), it can also be noted that the ultimate lateral load capacity has reduced significantly from 13.93 to 0.88 MN as the loading height is increased from pure lateral load (h = 0 m) to the maximum loading height (h = 100 m). The lateral load capacity versus lid rotation response and the resisting moment capacity versus lid rotation response of the bucket foundation (D = 12 m, L = 6 m) are depicted in Figures 5.4(b) and 5.4(c), respectively.

At any rotation angle, the resisting moment capacity has been calculated as the product of the lateral load capacity and the corresponding loading height. At ultimate condition corresponding to lid displacement of 1.2 m [Figure 5.4(a)], the respective

maximum lid centre rotation is noted to increase from 11.98° to 14.83° [Figure 5.4(b)], as the loading height is increased from h = 2.5 to h = 100 m. This is because the magnitudes of the respective overturning moment acting at the lid centre have increased from 25.78 to 88 MN-m. A still higher lid rotation of 15.51° is obtained when the bucket foundation is subjected to pure moment, and the corresponding resisting moment capacity is 101.82 MN-m [Figure 5.4(c)].

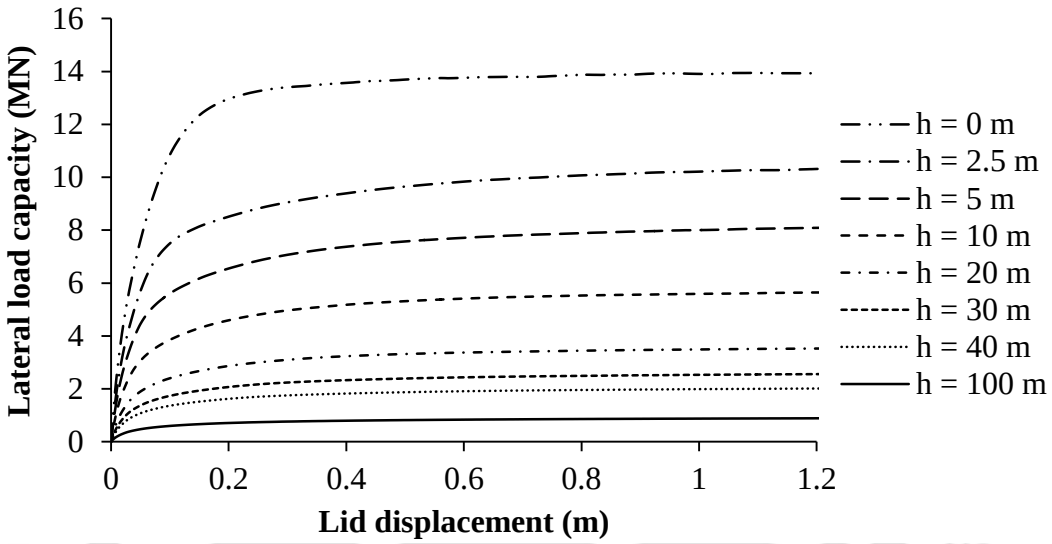

(a)

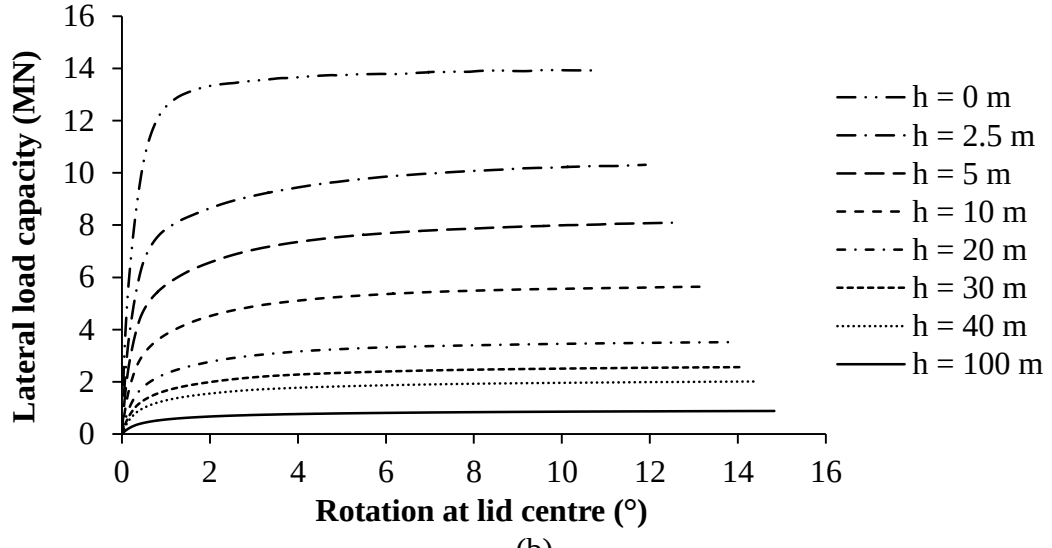

(b)

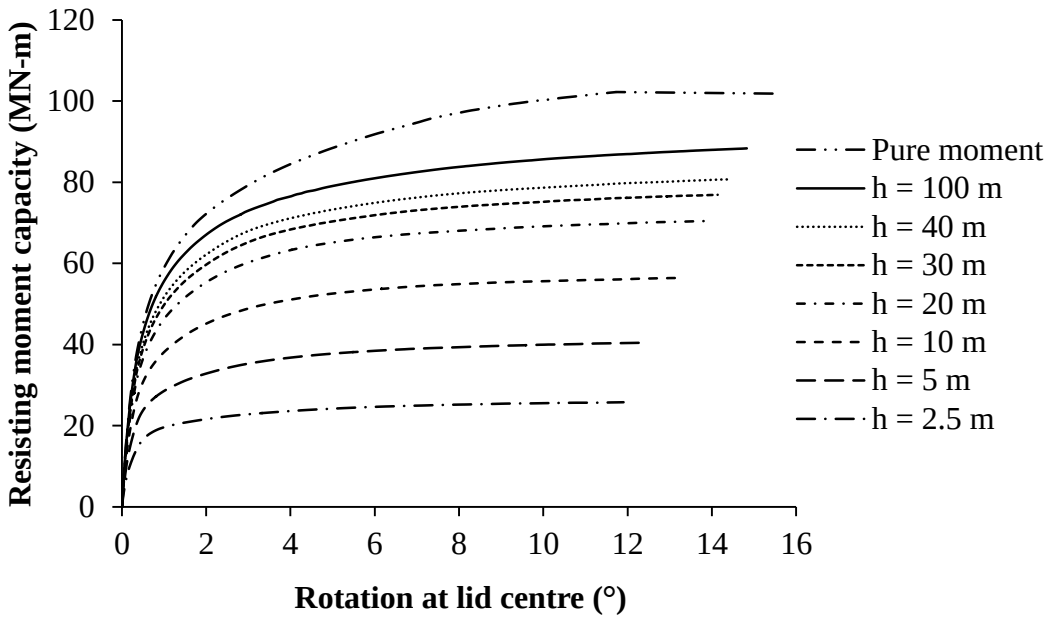

(c)

Figure 5.4 Response of bucket foundation (D = 12 m, L = 6 m and V = 5 MN) for varying lateral load cases: (a) Lateral load capacity vs. lid displacement; (b) Lateral load capacity vs. lid rotation; and (c) Resisting moment capacity versus lid rotation

The above trends of lateral load capacity and resisting moment capacity response in Figure 5.4(a)-(c) were observed for other geometries of the bucket foundation in both sand types, under the superstructure loads of 5, 10 and 15 MN.

The ultimate lateral load and resisting moment capacities of bucket foundations with diameters of 12, 15 and 18 m, in both medium dense and very dense sands, are summarized in Tables 5.3-5.5, respectively. The corresponding lid rotations at failure of the foundations are tabulated in Tables 5.6-5.8.

For both sand types, for a given loading height and superstructure load, the ultimate lateral capacity is observed to increase with increasing value of either bucket diameter or skirt length. The ultimate lateral capacity is also noted to increase considerably with superstructure load. Moreover, it can be noted that in very dense sand, the ultimate load and moment capacities are higher than those in medium dense sand (Table 5.3 to Table 5.5). In both sand types, for a given bucket geometry and loading height, the lid rotation at failure is noted to

decrease with superstructure load. In most of the cases, the lid rotation at failure is noted to higher for a bucket foundation embedded in very dense sand as compared to medium dense sand (Table 5.6 to Table 5.8).

Table 5.3 Comparison of load and moment capacities in medium dense and very dense sands (D = 12 m)

V (MN)	Geometry	Type of soil	Ultimate lateral load capacity, $H_{Ultimate}$ (MN)								Ultimate resisting moment capacity (MN-m)
			Loading height, h (m)								
			0	2.5	5	10	20	30	40	100	
5	D = 12 m, L = 6 m	MDS	13.93	10.31	8.09	5.64	3.52	2.56	2.02	0.88	101.82
		VDS	19.93	14.77	11.65	8.25	5.22	3.84	2.97	1.32	149.58
	D = 12 m, L = 9 m	MDS	20.02	15.86	13.07	9.54	6.25	4.65	3.70	1.64	200.68
		VDS	32.70	26.16	21.70	16.23	10.65	7.95	6.24	2.75	322.44
	D = 12 m, L = 12 m	MDS	28.02	22.89	19.35	14.88	10.15	7.71	6.18	2.83	324.01
		VDS	48.70	41.51	35.73	27.67	18.83	14.19	11.33	5.06	553.81
10	D = 12 m, L = 6 m	MDS	18.85	13.20	10.35	7.19	4.49	3.26	2.56	1.11	130.83
		VDS	24.13	18.05	14.25	10.08	6.35	4.59	3.64	1.60	171.27
	D = 12 m, L = 9 m	MDS	23.29	18.29	15.07	11.05	7.18	5.32	4.23	1.89	221.92
		VDS	36.49	28.72	23.91	18.05	11.76	8.73	6.89	3.02	329.27
	D = 12 m, L = 12 m	MDS	30.79	25.08	21.18	16.02	10.93	8.25	6.62	3.04	358.99
		VDS	52.08	44.03	37.74	29.15	19.78	14.88	11.87	5.32	560.97
15	D = 12 m, L = 6 m	MDS	22.73	15.67	12.20	8.48	5.28	3.82	2.99	1.29	138.54
		VDS	29.62	21.21	16.78	11.90	7.44	5.44	4.26	1.86	201.55
	D = 12 m, L = 9 m	MDS	26.22	20.48	16.87	12.25	7.93	5.86	4.66	2.06	242.29
		VDS	39.74	31.45	26.10	19.50	12.81	9.48	7.49	3.27	363.63
	D = 12 m, L = 12 m	MDS	33.33	27.12	22.84	17.34	11.73	8.85	7.09	3.23	381.85
		VDS	55.17	46.37	39.84	30.61	20.98	15.62	12.43	5.55	626.09

Table 5.4 Comparison of load and moment capacities in medium dense and very dense sands (D = 15 m)

V (MN)	Geometry	Type of soil	Ultimate lateral load, $H_{Ultimate}$ (MN) — Loading height, h (m)								Ultimate resisting moment capacity (MN-m)
			0	2.5	5	10	20	30	40	100	
5	D = 15 m, L = 7.5 m	MDS	22.14	17.06	13.87	10.02	6.44	4.71	3.72	1.65	200.47
		VDS	32.74	25.46	20.80	15.28	10.02	7.36	5.83	2.61	298.56
	D = 15 m, L = 11.25 m	MDS	34.90	28.72	24.29	18.12	12.59	9.54	7.64	3.52	388.71
		VDS	57.42	47.93	41.26	31.48	21.96	16.75	13.43	6.13	657.80
	D = 15 m, L = 15 m	MDS	49.83	42.15	37.11	29.44	20.73	16.02	13.05	6.17	694.64
		VDS	89.10	77.82	68.88	55.45	39.93	30.73	24.88	11.49	1246.97
10	D = 15 m, L = 7.5 m	MDS	26.72	20.29	16.52	12.13	7.67	5.62	4.42	1.95	222.36
		VDS	37.14	29.02	23.63	17.53	11.41	8.38	6.66	3.00	317.94
	D = 15 m, L = 11.25 m	MDS	38.26	31.51	26.63	19.72	13.64	10.46	8.38	3.82	422.83
		VDS	62.00	51.19	43.67	33.95	23.32	17.76	14.25	6.46	708.04
	D = 15 m, L = 15 m	MDS	52.38	45.15	39.27	31.03	21.73	16.77	13.66	6.43	724.32
		VDS	92.65	80.69	71.13	57.34	41.26	31.66	25.61	11.82	1277.91
15	D = 15 m, L = 7.5 m	MDS	31.54	23.79	19.01	13.68	8.73	6.45	5.04	2.21	248.58
		VDS	42.13	32.77	26.61	19.42	12.37	9.42	7.40	3.20	357.58
	D = 15 m, L = 11.25 m	MDS	41.48	33.88	28.74	22.03	14.98	11.22	9.00	4.12	452.74
		VDS	66.09	54.54	46.40	36.25	24.66	18.79	15.24	6.75	743.61
	D = 15 m, L = 15 m	MDS	55.37	47.24	40.70	32.54	22.57	17.42	13.65	6.42	751.89
		VDS	96.00	84.03	74.08	59.10	42.15	32.51	26.30	12.10	1314.51

Table 5.5 Comparison of load and moment capacities in medium dense and very dense sands (D = 18 m)

V (MN)	Geometry	Type of soil	Ultimate lateral load, $H_{Ultimate}$ (MN)								Ultimate resisting moment capacity (MN-m)
			Loading height, h (m)								
			0	2.5	5	10	20	30	40	100	
5	D = 18 m, L = 9 m	MDS	34.21	27.65	23.02	17.21	11.60	8.69	6.76	3.15	345.57
		VDS	52.30	43.81	36.42	27.38	18.40	13.87	11.16	5.12	587.45
	D = 18 m, L = 13.5 m	MDS	55.12	46.02	40.42	31.59	22.31	17.31	14.14	6.70	756.27
		VDS	94.56	80.71	70.57	56.76	40.32	31.28	25.41	12.14	1343.65
	D = 18 m, L = 18 m	MDS	79.36	69.26	61.26	50.05	37.10	29.01	23.85	11.56	1350.63
		VDS	145.87	130.23	117.86	97.80	71.35	56.83	46.89	22.25	2499.53
10	D = 18 m, L = 9 m	MDS	38.70	31.09	26.07	19.51	13.01	9.74	7.80	3.53	385.41
		VDS	56.80	47.26	39.56	29.71	19.92	15.02	12.05	5.55	615.79
	D = 18 m, L = 13.5 m	MDS	58.91	49.87	42.80	33.50	23.52	18.29	14.95	7.06	795.32
		VDS	98.48	83.78	73.58	59.19	41.98	32.76	26.57	12.27	1317.84
	D = 18 m, L = 18 m	MDS	82.53	71.57	63.35	51.71	38.03	29.87	24.58	11.88	1376.89
		VDS	149.09	133.84	119.66	99.59	73.36	57.74	47.58	22.68	2596.82
15	D = 18 m, L = 9 m	MDS	43.35	33.91	28.59	21.59	14.36	10.75	8.48	3.88	425.11
		VDS	61.39	50.83	42.65	32.02	21.46	16.18	13.00	5.94	684.12
	D = 18 m, L = 13.5 m	MDS	62.38	52.83	45.23	35.39	24.75	19.14	15.65	7.38	831.07
		VDS	102.44	86.73	76.07	60.99	43.36	34.10	27.56	12.70	1360.64
	D = 18 m, L = 18 m	MDS	85.34	74.02	65.49	53.48	39.18	30.77	25.30	12.33	1413.05
		VDS	152.85	136.93	122.58	101.62	74.12	58.66	48.28	23.06	2564.23

Table 5.6 Comparison of lid rotations at failure in medium dense and very dense sands (D = 12 m)

V (MN)	Geometry	Type of soil	Lid rotation at failure, Θ (°)								
			Loading height, h (m)								Pure moment loading
			0	2.5	5	10	20	30	40	100	
5	D = 12 m, L = 6 m	MDS	10.88	11.90	12.50	13.15	13.84	14.14	14.37	14.83	15.51
		VDS	11.51	12.15	12.56	13.06	13.59	13.89	14.05	14.52	15.73
	D = 12 m, L = 9 m	MDS	8.02	8.62	8.82	9.23	9.85	10.03	10.21	10.36	11.28
		VDS	8.32	8.79	9.02	9.50	9.92	10.12	10.33	10.73	11.74
	D = 12 m, L = 12 m	MDS	6.31	6.75	6.85	7.24	7.56	7.83	7.81	8.10	8.79
		VDS	6.59	6.91	7.13	7.42	7.74	7.97	8.08	8.44	9.37
10	D = 12 m, L = 6 m	MDS	9.63	11.43	12.16	13.02	13.83	14.28	14.52	15.09	16.16
		VDS	11.15	11.92	12.39	13.05	13.57	13.93	14.18	10.84	16.15
	D = 12 m, L = 9 m	MDS	7.79	8.43	8.69	9.20	7.18	10.16	10.26	10.69	11.51
		VDS	8.19	8.59	8.94	9.48	9.92	10.19	10.40	10.84	11.96
	D = 12 m, L = 12 m	MDS	6.21	6.66	6.78	7.28	7.52	7.69	7.72	8.13	8.73
		VDS	6.54	6.84	7.07	7.36	7.72	7.93	8.09	8.49	8.78
15	D = 12 m, L = 6 m	MDS	8.07	10.85	11.71	12.73	13.64	14.07	14.38	15.03	15.13
		VDS	10.57	11.67	12.25	12.93	13.67	14.10	14.41	15.16	16.76
	D = 12 m, L = 9 m	MDS	7.58	8.14	8.59	9.11	9.70	10.02	10.18	10.18	11.64
		VDS	8.07	8.48	8.87	9.37	9.94	10.23	10.45	10.97	12.26
	D = 12 m, L = 12 m	MDS	6.13	6.46	6.72	7.09	7.49	7.63	7.76	8.04	8.76
		VDS	6.48	6.80	7.06	7.36	7.79	7.95	8.09	8.50	8.75

Table 5.7 Comparison of lid rotations at failure in medium dense and very dense sands (D = 15 m)

V (MN)	Geometry	Type of soil	Lid rotation at failure, Θ (°)								
			Loading height, h (m)								Pure moment loading
			0	2.5	5	10	20	30	40	100	
5	D = 15 m, L = 7.5 m	MDS	11.29	12.16	12.77	13.49	14.18	14.52	14.75	15.28	15.78
		VDS	11.86	12.45	12.86	13.40	14.06	14.43	14.65	15.22	16.04
	D = 15 m, L = 11.25 m	MDS	8.13	8.50	8.83	9.27	9.66	10.07	10.06	10.46	10.72
		VDS	8.35	8.71	9.00	9.41	9.87	10.08	10.31	10.72	11.66
	D = 15 m, L = 15 m	MDS	6.31	6.72	6.82	7.10	7.51	7.66	7.79	8.07	8.32
		VDS	6.59	6.85	7.05	7.36	7.66	7.89	8.02	8.41	8.83
10	D = 15 m, L = 7.5 m	MDS	10.75	11.83	12.60	13.36	14.23	14.71	15.09	15.71	15.32
		VDS	11.57	12.25	12.71	13.35	14.07	14.49	14.79	16.16	16.85
	D = 15 m, L = 11.25 m	MDS	8.00	8.40	8.75	9.30	9.68	10.01	10.07	10.47	10.90
		VDS	8.29	8.67	8.96	9.39	9.82	10.12	10.27	10.75	11.22
	D = 15 m, L = 15 m	MDS	6.27	6.64	6.77	6.95	7.42	7.66	7.75	8.09	8.35
		VDS	6.56	6.86	6.99	7.27	7.68	7.87	8.04	8.44	8.89
15	D = 15 m, L = 7.5 m	MDS	10.00	11.65	12.33	14.30	14.30	14.62	15.02	15.79	16.44
		VDS	11.29	12.10	12.57	13.25	14.06	14.55	14.87	15.61	17.18
	D = 15 m, L = 11.25 m	MDS	7.87	8.30	8.59	9.08	9.67	9.90	10.08	10.50	10.88
		VDS	8.35	8.73	8.99	9.41	9.84	10.08	10.25	10.71	11.18
	D = 15 m, L = 15 m	MDS	6.21	6.47	6.73	6.98	7.38	7.58	7.71	8.02	8.35
		VDS	6.53	6.81	7.07	7.30	7.64	7.87	8.03	8.47	8.84

Table 5.8 Comparison of lid rotations at failure in medium dense and very dense sands (D = 18 m)

V (MN)	Geometry	Type of soil	Lid rotation at failure, Θ (°)								
			Loading height, h (m)								Pure moment loading
			0	2.5	5	10	20	30	40	100	
5	D = 18 m, L = 9 m	MDS	11.54	12.22	12.54	13.18	13.85	14.16	14.25	14.74	15.12
		VDS	11.96	12.45	12.70	13.17	13.63	13.90	14.15	14.64	16.52
	D = 18 m, L = 13.5 m	MDS	8.12	8.47	8.74	9.11	9.57	9.78	9.94	10.37	10.72
		VDS	8.41	8.74	8.95	9.30	9.72	9.96	10.14	11.07	11.60
	D = 18 m, L = 18 m	MDS	6.35	6.62	6.77	6.99	7.27	7.52	7.63	7.97	8.26
		VDS	6.56	6.76	6.93	7.20	7.53	7.76	7.90	8.30	8.70
10	D = 18 m, L = 9 m	MDS	11.21	11.96	12.43	13.19	13.78	14.05	14.38	15.00	15.41
		VDS	11.79	12.34	12.60	13.08	13.55	13.55	14.09	14.68	15.44
	D = 18 m, L = 13.5 m	MDS	8.05	8.40	8.68	9.06	9.46	9.71	9.92	10.39	10.80
		VDS	8.36	8.70	8.89	9.30	9.73	9.99	10.17	10.68	11.15
	D = 18 m, L = 18 m	MDS	6.31	6.53	6.70	6.96	7.35	7.49	7.63	7.93	8.27
		VDS	6.53	6.76	6.92	7.19	7.52	7.77	7.87	8.31	9.05
15	D = 18 m, L = 9 m	MDS	10.89	11.79	12.33	13.00	13.71	14.08	14.33	14.94	15.52
		VDS	11.63	12.22	12.50	13.03	13.54	13.86	14.10	14.76	15.58
	D = 18 m, L = 13.5 m	MDS	7.97	8.36	8.63	8.99	9.44	9.72	9.89	10.35	10.82
		VDS	8.30	8.65	8.88	9.23	9.70	10.01	10.20	10.72	11.23
	D = 18 m, L = 18 m	MDS	6.27	6.51	6.68	6.94	7.31	7.48	7.61	7.89	8.26
		VDS	6.52	6.75	6.90	7.18	7.51	7.76	7.90	8.34	8.77

5.4 VARIATION OF ULTIMATE LATERAL CAPACITY WITH GEOMETRY

The variation of ultimate lateral load capacity of the bucket foundation (D = 12 m) with aspect ratio in medium dense sand, for the superstructure load of 5 MN, is shown in Figure 5.5. The ultimate lateral capacity is seen to increase almost linearly with the increase of aspect ratio. Under pure lateral load, the ultimate lateral capacity is 13.93 MN for aspect ratio of 0.5, and it increases to 20.02 MN and 28.02 MN, respectively for aspect ratios to 0.75 and 1.0. However, for a given aspect ratio, the ultimate lateral capacity decreases with increased loading height. For the maximum loading height of 100 m, the ultimate lateral capacities are the minimum with values 0.88, 1.64 and 2.83 MN for aspect ratios of 0.5, 0.75 and 1, respectively.

For the superstructure load of 5 MN, the variation of ultimate lateral capacity of the bucket foundation (L/D = 0.5) with diameter is illustrated in Figure 5.6. Under pure lateral load, the ultimate lateral capacity for the bucket foundation of 12 m diameter is obtained as 13.93MN, and it enhances to 22.14, and 34.21 MN as the diameter is increased to 15 and 18 m, respectively. A lesser increase in ultimate lateral capacity is noted for higher loading heights. Similar variation is noted for higher superstructure loads of 10 and 15 MN.

The improvement in ultimate lateral capacity with increasing aspect ratio or diameter can be attributed to increased vertical surface area of the foundation, which experiences greater passive resistance exerted by the soil mass to the lateral displacement at ultimate condition. From a comparison of Figures 5.5 and 5.6, it is evident that as compared to skirt length, increasing diameter has greater influence on the ultimate lateral capacity. The variations of ultimate lateral capacity with aspect ratio and diameter remain similar for the foundation under the superstructure loads of 5, 10 and 15 MN embedded in medium dense and very dense sands.

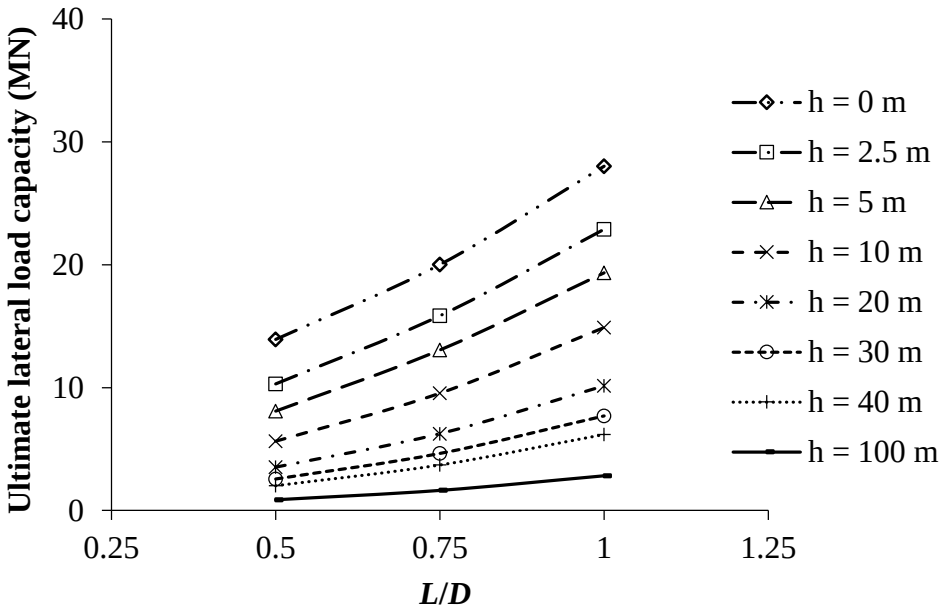

Figure 5.5 Variation of ultimate lateral load capacity with aspect ratio in medium dense sand (D = 12 m, V = 5 MN)

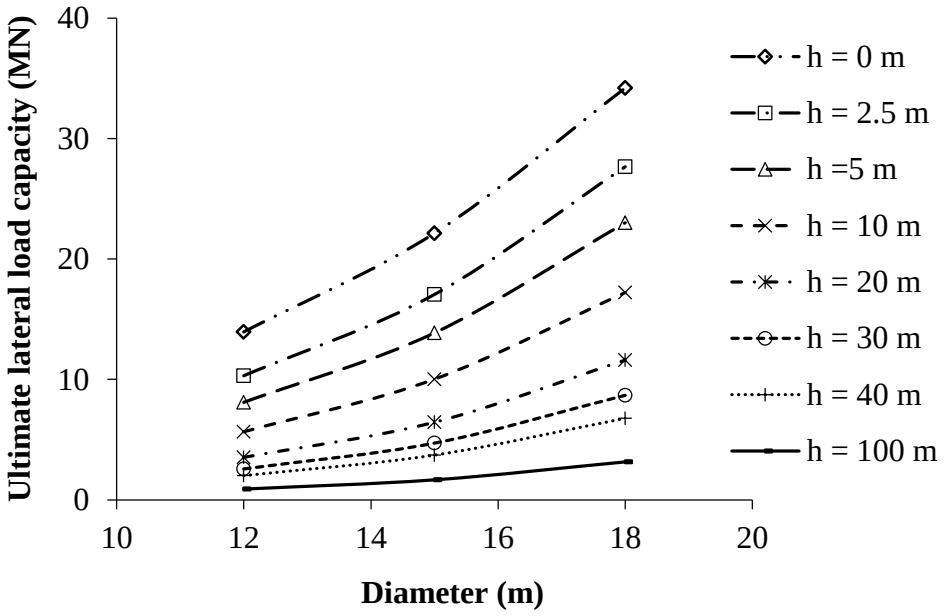

Figure 5.6 Variation of ultimate lateral load capacity with bucket diameter in medium dense sand (L/D = 0.5, V = 5 MN)

5.5 VARIATION OF ULTIMATE LATERAL CAPACITY WITH SUPERSTRUCTURE LOAD

Figure 5.7(a)-(b) shows the variation of ultimate lateral capacity with superstructure load in medium dense sand for bucket foundation of 12 m diameter and *L/D* ratios of 0.5 and 1.0.

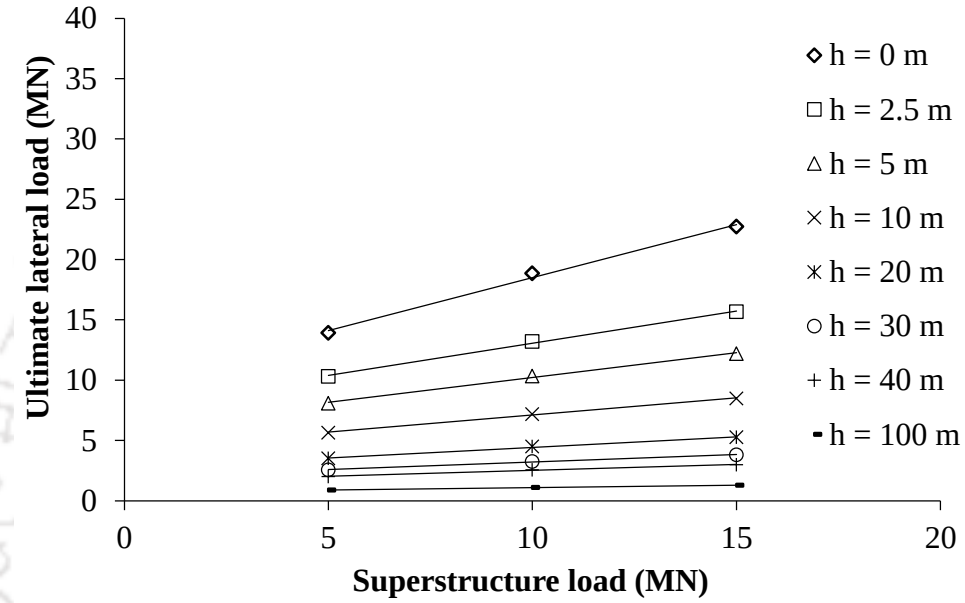

Figure 5.7 Variation of ultimate lateral load capacity with superstructure load in medium dense sand: (a) *D* = 12 m, *L* = 6 m; (b) *D* = 12 m, *L* = 12 m

From a comparison of the plots, it is observed that for all loading heights, when the superstructure load is varied from 5 to 10 and 15 MN, the ultimate lateral load capacity increases more noticeably in the case of shorter skirt length ($L = 6$ m) than in the case of longer skirt length ($L = 12$ m). For example, under pure lateral load, the ultimate lateral capacity varies from 13.93 to 18.85 and 22.73 MN for bucket length of 6 m, and from 28.02 to 30.79 and 33.33 MN for bucket with embedment length of 12 m, as the superstructure load is increased from 5 to 10 and 15 MN, respectively (Table 5.2). Similar variations are noted for increasing loading heights for all the bucket geometries in both sand types.

As noted above, the influence of superstructure load on ultimate lateral capacity keeps on decreasing with an increase in bucket skirt length. The behaviour can be attributed to the reduced intensity of vertical pressure at larger depths due to load dispersion effects. This will in turn lead to lesser changes in confining stresses at larger depths due to increasing superstructure load applied at the bucket lid level.

5.6 EARTH PRESSURE VARIATION ALONG SKIRT LENGTH

Due to lateral movement of the bucket foundation, passive and active earth pressures are exerted by the surrounding soil along the bucket skirt length at right exterior (RE), right interior (RI), left exterior (LE) and left interior (LI) sides. The schematic diagram of bucket foundation showing RE, RI, LE and LI sides are shown in Figure 5.8. Under the application of the lateral load up to failure, the bucket foundation tends to rotate about point C, which is the intersection of the initial vertical axis (YY) and the rotated vertical axis (Y′Y′), as shown in Figure 5.9.

On the RE and LI sides of the bucket foundation, passive earth pressure acts above the deformed horizontal axis X′X′, while active earth pressure acts below the axis. On the LE and RI sides, passive earth pressure acts below X′X′, whereas active earth pressure acts above the axis. However, from the numerical analysis, only the passive earth pressure is obtained.

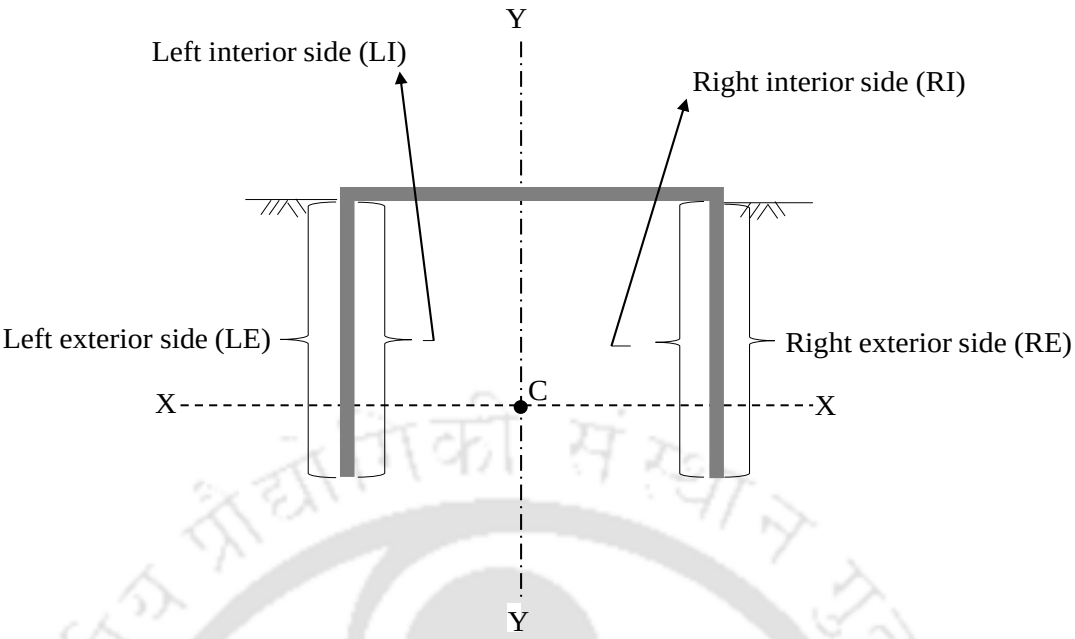

Figure 5.8 Schematic diagram indicating four different sides of bucket foundation

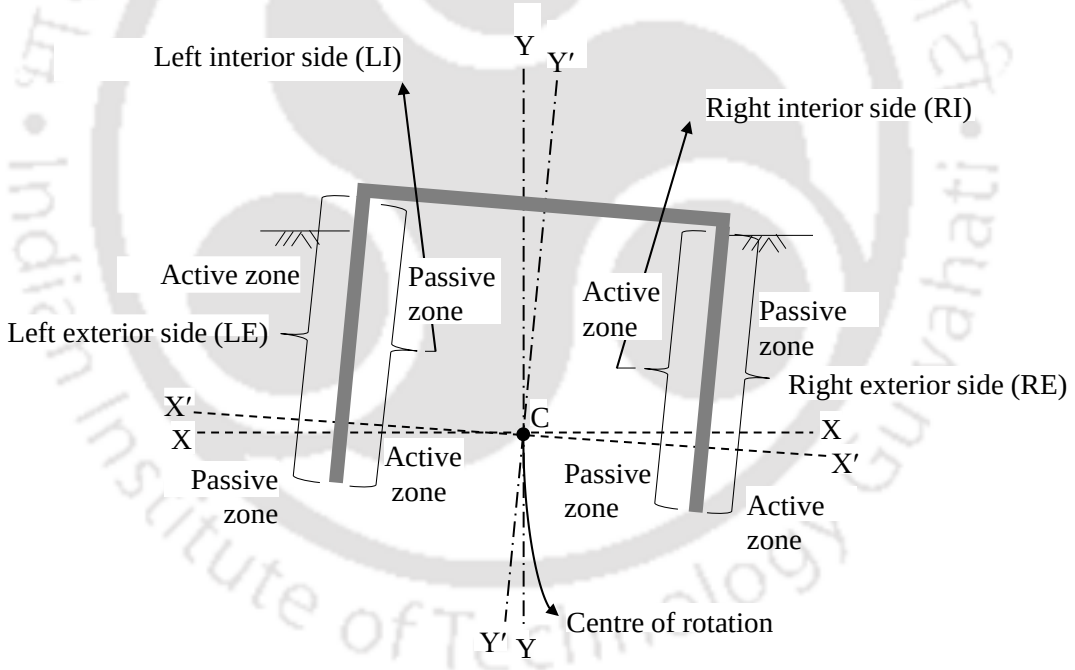

Figure 5.9 Schematic diagram representing failure state of the bucket foundation showing locations of active and passive earth pressures acting along the skirt length

At the large bucket lid displacement equal to 10% of the diameter, as the ultimate passive earth pressure conditions have been reached, the magnitude of the lateral load capacity is equal to the difference in total earth pressure reactions in the RE side (front side) and the LE side (back side) of the bucket. The variations of the passive earth pressure

distributions can be correlated with the observed reduction in the ultimate lateral load capacity of the bucket foundation with increased loading height. Typical variations of passive earth pressure at ultimate condition in the RE, RI, LE and LI sides, along the skirt length in the plane of symmetry for different loading heights, are shown in Figure 5.10(a)-(d).

5.6.1 Effect of Loading Height

The variations of passive earth pressure with loading height for bucket geometry (D = 12 m, L = 6 m) in both medium dense and very dense sands, supporting 5 MN superstructure load and under pure lateral load (h = 0 m), are presented in Figure 5.10(a)-(d)**.**

In both sand types, on the right exterior (RE) and left interior (LI) sides, the passive earth pressure is observed to increase parabolically from mud level to a maximum value up to a point along the skirt length (i.e. peak stress location), and then reduces gradually. However, along the left exterior (LE) and right interior (RI) sides, the passive earth pressure is seen to be prominent only at the lowermost one-third of the skirt length, with the maximum earth pressure exerted always at the skirt tip.

In medium dense sand, on the RE and LI sides, parabolic peak values of 361.55 and 32.39 kN/m^2 are noted at skirt depths of 4.62 m and 2.77 m, respectively. When the loading height is increased from h = 0 to 30 and 100 m, the magnitude of peak earth pressure decreases significantly to 267.34 and 234.85 kN/m^2 along the right exterior (RE) side, and to 29.39 and 28.56 kN/m^2 along the left interior (LI) side, respectively. Concurrently, the skirt depth location where the peak earth pressure is obtained, gradually moves upward from approximately from 4.62 to 4.15 m and 3.69 m in the RE side, and from 2.77 to 2.31 and 2.31 m in the LI side.

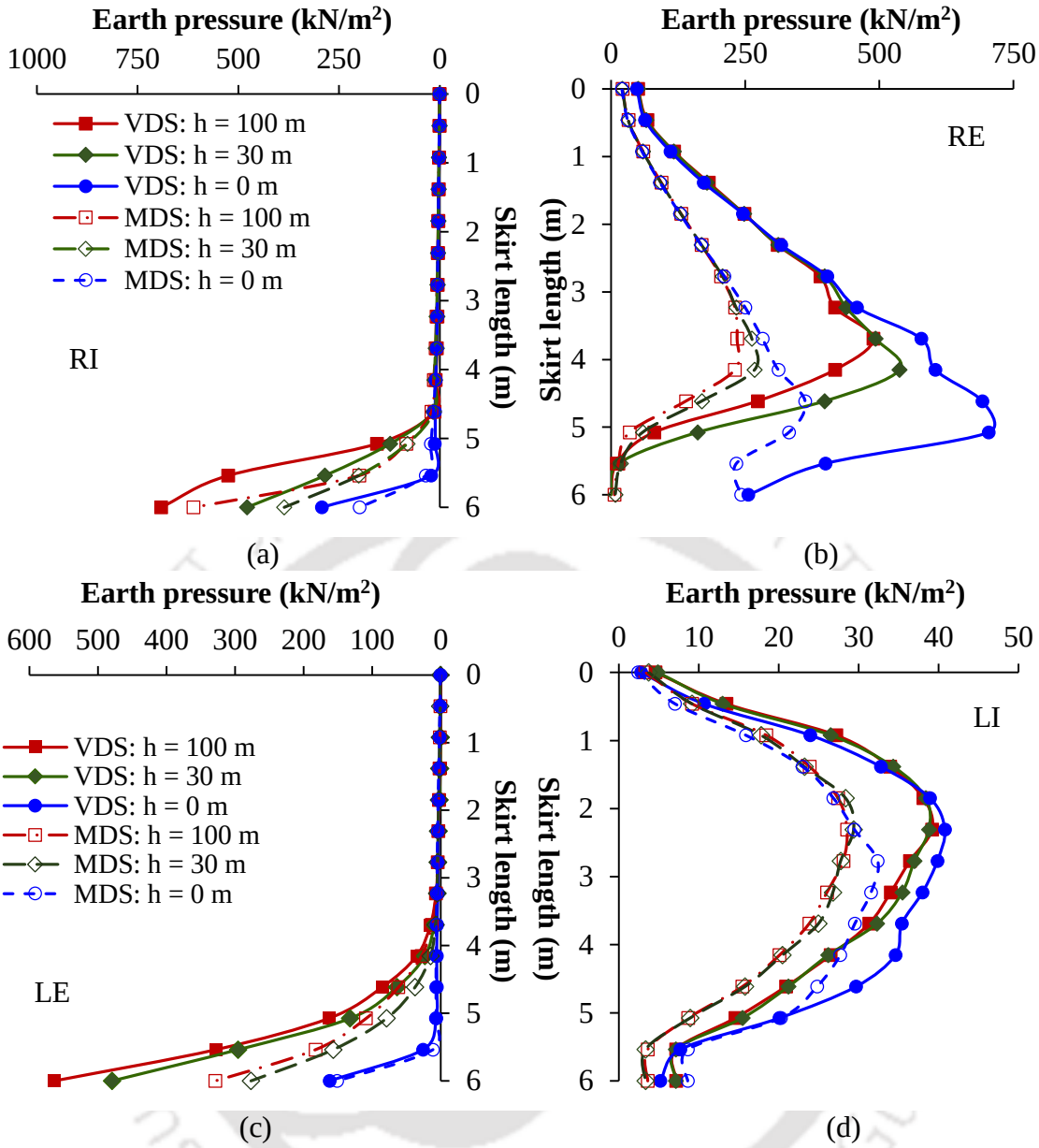

Figure 5.10 Variations of passive earth pressure along skirt length of bucket foundation (D = 12 m, L = 6 m and V = 5 MN) for different loading heights in both sand types: (a) RI side; (b) RE side; (c) LE side; and (d) LI side

In medium dense sand, on the LE and RI sides, respective maximum earth pressures at the skirt tip are 150.87 and 198.99 kN/m^2. With increasing loading height to 30 and 100 m, the maximum earth pressure values become 276.89 and 611.25 kN/m^2 on the LE side, while they are 386.29 and 399.52 kN/m^2 on the RI side.

In Figure 5.10(a)-(d), for the same bucket geometry (D = 12 m and L = 6 m) in very dense sand, though the passive earth pressure variations remain similar in the RE and LI

sides, the magnitudes are mostly greater along the entire skirt length, and the peak stress locations are always deeper (closer to the skirt tip). When the loading height is varied from *h* = 0 to 30 and 100 m, the magnitude of peak earth pressure is found to decrease respectively from 703.58 to 537.41 and 488.81 kN/m^2 along the RE side, and from 40.79 to 38.81 and 39.20 kN/m^2 along the LI side. The peak stress locations along the RE side are 5.08, 4.15 and 3.69 m for loading heights of 0, 30 and 100 m, respectively. Along the LI side, these locations are at 2.31, 2.30 and 2.31 m along the skirt length.

On the LE and RI sides, the maximum earth pressure values obtained at the tip of the skirt are 162.03, 479.59, 563.58 kN/m^2 and 292.61, 478.56, 691.76 kN/m^2, respectively for loading heights of 0, 30 and 100 m.

For both the sand types, with increasing values of loading height, the magnitude of peak earth pressure is noted to decrease and the location where the peak earth pressure is obtained, gradually moves upward along the skirt length in RE and LI sides. Along RI and LE sides, with increasing loading height, the maximum passive pressure is obtained at the skirt end, and the magnitude of passive earth pressure is noted to increase. From the comparison of passive earth pressure along bucket length in two sand types, higher magnitude of passive earth pressure is obtained along the skirt length in very dense sand. The trends of variation of earth pressure on the bucket foundation remain similar for other bucket geometries and superstructure loads for both the sand types.

5.6.2 Effect of Aspect Ratio

Figure 5.11(a)-(d) shows the variations of passive earth pressure with aspect ratio (0.5, 0.75 and 1) for bucket foundation of 12 m diameter, in medium dense and very dense sands, supporting 5 MN superstructure load and under lateral loading at 30 m height.

In medium dense sand, for aspect ratio of 0.5, the peak earth pressure of 267.34 kN/m^2 is obtained at 4.15 m along the skirt length in the RE side. In the LI side, the peak

earth pressure of 29.39 kN/m^2 is found at the skirt depth of 2.31 m. Along the RE and LI sides, with the increase of aspect ratio from 0.5 to 0.75, the peak earth pressures are found to be 374.86 and 34.93 kN/m^2 at depth locations of 4.85 and 4.15 m, respectively. Similarly, for the aspect ratio of 1.0, the peak earth pressures of 480.08 and 40.41 kN/m^2 have shifted to deeper locations of 5.54 and 4.62 m in the RE and LI sides, respectively.

For the aspect ratio of 0.5, maximum passive earth pressures of 386.27 kN/m^2 and 276.87 kN/m^2 are seen in the right interior (RI) and left exterior (LE) sides, respectively. For the higher aspect ratios of 0.75 and 1, the maximum values are 437.58, 447.86 kN/m^2 and 315.37, 491.91 kN/m^2, respectively at the RI and LE sides.

In very dense sand, along the RE side, the peak earth pressures are 537.41, 754.97 and 874.97 kN/m^2 at depths of 4.15, 4.85 and 5.54 m, respectively for the aspect ratios of 0.5, 0.75 and 1.0 m. In the LI side, peak earth pressure values of 38.31, 45.55 and 57.63 kN/m^2 are obtained at skirt depths of 2.30, 4.15 and 5.34 m as the aspect ratio is increased to 0.5, 0.75 and 1 m. In the RI and LE sides, the respective maximum earth pressures at the skirt tip are found to be 478.56, 793.08 and 801.80 kN/m^2 and 479.59, 650.04 and 993.66 kN/m^2, for the aspect ratios of 0.5, 0.75 and 1.0.

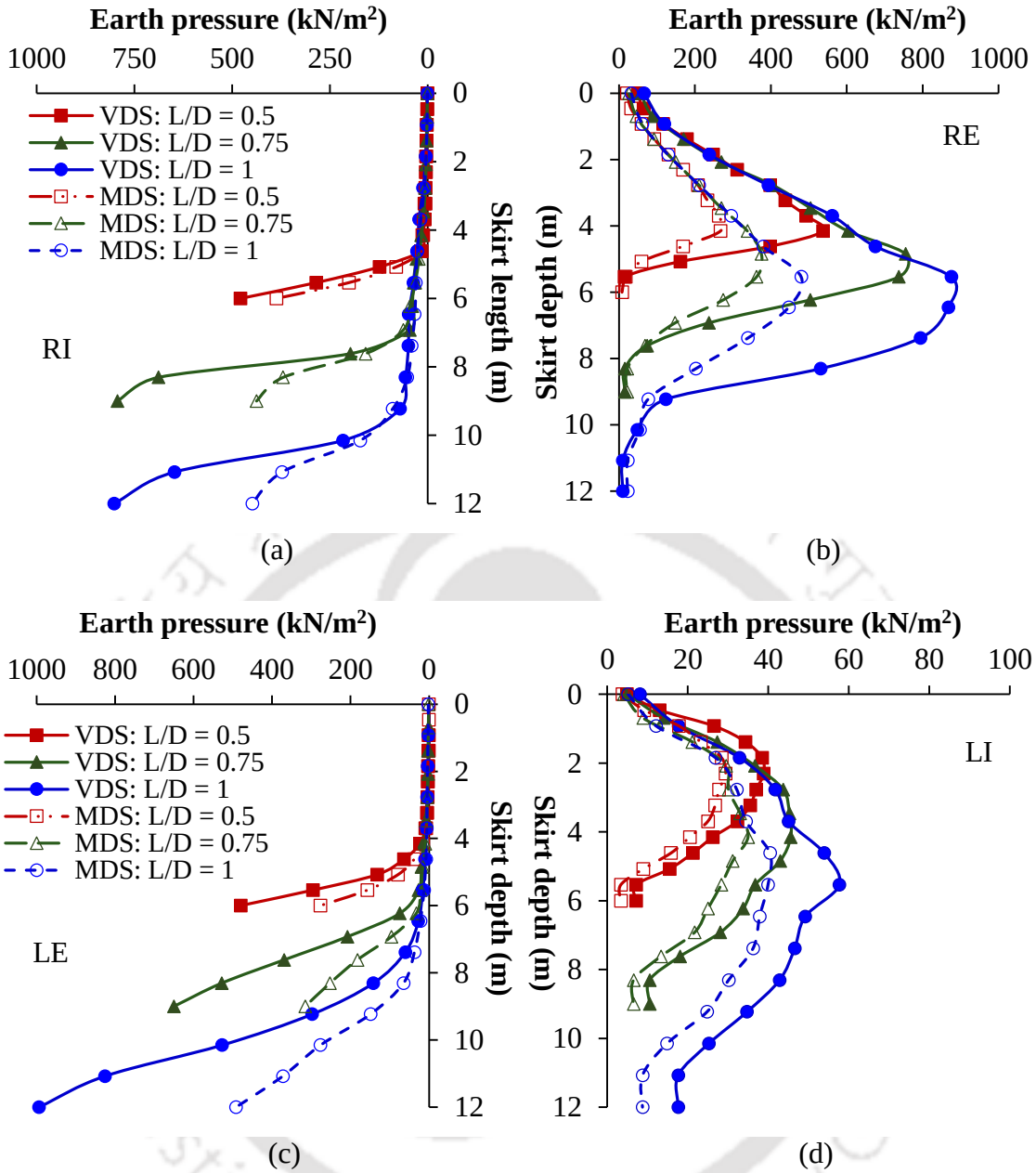

Figure 5.11 Variations of passive earth pressure along skirt length for different aspect ratios of bucket foundation (D = 12 m, V = 5 MN and h = 30 m) in both sand types: (a) RI side; (b) RE side; (c) LE side; and (d) LI side

In both sand types, on the right exterior (RE) and left interior (LI) sides, the peak passive earth pressure is observed to increase with aspect ratio (or skirt length), and is also located at a deeper depth from mud level. However, the ratio of peak stress location depth to the corresponding skirt length are different for all aspect ratios. Along the left exterior (LE) and right interior (RI) sides, the magnitude of maximum passive earth pressure at the skirt tip

is greater for a higher aspect ratio. Similar variation is observed for all the bucket geometries under superstructure loads of 5, 10 and 15 MN, for all loading heights.

5.7 DEPTH OF POINT OF ROTATION OF BUCKET FOUNDATION

The centre of rotation of the foundation at ultimate condition is defined as the point along the vertical axis of the bucket, which undergoes zero lateral displacement with respect to its initial position. The depth of the point of rotation is measured from the bucket lid centre. The rotated position of the axis is obtained from averaging the rotated positions of the RE and LE sides of the skirt. A schematic diagram of depth of point of rotation of bucket foundation under lateral load is shown in Figure 5.12.

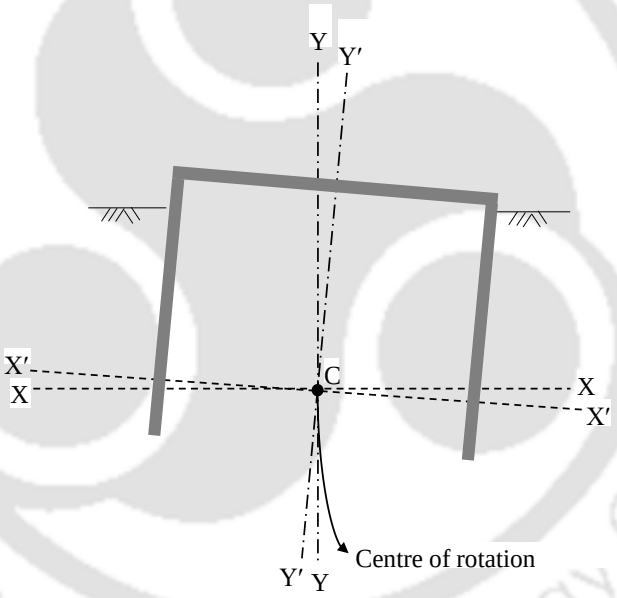

Figure 5.12 Schematic diagram of bucket foundation showing depth of point of rotation

The variations of depth of point of rotation with loading height and aspect ratio of the bucket foundations, in medium dense and very dense sands, are discussed in the following sub-sections.

5.7.1 Variation with Loading Height

Figure 5.13 shows the variation of depth of point of rotation with loading height for a bucket foundation (D = 12 m, L = 6 m) supporting superstructure load of 5 MN in medium dense sand. Under the application of pure lateral load (h = 0 m), the depth of point of rotation is found to be located at 6.31 m below the bucket lid centre. This point moves upward to 5.25, 5.00, 4.88 and 4.66 m, as the loading height is increased to 10, 20, 30 and 100 m, respectively. Due to upward movement of the point of rotation, the reaction due to passive pressure on the LE side produces a greater resisting moment below this point, which leads to an overall increase in the moment resisting capacity of the bucket foundation.

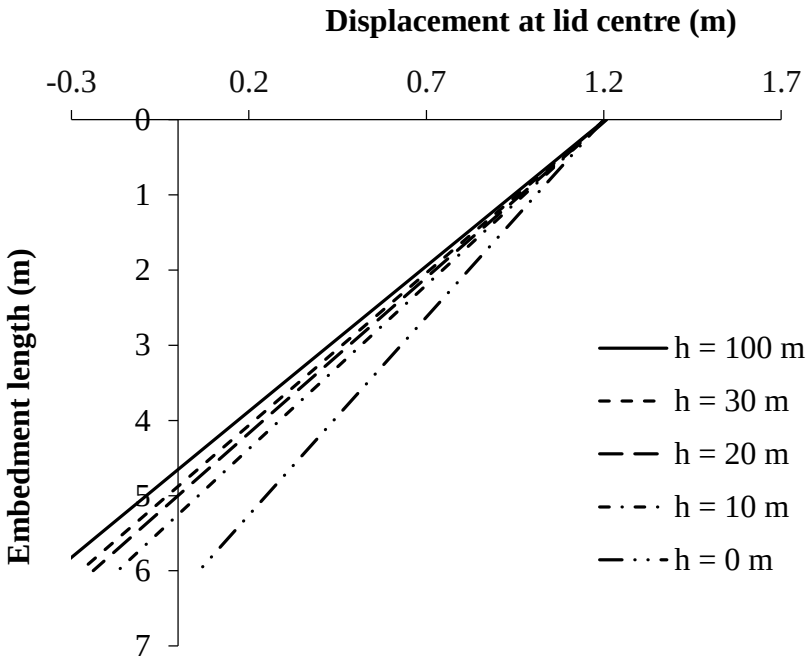

Figure 5.13 Variation of depth of point of rotation of bucket foundation (D = 12 m, L = 6 m and V = 5 MN) with increasing loading height

For a given bucket geometry and superstructure load, the depth of point of rotation is noted to move upward with increasing loading height. The response remained similar for all the bucket geometries under superstructure loads of 5, 10 and 15 MN in medium dense and very dense sands.

5.7.2 Variation with Aspect Ratio

Typical variation of the depth of point of rotation with aspect ratio of bucket foundation (D = 12 m) embedded in medium dense sand is presented in Figure 5.14. Under the superstructure load of 5 MN and loading height of 30 m, the depth of point of rotation is found to be 4.88 m for the aspect ratio of 0.5. The depth of point of rotation is noted to increase to 6.90 and 8.96 m, as the aspect ratio is increased to 0.75 and 1.

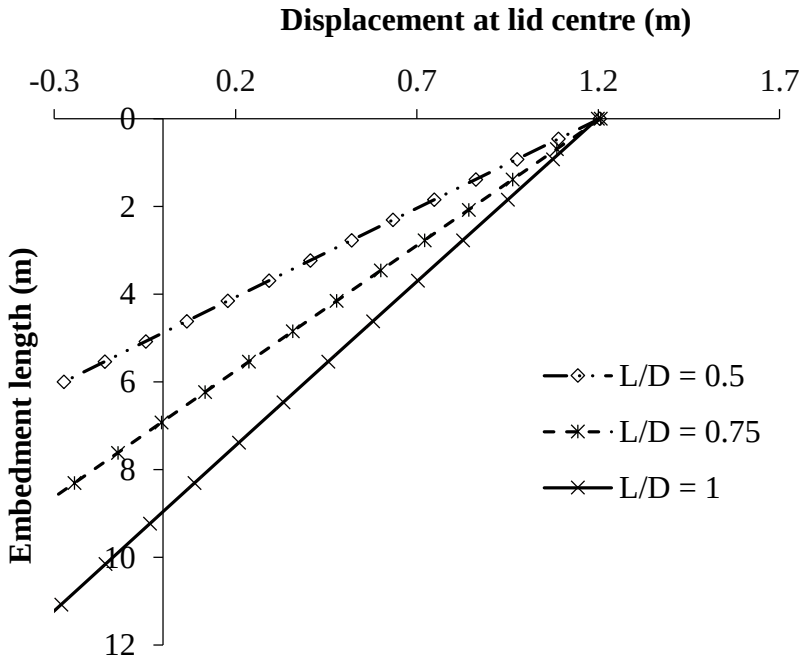

Figure 5.14 Variation of depth of point of rotation of bucket foundation with aspect ratio (D = 12 m, V = 5 MN and h = 30 m)

The variation of depth of point of rotation of bucket foundation for all bucket geometries, aspect ratios and superstructure loads are presented in Tables 5.9- 5.11 for medium dense sand, and in Tables 5.12- 5.14 for very dense sand.

For a given loading height, as either the bucket diameter or skirt length is increased keeping the other dimension constant, the depth of point of rotation shifts downward. Further, for the same loading height and bucket geometry, as the superstructure load is increased, the point of rotation is observed to shift marginally in the downward direction. In most of the

cases, for a given bucket geometry under any superstructure load and loading height, the depth of point of rotation is found to be located to be at deeper depth in medium dense sand as compared to very dense sand. There were cases when the analysis aborted before reaching failure condition (i.e., lateral displacement of 10% diameter) due to numerical instability, and therefore their rotation point depths could not be determined.

Table 5.9 Depth of point of rotation in medium dense sand (V = 5 MN)

V **(MN)**	**Geometry**	**Depth of point of rotation, *Z* (m)**								
		Loading height, *h* (m)								**Pure moment loading**
		0	**2.5**	**5**	**10**	**20**	**30**	**40**	**100**	
5	D = 12 m, L = 6 m	6.31	5.79	5.52	5.25	5.00	4.88	4.81	4.66	--
	D = 12 m, L = 9 m	8.57	8.13	7.83	7.45	7.07	6.90	6.80	6.60	5.79
	D = 12 m, L = 12 m	10.89	10.40	10.05	9.60	9.17	8.96	8.83	8.55	7.76
	D = 15 m, L = 7.5 m	7.61	7.07	6.76	6.42	6.10	5.95	5.85	--	--
	D = 15 m, L = 11.25 m	10.57	10.12	9.82	9.37	8.94	8.71	8.58	8.28	8.04
	D = 15 m, L = 15 m	13.61	13.09	12.75	12.23	11.62	11.30	11.13	10.73	10.40
	D = 18 m, L = 9 m	8.93	8.49	8.22	7.87	7.52	7.35	7.25	7.01	6.81
	D = 18 m, L = 13.5 m	12.69	12.18	11.83	11.36	10.86	10.58	10.41	10.00	9.65
	D = 18 m, L = 18 m	16.23	15.71	15.34	14.82	14.18	13.83	13.61	13.07	--

Table 5.10 Depth of point of rotation in medium dense sand (V = 10 MN)

V **(MN)**	**Geometry**	**Depth of point of rotation, *Z* (m)**								
		Loading height, *h* (m)								**Pure moment loading**
		0	**2.5**	**5**	**10**	**20**	**30**	**40**	**100**	
10	D = 12 m, L = 6 m	7.12	6.05	5.67	5.31	4.98	4.83	4.74	4.55	--
	D = 12 m, L = 9 m	8.82	8.27	7.92	7.49	7.06	6.86	6.74	6.51	--
	D = 12 m, L = 12 m	11.06	10.52	10.16	9.68	9.24	9.02	8.89	8.58	--
	D = 15 m, L = 7.5 m	7.98	--	6.85	6.51	6.05	5.87	5.76	5.51	--
	D = 15 m, L = 11.25 m	10.74	10.23	9.91	9.37	8.94	8.69	8.55	8.24	--
	D = 15 m, L = 15 m	13.69	13.25	12.79	12.35	11.64	11.34	11.16	10.74	10.38
	D = 18 m, L = 9 m	9.19	8.62	8.30	7.90	7.54	7.35	7.23	6.96	6.73
	D = 18 m, L = 13.5 m	12.80	12.29	11.91	11.44	10.92	10.62	10.42	9.99	9.63
	D = 18 m, L = 18 m	16.33	15.80	15.41	14.86	14.21	13.85	13.62	13.09	12.55

Table 5.11 Depth of point of rotation in medium dense sand (V = 15 MN)

V **(MN)**	**Geometry**	**Depth of point of rotation, *Z* (m)**								
		Loading height, *h* (m)								**Pure moment loading**
		0	**2.5**	**5**	**10**	**20**	**30**	**40**	**100**	
15	D = 12 m, L = 6 m	8.47	6.39	5.89	5.44	5.05	4.88	4.78	4.59	--
	D = 12 m, L = 9 m	9.06	8.40	8.02	7.56	7.10	6.89	6.77	6.54	5.77
	D = 12 m, L = 12 m	11.20	10.63	10.24	9.75	9.27	9.03	8.90	8.61	7.83
	D = 15 m, L = 7.5 m	8.57	7.43	6.97	6.47	6.03	5.92	5.74	5.45	--
	D = 15 m, L = 11.25 m	10.91	10.36	10.02	9.48	8.91	8.70	8.54	8.20	--
	D = 15 m, L = 15 m	13.83	13.33	12.80	12.35	11.70	11.39	11.20	10.77	10.40
	D = 18 m, L = 9 m	9.45	8.74	8.36	7.93	7.53	7.33	7.20	6.91	6.67
	D = 18 m, L = 13.5 m	12.92	12.38	11.98	11.49	10.96	10.66	10.46	10.01	9.62
	D = 18 m, L = 18 m	16.43	15.87	15.47	14.91	14.23	13.87	13.64	13.17	12.59

Table 5.12 Depth of point of rotation in very dense sand (V = 5 MN)

V **(MN)**	**Geometry**	**Depth of point of rotation, *Z* (m)**								
		Loading height, *h* (m)								**Pure moment loading**
		0	**2.5**	**5**	**10**	**20**	**30**	**40**	**100**	
5	D = 12 m, L = 6 m	5.96	5.67	5.50	5.30	5.08	4.97	4.91	4.76	--
	D = 12 m, L = 9 m	8.26	7.89	7.64	7.29	6.96	6.80	6.68	6.43	5.43
	D = 12 m, L = 12 m	10.41	9.98	9.69	9.32	8.92	8.69	8.55	8.19	--
	D = 15 m, L = 7.5 m	7.23	6.93	6.69	6.42	6.12	5.98	5.88	--	--
	D = 15 m, L = 11.25 m	10.27	9.89	9.57	9.16	9.83	8.56	8.42	8.05	--
	D = 15 m, L = 15 m	13.01	12.55	12.23	11.78	11.28	10.99	10.80	10.32	--
	D = 18 m, L = 9 m	8.61	8.31	8.12	7.87	7.60	7.45	7.34	7.07	--
	D = 18 m, L = 13.5 m	12.23	11.85	11.54	11.12	10.66	10.40	10.21	--	--
	D = 18 m, L = 18 m	15.67	15.24	14.89	14.40	13.82	13.44	13.20	12.56	--

Table 5.13 Depth of point of rotation in very dense sand (V = 10 MN)

V (MN)	Geometry	Depth of point of rotation, Z (m)								
		Loading height, h (m)								Pure moment loading
		0	2.5	5	10	20	30	40	100	
10	D = 12 m, L = 6 m	--	5.78	5.56	5.32	5.08	4.95	4.85	4.65	--
	D = 12 m, L = 9 m	8.39	8.02	7.72	7.31	6.95	6.76	6.64	6.36	--
	D = 12 m, L = 12 m	10.48	10.05	9.75	9.37	8.95	8.70	8.54	8.15	--
	D = 15 m, L = 7.5 m	7.41	7.03	6.78	6.47	6.12	5.95	5.83	--	--
	D = 15 m, L = 11.25 m	10.35	9.95	9.64	9.17	8.77	8.55	8.40	8.03	--
	D = 15 m, L = 15 m	13.06	12.59	12.27	11.85	11.29	10.99	10.78	10.27	--
	D = 18 m, L = 9 m	8.72	8.39	8.19	7.92	7.63	7.46	7.34	7.05	--
	D = 18 m, L = 13.5 m	12.31	11.90	11.61	11.16	10.66	10.37	10.18	9.70	--
	D = 18 m, L = 18 m	15.73	15.26	14.94	14.42	13.82	13.45	13.20	12.56	--

Table 5.14 Depth of point of rotation in very dense sand (V = 15 MN)

V **(MN)**	**Geometry**	**Depth of point of rotation, *Z* (m)**								
		Loading height, *h* (m)								**Pure moment loading**
		0	**2.5**	**5**	**10**	**20**	**30**	**40**	**100**	
15	D = 12 m, L = 6 m	--	5.89	5.62	5.33	5.06	4.88	4.88	4.54	--
	D = 12 m, L = 9 m	8.51	8.11	7.78	7.35	6.94	6.74	6.60	6.28	--
	D = 12 m, L = 12 m	10.59	10.13	9.80	9.40	8.94	8.70	8.54	8.16	--
	D = 15 m, L = 7.5 m	7.59	7.10	6.84	6.50	6.12	5.92	5.79	--	--
	D = 15 m, L = 11.25 m	10.27	9.89	9.57	9.23	8.77	8.56	8.41	8.05	--
	D = 15 m, L = 15 m	13.12	12.61	12.27	11.90	11.34	11.01	10.79	10.24	--
	D = 18 m, L = 9 m	8.84	8.47	8.25	7.95	7.65	8.83	7.33	7.03	--
	D = 18 m, L = 13.5 m	12.40	11.98	11.67	11.21	10.70	10.37	10.16	--	--
	D = 18 m, L = 18 m	15.78	15.29	14.96	14.44	13.85	13.46	13.21	12.54	--

5.8 INITIAL STIFFNESS

5.8.1 Initial Stiffness of Bucket Foundation

The natural frequency of an offshore wind turbine system is dependent on the seabed soil profile, bucket foundation geometry, turbine superstructure weight and elevation, and the loading height of the resultant lateral load. Under operating conditions, an offshore wind turbine is subjected to harmonic excitation from its rotor. The rotor's rotational frequency is the first excitation frequency and is commonly referred to as 1*P* frequency. The second excitation frequency is the blade passing frequency, often called as 2*P*/3*P* frequency, for a two-bladed or three-bladed wind turbine. The blades of the wind turbine, when passing in front of the tower, cause a shadowing effect and produce a reduction of wind load on the tower. This is a dynamic load having frequency equal to two times the rotational frequency of the turbine for a two-bladed turbine and three times the rotational frequency of the turbine for three-bladed wind turbines. The 2*P*/3*P* loading frequency bands (Figure 5.17) are simply obtained by multiplying the limits of the 1*P* band by the number of the turbine blades (Bhattacharya 2014; Houlsby et al. 2005; Ibsen et al. 2005).

The natural frequency of the offshore wind turbine system plays an important role for its safe operation. To avoid resonance, this natural frequency should be such that it does not coincide with either the 1*P* or the 2*P*/3*P* frequency ranges. For the determination of natural frequency, knowledge of the stiffness of the bucket foundation is necessary, either as initial stiffness or as rotational stiffness. In this study, the initial stiffness (K_{ini}) for design purpose, corresponding to a given loading height, is determined from the lateral load versus lid rotation plot [such as in Figure 5.4(b)], and can be defined as the slope of the line drawn from the origin to a rotation value of 0.5°, as shown in Figure 5.15 (Ahmed and Hawlader 2016). The rotational stiffness (K_{rot}) can be noted from the resisting moment versus lid rotation plot

[such as in Figure 5.4(c)], and is equal to the product of the value of K_{ini} and the corresponding loading height. In general, the value of the rotational stiffness is used directly in the determination of the natural frequency.

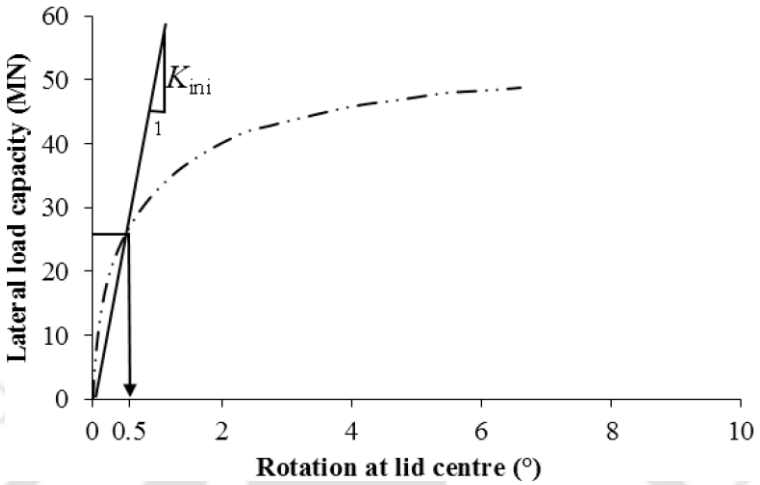

Figure 5.15 Determination of initial stiffness from lateral load capacity versus lid centre rotation plot of bucket foundation in medium dense sand (D = 12 m, L = 6 m, V = 5 MN and h = 0 m)

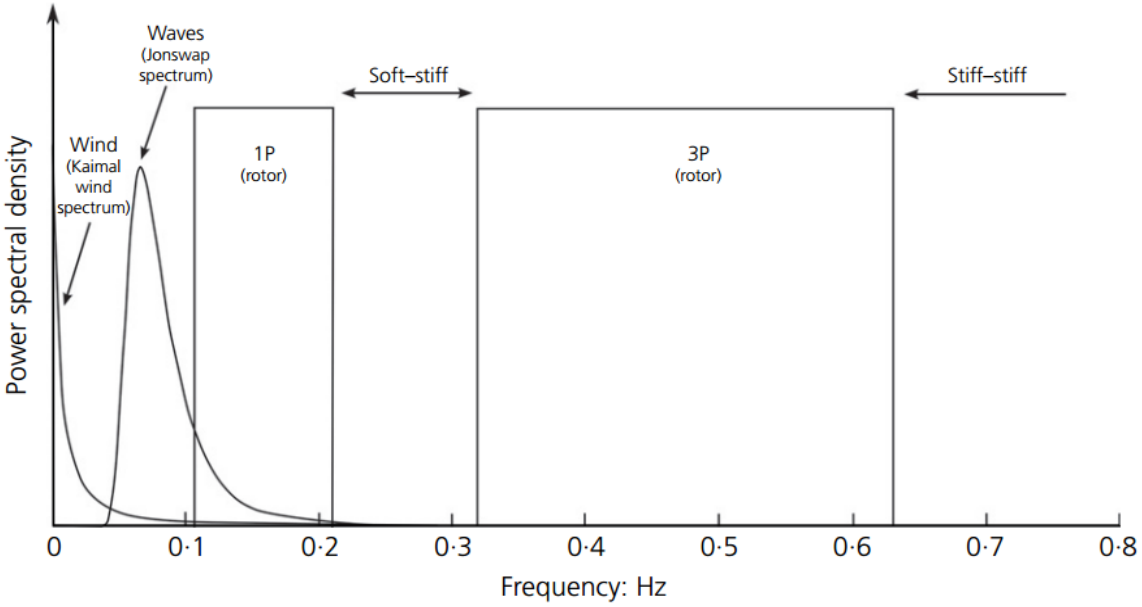

Figure 5.16 Typical frequency ranges for a three-bladed standard 5 MW wind turbine (Cox and Bhattacharya 2016)

5.8.2 Variation of Initial Stiffness with Aspect Ratio

The influence of aspect ratio and loading height on the initial stiffness of the bucket foundation of 12 m diameter, supporting superstructure load of 5 MN in both sand types, is shown in Figure 5.17. The initial stiffness is noted to be lesser with a smaller aspect ratio, and it also reduces nonlinearly with increasing loading height from 0 to 100 m. The initial stiffness is always greater in very dense sand for the same aspect ratio and loading height.

The initial stiffness values of bucket foundations in both medium dense and very dense sands, are summarized in Tables 5.15- 5.17, respectively for diameters of 12, 15 and 18 m.

For the aspect ratio of 0.5, the initial stiffness is seen to decrease from 20.99 to 0.86 MN/° in medium dense sand, and from 32.61 to 1.54 MN/° in very dense sand within the range of loading height from h = 0 m to h = 100 m (Figure 5.17 and Table 5.15). For the aspect ratio of 1, the respective initial stiffness values decrease from 27.04 to 2.16 MN/° in medium dense sand, and from 51.42 to 4.53 MN/° in very dense sand within the range of loading height.

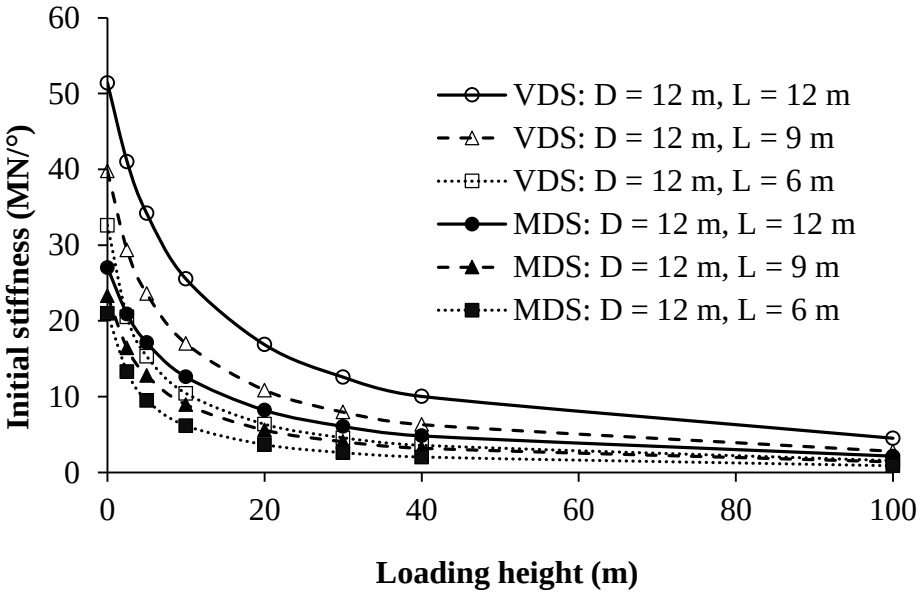

Figure 5.17 Variation of initial stiffness with aspect ratio and loading height (D = 12 m, V = 5 MN)

5.8.3 Variation of Initial Stiffness with Superstructure Load

The variation of initial stiffness of the bucket foundation (D = 12 m, L = 6 m) with superstructure load in both the sand types is presented in Figure 5.18. For the same bucket geometry, the initial stiffness is noted to be greater under higher superstructure load, reduces nonlinearly with increasing loading height, and is always greater in the denser sand.

Under the superstructure load of 5 MN, the initial stiffness of the bucket foundation in medium dense sand decreases from 20.99 to 0.86 MN/° as the loading height is increased from 0 to 100 m (Figure 5.18 and Table 5.15). As the superstructure load is increased further to 15 MN, the respective initial stiffness values of greater magnitude decrease from 24.04 and 1.02 MN/° in medium dense sand, and from 49.36 and 2.11 MN/° in very dense sand, for loading height increasing from pure lateral load case (h = 0 m) to hub height level (h = 100 m).

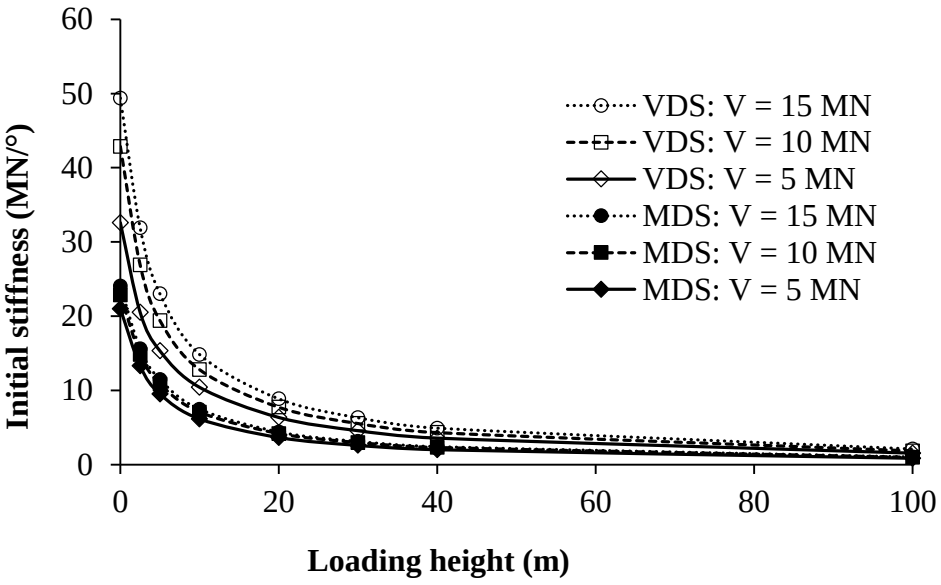

Figure 5.18 Variation of initial stiffness with superstructure load and loading height (D = 12 m, L = 6 m)

Table 5.15 Initial stiffness values of bucket foundation (D = 12 m) in both sand types

V (MN)	Geometry	Type of soil	Aspect ratio (L/D)	Initial stiffness, K_{ini} (MN/°)							
				Loading height, h (m)							
				0	**2.5**	**5**	**10**	**20**	**30**	**40**	**100**
5	D = 12 m, L = 6 m	MDS	0.5	20.99	13.30	9.51	6.16	3.65	2.59	2.01	0.86
		VDS	0.5	32.61	20.53	15.32	10.42	6.35	4.57	3.57	1.54
	D = 12 m, L = 9 m	MDS	0.75	23.31	16.43	12.80	8.96	5.59	4.07	3.20	1.39
		VDS	0.75	39.80	29.36	23.60	17.01	10.87	7.96	6.31	2.78
	D = 12 m, L = 12 m	MDS	1	27.04	20.91	17.14	12.60	8.21	6.08	4.83	2.16
		VDS	1	51.42	41.03	34.20	25.54	16.87	12.59	10.05	4.53
10	D = 12 m, L = 6 m	MDS	0.5	22.83	14.83	10.86	7.07	4.18	2.97	2.30	0.98
		VDS	0.5	42.86	26.91	19.41	12.80	7.73	5.54	4.32	1.86
	D = 12 m, L = 9 m	MDS	0.75	25.18	18.01	14.01	9.75	6.04	4.38	3.42	1.48
		VDS	0.75	47.11	34.01	27.07	19.31	12.27	8.98	7.08	3.11
	D = 12 m, L = 12 m	MDS	1	28.91	22.34	18.25	13.30	8.63	6.36	5.04	2.24
		VDS	1	56.90	44.94	37.26	27.67	18.22	13.57	10.82	4.86
15	D = 12 m, L = 6 m	MDS	0.5	24.04	15.59	11.44	7.46	4.39	3.12	2.41	1.02
		VDS	0.5	49.36	31.90	23.00	14.83	8.86	6.32	4.92	2.11
	D = 12 m, L = 9 m	MDS	0.75	26.24	18.93	14.76	10.22	6.33	4.56	3.58	1.54
		VDS	0.75	53.47	38.11	29.86	21.15	13.36	9.75	7.67	3.36
	D = 12 m, L = 12 m	MDS	1	30.22	23.34	18.96	13.76	8.91	6.55	5.15	2.29
		VDS	1	61.76	48.24	39.79	29.45	19.28	14.33	11.40	5.12

Table 5.16 Initial stiffness values of bucket foundation (D = 15 m) in both sand types

V (MN)	Geometry	Type of soil	Aspect ratio (L/D)	Initial stiffness, K_{ini} (MN/°)							
				Loading height, h (m)							
				0	**2.5**	**5**	**10**	**20**	**30**	**40**	**100**
5	D = 15 m, L = 7.5 m	MDS	0.5	32.51	21.27	15.69	10.51	6.45	4.65	3.64	1.58
		VDS	0.5	49.78	33.59	25.95	18.21	11.46	8.34	6.56	2.87
	D = 15 m, L = 11.25 m	MDS	0.75	37.03	27.70	22.29	16.19	10.47	7.75	6.14	2.74
		VDS	0.75	64.78	50.35	41.74	31.04	20.49	15.35	12.21	5.51
	D = 15 m, L = 15 m	MDS	1	48.21	35.95	30.37	23.16	15.73	11.85	9.49	4.34
		VDS	1	86.36	71.55	61.23	47.37	32.46	24.60	19.79	9.11
10	D = 15 m, L = 7.5 m	MDS	0.5	34.98	24.07	18.09	12.02	7.33	5.26	4.10	1.77
		VDS	0.5	61.26	40.49	30.77	21.08	13.18	9.57	7.51	3.27
	D = 15 m, L = 11.25 m	MDS	0.75	39.06	29.42	23.63	17.40	11.04	8.12	6.43	2.85
		VDS	0.75	72.39	55.47	45.57	33.70	22.25	16.57	13.20	5.92
	D = 15 m, L = 15 m	MDS	1	46.52	37.33	31.39	23.84	16.12	12.17	9.76	4.44
		VDS	1	91.76	75.66	64.56	49.73	34.01	25.77	20.73	9.51
15	D = 15 m, L = 7.5 m	MDS	0.5	36.30	25.06	18.96	12.78	7.77	5.57	4.34	1.87
		VDS	0.5	70.50	46.52	34.72	23.53	14.64	10.62	8.34	3.63
	D = 15 m, L = 11.25 m	MDS	0.75	39.96	30.28	24.39	17.50	11.32	8.32	6.56	2.90
		VDS	0.75	79.25	60.07	48.95	36.13	23.65	17.55	13.96	6.26
	D = 15 m, L = 15 m	MDS	1	46.63	37.81	32.12	24.10	16.32	12.29	9.85	4.47
		VDS	1	96.93	79.47	67.54	51.68	35.32	26.72	21.47	9.83

Table 5.17 Initial stiffness values of bucket foundation (D = 18 m) in both sand types

V (MN)	Geometry	Type of soil	Aspect ratio (L/D)	Initial stiffness, K_{ini} (MN/°)							
				Loading height, h (m)							
				0	**2.5**	**5**	**10**	**20**	**30**	**40**	**100**
5	D = 18 m, L = 9 m	MDS	0.5	47.43	32.47	24.62	16.99	10.68	7.80	6.14	2.70
		VDS	0.5	72.64	51.79	41.34	30.02	19.43	14.35	11.37	5.05
	D = 18 m, L = 13.5 m	MDS	0.75	55.12	55.12	55.12	55.12	55.12	55.12	55.12	55.12
		VDS	0.75	98.91	79.62	67.50	51.69	35.07	26.49	21.27	9.72
	D = 18 m, L = 18 m	MDS	1	67.02	56.28	48.71	38.25	26.65	20.43	16.55	7.74
		VDS	1	132.73	113.08	98.51	77.86	54.72	42.10	34.23	16.13
10	D = 18 m, L = 9 m	MDS	0.5	51.75	36.58	27.91	19.02	11.89	8.65	6.80	2.97
		VDS	0.5	85.01	59.52	46.72	33.48	21.50	15.80	12.51	5.56
	D = 18 m, L = 13.5 m	MDS	0.75	58.87	46.01	37.83	28.24	18.74	14.00	11.18	5.05
		VDS	0.75	106.94	85.47	71.75	54.79	37.05	27.92	22.45	10.26
	D = 18 m, L = 18 m	MDS	1	69.65	58.23	50.28	39.27	27.30	20.86	16.91	7.89
		VDS	1	138.41	117.40	102.39	80.50	56.45	43.45	35.29	16.59
15	D = 18 m, L = 9 m	MDS	0.5	53.44	38.52	29.89	20.50	12.78	9.29	7.29	3.17
		VDS	0.5	96.09	66.65	51.47	36.47	23.38	17.19	13.60	6.02
	D = 18 m, L = 13.5 m	MDS	0.75	60.45	47.40	38.96	29.05	19.20	14.35	11.43	5.15
		VDS	0.75	114.49	90.53	75.68	57.57	38.82	29.26	23.44	10.69
	D = 18 m, L = 18 m	MDS	1	71.58	59.66	51.27	39.96	27.67	21.17	17.11	7.95
		VDS	1	143.52	121.54	105.51	83.16	58.11	44.64	36.23	16.99

5.9 FAILURE MECHANISM UNDER LATERAL LOAD

A clear understanding of the lateral load transfer mechanism from the bucket foundation to the surrounding sandy seabed would lead to increased confidence in its design. The failure mechanism and deformation behaviour of the bucket foundation-sandy seabed system have been studied by considering several bucket geometries, superstructure loads and loading heights.

5.9.1 Variation of Failure Mechanism with Loading Height, Superstructure Load and Aspect Ratio

Under the application of lateral load at the bucket foundation, the sandy seabed in the vicinity of the foundation begins to yield plastically. The soil deformation at ultimate condition in terms of plastic strains and displacement vectors within and around the bucket foundation ($D = 12$ m and $L = 6$ m), supporting 5 MN superstructure load and under pure lateral load is illustrated in Figure 5.19(a)-(d).

Under the action of pure lateral load, the foundation begins to translate rigidly to the right (along the direction of loading) and the portion of the skirt below the depth of point of rotation moves toward the left, considering the installed position as reference or mean position. As a result of rigid translation, the soil experiences compression in the front side of the foundation and a heave formation is seen at bed surface. However, the soil located in the rear side of the bucket experiences tension as the foundation moves away from the soil mass, causing a depression on the bed surface.

As the bucket approaches ultimate condition, the entire left skirt has already begun to move upward from the surrounding soil. The plastic strain generated at the bed surface propagates along the left exterior side of the skirt and reaches the skirt tip to form a wedge shape in the rear side. From this tip of the left skirt, the plastic strain propagates through the

lower part of the soil plug toward the right skirt tip, forming a scoop mechanism [Figure 5.19(a) -(b)]. At this stage, the right skirt tip has already penetrated the soil. The zone of plastic strain along the right skirt, which has already extended from the bed surface to about mid-skirt length, expands further and then merges with the propagated plastic strain zone from the skirt tip of the right end, forming a wedge in the front side.

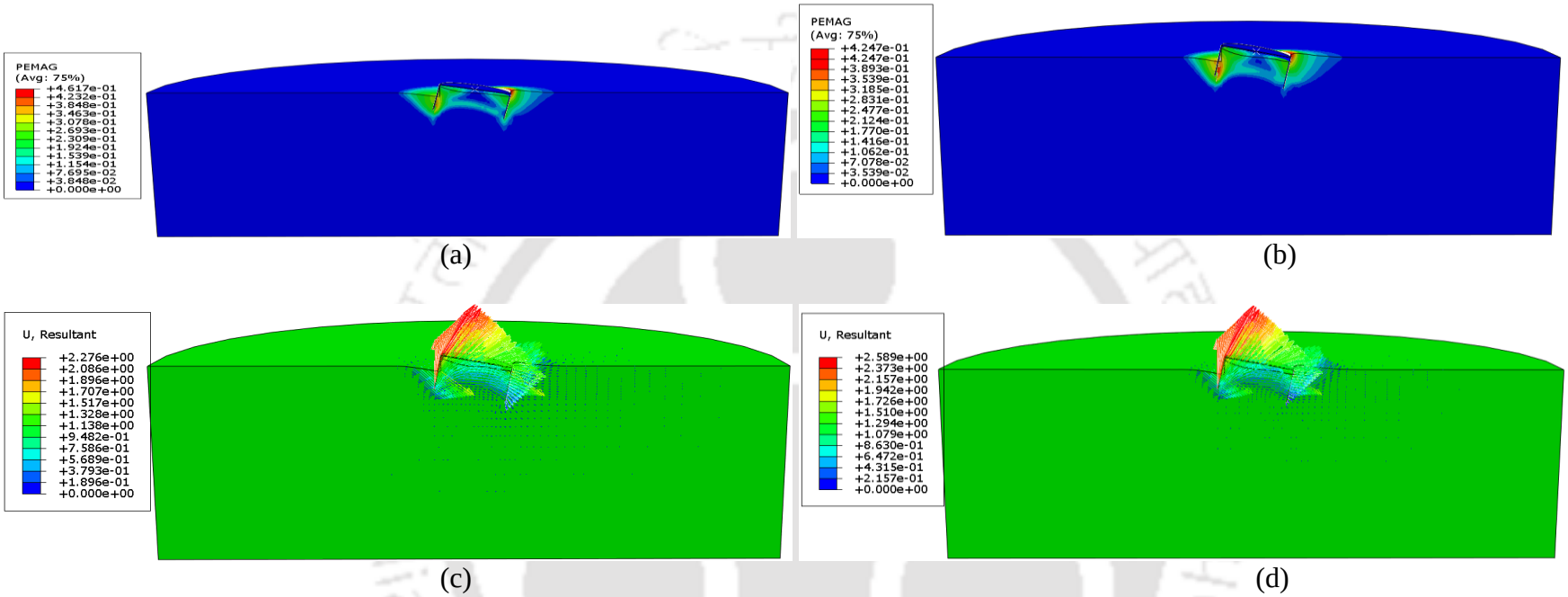

Figure 5.19 Soil deformation at failure of foundation under pure lateral loading (D = 12 m, L = 6 m, V = 5 MN): (a) Plastic strain magnitudes in MDS; (b) Plastic strain magnitudes in VDS; (c) Displacement vectors in MDS; (d) Displacement vectors in VDS

5.9.2 Variation of Extent of Plastic Deformation with Loading Height, Superstructure Load and Aspect Ratio

The ground deformation resulting from the yielding of the soil around the bucket foundation (D = 12 m) at failure in both sand types, represented in terms of plastic strains for lateral load acting at varying loading heights (h = 0, 30 and 100 m), is presented in Figures 5.20- 5.22 for aspect ratio of 0.5 and in Figures 5.23- 5.25 for the aspect ratio of 1.

Under any loading type (lateral load at any loading height or pure moment) till ultimate condition, the bucket foundation undergoes both lateral and rotational translation, produced due to coupling of lateral and rotational degrees of freedom. At the base of the foundation, internal inverted scoop mechanism is observed when lateral translation is dominant, whereas external upright scoop mechanism is seen when rotational translation is predominant.

For a bucket foundation with D = 12 m, under pure lateral load (h = 0), the lateral translation is more dominant than the rotational translation, and thus an internal inverted scoop mechanism is observed to develop above the base of soil plug, irrespective of the aspect ratio, as shown in Figure 5.20 and Figure 5.23.

Under greater loading heights (h = 30 and 100 m), for the lower aspect ratio of 0.5, the lateral translation still remains more dominant, and internal inverted scoop mechanism is always observed, as shown in Figure 5.21 and Figure 5.22. In contrast, for the higher aspect ratio of 1, rotational translation becomes predominant with the increase of loading height from pure lateral load, and external upright scoop mechanism is seen, as illustrated in Figure 5.24 and Figure 5.25. At failure condition, the soil around the bucket in the front and rear sides fail due to compressive and tensile stresses, respectively.

For the lower aspect ratio of 0.5, under superstructure load of 5 MN and pure lateral load, the corresponding extents of plastic deformation of the medium dense sand seabed in

the front and rear sides of the bucket foundation (D = 12 m) are 7.33 and 6.97 m. As the loading height is increased to 30 and 100 m, the respective plastic deformation extents in the front side decrease to 5.57 and 5.18 m, and to 5.68 and 5.30 m in the rear side.

Under the application of the same superstructure load of 5 MN and pure lateral load, for the higher aspect ratio to 1, greater extents of plastic deformation (10.34 and 9.40 m) are observed in the front and rear sides, respectively. The plastic deformation extents are noted to reduce in the front and rear sides to 7.66 and 7.30 m for h = 30 m and to 7.50 and 7.02 m for h = 100 m.

The variations of extent of plastically deformed soil in the front and rear sides are presented in Tables 5.18 & 5.20 and Tables 5.19 & 5.21, respectively for medium dense sand and very dense sand. The missing values in the tables indicate those cases, for which the analysis got terminated before reaching failure condition due to numerical instability.

For the same geometry and similar vertical and lateral loading conditions, in very dense sand, the extent is greater in the front side while it is lesser in the rear side, compared to that in medium dense sand. The general trend is that for a higher loading height, the plastic deformation extent in the front side is greater than that in the rear side. With a higher superstructure load, the deformation extent tends to reduce in the front side and to increase in the rear side. For a higher aspect ratio or larger diameter, the plastic deformations at both the front and rear sides are noted to increase.

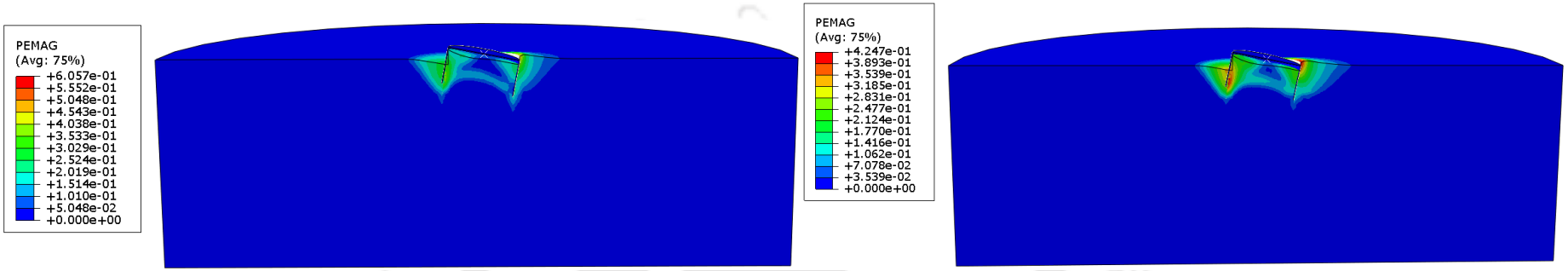

Figure 5.20 Plastic strain magnitudes at failure of foundation (D = 12 m, L = 6 m, V = 5 MN) for loading height of 0 m: (a) in MDS; (b) in VDS

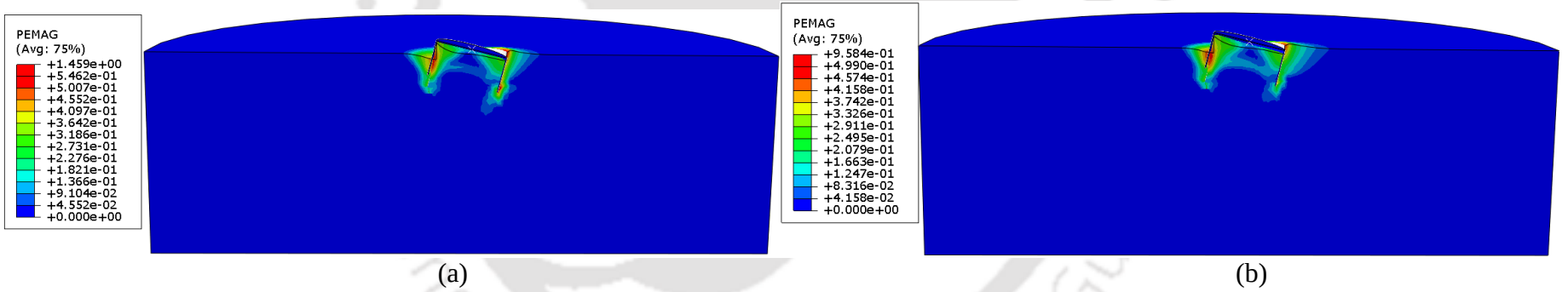

Figure 5.21 Plastic strain magnitudes at failure of foundation (D = 12 m, L = 6 m, V = 5 MN) for loading height of 30 m: (a) in MDS; (b) in VDS

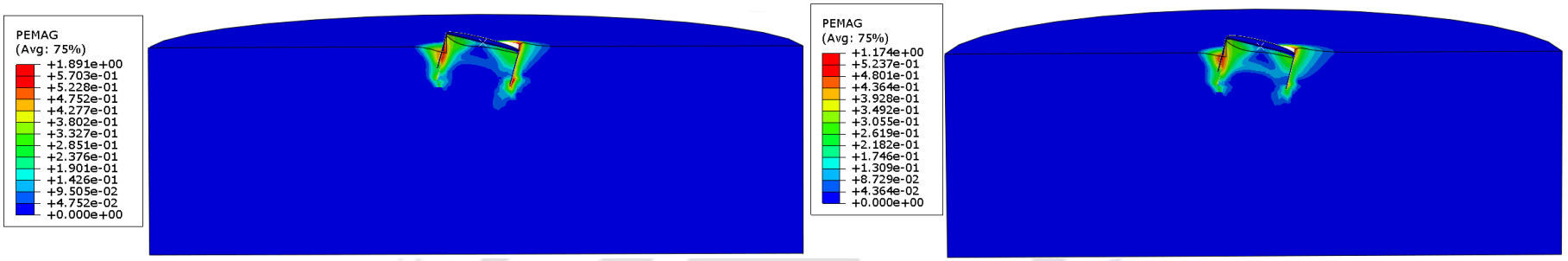

Figure 5.22 Plastic strain magnitudes at failure of foundation (D = 12 m, L = 6 m, V = 5 MN) for loading height of 100 m: (a) in MDS; (b) in VDS

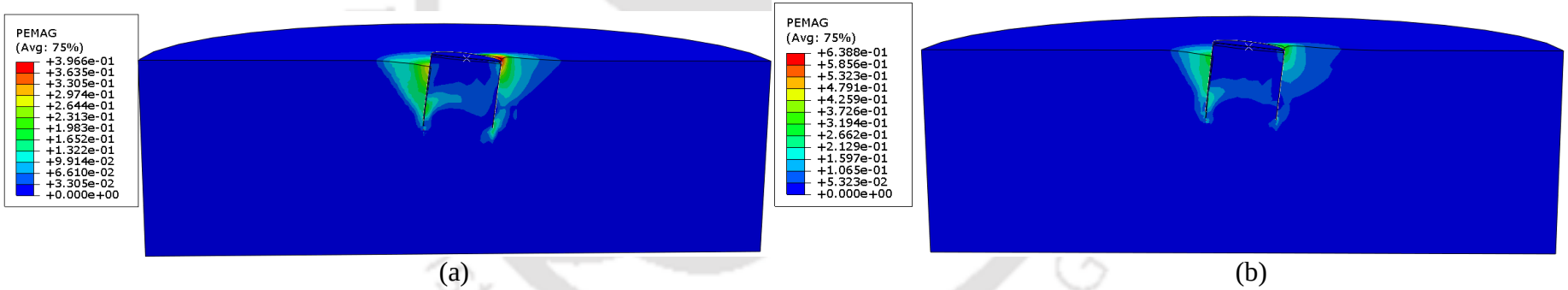

Figure 5.23 Plastic strain magnitudes at failure of foundation (D = 12 m, L = 12 m, V = 5 MN) for loading height of 0 m: (a) in MDS; (b) in VDS

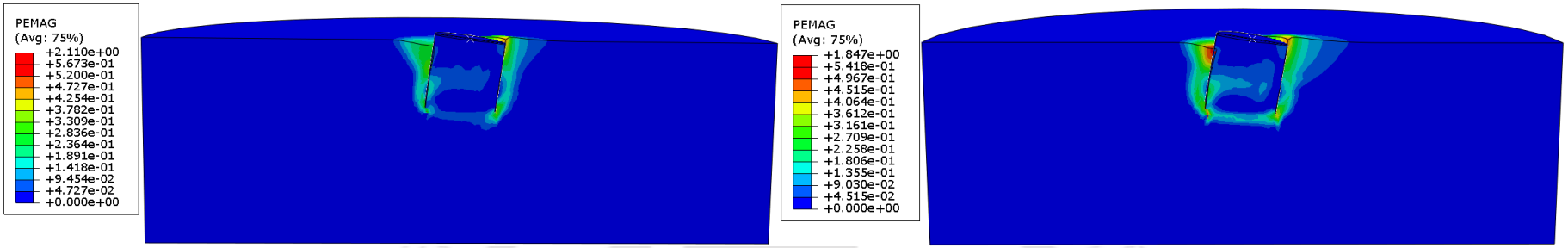

(a) (b)

Figure 5.24 Plastic strain magnitudes at failure of foundation (D = 12 m, L = 12 m, V = 5 MN) for loading height of 30 m: (a) in MDS; (b) in VDS

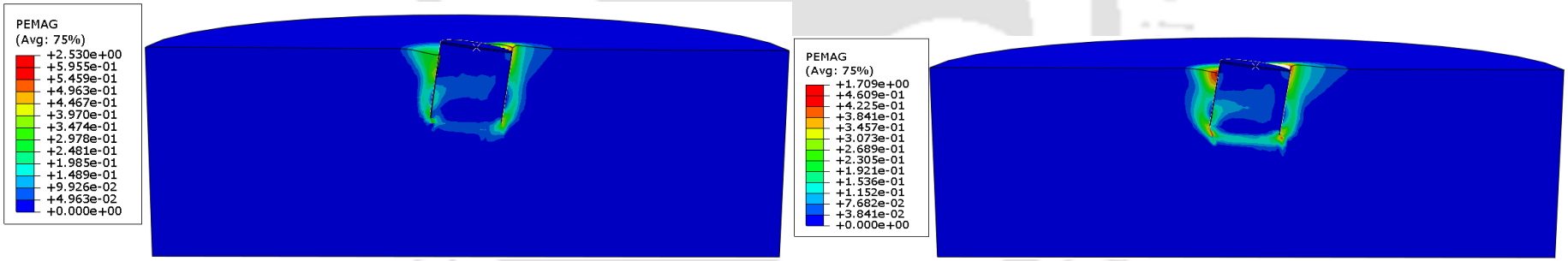

(a) (b)

Figure 5.25 Plastic strain magnitudes at failure of foundation (D = 12 m, L = 12 m, V = 5 MN) for loading height of 100 m: (a) in MDS; (b) in VDS

Table 5.18 Lateral extent of soil failing plastically in front side of the bucket foundation in medium dense sand

Superstructure load, *V* (MN)	Loading height, *h* (m)	Failure extent in the front side (m)								
		D = 12 m			*D* = 15 m			*D* = 18 m		
		L/*D*			*L*/*D*			*L*/*D*		
		0.5	0.75	1	0.5	0.75	1	0.5	0.75	1
5	0	7.33	8.69	10.34	8.16	10.85	12.44	10.00	11.88	13.81
	10	6.08	7.51	8.70	6.63	8.81	10.53	8.56	10.31	12.09
	20	5.82	6.93	8.00	6.31	8.61	10.12	8.14	9.78	11.52
	30	5.57	6.78	7.66	6.18	8.37	9.56	7.85	9.39	10.73
	40	5.44	6.72	7.65	5.90	8.01	9.56	7.67	9.01	10.74
	100	5.18	6.39	7.50	--	7.49	9.13	7.19	8.65	9.99
10	0	7.62	8.77	10.26	8.14	16.25	11.66	10.15	11.87	13.60
	10	5.89	7.37	8.76	5.09	9.30	10.53	7.76	10.12	12.05
	20	4.95	6.68	7.66	6.18	8.60	9.77	8.14	9.76	11.50
	30	4.65	6.61	7.52	5.76	8.25	9.56	7.93	9.05	10.54
	40	4.99	6.25	7.39	5.05	7.84	9.40	7.60	8.68	10.15
	100	4.35	6.16	7.36	5.48	7.48	8.88	7.16	8.59	9.91
15	0	8.38	8.70	10.11	7.73	10.31	12.05	10.31	11.31	13.39
	10	5.34	7.24	8.26	6.47	9.18	10.94	8.42	10.12	12.00
	20	5.06	6.77	7.65	6.17	8.24	10.10	8.03	9.67	11.14
	30	4.48	6.32	7.50	4.56	8.17	9.56	7.71	9.22	10.23
	40	4.25	6.39	7.51	5.63	7.80	9.21	7.47	8.87	10.15
	100	4.23	6.11	7.36	4.88	7.47	9.04	7.04	8.30	9.67

Table 5.19 Lateral extent of soil failing plastically in rear side of the bucket foundation in medium dense sand

Superstructure load, *V* (MN)	Loading height, *h* (m)	Failure extent in the front side (m)								
		D = 12 m			*D* = 15 m			*D* = 18 m		
		L/D			*L/D*			*L/D*		
		0.5	0.75	1	0.5	0.75	1	0.5	0.75	1
5	0	6.97	8.25	9.40	7.99	10.07	11.93	9.89	11.73	13.71
	10	6.00	7.00	8.20	6.93	8.72	10.40	8.67	10.26	12.64
	20	5.85	6.48	7.71	6.62	8.56	9.78	8.18	8.33	11.74
	30	5.68	6.20	7.30	6.30	8.37	10.10	7.99	9.50	11.42
	40	5.46	6.15	7.18	6.21	7.60	9.22	7.89	9.36	11.32
	100	5.30	5.90	7.02	--	7.69	9.00	7.64	8.64	10.72
10	0	7.60	8.31	9.54	6.93	10.22	11.74	10.15	11.77	13.51
	10	6.07	7.06	6.15	6.47	8.75	10.56	8.42	10.51	12.75
	20	5.56	6.49	7.75	6.39	7.94	9.93	8.18	9.80	11.77
	30	5.23	6.20	7.31	8.18	7.94	9.45	8.05	9.50	11.44
	40	5.36	6.08	7.30	6.05	7.64	9.29	7.99	9.30	11.34
	100	4.82	5.91	7.02	5.74	7.39	9.00	7.54	8.86	10.78
15	0	8.04	8.43	9.59	8.50	10.30	11.76	10.28	11.78	13.70
	10	6.09	7.06	8.19	6.95	8.99	10.58	8.65	10.59	13.61
	20	5.57	6.49	7.82	6.31	8.35	9.95	8.31	9.96	12.16
	30	5.03	6.12	7.44	6.33	8.09	9.46	8.09	9.51	11.58
	40	4.93	6.02	7.31	5.92	7.68	9.16	7.99	9.39	11.37
	100	4.85	5.93	7.07	5.34	7.40	9.09	7.54	8.64	10.97

Table 5.20 Lateral extent of soil failing plastically in front side of the bucket foundation in very dense sand

Superstructure load, *V* (MN)	Loading height, *h* (m)	Failure extent in the front side (m)								
		D = 12 m			*D* = 15 m			*D* = 18 m		
		L/D			*L/D*			*L/D*		
		0.5	0.75	1	0.5	0.75	1	0.5	0.75	1
5	0	8.94	11.40	13.75	10.02	13.41	16.49	13.01	15.83	19.15
	10	8.05	9.87	12.80	9.10	12.69	15.11	12.13	14.42	15.88
	20	7.67	9.15	11.59	8.79	11.42	14.26	11.35	13.76	15.53
	30	7.60	8.92	10.74	8.58	11.06	13.94	11.20	13.35	14.94
	40	7.33	8.84	10.27	8.35	10.95	13.41	10.60	12.90	15.16
	100	6.92	8.54	9.92	--	10.22	12.41	9.70	--	14.22
10	0	9.02	11.40	13.83	10.18	14.04	16.49	13.34	15.61	17.12
	10	8.18	9.70	12.02	9.26	11.99	15.55	12.21	14.16	15.19
	20	7.60	9.13	11.59	8.77	11.42	14.26	11.67	14.17	15.53
	30	7.33	8.77	11.17	7.58	11.05	13.94	11.35	13.10	15.17
	40	7.24	8.76	10.74	7.72	10.96	13.83	10.97	12.89	15.05
	100	6.91	8.38	9.62	--	10.67	12.22	9.70	12.24	14.22
15	0	9.50	16.18	12.75	10.27	13.94	16.48	13.42	15.39	16.61
	10	7.97	9.91	12.42	9.10	12.20	14.29	12.44	14.10	15.31
	20	7.60	8.77	11.23	8.74	11.42	14.37	11.66	13.70	15.19
	30	7.25	8.40	11.06	7.96	11.04	14.04	11.34	13.52	15.05
	40	6.91	8.64	10.73	7.63	10.96	13.83	11.04	13.10	14.70
	100	6.57	8.09	9.77	--	10.47	12.81	9.57	--	14.21

Table 5.21 Lateral extent of soil failing plastically in rear side of the bucket foundation in very dense sand

Superstructure load, *V* (MN)	Loading height, *h* (m)	Failure extent in the front side (m)								
		D = 12 m			*D* = 15 m			*D* = 18 m		
		L/*D*			*L*/*D*			*L*/*D*		
		0.5	0.75	1	0.5	0.75	1	0.5	0.75	1
5	0	6.67	7.28	8.05	7.34	9.11	10.07	9.07	10.48	11.90
	10	5.88	6.40	7.01	6.54	7.65	9.00	8.06	9.34	10.67
	20	5.65	5.79	6.41	6.19	7.31	8.55	7.84	8.62	10.12
	30	5.42	5.59	6.12	5.97	7.24	8.03	7.60	8.06	9.82
	40	5.31	5.49	6.00	5.75	6.95	7.66	7.42	8.08	9.52
	100	4.90	5.43	5.89	--	6.74	7.67	6.91	--	9.05
10	0	6.79	7.53	8.18	7.67	9.13	10.32	9.25	10.73	11.92
	10	5.89	6.03	7.49	6.60	7.65	9.13	8.17	9.36	10.75
	20	5.65	5.56	6.47	6.19	7.38	8.55	7.96	8.63	10.12
	30	5.42	5.55	6.12	5.75	7.10	8.05	7.60	8.08	9.83
	40	5.20	5.49	6.06	5.54	6.95	7.82	7.48	7.93	9.67
	100	4.93	5.44	6.01	--	6.60	7.66	6.90	7.58	9.05
15	0	6.81	7.66	8.25	7.73	9.16	10.35	9.29	10.76	11.95
	10	5.92	6.34	7.20	6.71	7.93	9.15	8.29	9.39	10.75
	20	5.65	5.78	6.49	6.19	7.38	8.59	7.96	8.66	10.12
	30	5.31	5.59	6.23	5.86	7.10	8.09	7.72	8.29	9.74
	40	4.98	5.54	6.12	5.45	6.95	7.89	7.48	8.08	9.51
	100	4.94	5.43	6.07	--	6.69	7.66	6.78	--	9.06

5.10 FAILURE STATE AND OTHER LIMIT STATES

The design of offshore wind turbine foundation is governed by several limit states, namely, serviceability limit state (SLS), fatigue limit state (FLS), worst expected transient load limit state, and ultimate limit state (ULS).

The allowable or serviceable limit load of the wind turbine foundation system corresponds to the lateral foundation displacement corresponding to a maximum allowable rotation of either 0.25° (Cox and Bhattacharya 2016; Zhu et al. 2013) or 0.5° at the centre of the lid level (Golightly 2014; Harte et al. 2012; Malhotra 2011). The fatigue limit load corresponds to 30% of ultimate load (Zhu et al. 2013), whereas the worst expected transient load corresponds to a value of ultimate load/1.35 (Zhang et al. 2016). During a 20-year design period, the wind turbine reaches the fatigue load about 10^7 times under the action of resultant cyclic wind and water loads (DNV 2007).

5.10.1 Failure Envelopes of Bucket Foundation

The values of ultimate lateral load capacity and ultimate resisting moment capacity obtained for different loading heights of a particular bucket geometry (Table 5.3 to Table 5.5) can be utilized to plot its failure envelope corresponding to ultimate limit state. Figures 5.26 and 5.27 respectively show failure envelopes for all bucket foundations of 12 and 18 m diameters, in both sand types under superstructure load of 5 MN.

The failure envelope is noted to expand with an increased value of aspect ratio. For a given bucket geometry, the failure envelope size for very dense sand is larger as compared to that for medium dense sand. The trends remain similar across all the bucket geometries and superstructure loads. During extreme environmental conditions, combined loading from wind, waves and currents can become unidirectional (Byrne and Houlsby 1999). For a given bucket geometry, if the combination of acting lateral load and overturning moment lies within

the envelope, it indicates that the ultimate limit state of the bucket foundation has not been reached.

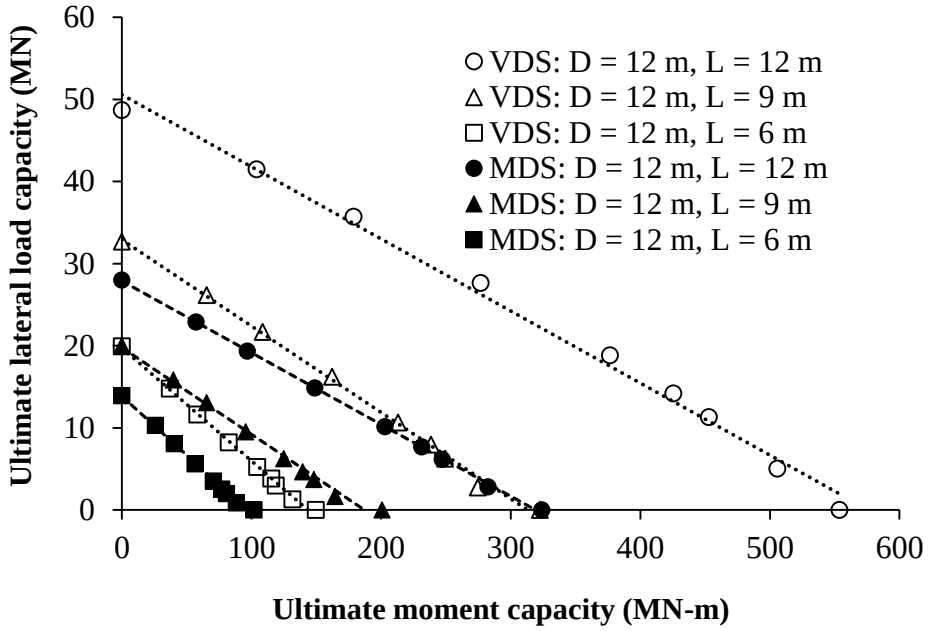

Figure 5.26 Interaction diagram of bucket foundation at failure (D = 12 m, V = 5 MN)

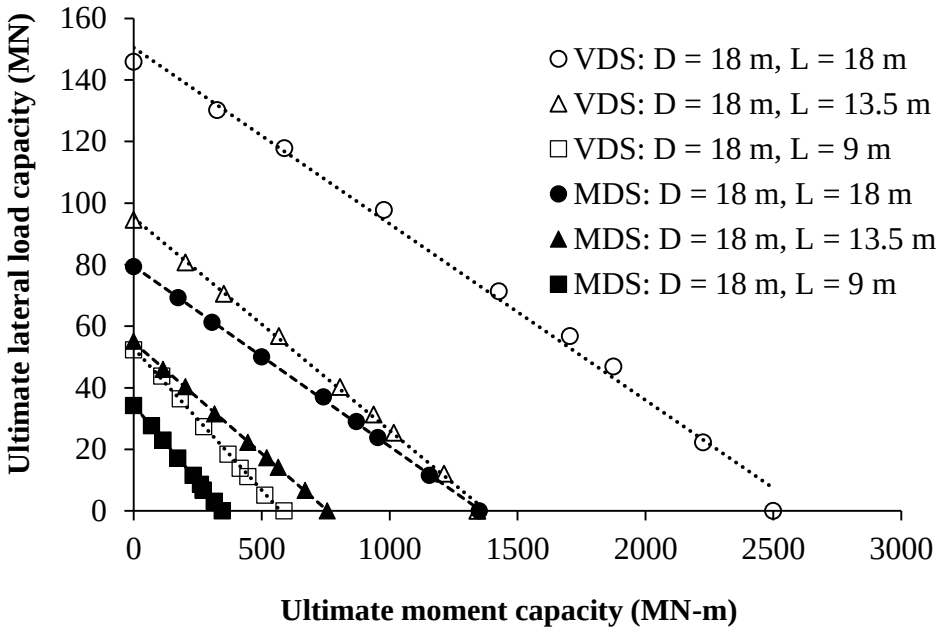

Figure 5.27 Interaction diagram of bucket foundation at failure (D = 18 m, V = 5 MN)

5.10.2 Allowable Envelopes for Serviceability Limit State (Θ = 0.5°)

Determination of the allowable lateral capacity of the monopod bucket foundation is crucial for the stability of the offshore wind turbine structure. The maximum allowable angular rotation of the wind turbine is limited by serviceability constraints of the turbine. In this section allowable lateral load capacity of bucket foundation corresponding to the lid rotation value of 0.5° has been chosen and presented in Figures 5.28-5.29. Depending upon the site conditions, for the specific bucket geometry, if the combination of acting lateral load and overturning moment lies inside the respective envelope, the wind turbine foundation system is safe and serviceability limit state is not reached.

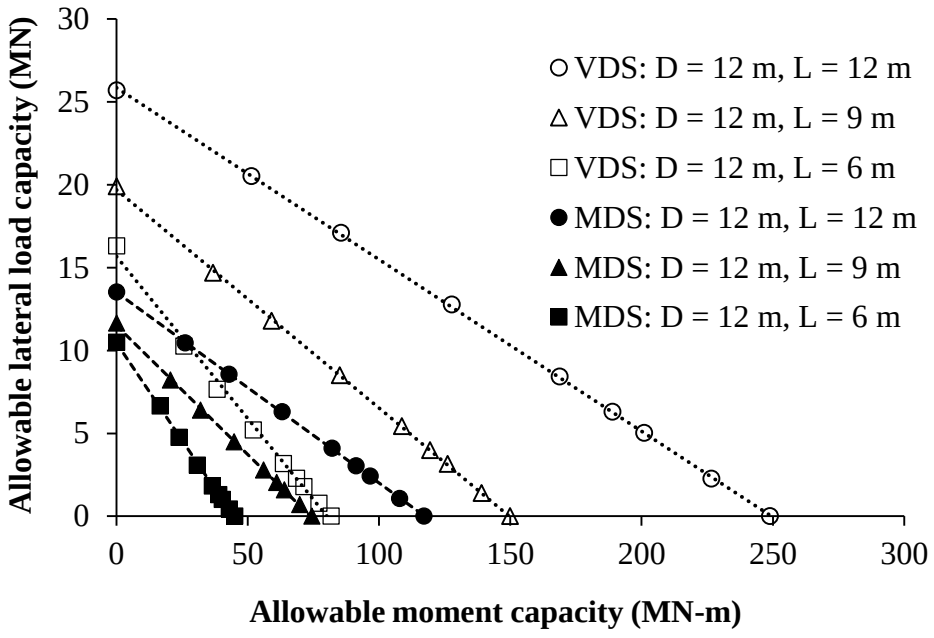

Figure 5.28 Interaction diagrams of bucket foundation for lid level rotation of 0.5° (D = 12 m, V = 5 MN)

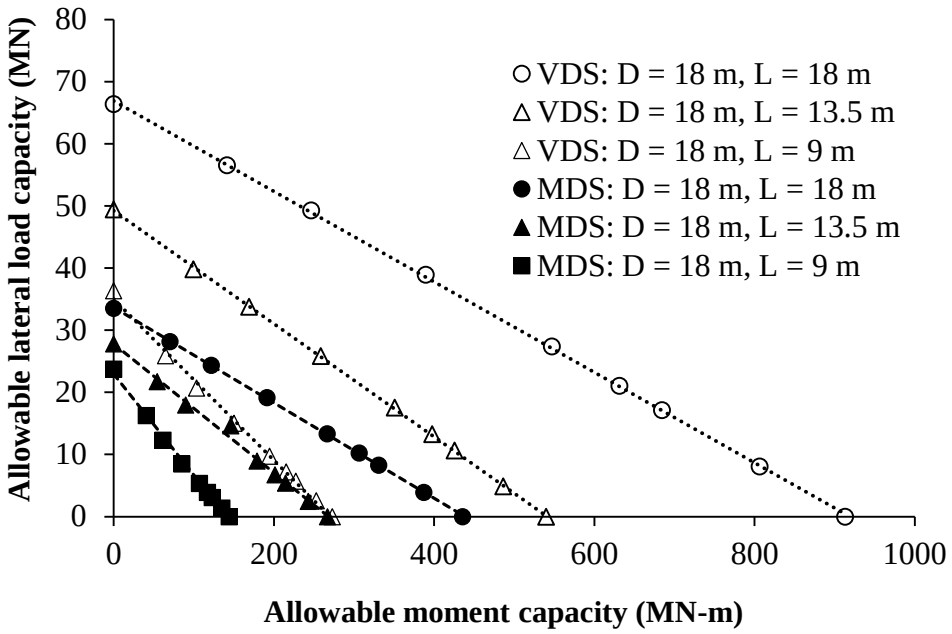

Figure 5.29 Interaction diagrams of bucket foundation for lid level rotation of 0.5° (D = 18 m, V = 5 MN)

5.10.3 Envelopes for all Limit States of Bucket Foundation

The interaction plots for all the limit states, derived for the bucket foundations of 12 and 18 m diameters with aspect ratio of 1, are illustrated in Figure 5.30. From the figure, it can be noted that the interaction diagram for the fatigue limit state is the smallest followed by that of the serviceability limit state, the worst expected transient load limit state and the ultimate limit state.

The graphical representation explicitly allows to identify the combination of lateral load and overturning moment capacity at various loading heights, for any specific or for all the limit states. Similar design envelopes can be arrived at, for all the bucket geometries considered in this study, based on the plots of lateral load capacity versus lateral displacement and of resisting moment capacity versus rotation at the lid centre.

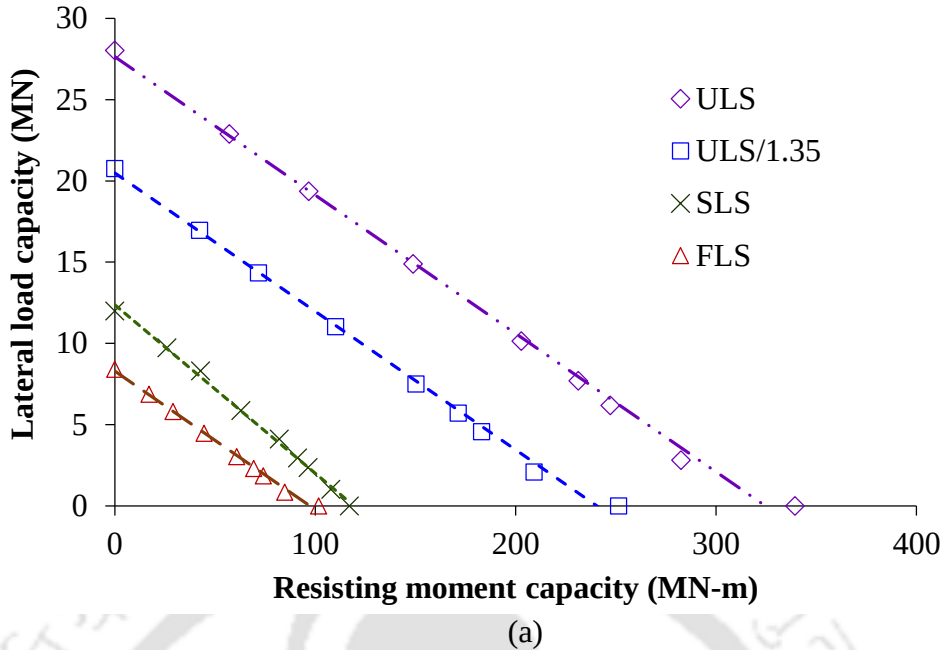

(a)

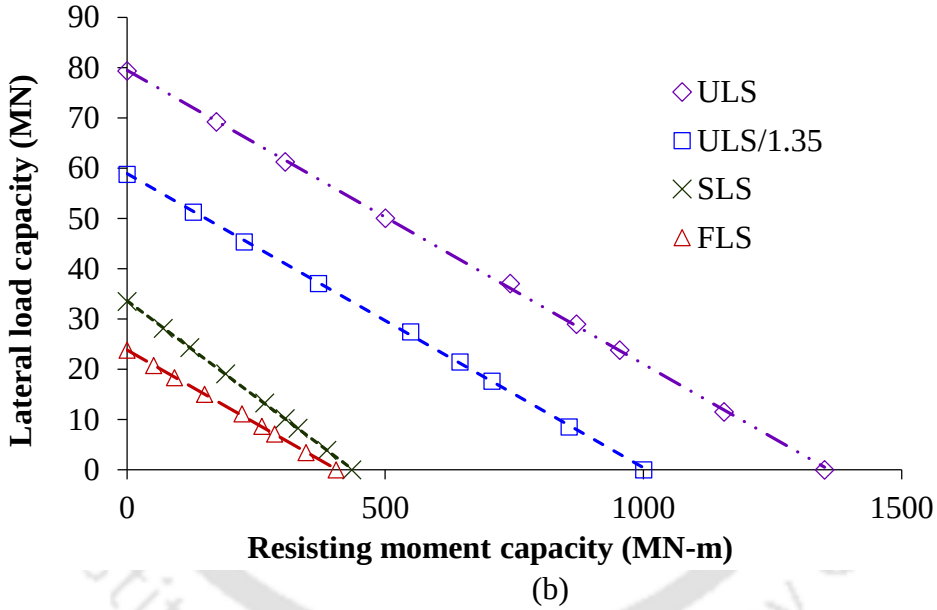

(b)

Figure 5.30 Interaction diagrams representing all the limit states of: (a) D = 12 m, L = 12 m; (b) D = 18 m, L = 18 m in medium dense sand under V = 5 MN

5.11 DESIGN EXPRESSIONS

The results obtained from the numerical analysis of bucket foundations in medium dense and very dense sands for several bucket geometries under several superstructure loads are utilized to formulate expressions which can be utilized for the design of bucket foundations subjected to loads arising from offshore environments.

5.11.1 Depth of Point of Rotation

Figure 5.31(a)-(c) and Figure 5.32(a)-(c) show the variation of depth of point of rotation (*Z*) with overturning moment capacity in normalized form for bucket foundation under the superstructure loads of 5, 10 and 15 MN, in medium dense and very dense sand, respectively. The depth of point of rotation is scaled with respect to the skirt length of the foundation and the overturning moment is scaled with respect to the lateral capacity and diameter of bucket foundation. Based on the data, curves were fitted and Equations (5.1)-(5.2) were developed to determine the depth of point of bucket foundation in medium dense and very dense sands. The values of coefficients (a, b, c, t_1, t_2) in this equation for different superstructure loads for the foundations in medium dense and very dense sands are presented in Table 5.22.

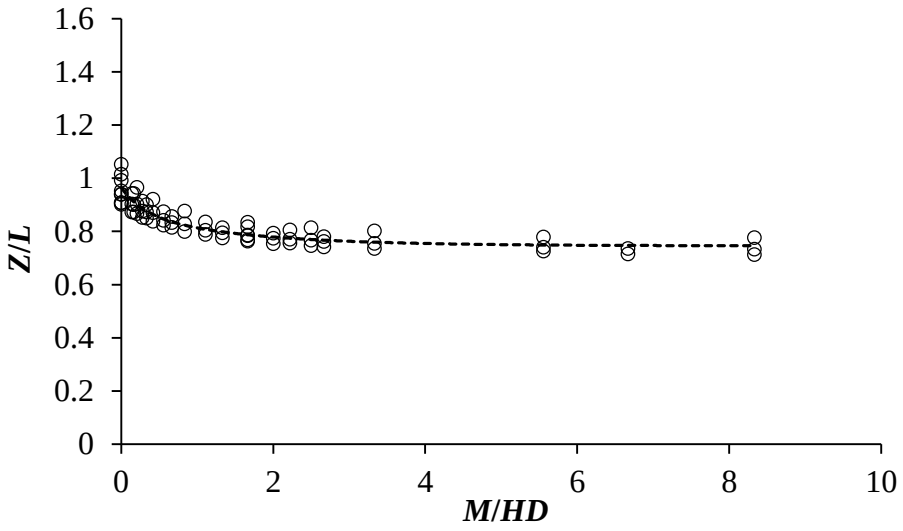

(a)

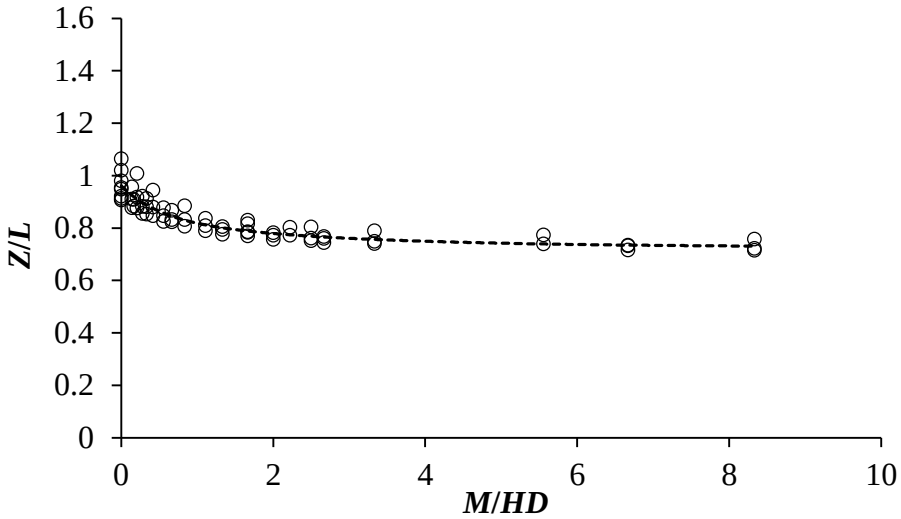

(b)

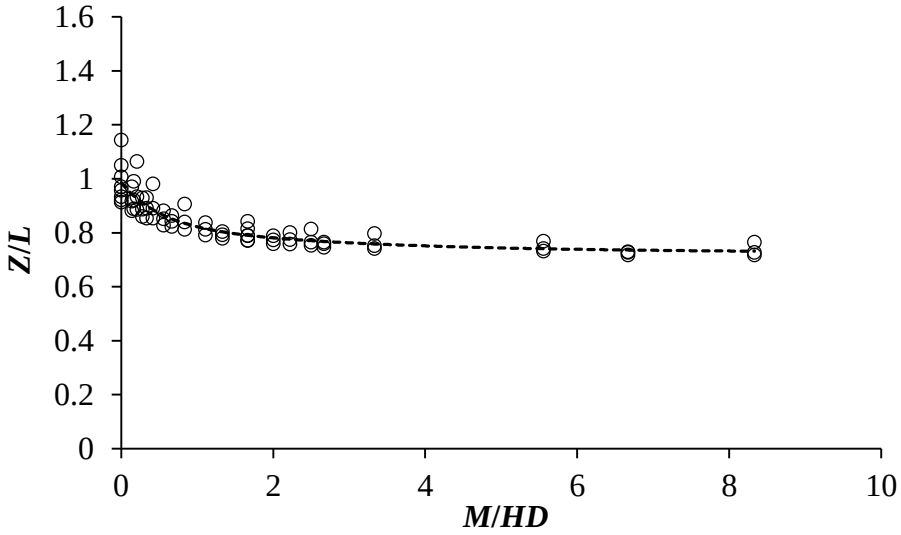

(c)

Figure 5.31 Normalized depth of point of rotation of bucket foundation in medium dense sand for different superstructure loads: (a) V = 5 MN; (b) V = 10 MN; (c) V = 15 MN

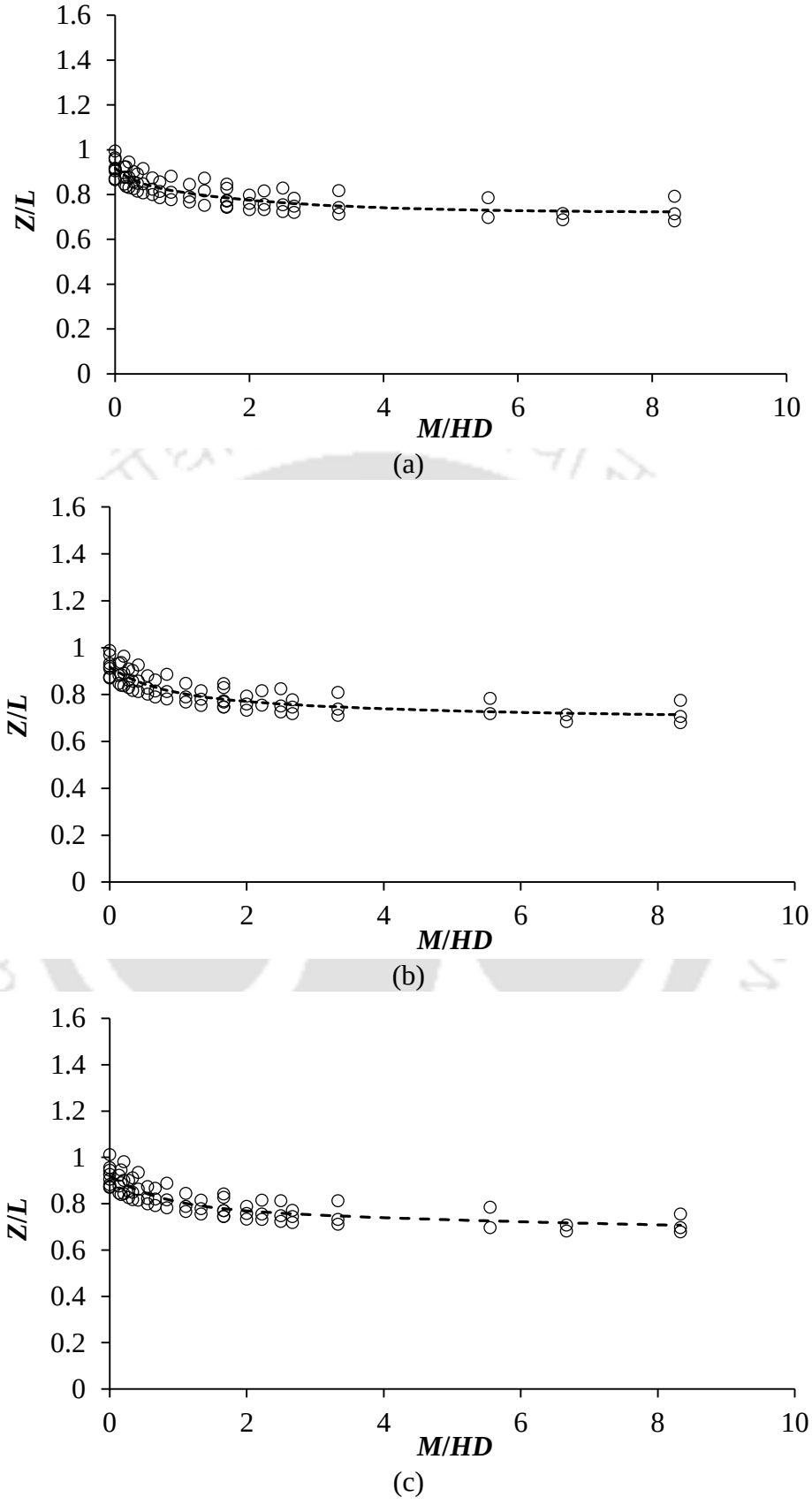

Figure 5.32 Normalized depth of point of rotation of bucket foundation in very dense sand for different superstructure loads: (a) V = 5 MN; (b) V = 10 MN; (c) V = 15 MN

$$Z = L\left(ae^{\left(\frac{M}{HDt_1}\right)} + be^{\left(\frac{M}{HDt_2}\right)} + c \right) \tag{5.1}$$

The above expression can also be given as Equation (5.2)

$$Z = L\left(ae^{\left(\frac{h}{Dt_1}\right)} + be^{\left(\frac{h}{Dt_2}\right)} + c \right) \tag{5.2}$$

Table 5.22 Values of coefficients to determine the depth of point of rotation of bucket foundation

Sand type	**Coefficients**	**Depth of point of rotation (m)**		
		***V* = 5 MN**	***V* = 10 MN**	***V* = 15 MN**
Medium dense sand	a	0.0954	0.1104	0.1517
	b	0.1233	0.1235	0.1067
	c	0.7427	0.7373	0.7368
	t_1	-0.3073	-2.4995	-0.5121
	t_2	-1.5242	-0.4001	-2.7299
Very dense sand	a	-0.1438	0.1056	0.1315
	b	0.0538	0.1095	0.1343
	c	0.7199	0.7027	0.6645
	t_1	-2.0950	-0.6304	-8.8690
	t_2	-0.2607	-3.6628	-0.7393

5.11.2 Initial Stiffness of Bucket Foundation

Figure 5.33(a)-(c) shows the variation of initial stiffness with loading height in normalized form for bucket in medium dense sand. The initial stiffness values were scaled with respect to bucket diameter (D), normalized skirt length (L/L_{ref}), and reference modulus of elasticity of soil (Achmus et al. 2013), where L_{ref} is taken as unity and $E_{soil,ref} = \kappa.\sigma_{at}$ with κ and σ_{at} being the empirical parameter and atmospheric pressure, as explained earlier. The normalized initial stiffness values for the superstructure load of 5, 10 and 15 MN were utilized to fit a curve which represented all the data points adequately [Figure 5.33(a)-(c)], and similar fits were made for data obtained for foundation in very dense sands [Figure

5.34(a)-(c)]. Based on the fits, expressions were developed to determine the initial stiffness for preliminary design of a bucket foundation, and the general expression is given in Equation (5.3). The values of coefficients (a^*, b^* and c^*) in this equation for different superstructure loads for the foundations in medium dense and very dense sands are presented in Table 5.23.

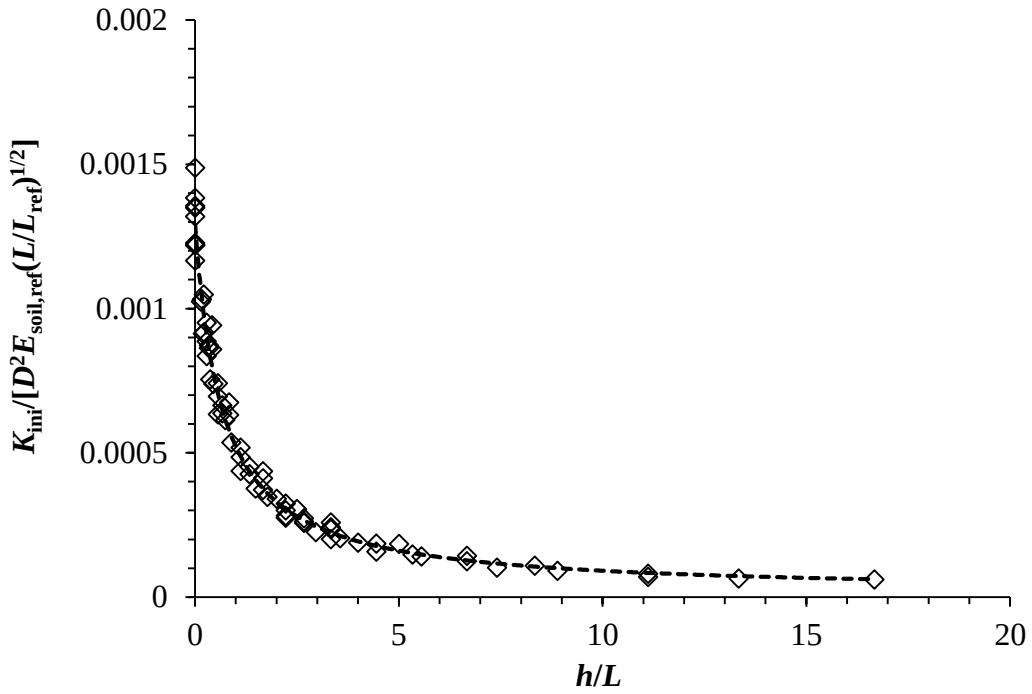

(a)

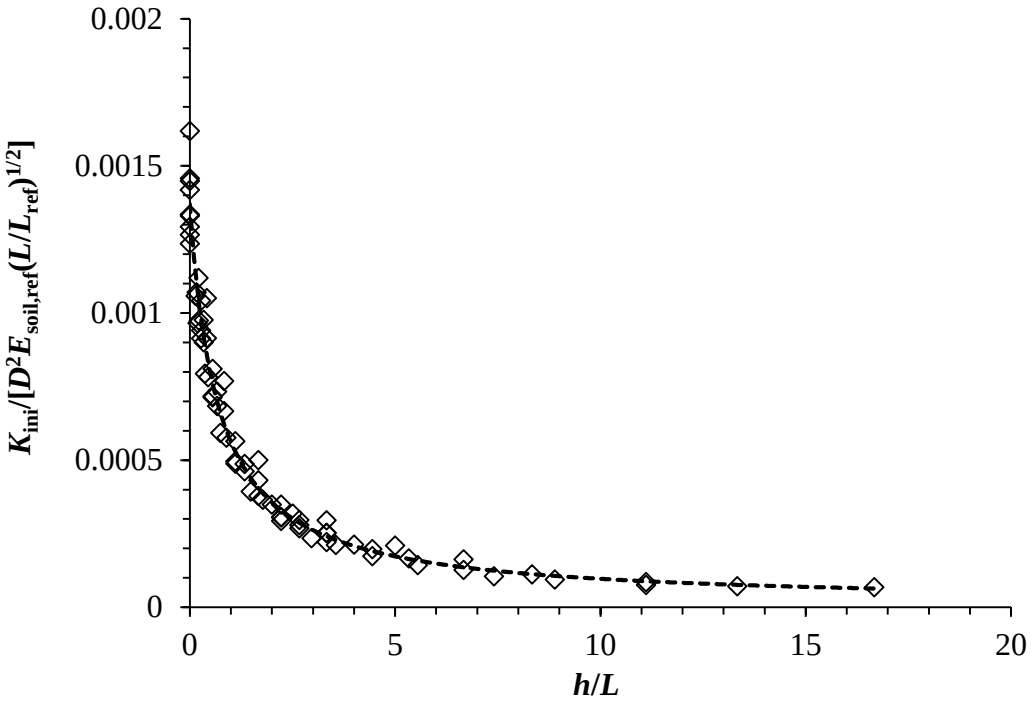

(b)

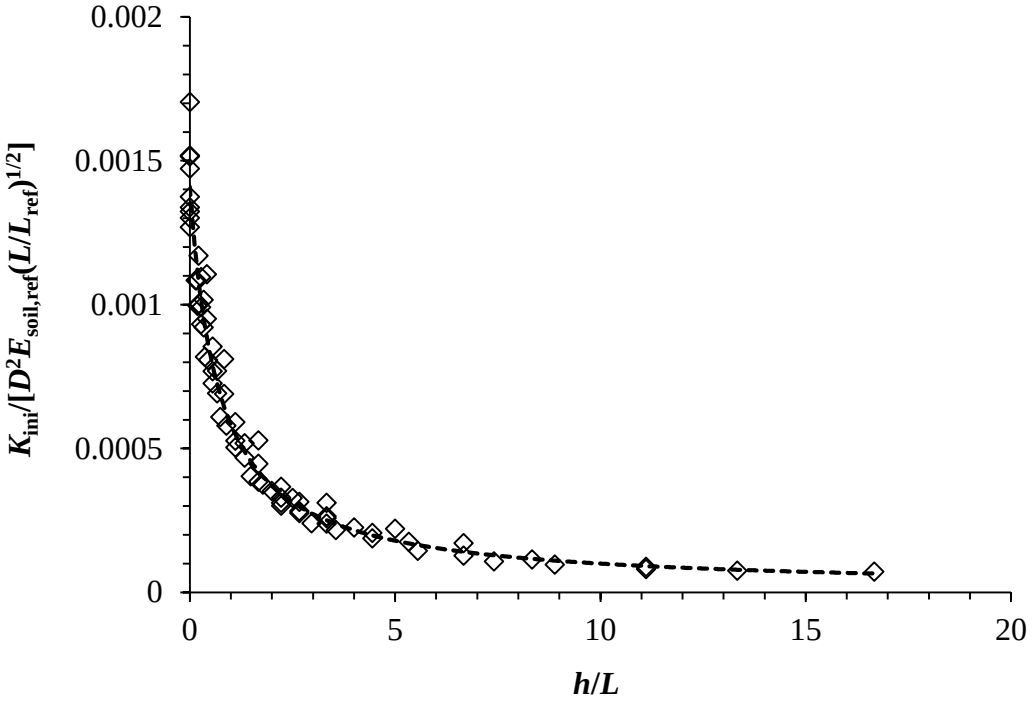

(c)

Figure 5.33 Normalized initial stiffness of bucket foundation in medium dense sand and for superstructure load (a) V = 5 MN; (b) V = 10 MN; (c) V = 15 MN

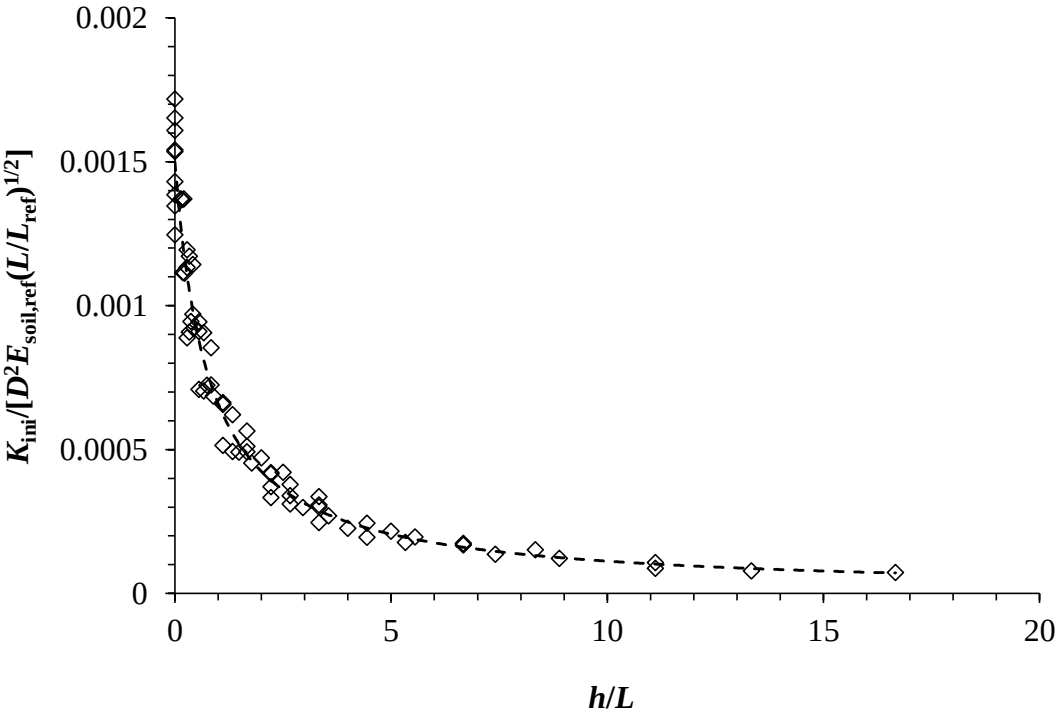

(a)

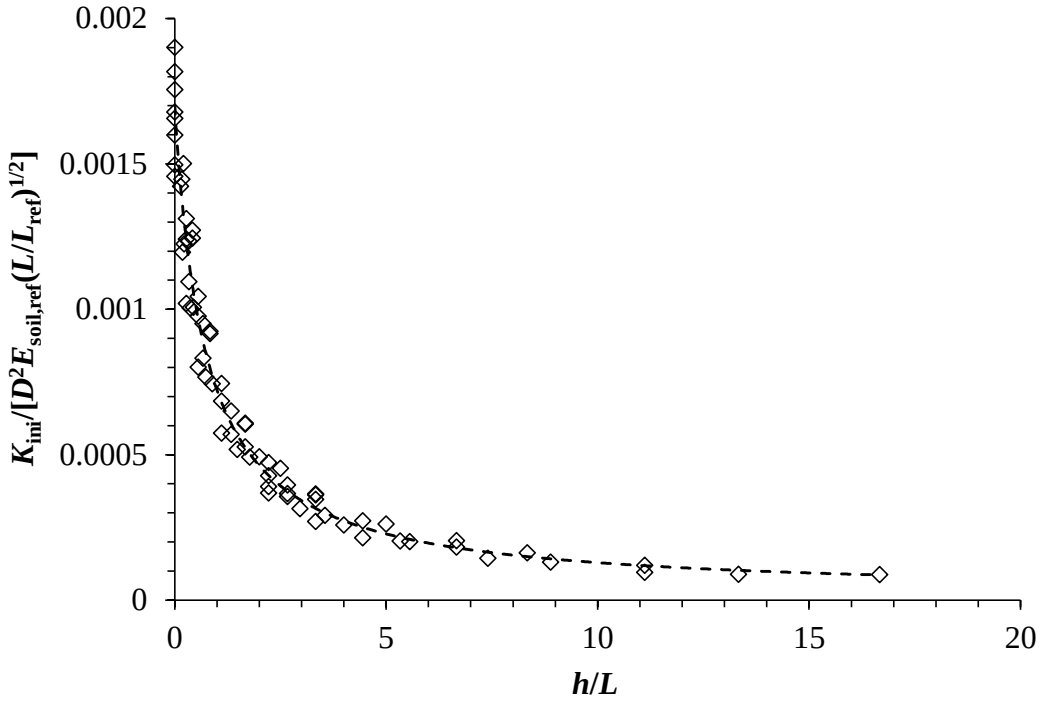

(b)

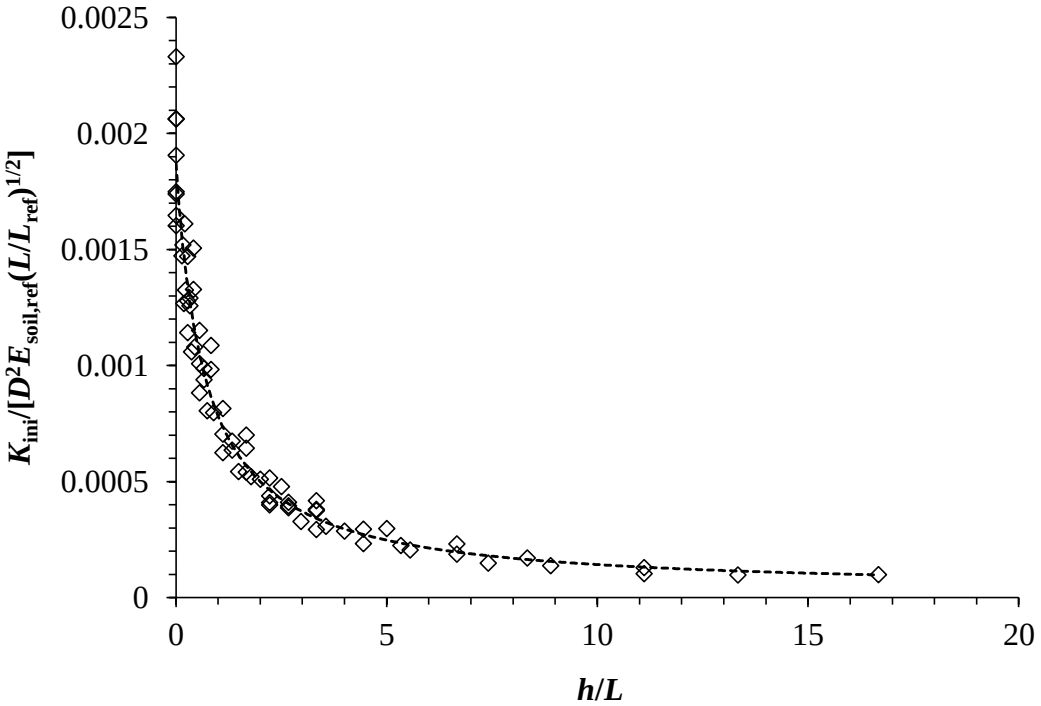

(c)

Figure 5.34 Normalized initial stiffness of bucket foundation in very dense sand and for superstructure load (a) V = 5 MN; (b) V = 10 MN; (c) V = 15 MN

$$K_{ini} = \frac{D^2 E_{soil,ref} \left(\frac{L}{L_{ref}} \right)^{0.5}}{a^* + b^* \left(\frac{h}{L} \right) + c^* \left(\frac{h}{L} \right)^2} \tag{5.3}$$

Table 5.23 Values of coefficients to determine the initial stiffness of bucket foundation

Sand type	Rotation of lid at bed level (°)	Co-efficient	Initial stiffness (K_{ini}) in MN/°		
			V = 5 MN	V = 10 MN	V = 15 MN
Medium dense sand	Θ = 0.25°	a^*	546.640	526.671	516.444
		b^*	819.936	798.572	793.387
		c^*	-6.832	-4.187	-3.170
	Θ = 0.5°	a^*	773.324	731.290	708.258
		b^*	1155.985	1056.540	1013.670
		c^*	-13.782	-9.636	-8.556
Very dense sand	Θ = 0.25°	a^*	418.262	372.043	345.499
		b^*	613.385	565.930	532.644
		c^*	-6.802	-7.771	-8.049
	Θ = 0.5°	a^*	667.849	589.400	534.882
		b^*	852.179	803.520	752.498
		c^*	-2.775	-8.699	-10.334

5.11.3 Ultimate Lateral Capacity of Bucket Foundation

Figures 5.35(a)-(c) and 5.36(a)-(c) show the variation of ultimate lateral capacity with loading height in a non-dimensional form, for superstructure load of 5, 10 and 15 MN. Based on the best-fit curve, general expression of ultimate lateral capacity ($H_{Ultimate}$) with soil density (γ'), bucket diameter (D), skirt length (L), and loading height (h) is given in Equation (5.4). The values of coefficients (a', b', c') in this equation for different superstructure loads for medium dense and very dense sands are given in Table 5.24.

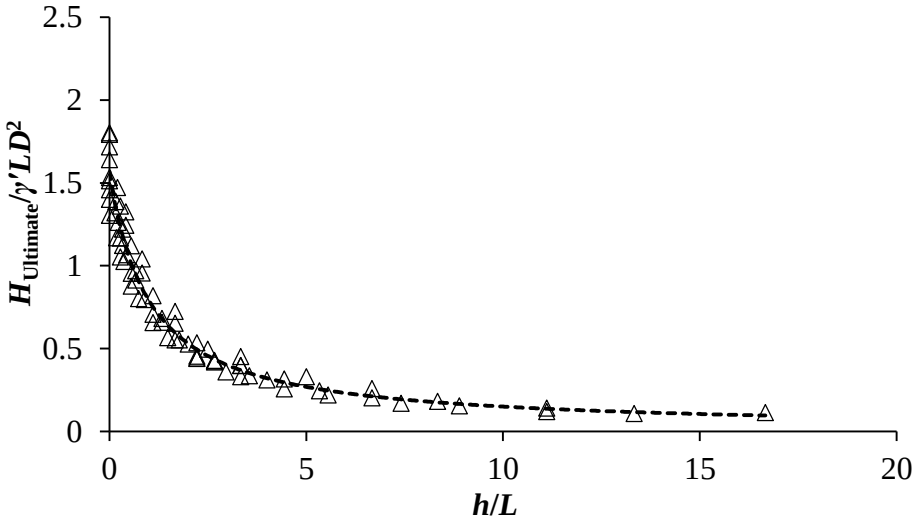

(a)

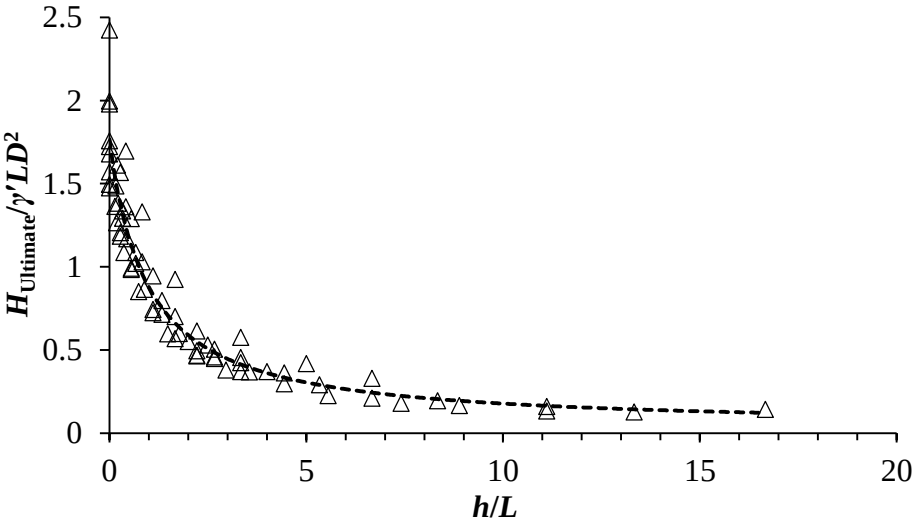

(b)

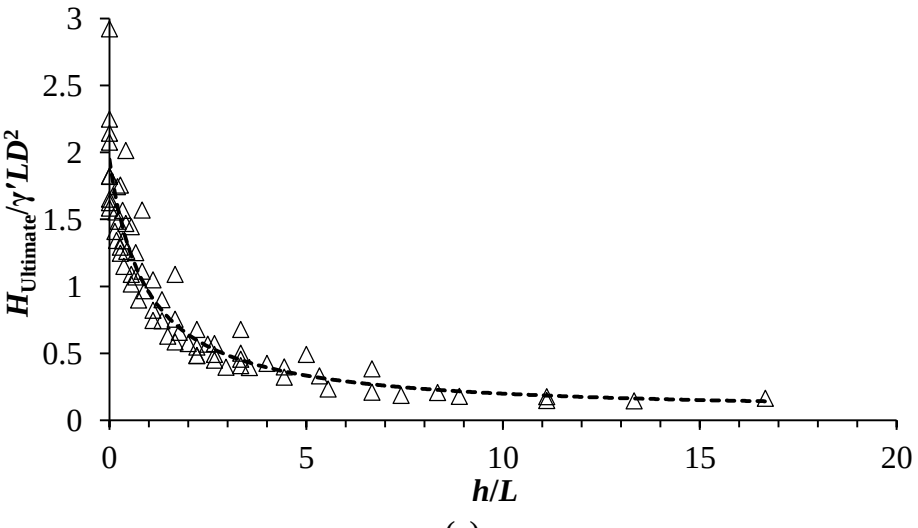

(c)

Figure 5.35 Normalized ultimate lateral capacity of bucket foundation in medium dense sand and for superstructure load (a) V = 5 MN; (b) V = 10 MN; (c) V = 15 MN

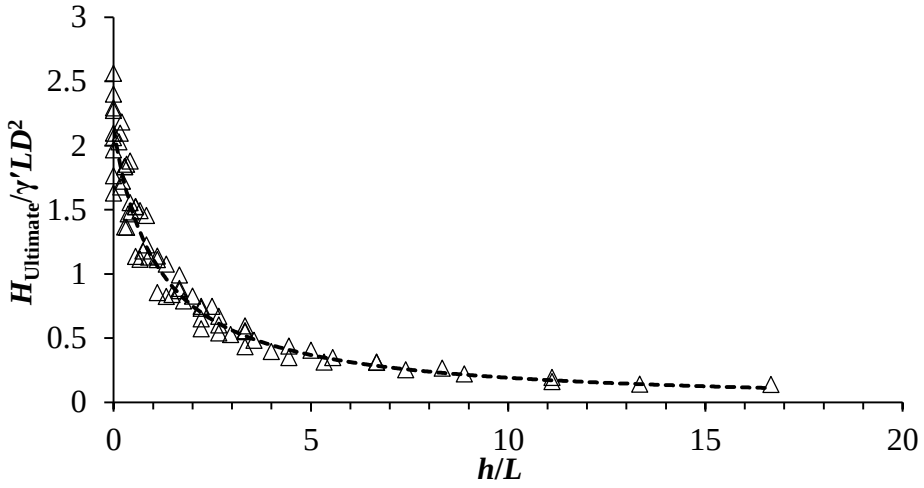

(a)

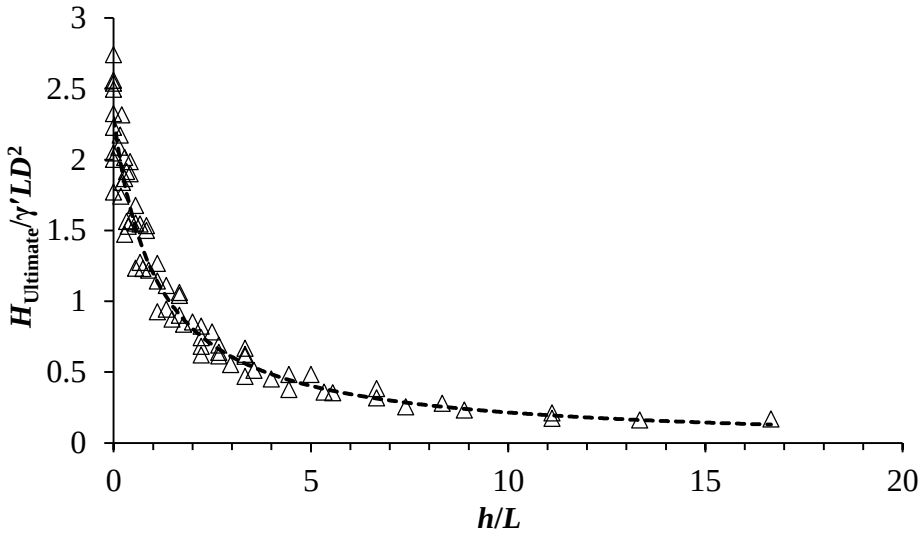

(b)

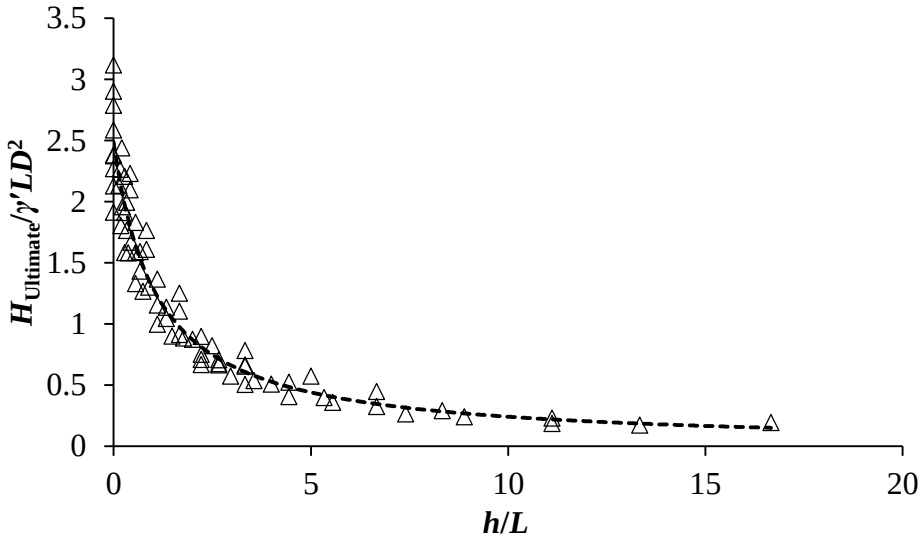

(c)

Figure 5.36 Normalized ultimate lateral capacity of bucket foundation in very dense sand and for superstructure load (a) V = 5 MN; (b) V = 10 MN; (c) V = 15 MN

$$H_{Ultimate} = \frac{\gamma' L D^2}{a' + b'\left(\frac{h}{L}\right) + c'\left(\frac{h}{L}\right)^2} \tag{5.4}$$

Table 5.24 Values of coefficients to determine the ultimate lateral capacity of bucket foundation

Sand type	Co-efficient	Ultimate lateral capacity ($H_{Ultimate}$) in MN		
		V = 5 MN	V = 10 MN	V = 15 MN
Medium dense sand	a′	0.6376	0.5659	0.5134
	b′	0.6286	0.5796	0.5408
	c′	-0.0026	-0.0073	-0.0090
Very dense sand	a′	0.4702	0.4361	0.4019
	b′	0.4208	0.3962	0.3733
	c′	0.0056	0.0025	3.71E-05

5.11.4 Allowable Lateral Capacity of Bucket Foundation

The variation of allowable lateral capacity with ultimate lateral capacity of the bucket foundations in medium dense and very dense sand are shown in Figures 5.37-5.40 in a non-dimensional form. The general expression for the relationship between the allowable lateral capacity ($H_{Allowable}$) and ultimate lateral capacity ($H_{Ultimate}$) of bucket foundation can be expressed in the form of Equation (5.5). The values of coefficients (a″, b″ and c″) in this equation for respective superstructure loads can be referred from Table 5.25.

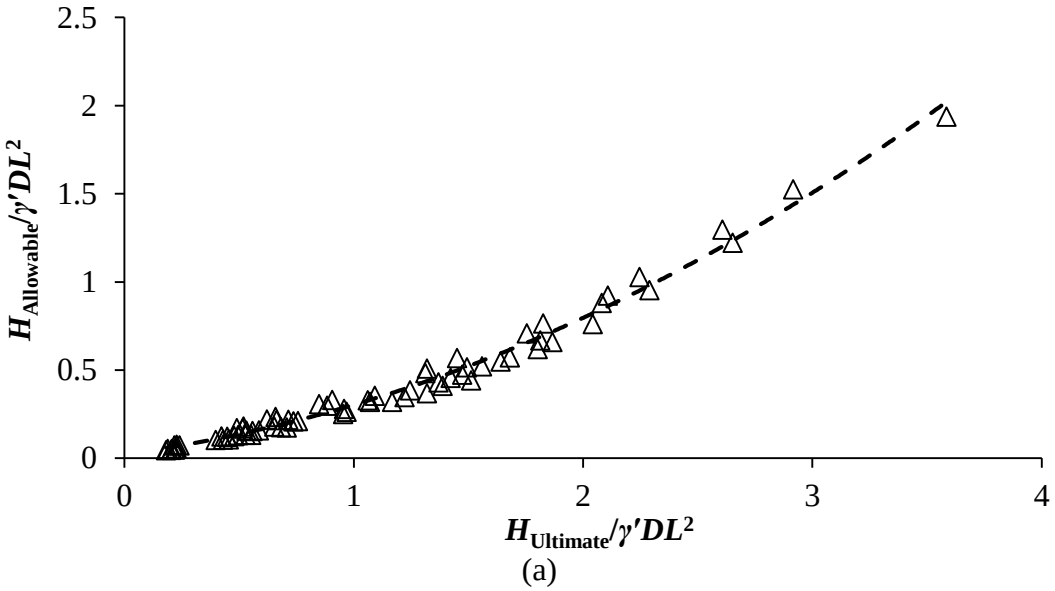

(a)

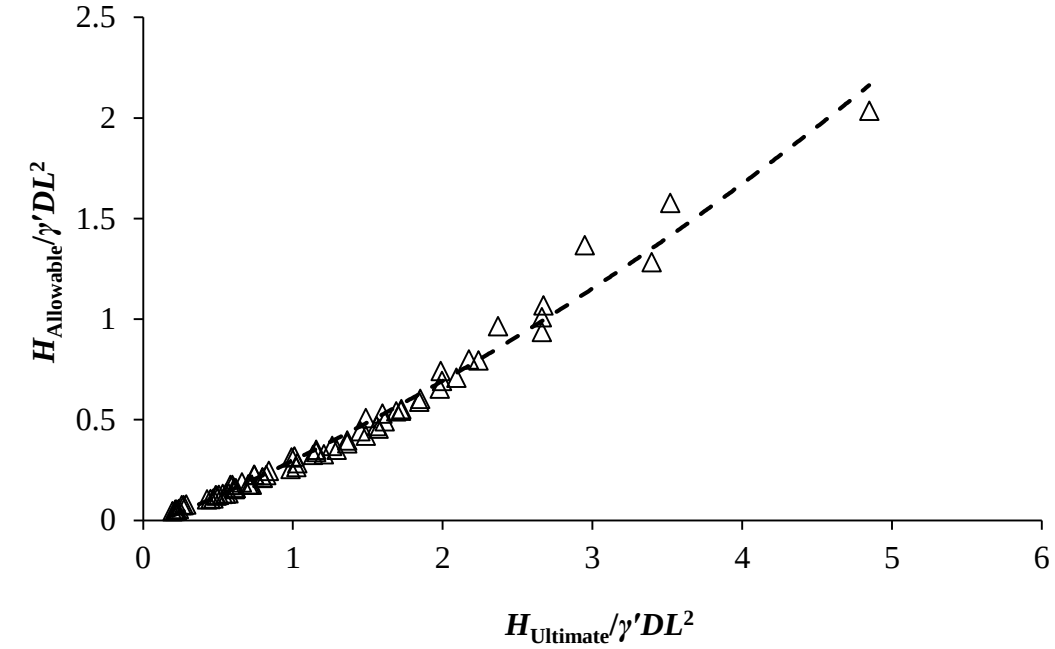

(b)

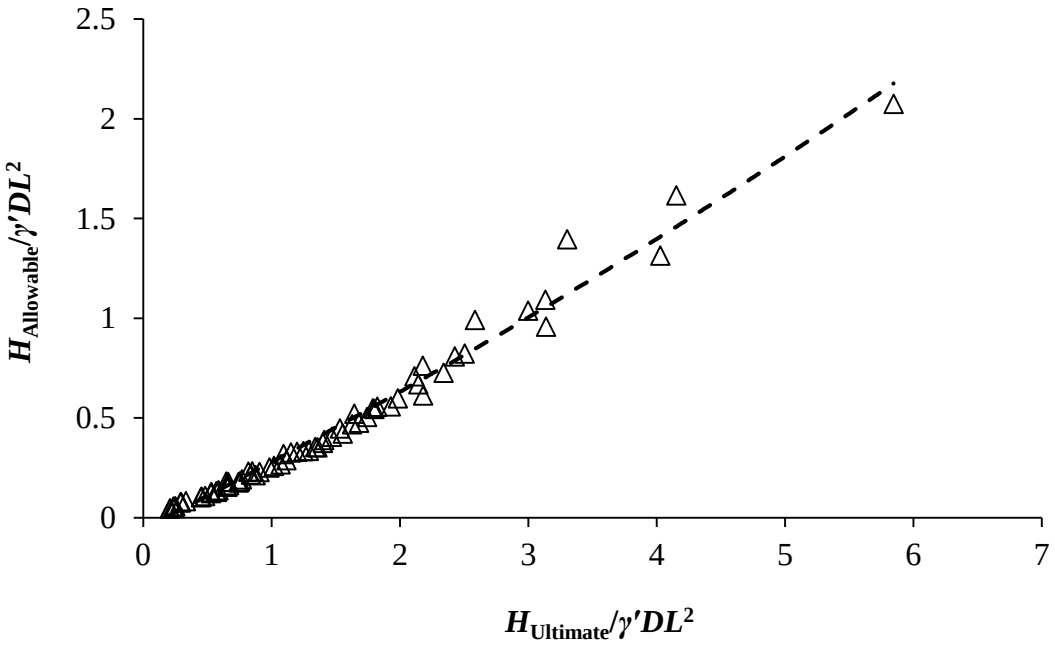

(c)

Figure 5.37 Normalized lateral capacity of bucket foundation in medium dense sand and under the superstructure load of (a) V = 5 MN; (b) V = 10 MN; (c) V = 15 MN at lid rotation of 0.25°

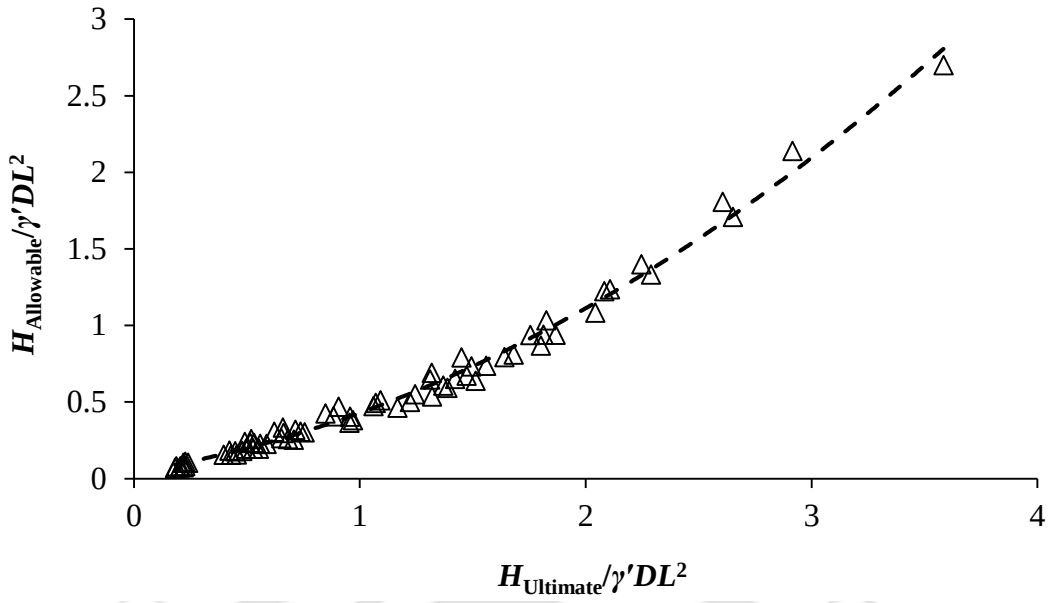

(a)

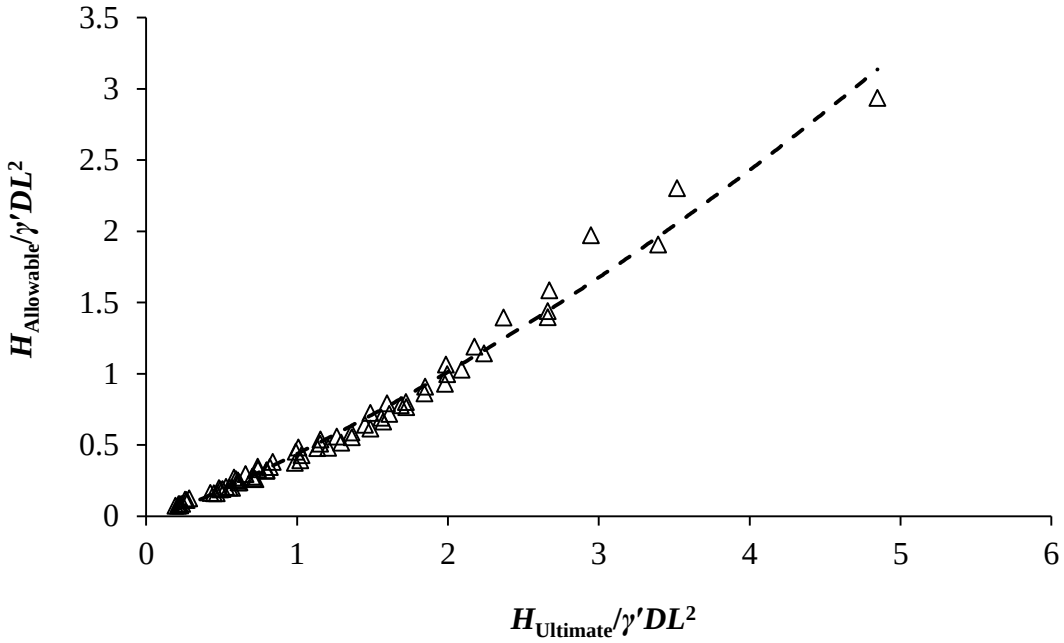

(b)

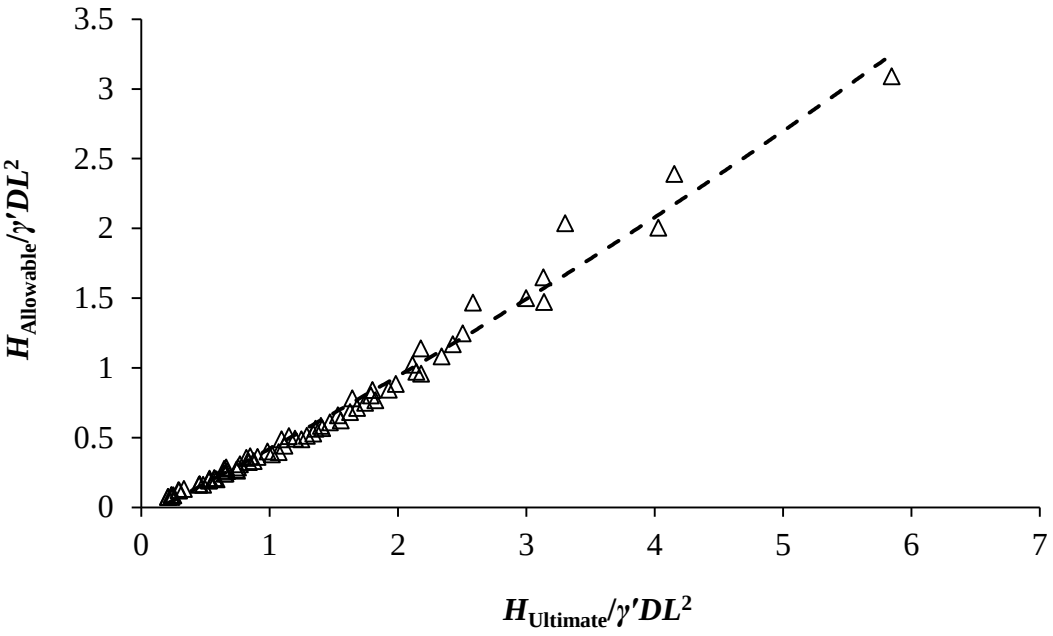

(c)

Figure 5.38 Normalized lateral capacity of bucket foundation in medium dense sand and under the superstructure load of (a) V = 5 MN; (b) V = 10 MN; (c) V = 15 MN at lid rotation of 0.5°

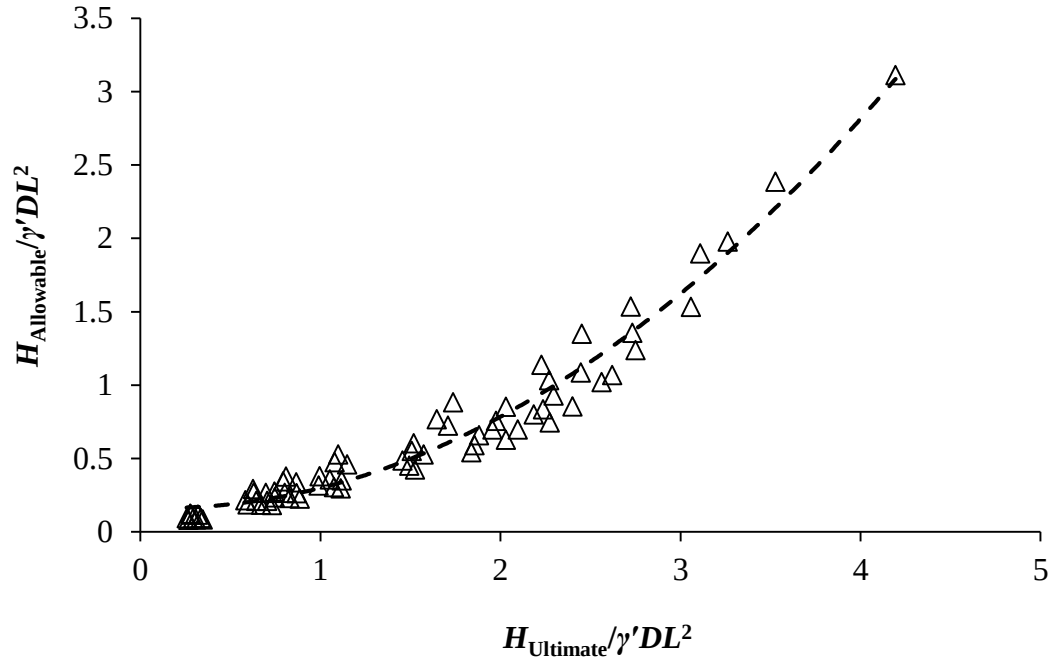

(a)

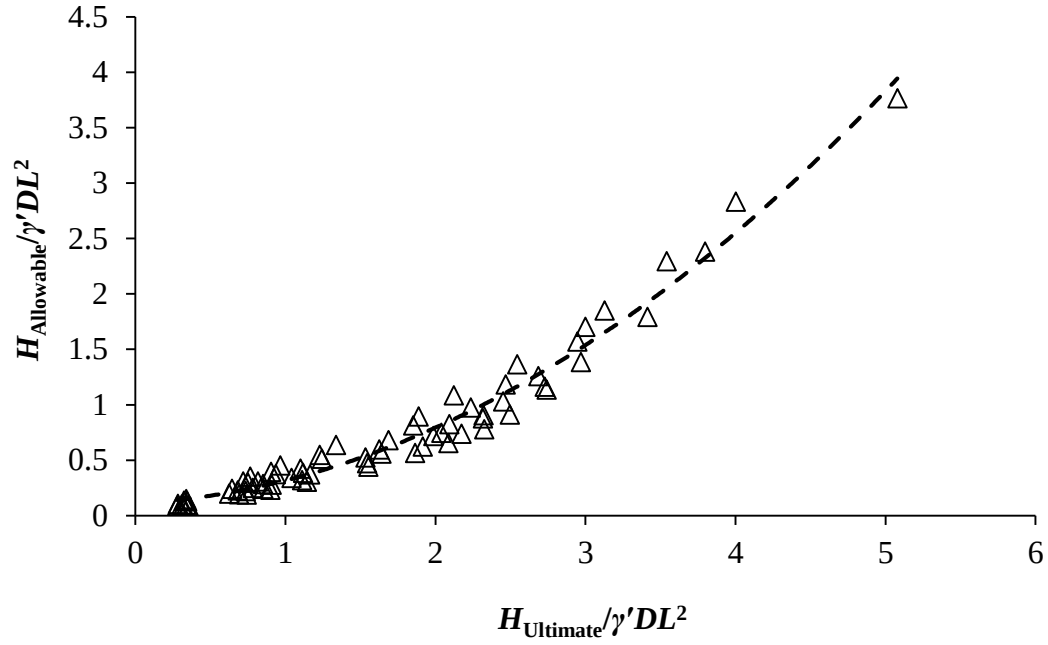

(b)

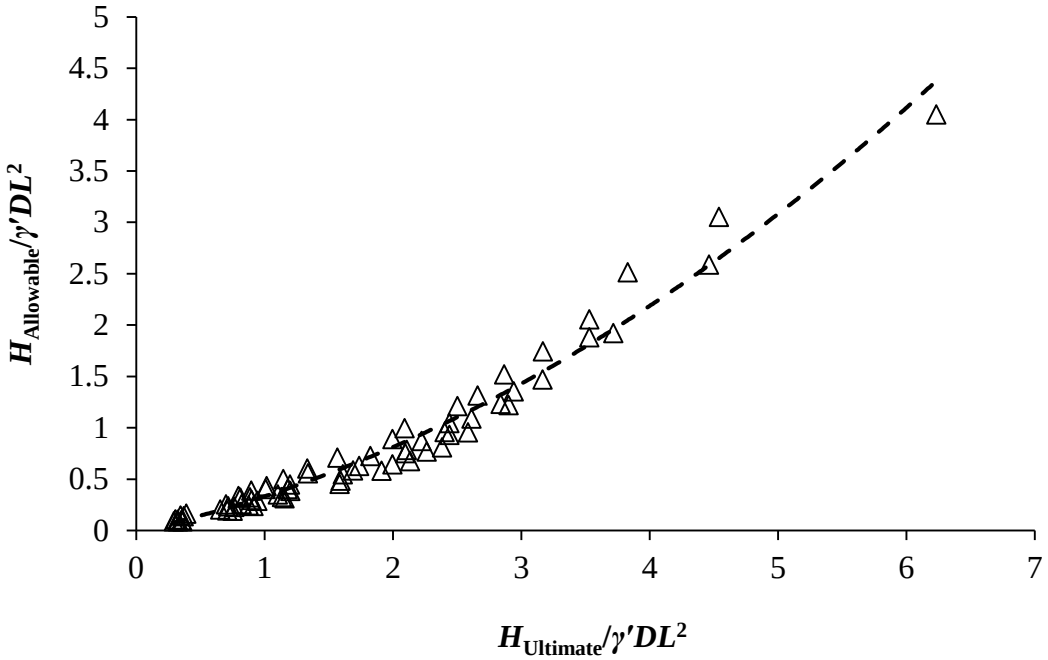

(c)

Figure 5.39 Normalized lateral capacity of bucket foundation in very dense sand and under the superstructure load of (a) V = 5 MN; (b) V = 10 MN; (c) V = 15 MN at lid rotation of 0.25°

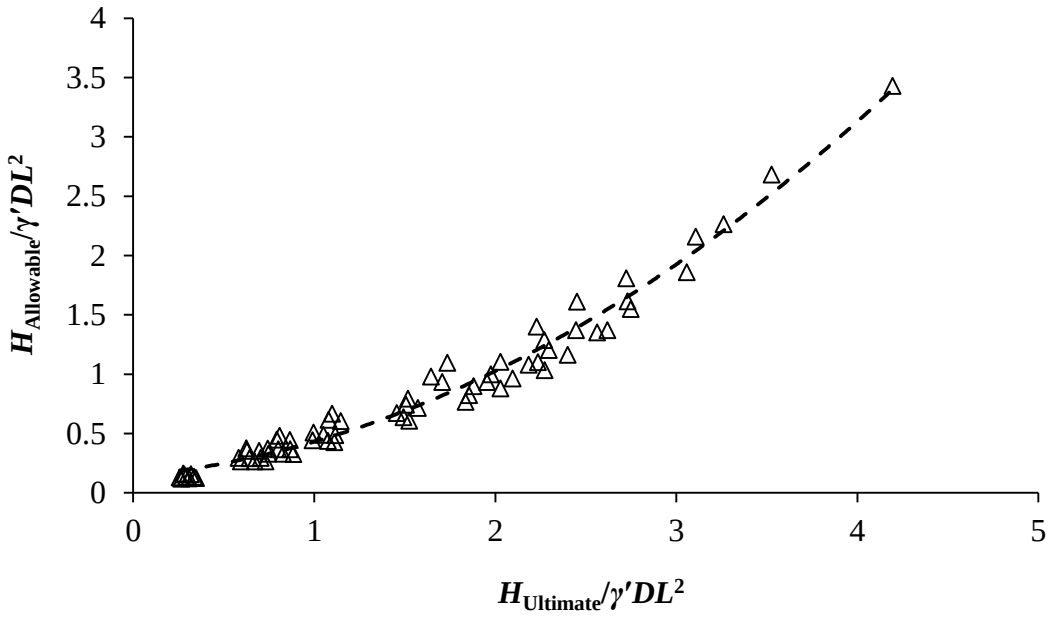

(a)

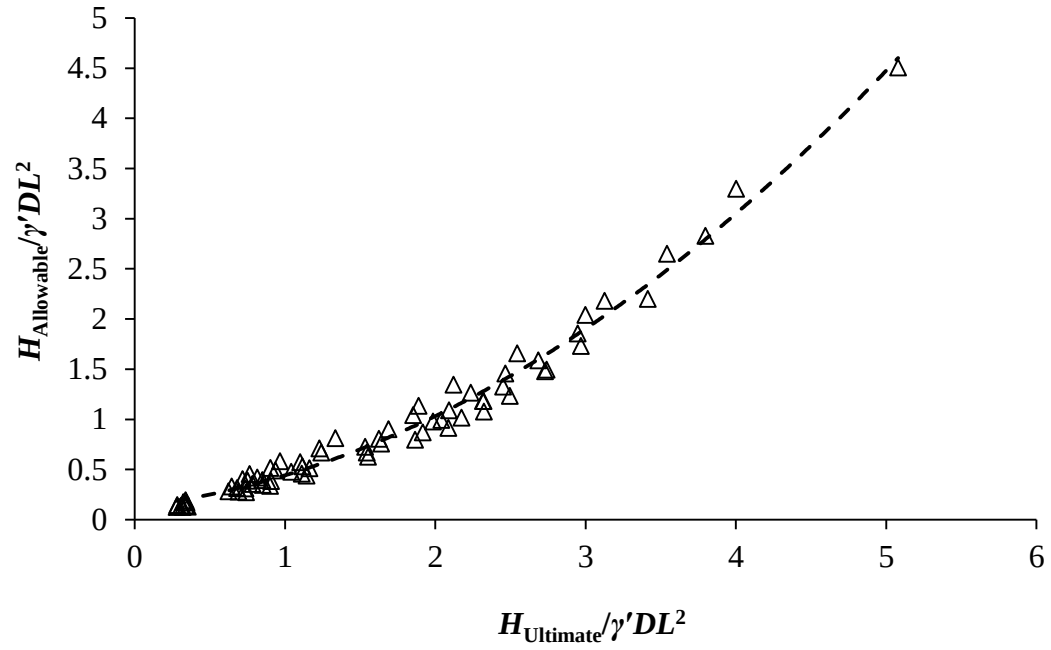

(b)

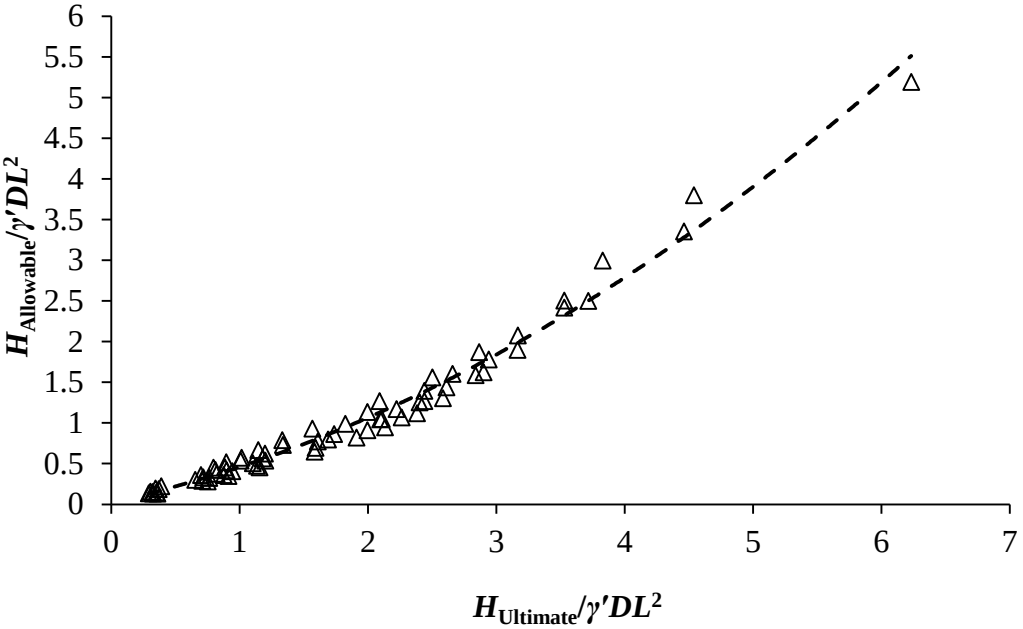

(c)

Figure 5.40 Normalized lateral capacity of bucket foundation in very dense sand and under the superstructure load of (a) V = 5 MN; (b) V = 10 MN; (c) V = 15 MN at lid rotation of 0.5°

$$H_{Allowable} = a''(\gamma' DL^2) + b''(H_{Ultimate}) + c''\frac{(H_{Ultimate})^2}{\gamma' DL^2} \quad (5.5)$$

Table 5.25 Values of coefficients to determine the allowable lateral capacity of bucket foundation

Sand type	Rotation of lid at bed level (°)	Coefficients	Allowable lateral capacity ($H_{Allowable}$) in MN		
			V = 5 MN	V = 10 MN	V = 15 MN
Medium dense sand	Θ = 0.25°	a″	0.0254	-0.0379	-0.0542
		b″	0.1697	0.3036	0.3220
		c″	0.1079	0.0310	0.0102
	Θ = 0.5°	a″	0.0431	-0.0465	-0.0684
		b″	0.2368	0.4400	0.4716
		c″	0.1490	0.0447	0.0163
Very dense sand	Θ = 0.25°	a″	0.1652	0.1087	-0.0089
		b″	-0.0429	0.0740	0.2714
		c″	0.1763	0.1341	0.0693
	Θ = 0.5°	a″	0.1423	0.1295	0.0232
		b″	0.1370	0.1730	0.3509
		c″	0.1525	0.1393	0.0850

5.12 SUMMARY

Based on the response of monopod bucket foundations under lateral loading, the following main conclusions have been drawn:

1. With increase of loading height, the ultimate lateral capacity of bucket foundation is noted to decrease; however, the ultimate resisting moment capacity and angular rotation at lid level are noted to increase.
2. The depth of point of rotation at failure of bucket foundation is noted to move upward with increasing values of loading height. In most of the cases, for a given bucket geometry under any superstructure load and loading height, the depth of point of rotation is found to be located to be at higher depth in medium dense sand as compared to very dense sand.
3. The initial stiffness of bucket foundation is noted to decrease with loading height. However, the initial stiffness increases with aspect ratio and superstructure load. Greater magnitude of initial stiffness value was obtained for a foundation embedded in very dense sand as compared to medium dense sand.
4. Under pure lateral load, an internal inverted scoop failure mechanism is observed to develop above the base of soil plug, irrespective of the aspect ratio. For the lower aspect ratio of 0.5, under greater loading heights, internal inverted scoop mechanism is always observed. In contrast, for the higher aspect ratio of 1, with the increase of loading height from pure lateral load, external upright scoop mechanism is noted.
5. Combinations of lateral load and overturning moment capacity at various loading heights have been represented graphically for all the limit states.
6. Predictive expressions have been proposed for the depth of point of rotation, initial stiffness, ultimate lateral capacity and allowable capacity of bucket foundations in medium and very dense sands.

Chapter 6

SUMMARY AND CONCLUSIONS

6.1 SUMMARY

In this research work, vertical response and lateral response of bucket foundations embedded in sandy seabeds were studied using three-dimensional finite element method, considering non-linear behaviour of the soil.

The vertical response of bucket foundation was studied by considering three bucket diameters, 12 m, 15 m and 18 m, each having aspect ratios of 0.5, 0.75 and 1.0. Two other foundation types, namely, surface circular foundation and embedded solid foundation were also considered to study the effect of skirt length and that of internal soil plug, respectively on the vertical capacity of bucket foundation.

The lateral response of bucket foundation was studied for the same bucket geometries. Three superstructure loads of 5, 10 and 15 MN representative of the self-weight of the wind turbine were considered. Eight loading heights ranging from 0 to 100 m were considered for the resultant lateral load due to wind force and water currents.

6.2 CONCLUSIONS

Based on the numerical analyses carried out, the following conclusions have been drawn:

6.2.1 Vertical Load-Response of Monopod Bucket Foundations

1. For a given diameter and aspect ratio, the ultimate vertical capacity of surface circular foundation is noted to be minimum followed by bucket foundation and embedded solid foundation. The ultimate vertical capacities of all the foundation types are noted to be higher in case of very dense sand as compared to medium dense sand.
2. At failure, lateral outward movement of the soil mass is noted to be at around mid-depth of bucket and embedded solid foundations. For all the foundation types, the magnitude of soil movement at the tip is noted to be higher in the case of very dense sand as compared to that of medium dense sand. The magnitude of lateral expulsion is noted to decrease with higher aspect ratio in the case of bucket foundation. However, in the case of embedded solid foundation, the magnitude of lateral expulsion is noted to increase with aspect ratio.
3. The ultimate vertical capacity of bucket foundation in both the sand types is noted to increase in near linear manner with aspect ratio and bucket diameter. As compared to skirt length, increasing bucket diameter has higher influence on the ultimate vertical capacity.
4. The comparison of plastic strain magnitude of bucket foundation with solid foundation shows that both the foundations failed under punching shear, and a confined deep flow mechanism of the soil is observed along with the formation of an elastic zone in the shape of a wedge. This indicates that the soil plug located inside the bucket foundation acts as an integral part of the bucket foundation.

5. The displacement vector diagram beneath the bucket foundation resembles the shape of an inverted parabola, in which the minimum and maximum displacements of the soil are noted at the centre and at the edges, respectively. The displacement vector diagram at the embedded solid foundation base resembles the shape of an upright parabola, with the maximum and minimum vertical displacements of the soil at the centre and at the edges, respectively. From the comparison of displacement vector diagram, it can be inferred that the soil plug inside bucket foundation provides a cushion effect while transferring the end-bearing load from the superstructure to the soil mass underneath.
6. Vertical capacity depth factor (the ratio between the ultimate vertical bearing capacity of bucket foundation of a particular skirt depth to that of surface circular foundation of the same diameter) is noted to increase non-linearly with aspect ratio.
7. The magnitude of reduction in the end-bearing capacity of bucket foundation is noted to increase with aspect ratio. For a constant aspect ratio, increasing the bucket diameter shows greater effect in the reduction in end-bearing capacity, which is observed to increase with higher diameter values. The magnitude of reduction of the end-bearing capacity of bucket foundation is noted to be higher when embedded in very dense sand as compared to that of the one founded in medium dense sands. For all the bucket geometries, the reduction in the end-bearing capacity is found to be in range between 18-25% in medium dense sand and between 17-23% in very dense sand.
8. With the proposed predictive equations, it is feasible to determine the ultimate bearing capacity of the bucket foundation of any geometry and its settlement under superstructure load.

6.2.2 Lateral Load-Response of Monopod Bucket Foundations

1. For both sand types, for a given loading height and superstructure load, the ultimate lateral capacity is observed to increase with increasing value of either bucket diameter or

skirt length. The ultimate lateral capacity is also noted to increase considerably with superstructure load. Moreover, it can be noted that in very dense sand, the ultimate lateral load and moment capacities are higher than those in medium dense sand.

2. In both sand types, for a given bucket geometry and loading height, the lid rotation at failure is noted to decrease with superstructure load. In most of the cases, the lid rotation at failure is noted to be higher for a bucket foundation embedded in very dense sand as compared to medium dense sand.
3. The ultimate lateral capacities of all the bucket foundations are noted to increase with skirt length and diameter. Increasing bucket diameter showed greater influence on the ultimate lateral capacity as compared to skirt length. Moreover, the ultimate lateral capacity is noted to increase with superstructure load in almost a linear manner. The influence of superstructure load on ultimate lateral capacity keeps on decreasing with an increase in bucket skirt length.
4. For a given bucket geometry and superstructure load, the depth of point of rotation is noted to move upward with increasing loading height. The response remains similar for all the bucket geometries and superstructure loads in both sand types. In most of the cases, for a given bucket geometry under any superstructure load and loading height, the depth of point of rotation is found to be located at higher depth in medium dense sand as compared to very dense sand.
5. The initial stiffness is noted to be lesser with a smaller aspect ratio, and it also reduces nonlinearly with increasing loading height from 0 to 100 m. The initial stiffness is always greater in very dense sand for the same aspect ratio and loading height. For the same bucket geometry, the initial stiffness is noted to be greater under higher superstructure load, reduces nonlinearly with increasing loading height, and is always greater in the denser sand.

6. Combinations of lateral load and overturning moment capacity at various loading heights have been represented graphically for serviceability limit state (SLS), fatigue limit state (FLS), worst expected transient load limit state, and ultimate limit state (ULS).
7. Predictive expressions have been proposed for the depth of point of rotation, initial stiffness, ultimate lateral capacity and allowable capacity of bucket foundations in medium and very dense sands.

6.2.3 Future Scope

The current numerical study has been primarily concerned with the static response of monopod bucket foundation under vertical compressive and lateral loading in medium dense and very dense sandy seabed. Further works could be carried by considering the effect of self-weight and suction installation on static response of monopod bucket foundation in prototype scale, under vertical and lateral loads, in sands and clays. Further, the study can be extended to explore the cyclic response of these foundations. Under these static and cyclic loading conditions, monopod bucket foundations can be analyzed in layered soil profiles.

Appendix A

MODELLING OF SOIL NON-LINEARITY

A.1 ELEMENT TEST FOR MATERIAL NONLINEARITY

In general, as soil is neither isotropic nor homogeneous, its behaviour is non-uniform throughout a soil mass. Kondner (1963) proposed the existence of a hyperbolic relationship between strain and stress in soils. Experimental studies of Janbu (1963) indicated the influence of confining stress on the initial modulus of elasticity. Duncan and Chang (1970) extended the hyperbolic model and proposed parameters for use in the finite element analysis method.

The parameters of the model can be determined from conventional laboratory drained triaxial shear tests performed for the determination of the shear strength parameters. In the first step, the test results are plotted in terms of deviator stress versus axial strain, as shown in Figure A.1, where σ_3 is the minor principal stress or confining pressure, σ_1 is major principal stress and ε is the axial strain. The initial elastic modulus (E_i) is the slope of the tangent line drawn from origin.

In the second step, the test results for several confining pressure are plotted in terms of σ_3 versus logarithm of E_i, as shown in Figure A.2. In the third step, a straight line is fitted to the data points. The values of the non-linear soil strength parameters, κ and λ, are respectively the intercept and the slope of this straight line.

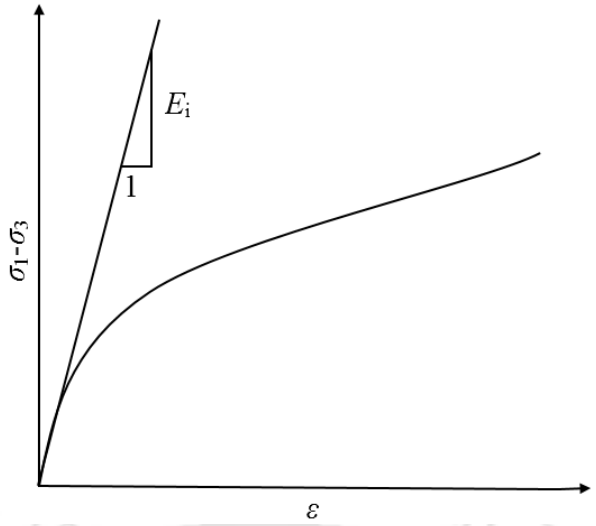

Figure A.1 Plot of σ_1-σ_3 versus ε obtained from drained triaxial test

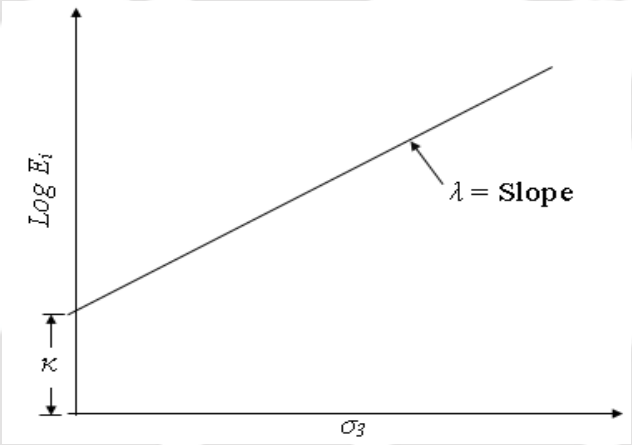

Figure A.2 Plot of σ_3 versus E_i in logarithmic scale

Accordingly, in this numerical study, in order to simulate the non-linear behaviour of sands realistically under drained condition, the relationship between modulus of elasticity of soil (E_{soil}) of any element within the domain and the mean principal stress (σ_m), has been implemented as follows:

$$E_{soil} = \kappa.\sigma_{at}.\left(\frac{\sigma_m}{\sigma_{at}}\right)^{\lambda} \qquad \text{(A.1)}$$

where, σ_{at} = 100 kN/m^2 is reference stress, κ is the soil stiffness at the reference stress state, λ is the strength parameter determining the variation of soil stiffness with the mean

principal stress. The values of κ and λ for sandy soils considered in the present study have been obtained from EAU (2004).

For the simulation of non-linear behaviour of the sandy soil in Abaqus, a user defined subroutine is introduced, in which the modulus of elasticity is updated depending on the mean principal stress as a result of the vertical and lateral loads acting on the bucket foundation. The subroutine has been tested considering a single 8 node brick element with reduced integration (*C3D8R*) subjected to hydrostatic loading condition, as shown in the Figure A.3. Boundary conditions constraining normal displacement are applied on three faces of the element. Compressive displacement-controlled load is then applied on the remaining opposite three faces of the element.

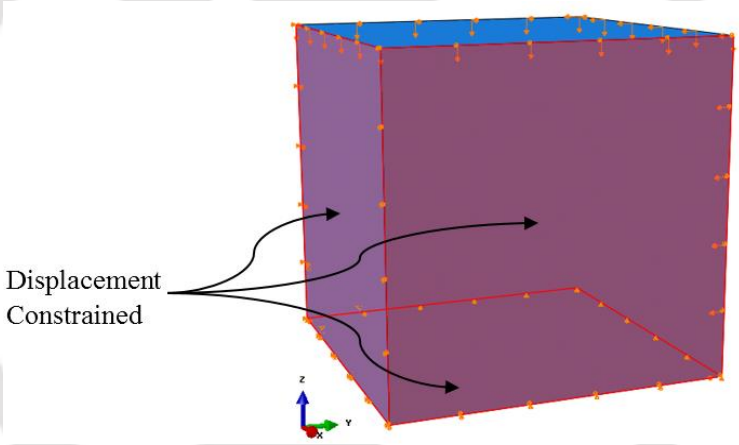

Figure A.3 Hydrostatic test considering a single element (*C3D8R*)

The modulus of elasticity values, calculated from different mean stresses using Equation (A.1) and used as input parameters, are presented in Table A.1. In other words, the modulus of elasticity (E_{soil}) is made to be dependent on the mean stress (σ_m). The values of mass density, κ and λ used for verification of the subroutine program are 1100 kg/m^3, 600 and 0.55, respectively.

Table A.1 Mean stress and corresponding modulus of elasticity used in *Abaqus*

Sl. no.	Mean stress (Pa)	E_{soil} (Pa)
	SDV2	SDV1
1	0.01	8475.23
2	2	156213
3	4	228710
4	6	285848
5	8	334850
6	10	378574
7	12	418505
8	14	455535

When the execution of program starts, in the first iteration of a load increment, the subroutine is called twice. During the first call, the initial stiffness matrix is formed using the configuration of the model at the start of the increment. During the second call, a new stiffness matrix based on the updated configuration of the model, is created. In subsequent iterations, the subroutine is called only once, and the corrections to the model's configuration are calculated using the stiffness matrix from the end of the previous iteration.

In this program, for all the calls of the subroutine, the stresses taken from the material points are used to calculate the mean stress, which is then saved as the value of field variable on which E_{soil} is dependent on. Corresponding to this mean stress value, the program calculates the value of modulus of elasticity from the material property deck (Table A.1), which would then be used for stress calculation in the next increment.

As shown in Figure A.4(a)-(c), input values of 4, 8 and 14 Pa for the mean stress (SDV2) give the corresponding output values of 2,28,710 Pa, 3,34,850 Pa and 4,55,535 Pa for the modulus of elasticity (SDV1). The output obtained from the visualization module of Abaqus indicates that the subroutine can effectively simulate the variation of modulus of elasticity with mean stress.

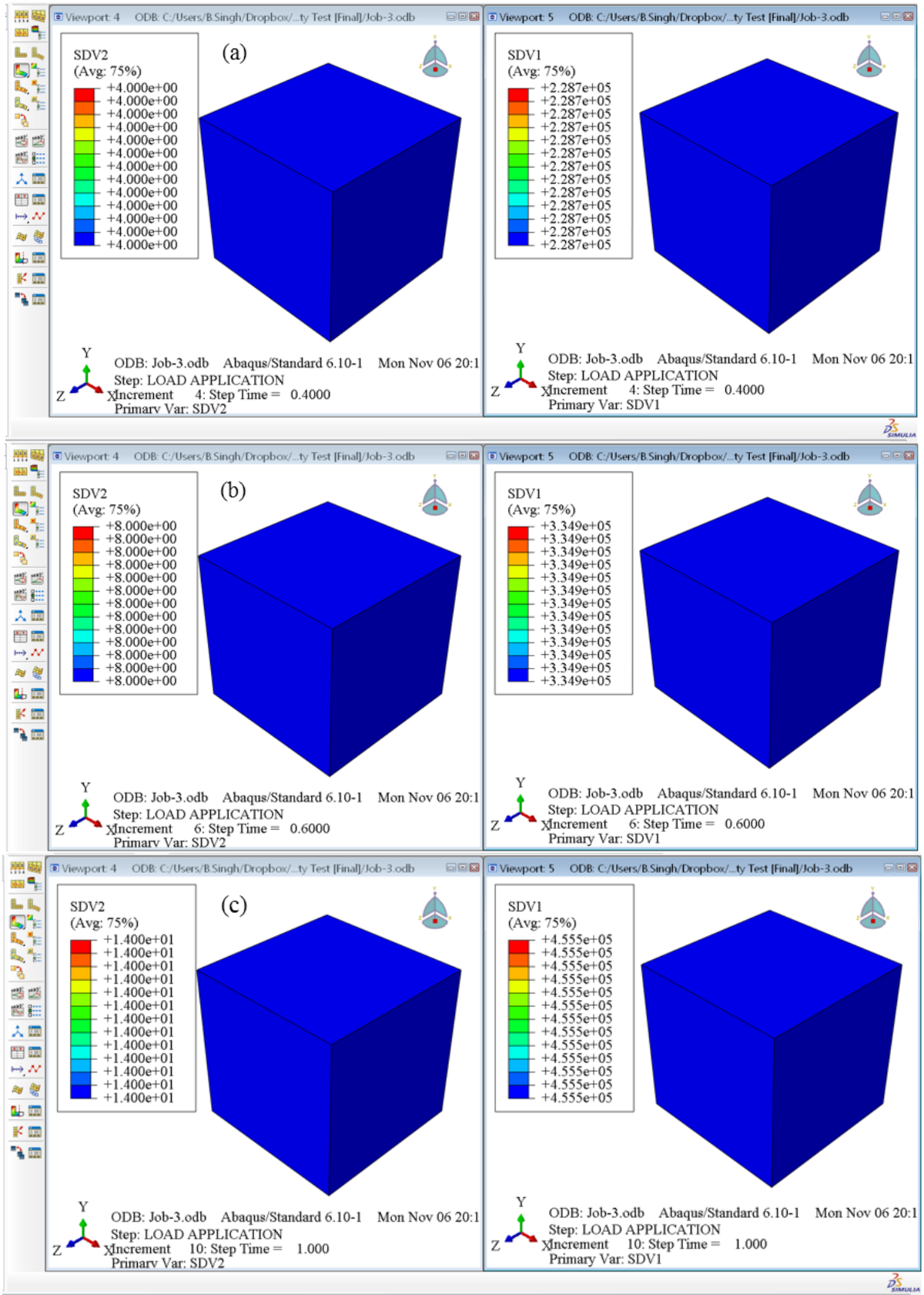

Figure A.4 Element test to check the variation of modulus of elasticity with mean stress of (a) 4 Pa; (b) 8 Pa, and; (c) 14 Pa

A.2 SUBROUTINE CODE

```
      subroutine usdfld (field, statev, pnewdt, direct, t, celent,
     1 time, dtime, cmname, orname, nfield, nstatv, noel, npt, layer,
     2 kspt, kstep, kinc, ndi, nshr, coord, jmac, jmatyp, matlayo,
     3 laccfla)
      include 'aba_param.inc'
      character*80 cmname, orname
      character*3 flgray (15)
      dimension field(nfield), statev (nstatv), direct (3,3),
     1 t (3,3), time (2)
      dimension array (15), jarray (15), jmac (*), jmatyp (*),
     1 coord (*)
c     ----------------------------------------------------------------------
c     USER CODE START
c     do it only for specific material
      if (cmname = = 'SOIL') then
c       get principal stresses
        call GETVRM ('SP', array, jarray, flgray, jrcd, jmac, jmatyp, matlayo, laccfla)
c       test result of GETVRM
        if (jrcd = = 1) then
          ! write error to dat file
          Write (6,*) "GETVRM routine error!!!"
          call XIT ! stop abaqus
        endif
        SP1 = array (1) ! assign min. principal stress
```

```
      SP2 = array (2) ! assign mid. principal stress
      SP3 = array (3) ! assign max. principal stress
      Mean_stress = (array (1) + array (2) + array (3)) / 3
c     Calculate the modulus of elasticity
      field (1) = Mean_stress
            E = 600.d0*100.d3*(abs(Mean_stress/100.d3))**0.55e0
      statev(1) = E !Save the value of E
      statev (2) = abs(Mean_stress)
c       statev (3) = SP1
c       statev (4) = SP2
c       statev (5) = SP3
        statev (3) = array (1)! assign min. principal stress
        statev (4) = array (2)! assign mid. principal stress
        statev (5) = array (3)! assign max. principal stress
              end if
c   USER CODE END
c   ----------------------------------------------------------------------
    return
    end
```

Appendix B

DOMAIN SIZE AND MESH CONVERGENCE ANALYSIS

B.1 INTRODUCTION

This appendix presents the basis for determining the diameter and depth of soil domain as well as the number of finite elements required to discretize the soil domain and the foundation, in order to get reasonably accurate results from the numerical simulations.

The domain analysis is necessary for deciding the minimum vertical depth and lateral width of the seabed to be modeled, which would not have any boundary effect on the vertical and lateral response of the bucket foundation.

Separate domain analyses are necessary for the foundation under only vertical loading and only lateral loading. For the domain analysis under vertical loading, embedded solid foundations has been used instead of bucket foundations, in order to reduce the computational time. Once the soil domain dimensions are fixed, mesh convergence study is carried out to determine the optimum number of elements necessary to represent the soil domain. Similar steps have been followed for the domain analysis under lateral loading, using a bucket foundation.

B.2 VERTICAL BEARING CAPACITY

B.2.1 Domain Analysis Study

The domain analysis of the embedded solid foundation in very dense sandy soil has been carried out by means of several trials. Initially, the lateral extent of the soil domain is to be selected such that the domain boundary does not have any influence on the vertical load carrying behaviour of the foundation.

From the trials, the lateral extent of the soil domain has been determined to be 9 times the diameter of the foundation (9*D*). Thereafter, the vertical extent is to be fixed.

Figure B.1(a) shows the vertical stress contours of the embedded solid foundation (*D* = 12 m, *L* = 12 m) in soil domain of 108 m diameter (9*D*) and length of 36 m (3*L*). As shown in Figures B.1(b) to B.1(e), the soil domain depth has been increased gradually to 4*L*, 6*L*,8*L* and 10*L*.

In Figures B.1(a) and B.1(b), the vertical stress contour diagrams indicate that the soil domain depth is insufficient to capture the complete stress variation. In contrast, from the vertical stress contour diagrams of Figures B.1(c) to B.1(e), it can be noted that the soil domain depths of 6*L*, 8*L* and 10*L* are sufficient for simulating the bearing capacity of embedded solid foundation under vertical load. The values of ultimate vertical capacity for the three geometries of embedded solid foundation in varying soil domain sizes are presented separately in Tables B.1-B.3.

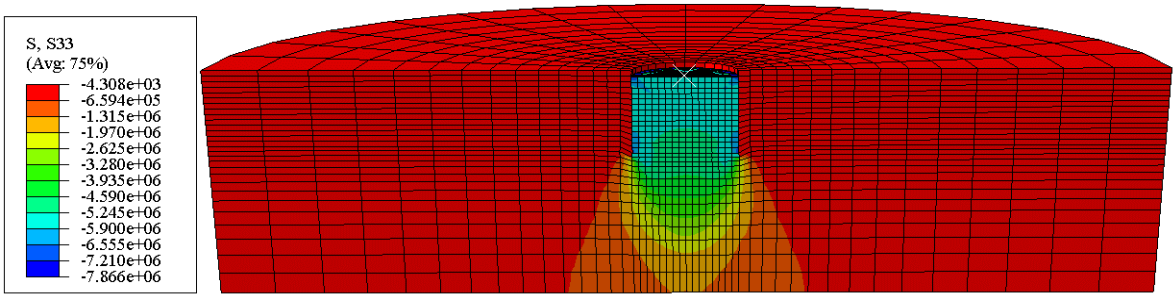

(a)

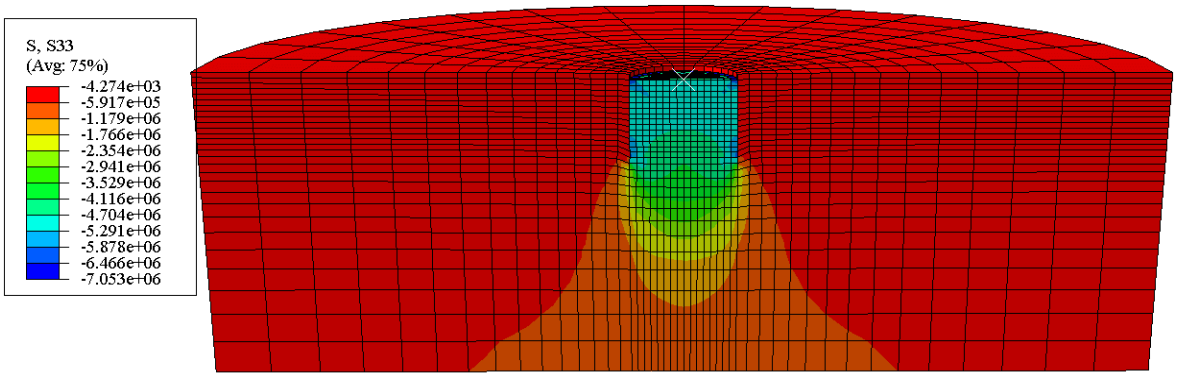

(b)

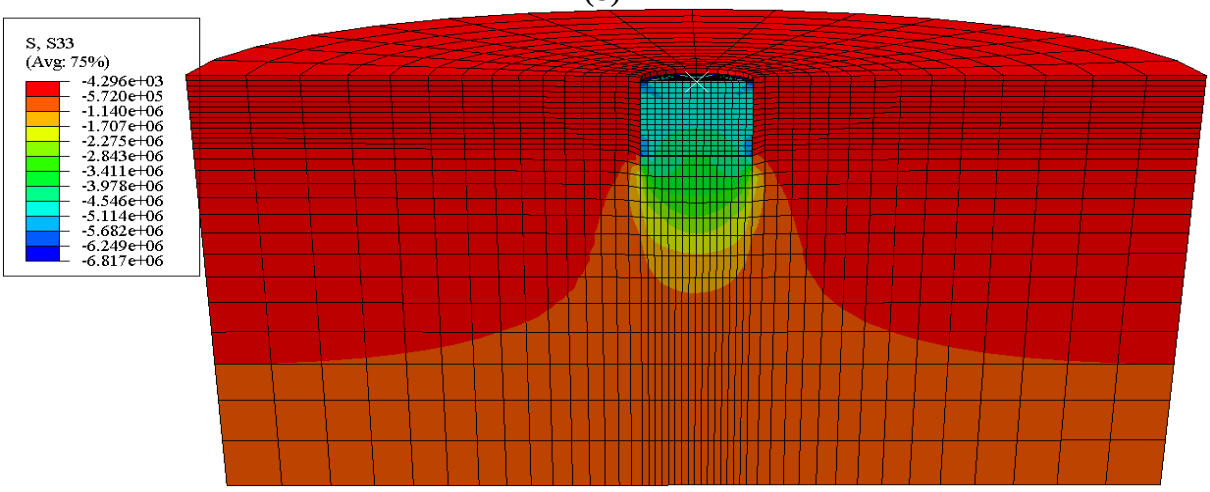

(c)

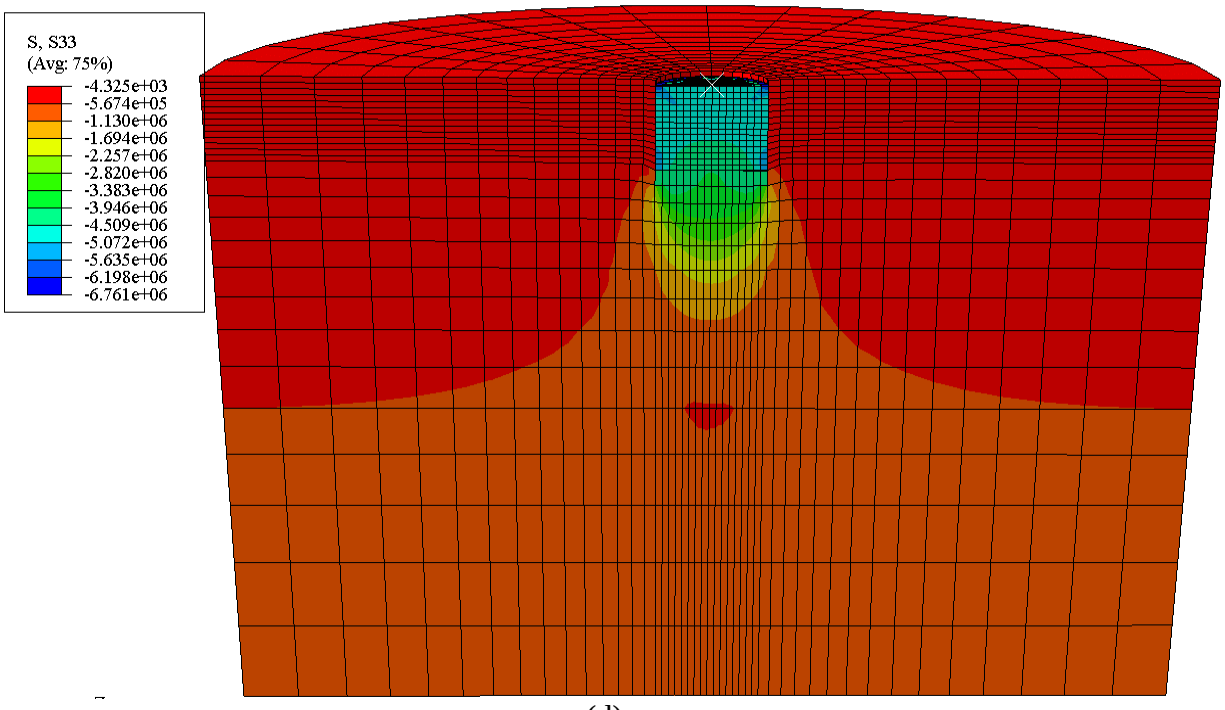

(d)

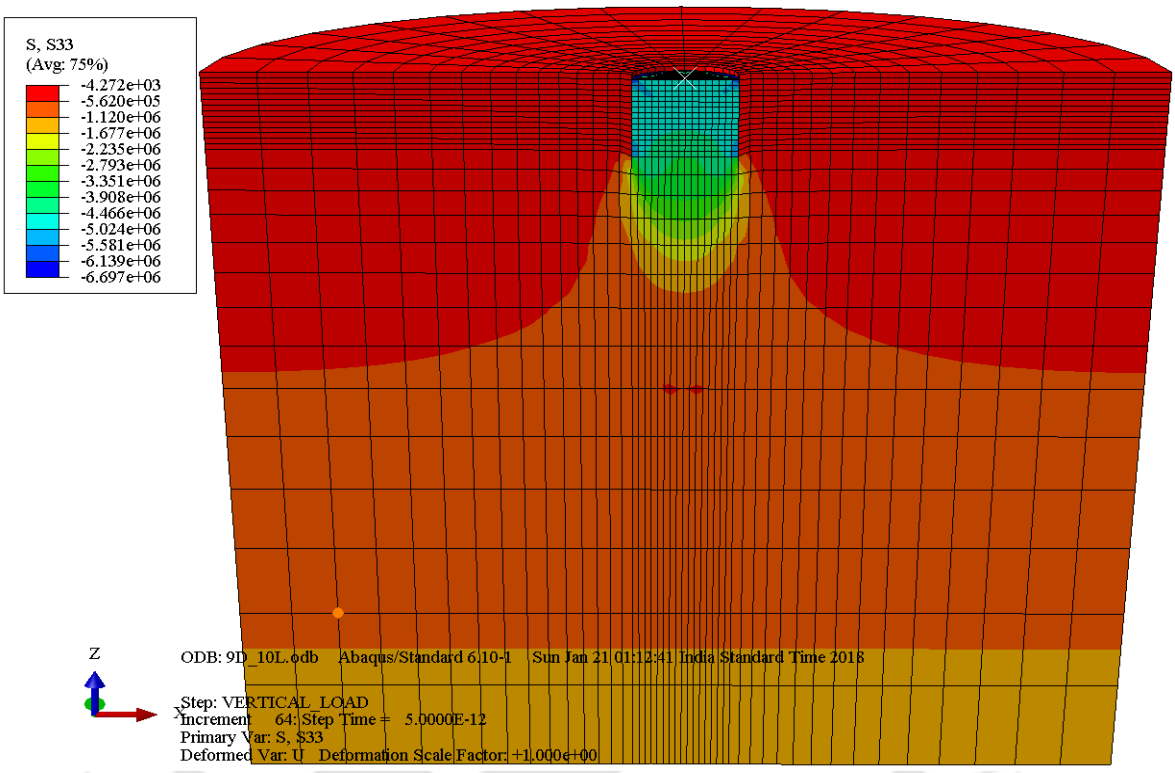

(e)

Figure B.1 Vertical stress contour diagrams at failure of embedded solid foundation (D = 12 m & L = 12 m) in soil domain of 9D diameter and varying depths: (a) 3L; (b) 4L; (c) 6L; (d) 8L; (e) 10L

Table B.1 Ultimate vertical capacity of embedded solid foundation (D = 12 m & L = 12 m) in varying soil domain sizes

Sl. No.	Domain geometry		Ultimate vertical capacity (MN)	Decrease of capacity (MN)	% decrease of capacity
	Diameter (m)	Depth (m)			
1.	9D	3L	655.51	-	-
2.	9D	4L	590.26	65.26	9.95
3.	9D	6L	571.54	18.72	3.17
4.	9D	8L	567.28	4.26	0.75
5.	9D	10L	562.11	5.17	0.91

Table B.2 Ultimate vertical capacity of embedded solid foundation (D = 15 m & L = 15 m) in varying soil domain sizes

Sl. No.	Domain geometry		Ultimate vertical capacity (MN)	Decrease of capacity (MN)	% decrease of capacity
	Diameter (m)	Depth (m)			
1.	9D	3L	1,070.66	-	-
2.	9D	4L	972.58	98.08	9.16
3.	9D	6L	941.29	31.29	3.22
4.	9D	8L	937.48	3.81	0.40
5.	9D	10L	928.04	9.44	1.01

Table B.3 Ultimate vertical capacity of embedded solid foundation (D = 18 m & L = 18 m) in varying soil domain sizes

Sl. No.	Domain geometry		Ultimate vertical capacity (MN)	Decrease of capacity (MN)	% decrease of capacity
	Diameter (m)	Depth (m)			
1.	9D	3L	1601.29	-	-
2.	9D	4L	1457.32	143.97	8.99
3.	9D	6L	1422.73	34.59	2.37
4.	9D	8L	1409.34	13.39	0.94
5.	9D	10L	1397.83	11.51	0.82

The vertical load applied at the top of the embedded solid foundation (D = 12 m & L = 12 m) and its corresponding settlement till failure has been plotted for several soil domains in Figure B.2(a).

For all the domain boundaries, the load was applied up to a settlement equal to 10% of foundation diameter, which is considered as the failure condition in this study. From the figure, it can be noted that the vertical load at failure reduces with increasing value of domain depth. For an embedded solid foundation of 12 m diameter and aspect ratio of 1, the ultimate vertical capacity decreases substantially from 9.95% to 3.17% (Table B.1) as the soil domain depth is increased from 3L to 4L and 6L, for a constant domain diameter of 9D. Beyond the domain depth of 6L, the percentage reduction in vertical capacity becomes insignificant (<1% approx.). Therefore, keeping the computational cost into consideration, the soil domain

diameter of 9*D* and depth of 8*L* have been selected to simulate the vertical bearing capacity of embedded solid foundation (*D* = 12 m & *L* = 12 m). The same domain dimensions have been kept unchanged for the analyses of the other embedded solid foundations with the same diameter (*D* = 12 m) and smaller lengths (*L* = 6 and 9 m).

Similarly, the domain analyses have also been carried out for embedded solid foundations with geometric details, *D* = 15 m & *L* = 15 m and *D* = 18 m & *L* = 18 m. The soil domain diameter is kept as 9*D* and the soil depth has been gradually increased from 3*L* to 10*L* in intervals. The vertical load versus settlement curves of these geometries for several domain dimensions are shown in Figures B.2(b) and B.2(c).

In the case of embedded solid foundation with *D* = 15 m & *L* = 15 m, for a soil domain diameter of 9*D*, the ultimate vertical capacity decreases to 9.16% and 3.22% as the depth of soil domain is increased from 3*L* to 4*L* and 6*L*, for the soil domain diameter of 9*D*, given in Table B.2. Furthermore, at failure, the vertical capacity decreases and remains within 1% with the increase of domain depth from 6*L* to 10*L*. Similarly, for *D* = 18 m & *L* = 18 m, for the diameter of soil domain of 9*D*, the ultimate vertical capacity decreases from 8.99% to 2.37%, as the depth of the soil domain is increased from 3*L* to 4*L* and 6*L*, presented in Table B.3. Further, at failure, the vertical capacity reduces insignificantly by 0.82% as the domain depth is increased from 8*L* to 10*L*. Hence, for both the foundation geometries of *D* = 15 m & *L* = 15 m and *D* = 18 m & *L* = 18 m, the domain depth of 8*L* is considered as appropriate to simulate the vertical response within reasonable accuracy. For the same diameters (*D* = 15 m and *D* = 18 m), the soil domain dimensions are kept fixed for smaller embedment lengths.

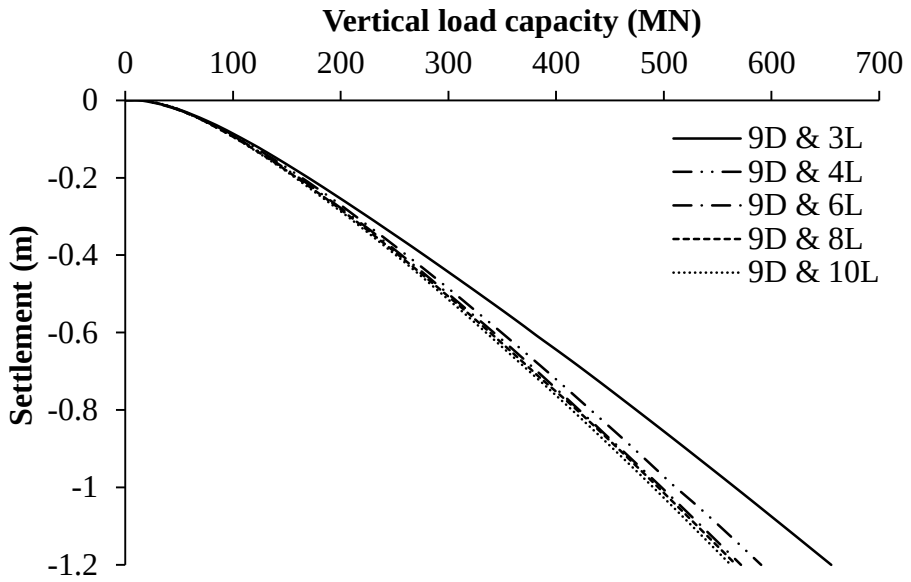

(a)

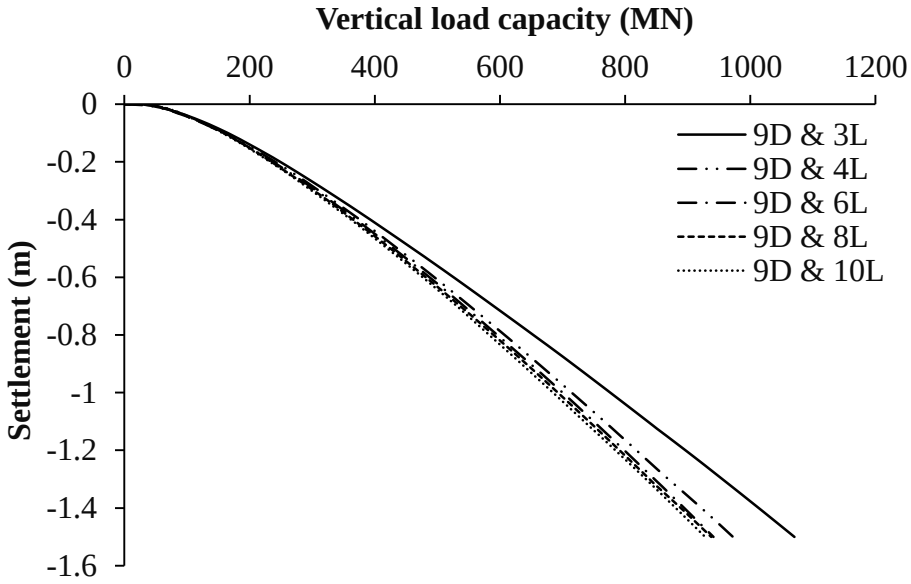

(b)

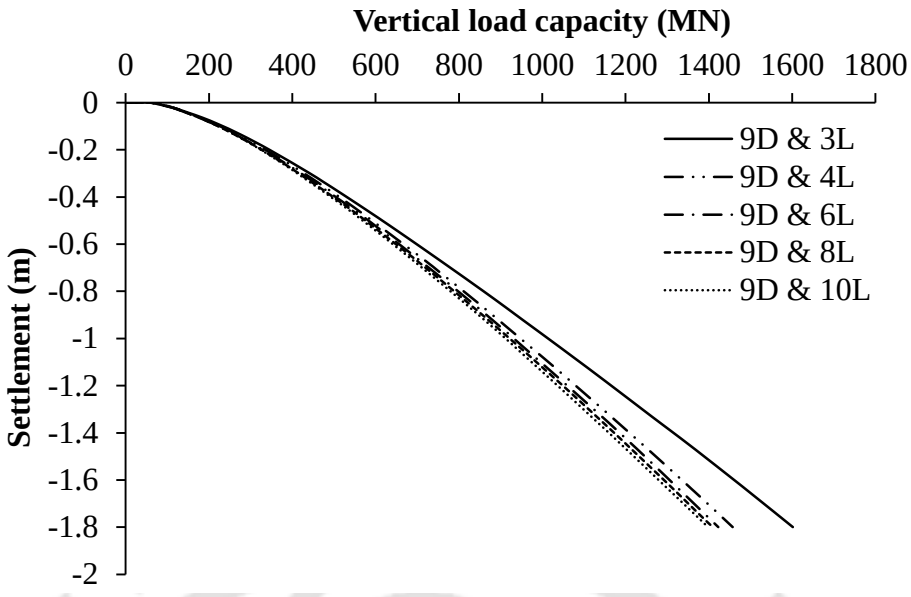

(c)

Figure B.2 Vertical load versus settlement plots for embedded solid foundations of varying geometries: (a) D = 12 m, L = 12 m; (b) D = 15 m, L = 15 m; and (c) D = 18 m, L = 18 m

Once the domain dimensions have been determined for several embedded solid foundation geometries in very dense sands, the same geometric details have also been utilized for medium dense sandy soil.

B.2.2 Mesh Convergence Study

This section presents the results of the mesh convergence study of embedded solid foundations in very dense sandy soil. In order to ensure sufficient accuracy of the results of numerical simulations, it becomes essential to discretize the soil domain with adequate numbers of elements. In general, a highly refined model with finer elements yields better results. However, finely meshed model demands longer time duration and more computational resource. Hence, mesh convergence study enables the determination of the optimum number of elements required to produce accurate results at reasonable computational time and resource.

The results of mesh convergence analyses are presented for embedded solid foundations of three diameters and aspect ratio of 1 (D = 12 m & L = 12 m, D = 15 m & L =

15 m, and D = 18 m & L = 18 m). The foundation and soil domain are discretized using first order brick elements with reduced integration scheme (*C*3*D*8*R*). The soil domain is meshed in such a way that the elements are finer in the vicinity of the interface between the foundation and soil, and the element sizes are gradually made coarser further away from the foundation. The various mesh configurations of solid foundation (D = 12 m & L = 12 m) embedded in the very dense sand domain are shown in Figures B.3(a) to B.3(f).

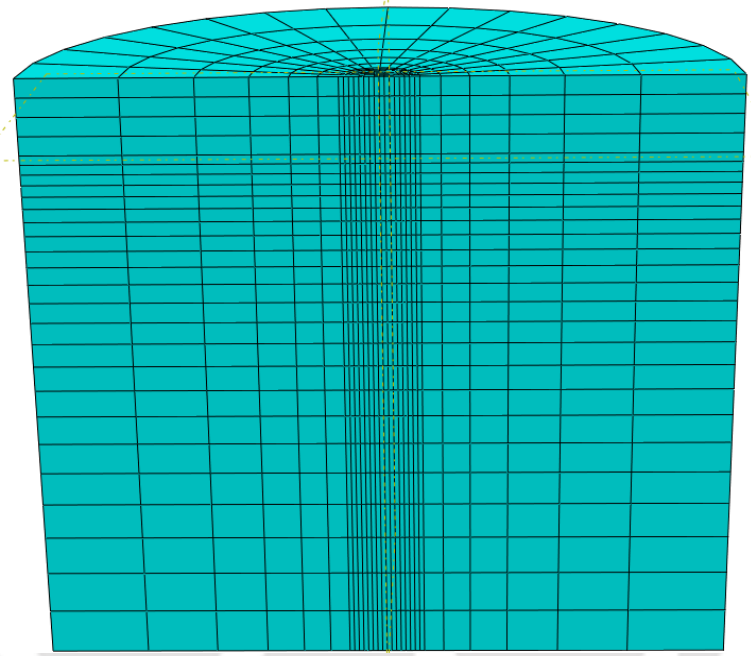

(a)

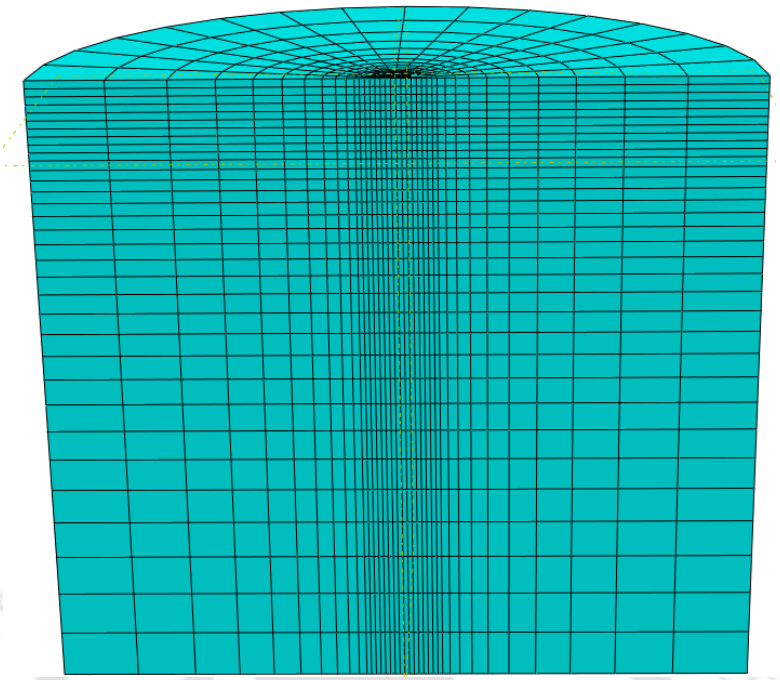

(b)

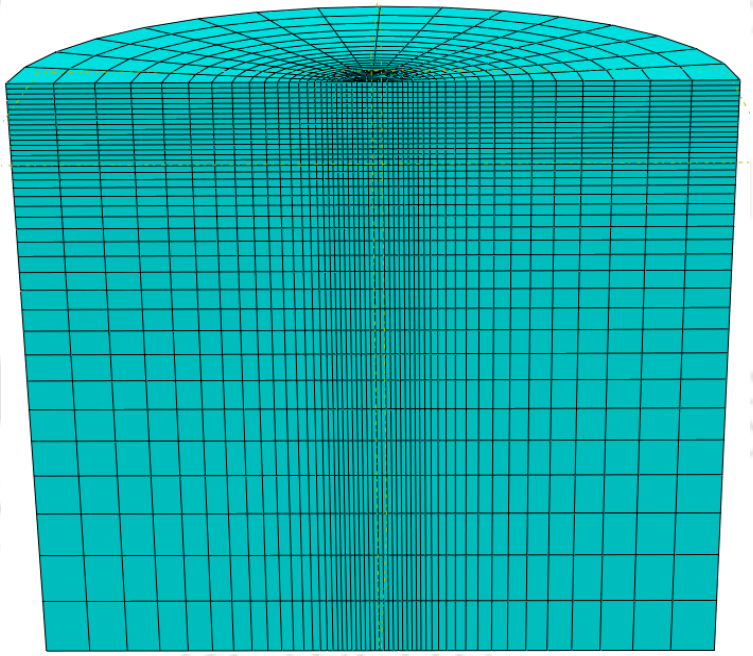

(c)

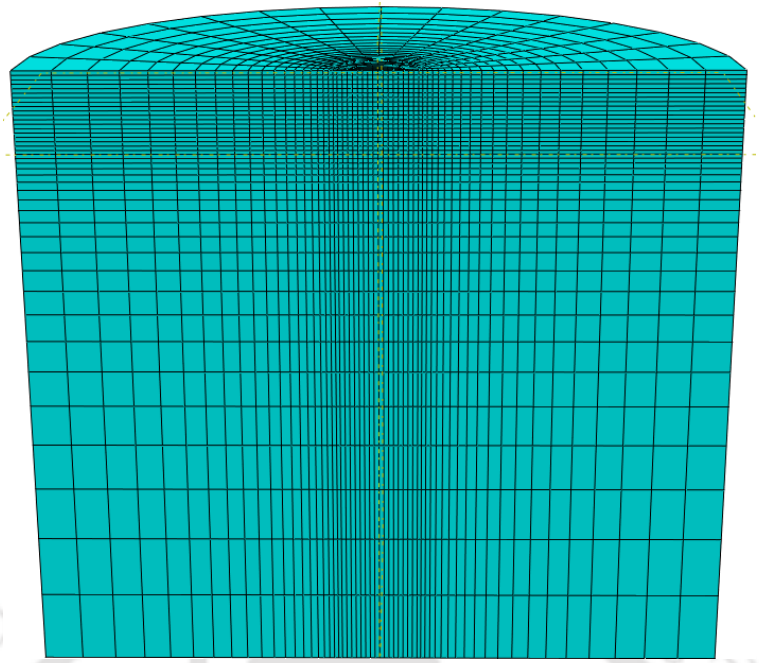

(d)

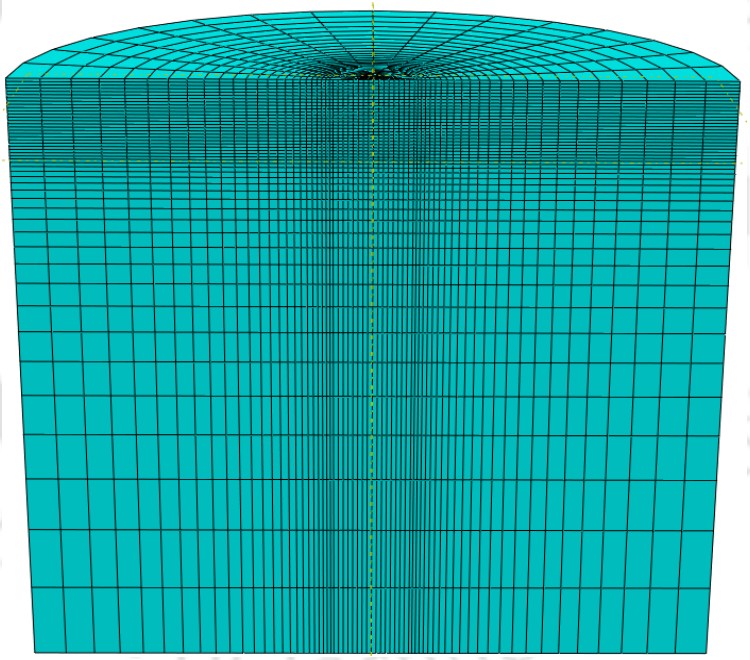

(e)

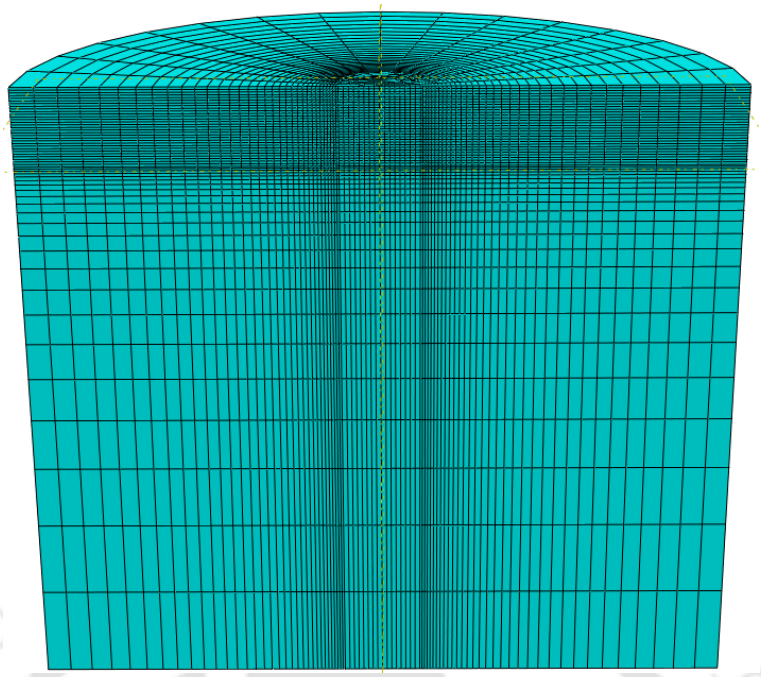

(f)

Figure B.3 Mesh configurations of soil domain for foundation size (D = 12 m & L= 12 m) and varying element numbers: (a) 5,184 elements; (b) 8,448 elements; (c) 13,984 elements; (d) 17,506 elements; (e) 22,560 elements; and (f) 33,072 elements

Based on the discretization of soil domain and the embedded foundation, simulations were carried out and the variation of vertical load versus settlement curves with number of elements are presented in Figures B.4(a), B.5(a) and B.6(a) for the three foundation diameters (D = 12, 15 and 18 m). From Figure B.4(a), the vertical capacity of the embedded solid foundation (D = 12 m & L = 12 m) is noted to decrease with increased mesh density.

The values of ultimate vertical capacity for the three geometries of embedded solid foundation (D = 12, 15 and 18 m) are presented separately in Tables B.4-B.6 for the same soil domain size (9D & 8L) with varying no. of elements.

The vertical capacity of embedded solid foundation of D = 12 m & L= 12 m, at failure is noted to be 600.57 MN, when the soil domain is discretized with 5,184 elements. Further, the ultimate vertical capacities are noted to reduce with increased number of elements used for the domain discretization. The vertical capacity is found to be 526.28 MN when a

maximum of 33,072 numbers of elements is used in the convergence study, presented in Table B.4.

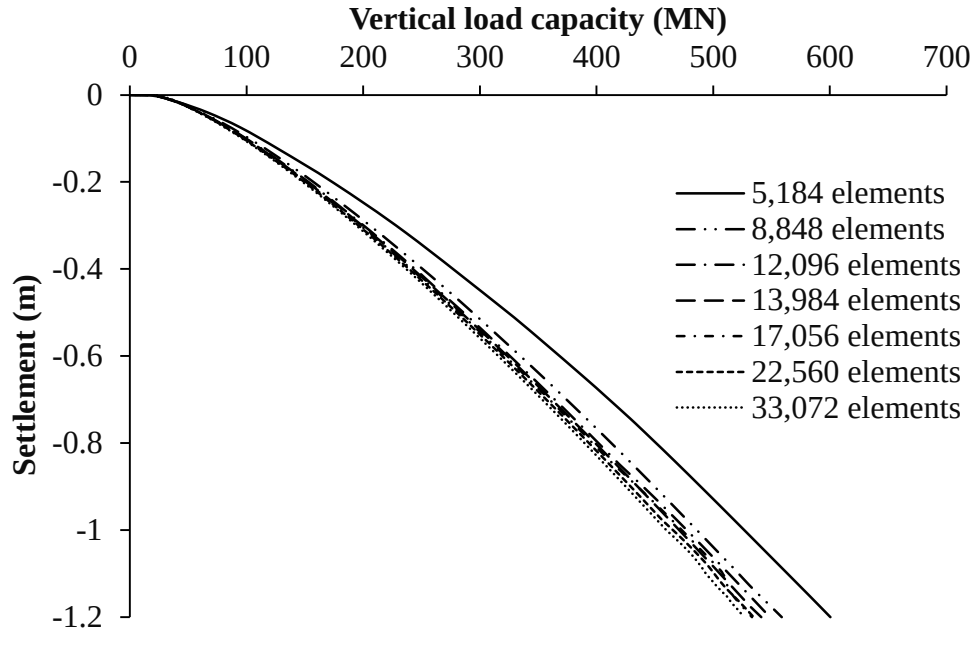

(a)

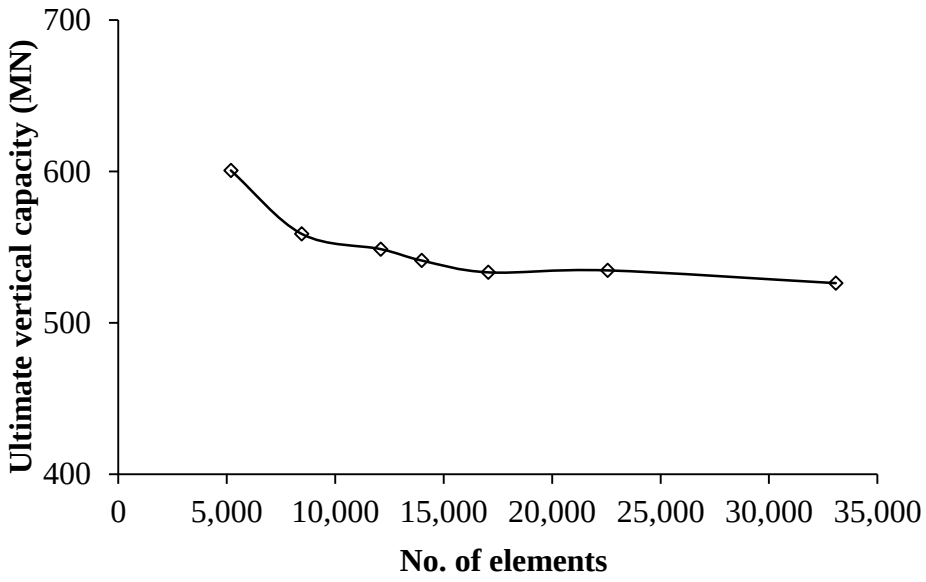

(b)

Figure B.4 Mesh convergence analysis for embedded solid foundation (D = 12 m, L = 12 m): (a) Plots of vertical load versus settlement; and (b) Plot of ultimate vertical capacity versus no. of elements

Table B.4 Ultimate vertical capacity of embedded solid foundation (D = 12 m & L = 12 m) in soil domain size (9D & 8L) with varying no. of elements

Sl. No.	No. of elements	Ultimate vertical capacity (MN)	Decrease of capacity (MN)	% decrease of capacity
1.	5,184	600.57	-	-
2.	8,448	558.77	41.8	6.96
3.	13,984	541.19	17.58	3.15
4.	17,506	533.39	7.80	1.44
5.	22,560	534.69	-1.30	-0.24
6.	33,072	526.28	8.41	1.57

For embedded solid foundation of D = 12 m & L = 12 m, based on the convergence study, a plot of the variation of ultimate vertical capacity versus the number of elements used for discretizing the soil domain is presented Figure B.4(b). From the figure, the percentage by which the vertical capacity decreases is noted to reduce with the increased number of soil elements. From Table B.4, the ultimate vertical capacity decreases to 6.96% as the soil elements are increased from 5,184 to 8,448. The maximum reduction of the ultimate vertical capacity remains within 2% as the number of elements is increased to 33,072. Based on this trend, approximately 17,000 elements can be used to discretize the soil domain for embedded solid foundation of D = 12 m & L = 12 m. The same number of elements can be kept constant for lower foundation aspect ratios with the same diameter (D = 12 m).

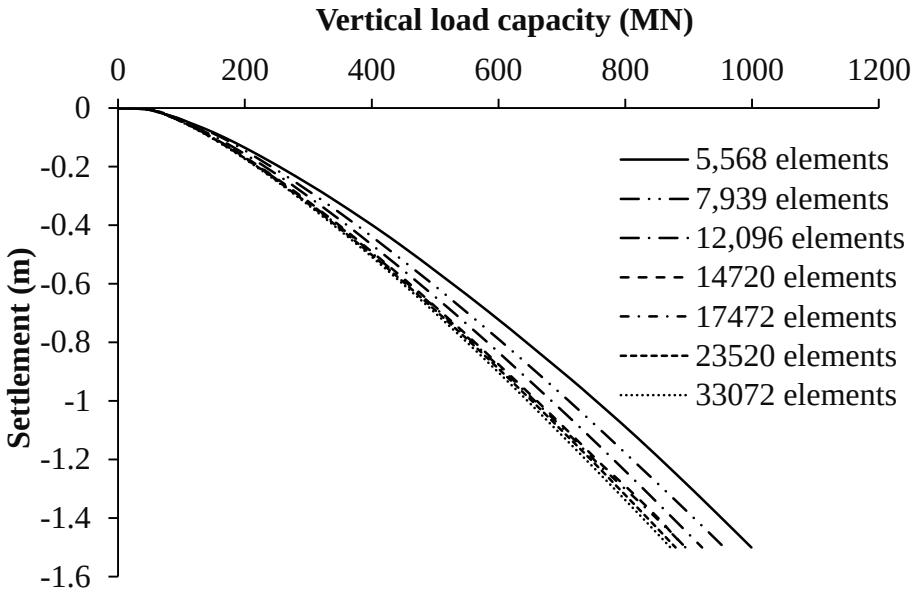

(a)

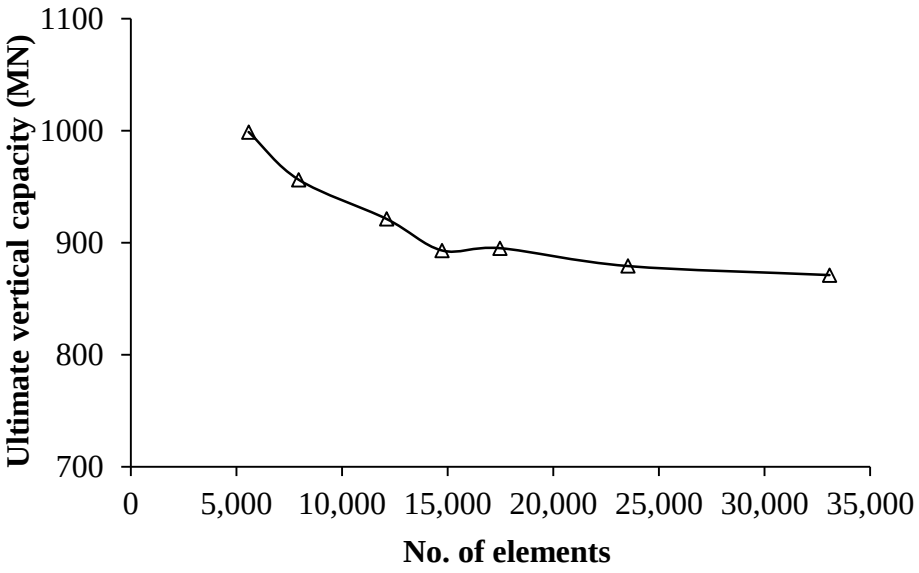

(b)

Figure B.5 Mesh convergence analysis for embedded solid foundation (D = 15 m, L = 15 m): (a) Plots of vertical load versus settlement; and (b) Plot of ultimate vertical capacity versus no. of elements

The results of similar convergence analysis are presented in Figure B.5 and Figure B.6, respectively for the other foundation geometries of D = 15 m & L = 15 m and D = 18 m & L = 18 m.

Table B.5 Ultimate vertical capacity of embedded solid foundation (D = 15 m & L = 15 m) in soil domain size (9D & 8L) with varying no. of elements

Sl. No.	No. of elements	Ultimate vertical capacity (MN)	Decrease of capacity (MN)	% decrease of capacity
1.	5,568	998.86	-	-
2.	7,939	956.29	42.57	4.26
3.	12,096	921.33	34.96	3.65
4.	14,720	893.19	28.14	3.05
5.	17,472	895.21	-2.02	-0.23
6.	23,520	879.27	15.94	1.78
7.	33,072	871.24	8.03	0.91

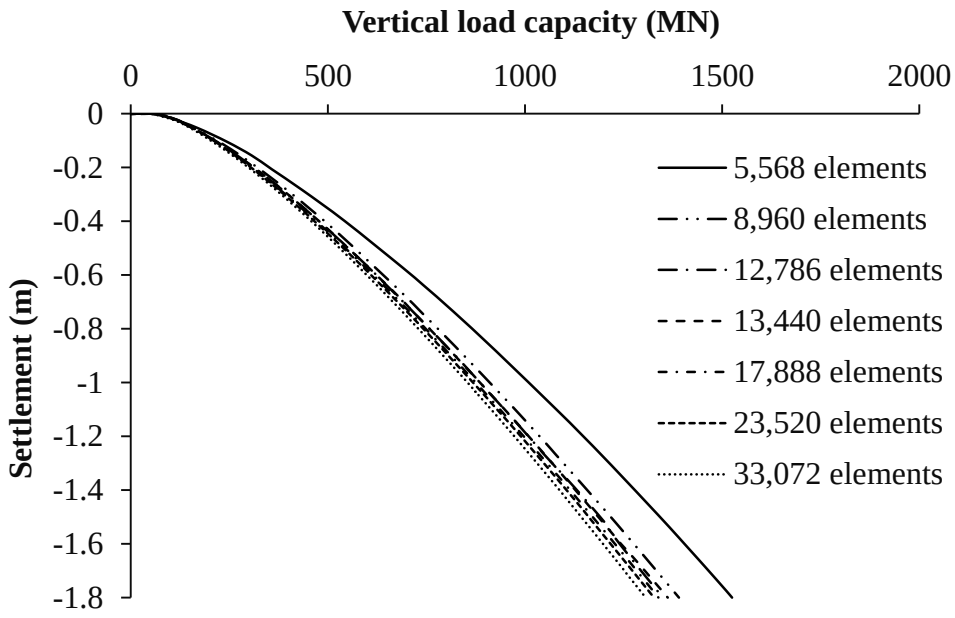

(a)

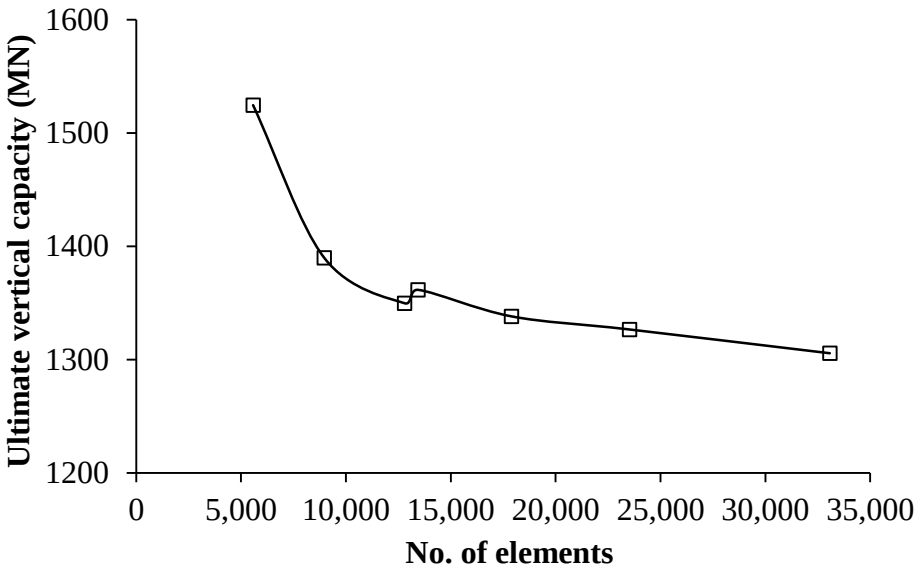

(b)

Figure B.6 Mesh convergence analysis for embedded solid foundation (D = 18 m, L = 18 m): (a) Plots of vertical load versus settlement; and (b) Plot of ultimate vertical capacity versus no. of elements

Table B.6 Ultimate vertical capacity of embedded solid foundation (D = 18 m & L = 18 m) in soil domain size (9D & 8L) with varying no. of elements

Sl. No.	No. of elements	Ultimate vertical capacity (MN)	Decrease of capacity (MN)	% decrease of capacity
1.	5,568	1524.46	-	-
2.	8,960	1389.78	134.68	8.83
3.	12,786	1349.70	40.08	2.88
4.	13,440	1361.46	-11.76	-0.87
5.	17,888	1338.10	23.36	1.71
6.	23,520	1326.52	11.58	0.86
7.	33072	1305.54	20.98	1.58

In the case of embedded solid foundation of D = 15 m & L = 15 m, when the soil domain is discretized with 5,568 numbers of elements, the ultimate vertical capacity is obtained as 998.86 MN. The vertical capacity is found to be 871.24 MN, as the number of discretized elements are increased to 33,072 elements. Details of ultimate vertical capacity and percentage decrease in the capacity with increasing number of discretization elements are presented in Table B.5. Similarly, the variation ultimate vertical capacity and percentage

reduction in the capacity with increasing number of discretized numbers of soil elements are presented in Table B.6 for a solid embedded foundation of D = 18 m & L = 18 m. From the above tables, it can be noted that approximately 18,000 and 19,000 elements can be used to discretize the respective soil domains for solid foundations of 15 and 18 m diameter.

Once the number of elements required to represent the very dense sandy soil domain has been determined, the same mesh configurations have been adopted for respective diameters of embedded solid foundations in medium dense sandy bed.

B.3 LATERAL LOAD CARRYING CAPACITY

B.3.1 Domain Analysis Study

The domain analysis under lateral loading has been carried out using bucket foundations. For all the simulations, a superstructure load of 10 MN is considered and the lateral load is applied directly at the bucket lid (h = 0 m).

The domain analyses have been carried out for three geometries (D = 12 m & L = 12 m, D = 15 m & L = 15 m, and D = 18 m & L = 18 m). The soil domain dimensions are selected based on several trials. The basis of the trial is that the diameter and the depth of the soil domain should be large enough so that the lateral load carrying capacity of the bucket foundation remains unaffected. The initial lateral extent of the soil domain is taken as six times the foundation diameter (6D).

Based on the trials, the depth of soil domain has been fixed as 3L, as extending the domain depth beyond that has not contributed any significant difference in the lateral response of the foundations. The lateral extent of the soil domain is then increased gradually from 6D to 10D in intervals. For the bucket foundation of D = 12 m & L = 12 m, the corresponding lateral stress contours in the soil domain at failure of the bucket foundation are shown in Figures B.7(a) to B.7(d). In these figures, the lateral stress contours are seen to become horizontal near the domain boundary.

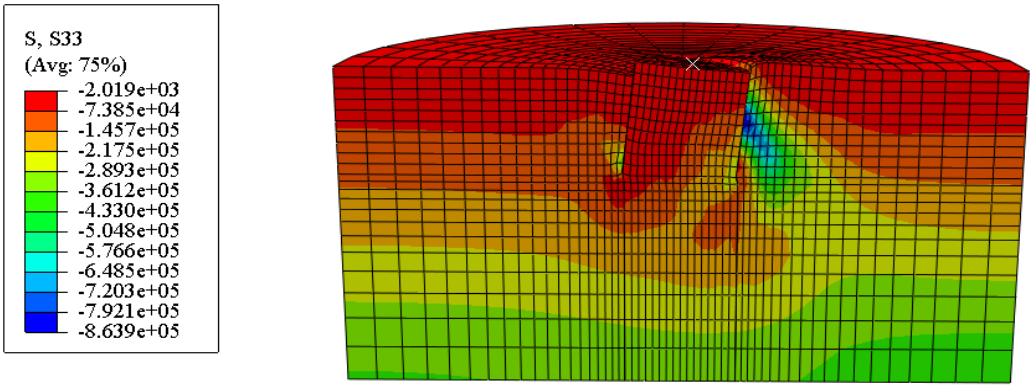

(a)

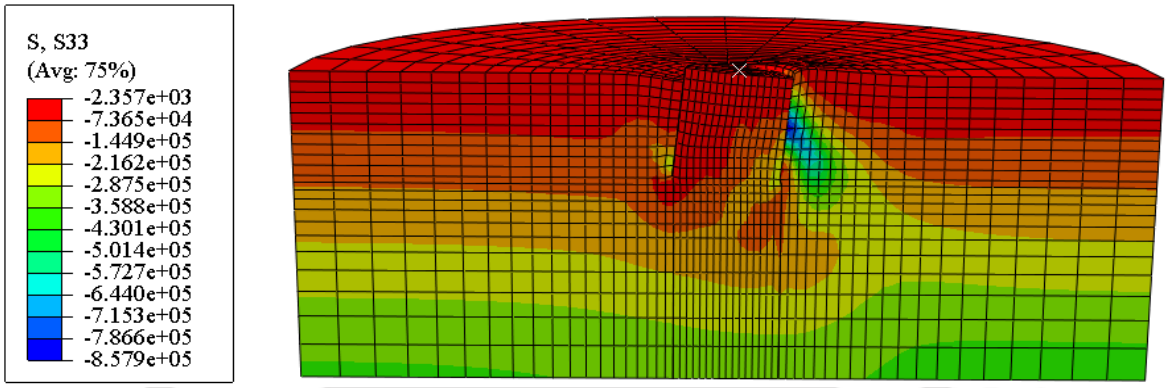

(b)

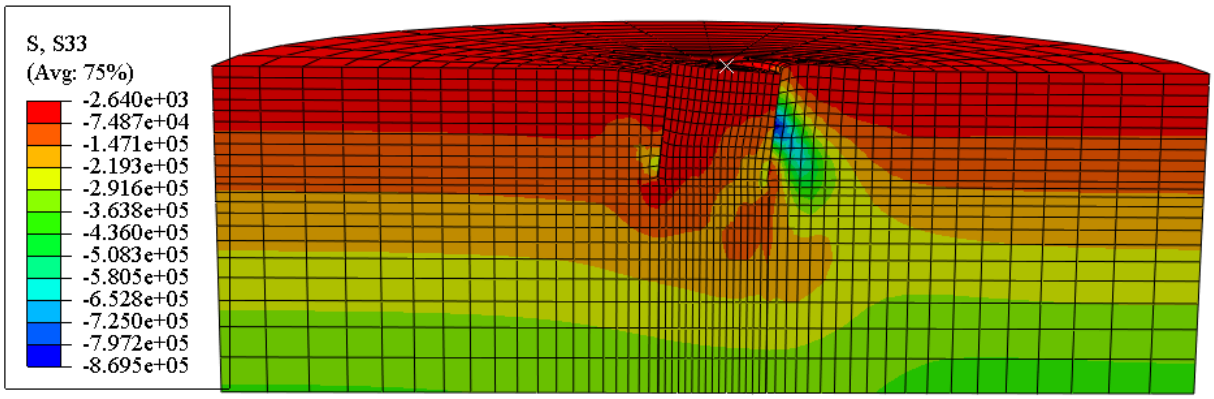

(c)

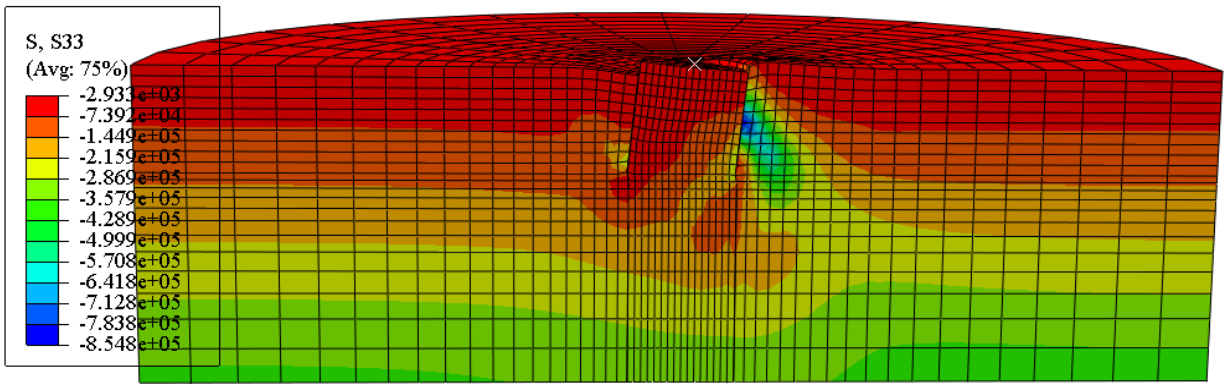

(d)

Figure B.7 Lateral stress contour diagrams under applied lateral load (h = 0 m) at failure of bucket foundation (D = 12 m & L = 12 m) in soil domain of 3L depth and varying diameters: (a) 6D; (b) 8D; (c) 9D; and (d) 10D

The values of ultimate lateral capacity for the three geometries of bucket foundation in varying soil domain sizes are presented separately in Tables B.7-B.9.

For the bucket foundation with D = 12 m and L = 12 m, the lateral capacity versus bucket lid lateral displacement response is plotted for several soil domain dimensions in Figure B.8(a). From the figure, the lateral capacity of bucket foundation at failure is noted to decrease from 62.38 to 60.87 MN for soil domain diameters of 6D and 8D, respectively. The lateral capacity further reduces to 60.32 MN as the domain diameter is further increased to 10D. The variation of lateral capacity soil with domain dimensions for a bucket foundation of D = 12m and L = 12 m are presented in Table B.7.

From Figures B.7(a) to B.7(d), the lateral stress contours become nearly horizontal at the near the domain boundary (9D diameter and 3L length) and beyond which, increase in domain diameter has negligible effect in the capacity. Hence, for this bucket geometry (D = 12 m & L = 12 m), the soil domain diameter of 9D and length of 3L are found to be adequate for carrying out further numerical analyses. The same domain dimensions are kept fixed for the remaining numerical analyses with smaller skirt lengths.

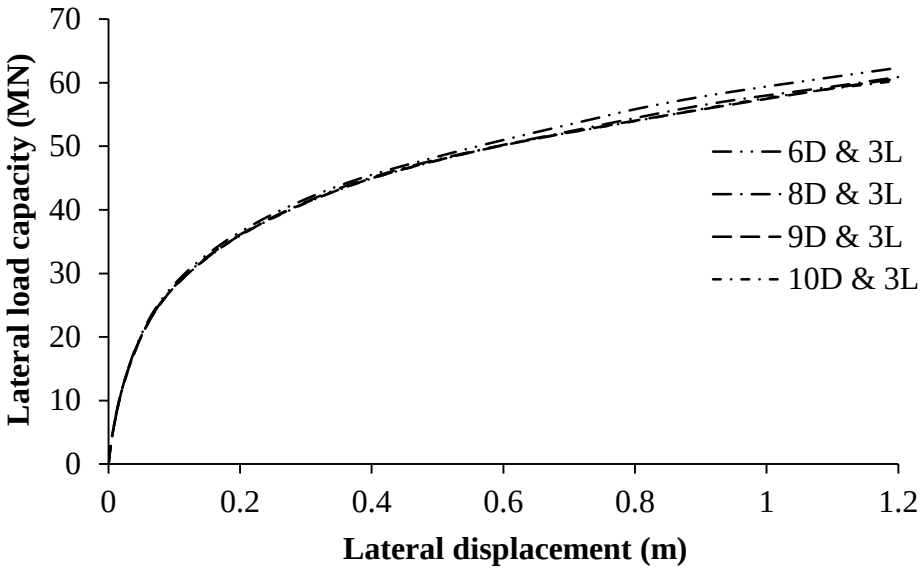

(a)

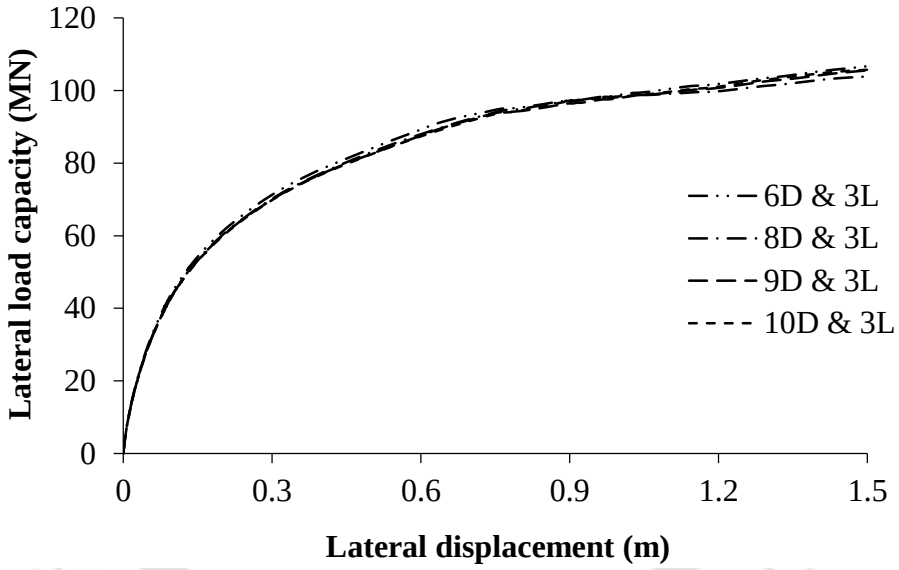

(b)

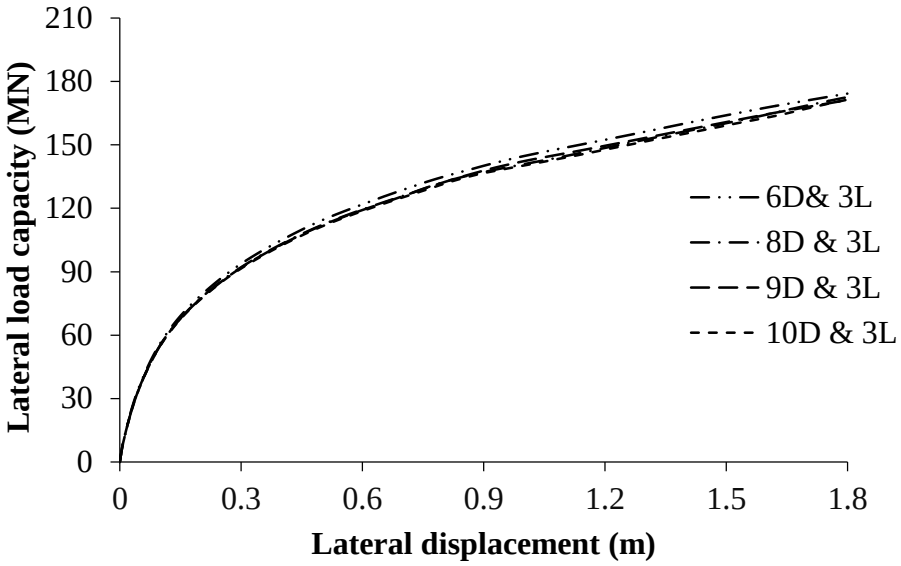

(c)

Figure B.8 Lateral load versus lid displacement plots for bucket foundations of varying geometries: (a) D = 12 m & L = 12 m; (b) D = 15 m & L = 15 m; and (c) D = 18 m & L = 18 m

Table B.7 Ultimate lateral capacity of bucket foundation (D = 12 m & L = 12 m) in varying soil domain sizes

Sl. No.	Domain geometry		Ultimate lateral capacity (MN)	Decrease of capacity (MN)	% decrease of capacity
	Diameter (m)	Depth (m)			
1.	6D	3L	62.38	-	-
2.	8D	3L	60.87	1.51	2.42
3.	9D	3L	60.67	0.21	0.34
4.	10D	3L	60.32	0.34	0.56

Table B.8 Ultimate lateral capacity of bucket foundation (D = 15 m & L = 15 m) in varying soil domain sizes

Sl. No.	Domain geometry		Ultimate lateral capacity (MN)	Decrease of capacity (MN)	% decrease of capacity
	Diameter (m)	Depth (m)			
1.	6D	3L	98.65	-	-
2.	8D	3L	97.61	1.04	1.05
3.	9D	3L	97.74	-0.14	-0.14
4.	10D	3L	98.69	-0.94	-0.97

Table B.9 Ultimate lateral capacity of bucket foundation (D = 18 m & L = 18 m) in varying soil domain sizes

Sl. No.	Domain geometry		Ultimate lateral capacity (MN)	Decrease of capacity (MN)	% decrease of capacity
	Diameter (m)	Depth (m)			
1.	6D	3L	174.34	-	-
2.	8D	3L	172.67	1.67	0.96
3.	9D	3L	171.19	1.48	0.86
4.	10D	3L	171.36	-0.17	-0.10

The plots of similar domain analysis are presented in Figures B.8(b) and B.8(c), respectively for the other foundation geometries of D = 15 m & L = 15 m and D = 18 m & L = 18 m. Tables B.8 and B.9 show the variation of lateral capacity with domain dimensions are presented for D = 15 m & L = 15 m and D = 18 m & L = 18 m. It is observed that for these two geometries also, the soil domain diameter and depth of 9D and 3L can be considered to be adequate. Once the domain dimensions are set for the respective geometries of bucket foundations, similar dimensions are adopted for the respective geometries embedded in medium dense sands.

B.3.2 Mesh Convergence Study

For respective bucket geometries, Firstly, the soil domain boundaries have been determined. Then, the soil domain needs to be discretized adequately with sufficient number of elements in order to obtain results with reasonable accuracy. The mesh convergence analysis has been carried out for the soil domains of the three bucket foundation geometries, under a superstructure load of 10 MN and lateral loading at the lid level (h = 0 m).

For the bucket foundation of D = 12 m & L = 12 m, the soil domain of 9D diameter and 3L depth is initially discretized with 4,080 elements. The domain is discretized with smaller sized elements in the vicinity of the bucket foundation, and the size of the elements has been increased gradually towards the domain boundary. Thereafter, simulations were run with number of soil domain elements ranging from 4,080 to 37,840 elements, as shown in in

Figures B.9(a)- B.9(f). In all cases, the depth to width ratio of the adjacent elements located in the left and right sides of the foundation is kept to 1.

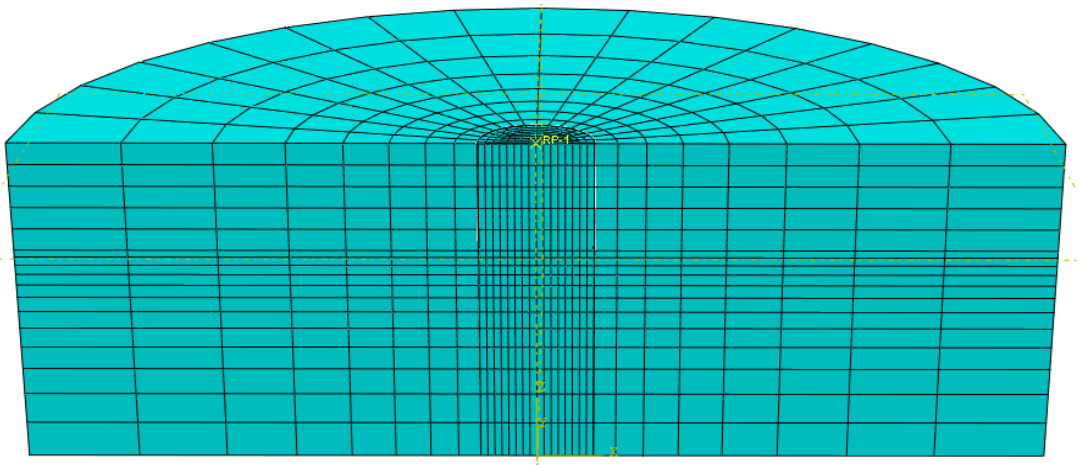

(a)

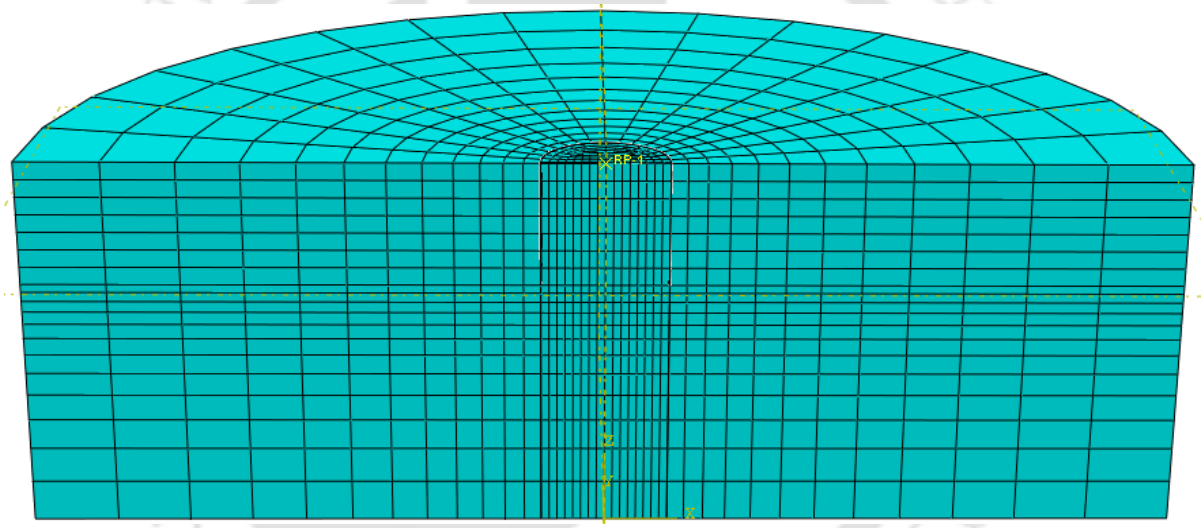

(b)

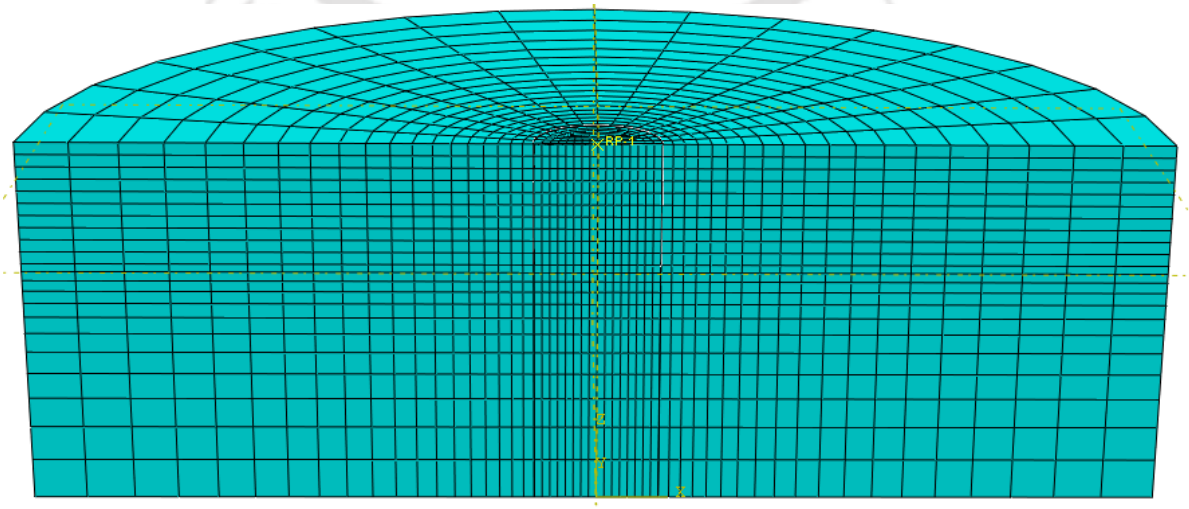

(c)

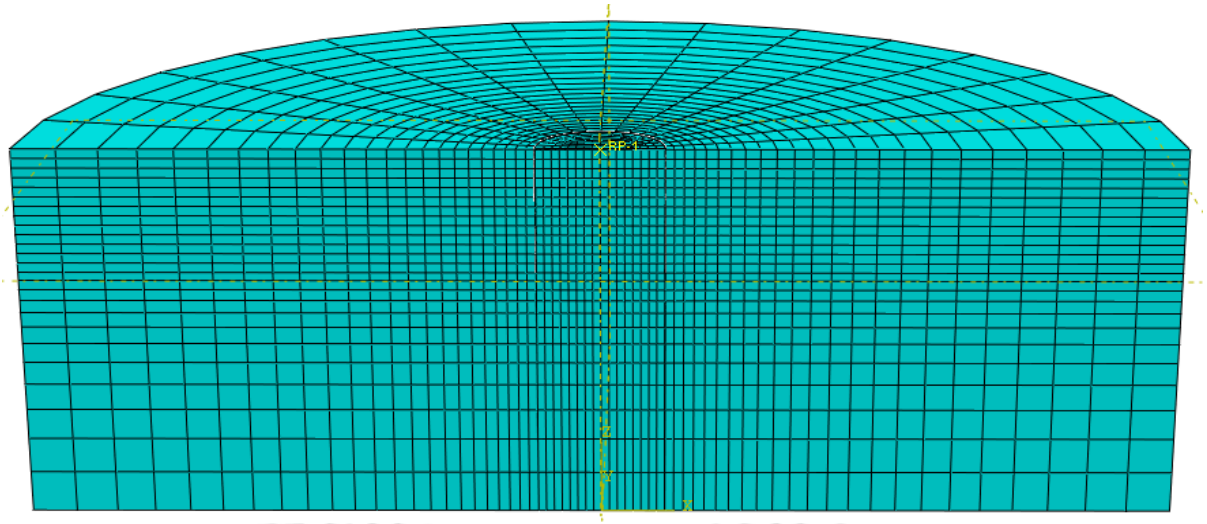

(d)

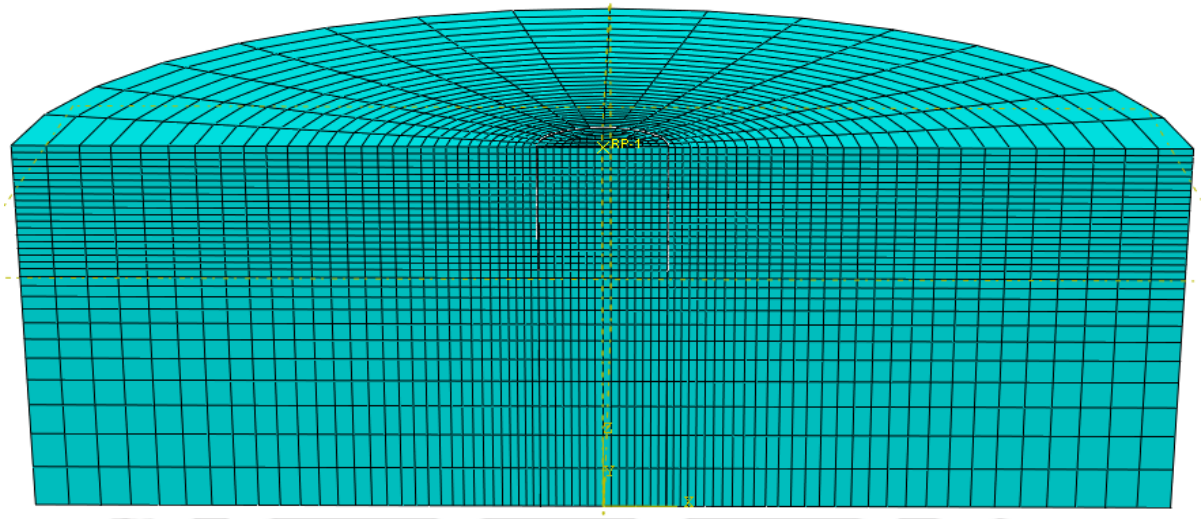

(e)

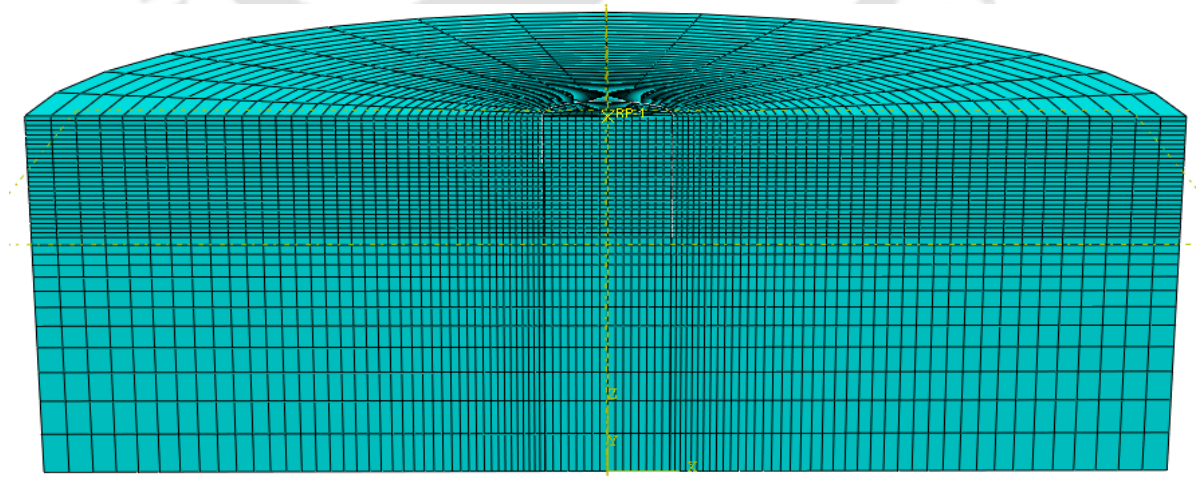

(f)

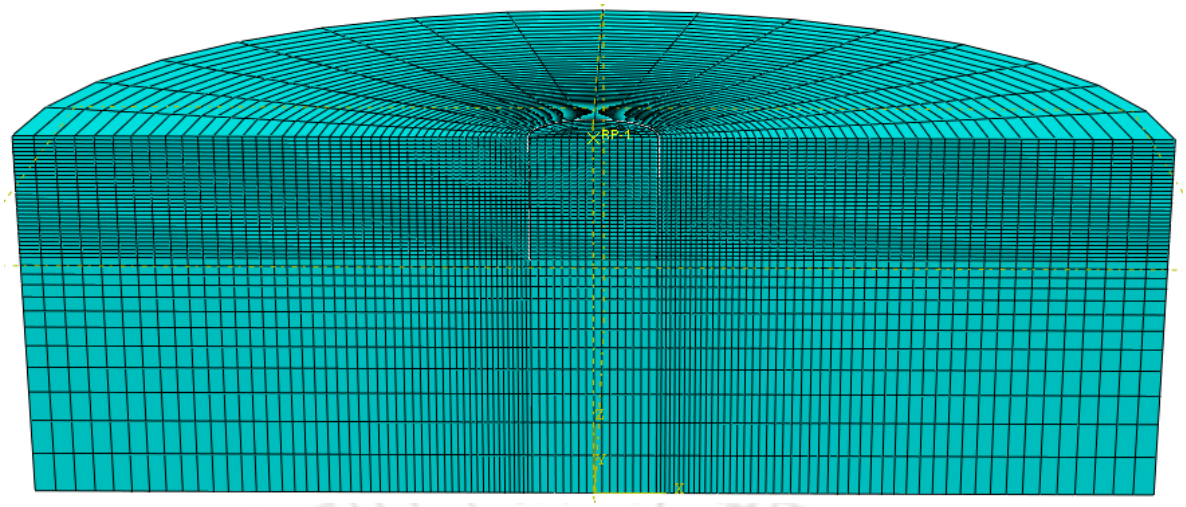

(g)

Figure B.9 Mesh configurations of soil domain for foundation size (D = 12 m & L = 12 m) and varying element numbers: (a) 4,080 elements; (b) 5,776 elements; (c) 9,512 elements; (d) 11,200 elements; (e) 17,760 elements; (f) 28,576 elements; and (g) 37,840 elements

Based on the numerical simulations, the lateral load versus lid displacement response of the bucket foundation of D = 12 m & L = 12 has been plotted for several numbers of elements, as shown in Figure B.10(a). At failure, the lateral load capacity for 4,080 elements is obtained as 65.73 MN. The ultimate lateral capacity is noted to decrease to 58.23 MN, as the soil domain is discretized with 37,840 elements. The variation of lateral load capacity versus the number of elements is shown in Figure B.10(b). From the figure, the ultimate lateral capacity is noted to reduce gradually and becomes nearly constant with increased numbers of elements. The variation of ultimate lateral capacity with number of discretized numbers of soil elements are presented in Table B.10.

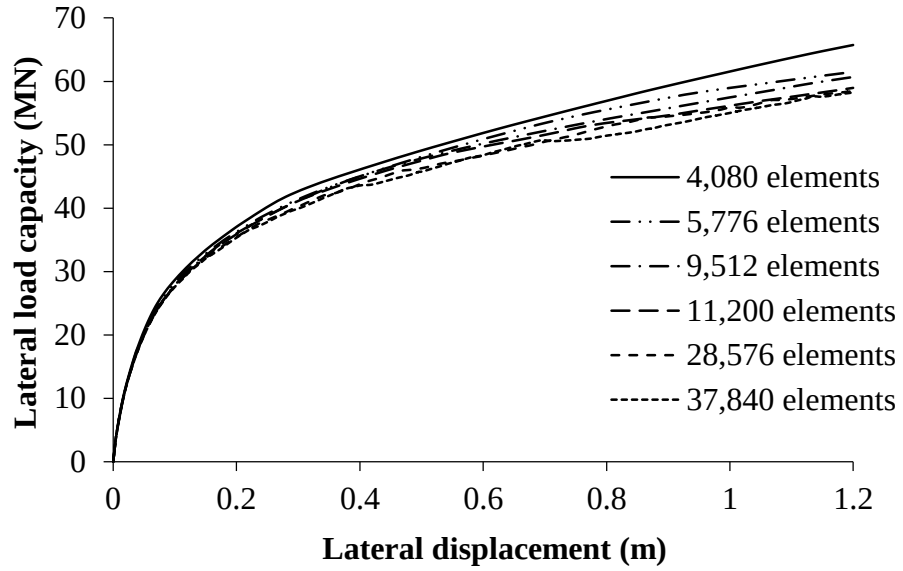

(a)

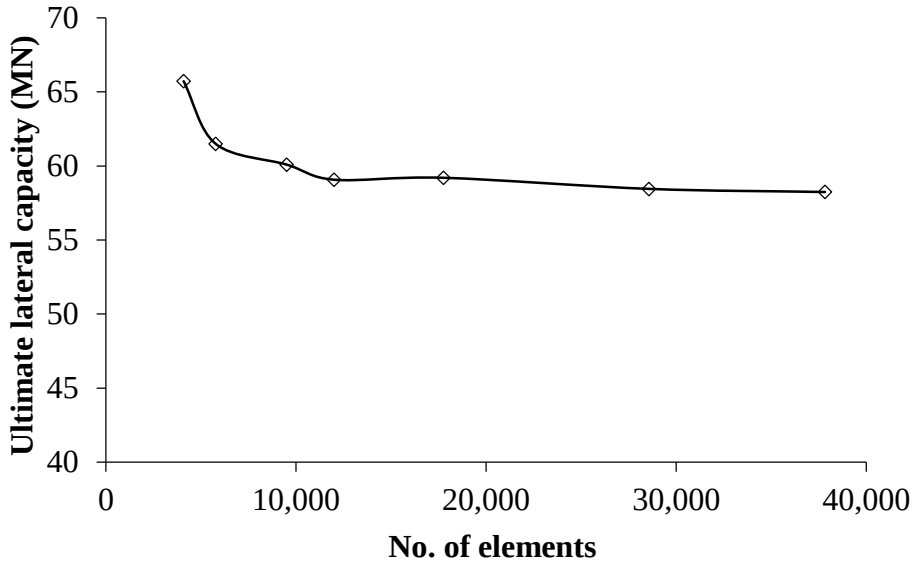

(b)

Figure B.10 Mesh convergence analysis for bucket foundation (D = 12 m, L = 12 m): (a) Plots of lateral load versus displacement; and (b) Plot of ultimate lateral capacity versus no. of elements

The mesh convergence results for the other two bucket foundation geometries (D = 15 m & L = 15 m and D = 18 m & L = 18 m) are shown in Figures B.11-B.12. Figures B.11(b) and B.12(b) show that the ultimate lateral capacity is noted to decrease with increasing numbers of discretized soil elements for both the bucket diameters.

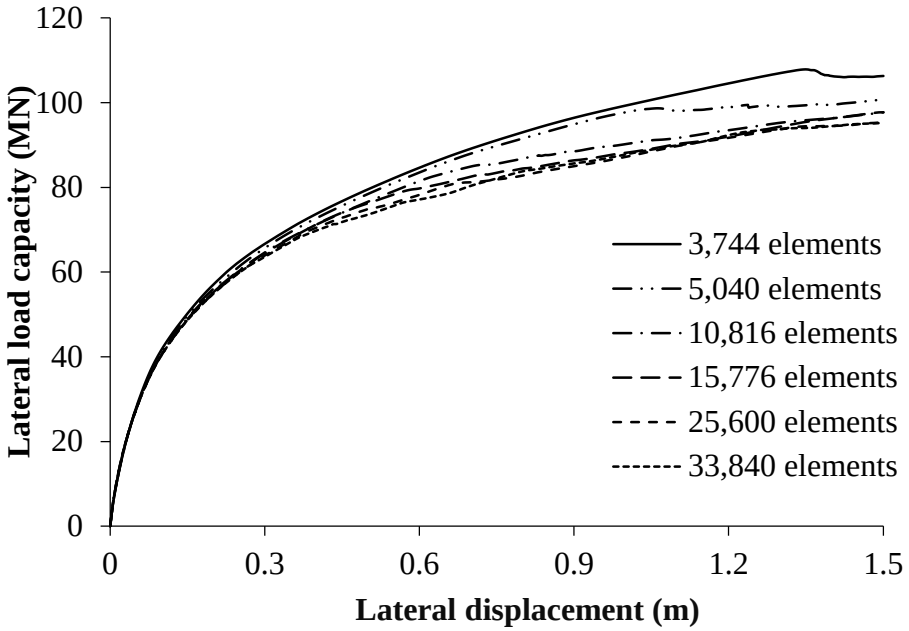

(a)

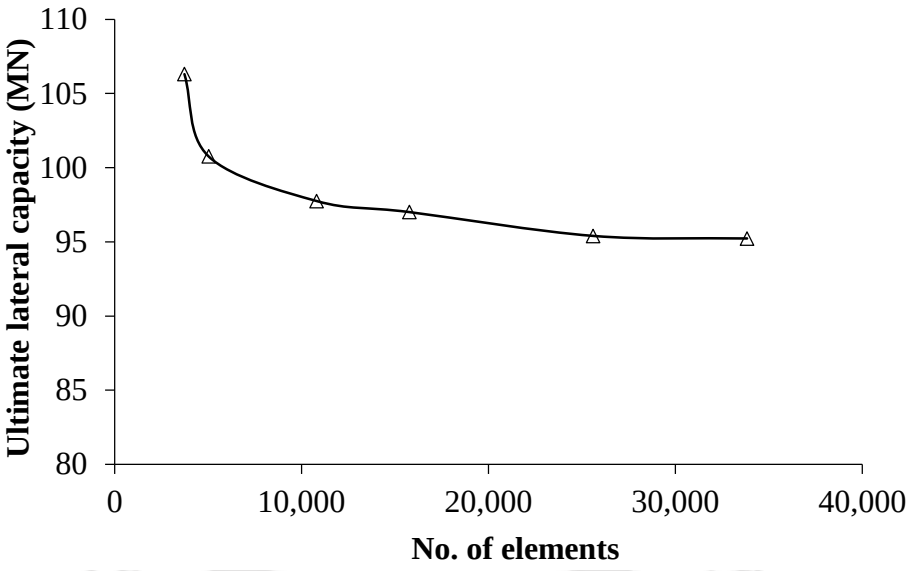

(b)

Figure B.11 Mesh convergence analysis for bucket foundation (D = 15 m, L = 15 m): (a) Plots of lateral load versus displacement; and (b) Plot of ultimate lateral capacity versus no. of elements

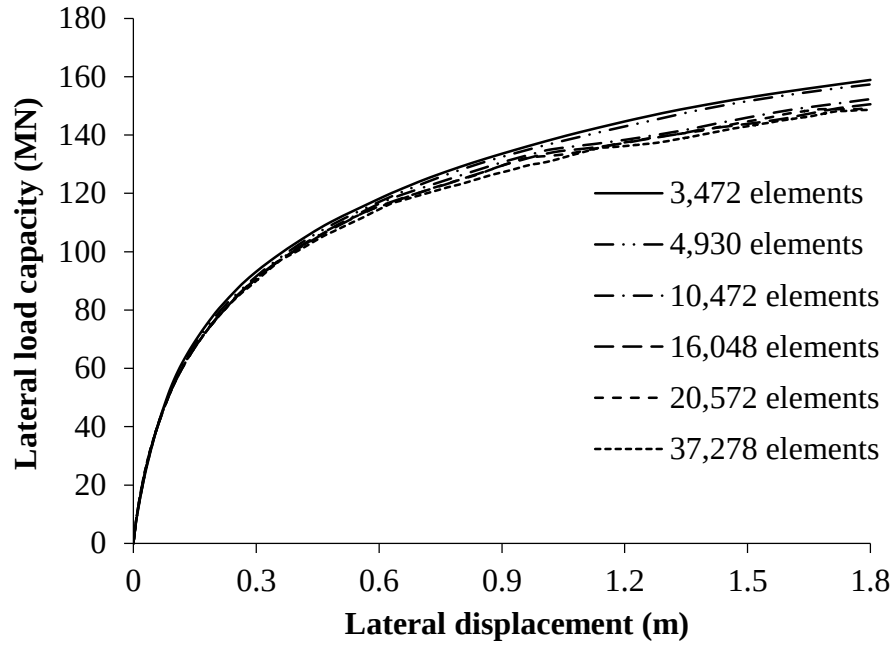

(a)

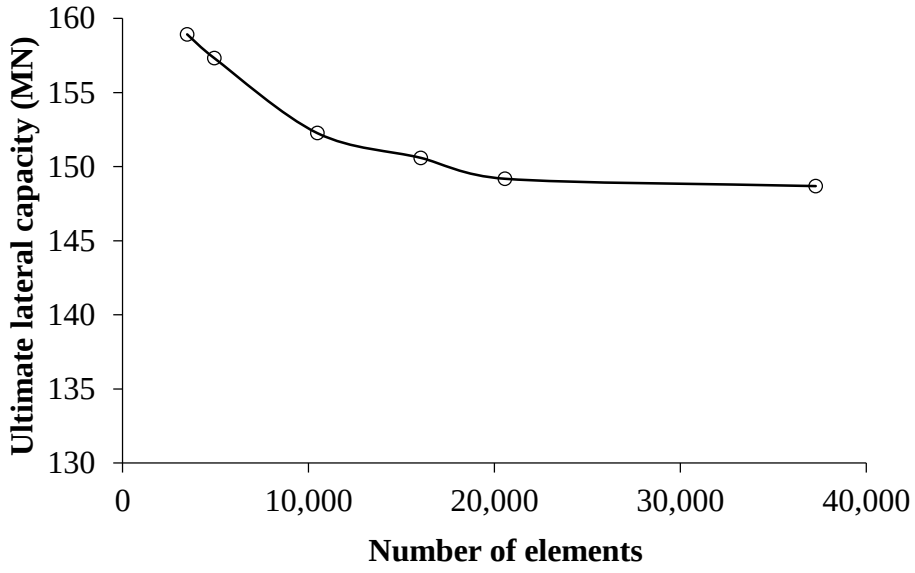

(b)

Figure B.12 Mesh convergence analysis for bucket foundation (D = 18 m, L = 18 m): (a) Plots of lateral load versus displacement; and (b) Plot of ultimate lateral capacity versus no. of elements

The values of ultimate lateral capacity for the bucket foundation of D = 15 m and D = 18 m are presented in Tables B.11 and B.12 for the same soil domain size (9D & 3L) with varying no. of elements.

Table B.10 Ultimate lateral capacity of bucket foundation (D = 12 m & L = 12 m) in soil domain size (9D & 3L) with varying no. of elements

Sl. No.	No. of elements	Ultimate lateral capacity (MN)	Decrease of capacity (MN)	% decrease of capacity
1.	4,080	65.73	-	-
2.	5,776	61.48	4.25	6.46
3.	9,512	60.08	1.40	2.28
4.	12,000	59.07	1.02	1.70
5.	17,760	59.20	-0.13	-0.22
6.	28,576	58.45	0.75	1.27
7.	37,840	58.23	0.21	0.36

Table B.11 Ultimate lateral capacity of bucket foundation (D = 15 m & L = 15 m) in soil domain size (9D & 3L) with varying no. of elements

Sl. No.	No. of elements	Ultimate lateral capacity (MN)	Decrease of capacity (MN)	% decrease of capacity
1.	3,744	106.30	-	-
2.	5,040	100.75	5.55	5.22
3.	10,816	97.75	3.01	2.98
4.	15,776	97.00	0.74	0.76
5.	25,600	95.39	1.61	1.66
6.	33,840	95.22	0.17	0.18

Table B.12 Ultimate lateral capacity of bucket foundation (D = 18 m & L = 18 m) in soil domain size (9D & 3L) with varying no. of elements

Sl. No.	No. of elements	Ultimate lateral capacity (MN)	Decrease of capacity (MN)	% decrease of capacity
1.	3,472	158.92	-	-
2.	4,930	157.32	1.60	1.01
3.	10,472	152.27	5.05	3.21
4.	16,048	150.60	1.67	1.10
5.	20,572	149.19	1.41	0.93
6.	37,278	148.70	0.49	0.33

Based on the mesh convergence analysis, for the bucket foundation geometries of D = 12 m & L = 12 m, D = 15 m & L = 15 m, and D = 18 m & L = 18 m, the respective soil domains can be discretized with approximately 12,000, 13,000 and 16,000 elements. Beyond

which, increasing the number of elements does not contribute to any significant change in ultimate lateral capacity. For all the three diameters, the magnitude of percentage decrease in the ultimate lateral capacity remains with 1-2% approximately. For the same diameter and for smaller bucket lengths, the number of elements can be kept unchanged. For the respective geometries, similar number of elements are adopted when embedded in medium dense sand.

Appendix C

VALIDATION OF THE NUMERICAL MODEL

C.1 BACK CALCULATION

The first large scale field test on a model bucket foundation was carried out in October 2002 in Frederikshavn, Denmark (Ibsen et al. 2005), as shown in Figure C.1. Figure C.2 shows the steel bucket foundation, with both its outer diameter and length equal to 2 m. The test was carried out in sandy soil site. The soil had mean grain size (d_{50}) of 0.15 mm, unit weight (γ) of 19.5 kN/m^3 and relative density (I_D) of 90%. The applied vertical load was 37.3 kN and the lateral loading height (h) was 17.4 m.

The moment-rotation response of this field test was used to validate the parameters to model soil nonlinearity in the numerical analysis. From the soil domain analysis (Appendix-B), a domain diameter of 18 m (equal to 9D) and a depth of 6 m (equal to 3L) were found to be suitable. The discretized model of bucket foundation embedded in soil domain is shown in Figure C.3. The bucket foundation and the soil domain were respectively discretized into 421 and 9750 numbers of brick elements (*C*3*D*8*R*). The vertical load and lateral load were applied at reference points, RP_1 and RP_2, respectively.

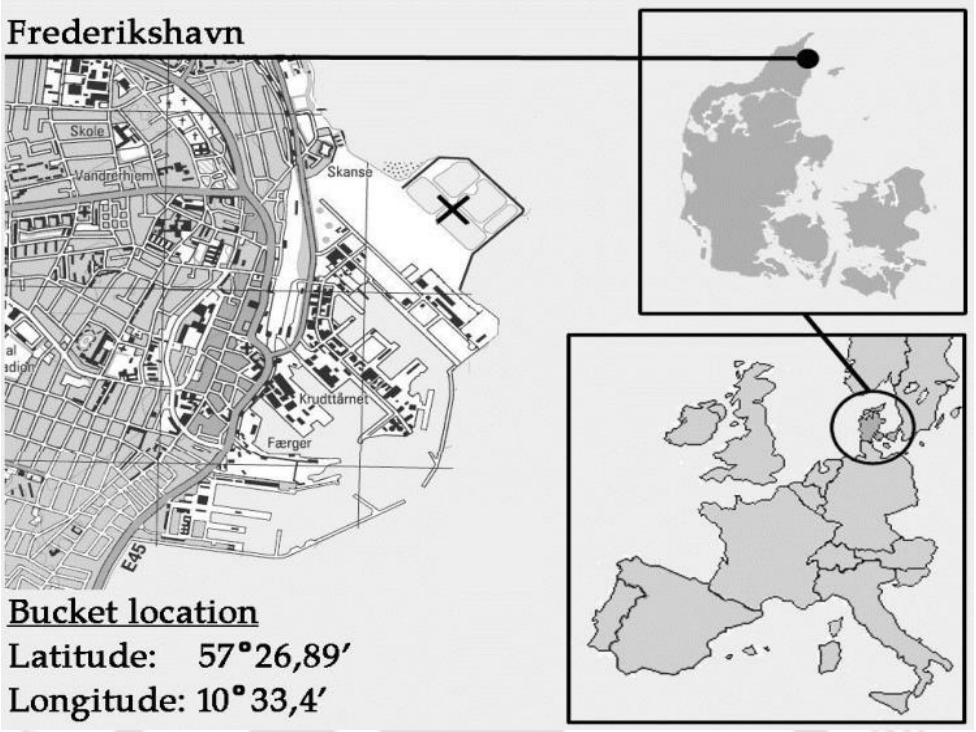

Figure C.1 Site for the field test on bucket foundation in Frederikshavn (Ibsen et al. 2005)

Figure C.2 Field model bucket foundation in Frederikshavn (Houlsby et al. 2005)

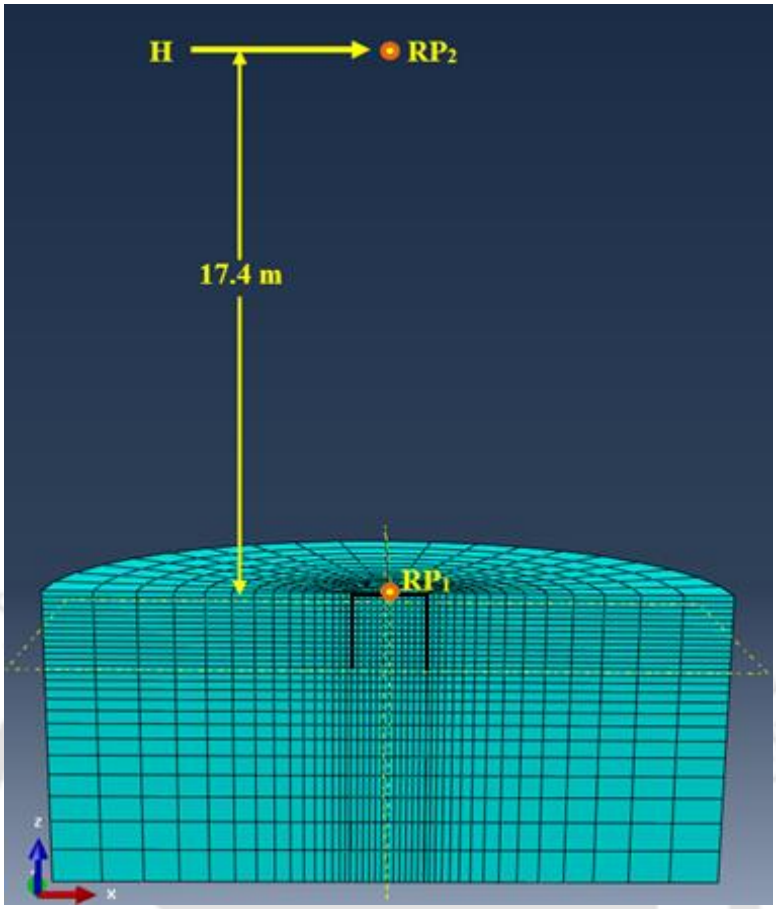

Figure C.3 Discretized model of bucket foundation embedded in soil domain

The non-linear behaviour of soil mass is modelled by defining its modulus of elasticity (E_{soil}) as a function of mean stress, as in Equation (C.1).

$$E_{soil} = \kappa.\sigma_{at}.\left(\frac{\sigma_m}{\sigma_{at}}\right)^{\lambda} \qquad \text{(C.1)}$$

where, σ_{at} is atmospheric pressure, σ_m is mean principal stress, and κ and λ are oedometric stiffness parameters. Parameter κ determines the soil stiffness at the reference stress state whereas parameter λ rules the stress dependency of the soil stiffness.

The dimensions of the field model bucket and its loading details were used in the numerical study. Since the values of the parameters (κ and λ) of the field test site were not available, they were taken from the range of properties provided in EAU (2004). The soil parameters used in the analyses were categorized for three sand types and are presented in Table C.1.

Table C.1 Soil parameters used in the validation (EAU 2004)

Sand type	κ	λ	ϕ'
Medium dense sand	400	0.60	32.5°
			35°
			37.5°
Very dense sand	600	0.55	35°
			37.5°
			40°
Dense sand	500	0.575	33.75
			36.25°
			38.75°

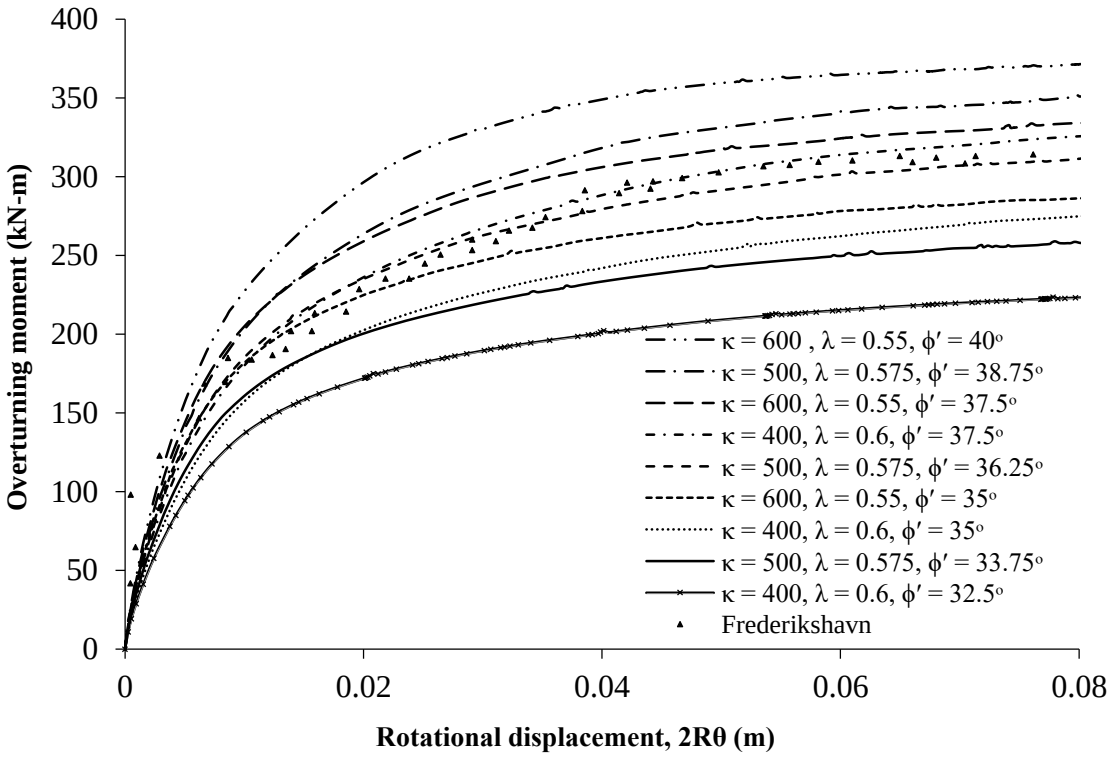

Figure C.4 Comparison of finite element analysis results with field model test result

The overturning moment versus rotation curves obtained from the numerical analyses are shown in Figure C.4. From the figure, the field test results are in best agreement with the curve for the parameters set of κ = 500, λ = 0.575 and ϕ' = 36.25°, which are possible parameters for dense sand.

These specific parameter values can be considered to represent the sandy soil of the test site at Frederikshavn. This confirms the acceptability of the soil parameters for modelling

non-linearity of the medium dense and very dense sands, which are then used in the subsequent parametric study of bucket foundation under vertical loading in Chapter 4 and under lateral loading in Chapter 5.

C.2 NUMERICAL VALIDATION OF LATERAL LOAD CAPACITY

In offshore conditions, bucket foundations are subjected to lateral loads. These lateral loads arise from the combined action of wind currents and water waves. These loads act at loading height above the seabed.

The numerical simulation of lateral response of bucket foundation is commenced by validating the modelling steps followed in the present study with Abdel-Rahman and Achmus (2006). A steel bucket foundation with a diameter of 20 m and a length of 15 m, embedded in medium dense sand was modeled, considering the soil properties used by Abdel-Rahman and Achmus (2006) and presented in Table C.2. Based on the domain analyses, the diameter is taken 8 times the diameter of the foundation and depth of soil domain and 3 times the length of bucket foundation. The bucket foundation and soil domain were discretized with 8 node linear brick elements with reduced integration (*C*3*D*8*R*). The bucket foundation and soil domain were discretized with 256 and 10912 soil elements, respectively.

Table C.2 Soil parameters used for numerical validation

Soil Parameters	Value
Effective unit weight, (γ'_{Steel}) in kN/m^3	11.00
Empirical parameters, κ	400
Empirical parameter, λ	0.60
Poisson's ratio, μ_{soil}	0.25
Internal friction angle, ϕ'	35°
Dilation angle, ψ'	5°

Three loading heights of 0 m, 50 m and 100 m were considered in the present study for the numerical validation. Following steps have been followed to simulate the numerical behaviour of bucket foundation. In the first step, geostatic load was applied to achieve the

initial stress state in the whole soil domain. In the second step, contact between the bucket and the soil was established. The interface between the bucket surface and the corresponding adjacent soil surface was modeled using master-slave contact pair algorithm. The bucket foundation being stiffer was chosen as master surface and the soil surface was selected as slave surface. The interface friction angle between master and slave surfaces was considered as two-thirds of the internal friction angle (ϕ'). Details of the contact establishment between bucket surface and soil under lateral loads have been discussed in Chapter 2. Once the interaction is assigned, the self-weight of the bucket foundation is applied in this step. In the third step, superstructure load representing the self-weight of the of 10 MN is applied at the centre of the bucket lid. In the final step, resultant water wave and wind load was simulated by displacement-controlled lateral load, applied at an eccentric location of 0 m, 50 m and 100 m measured vertically above the centre of the caisson lid. Figure C.5 presents a comparison of the results in the form of published lateral load–displacement curves and those of the present investigation. It can be noted that there is a good agreement of the results.

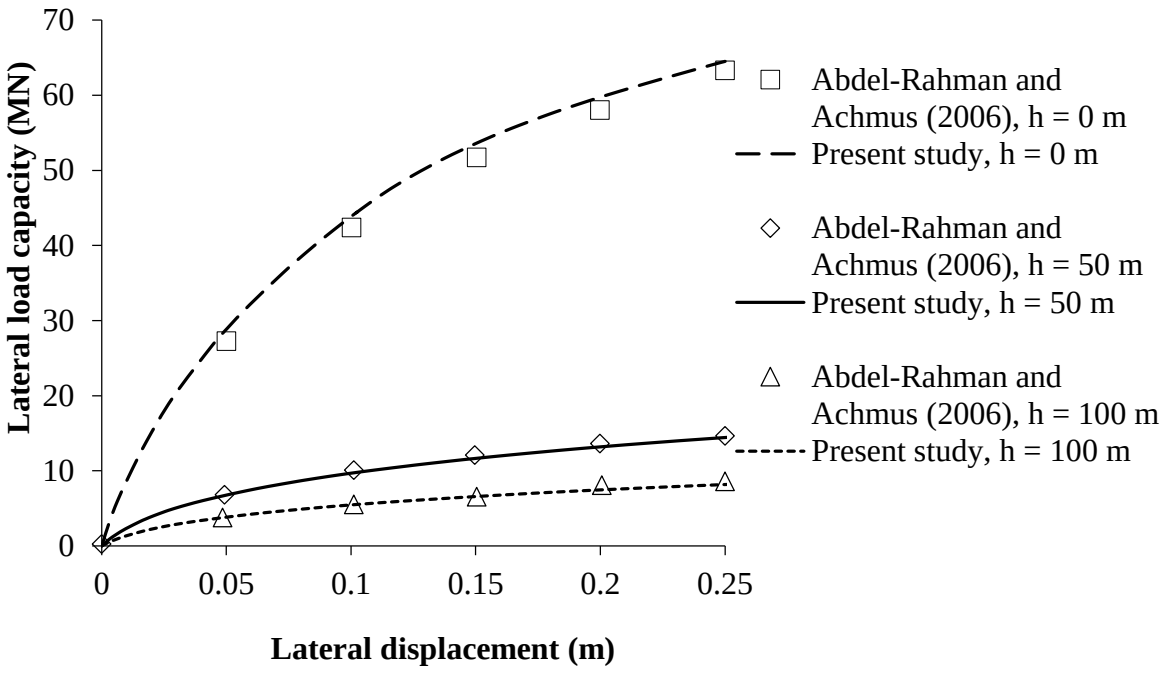

Figure C.5 Validation of numerical modelling steps of present study

Appendix D

DIMENSIONAL ANALYSIS

D.1 DIMENSIONSIONAL ANALYSIS

Dimensional analysis is a powerful method of normalizing variables in order to determine the relationships between the key variables determined from the numerical study. In this section, the analysis has been carried out to normalize the vertical capacity as well as lateral capacity of the bucket foundation and present the results in a non-dimensional form.

D.1.1 Vertical Response of Bucket Foundation

The important parameters that influence the vertical capacity of a bucket foundation are vertical displacement of the foundation (w), diameter (D), skirt length (L), mean vertical load acting on the foundation (V_m) and shear modulus (G) of the soil bed, which can be expressed as function as given by Equation (D.1).

$$V_{load} = f(w, D, L, V_m, G) \tag{D.1}$$

Further, the shear modulus of the soil depends on atmospheric pressure and representative vertical stress, as given in Equation (D.2).

$$\frac{G}{p_a} = A\left(\frac{\sigma'_V}{p_a}\right)^n \tag{D.2}$$

where p_a is atmospheric pressure, σ'_v is representative effective vertical stress, A is a dimensionless constant and n is the pressure exponent. Equation (D.1) can be also be written as:

$$V_{load} = f(w, D, L, V_m, p_a, \gamma') \tag{D.3}$$

The primary dimensions associated with the respective variables used in the study are listed in Table D.1.

Table D.1 List of dimensions of variables for vertical capacity

Symbol	Parameter	Dimension
D	Diameter of bucket foundation	L^*
G	Shear modulus	$M^*L^{*-1}T^{-2}$
L	Skirt length of bucket foundation	L^*
p_a	Atmospheric pressure	$M^*L^{*-1}T^{-2}$
V_{load}	Vertical load	$M^*L^*T^{-2}$
V_m	Mean vertical load	$M^*L^*T^{-2}$
w	Vertical displacement of bucket	L^*
γ'	Unit weight of soil	$M^*L^{*-2}T^{-2}$

Using Buckingham's theorem to find the dimensionless products, excluding the non-dimensional parameters:

Total number of parameters in the problem, $n = 7$

Number of repeating variables, $j = 2$

Expected number of π's, $k = 7 - 2 = 5$

D and γ' are chosen as the repeating variables. These repeating variables are combined with each of the remaining parameters one at a time to create the π's (dimensionless products).

First independent π:

$$\pi_1 = V_{load}\gamma'^a D^b \tag{D.4}$$

i.e.

$$\left\{M^{*0}L^{*0}T^0\right\} = \left\{\left(\frac{M^*L^*}{T^2}\right)\left(\frac{M^*}{L^{*2}T^2}\right)^a \left(L^*\right)^b\right\}$$

Equating the exponents:

Mass: $1 + a = 0$

Length: $1 - 2a + b = 0$

Time: $-2 - 2a = 0$

Solving simultaneously, we obtain $a = -1$ and $b = -3$

Substituting the values of a and b in Equation (D.4),

$$\pi_1 = \frac{V_{load}}{\gamma' D^3} \tag{D.5}$$

Second independent π:

$$\pi_2 = w\gamma'^a D^b \tag{D.6}$$

i.e.

$$\left\{M^{*0}L^{*0}T^0\right\} = \left\{\left(L^*\right)\left(\frac{M^*}{L^{*2}T^2}\right)^a \left(L^*\right)^b\right\}$$

Equating the exponents:

Mass: $a = 0$

Length: $1 - 2a + b = 0$

Time: $-2a = 0$

Solving simultaneously, we obtain $a = 0$ and $b = -1$

Substituting the values of a and b in Equation (D.6),

$$\pi_2 = \frac{w}{D} \tag{D.7}$$

Third independent π:

$$\pi_3 = L^*\gamma'^a D^b \tag{D.8}$$

i.e.

$$\left\{M^{*0}L^{*0}T^0\right\} = \left\{\left(L^*\right)\left(\frac{M^*}{L^{*2}T^2}\right)^a \left(L^*\right)^b\right\}$$

Equating the exponents:

Mass: $a = 0$

Length: $1 - 2a + b = 0$

Time: $- 2a = 0$

Solving simultaneously, we obtain $a = 0$ and $b = -1$

Substituting the values of a and b in Equation (D.8),

$$\pi_3 = \frac{L^*}{D} \tag{D.9}$$

Fourth independent π:

$$\pi_4 = V_m \gamma'^a D^b \tag{D.10}$$

i.e.

$$\left\{M^{*0} L^{*0} T^0\right\} = \left\{\left(\frac{M^* L^*}{T^2}\right)\left(\frac{M^*}{L^{*2} T^2}\right)^a \left(L^*\right)^b\right\}$$

Equating the exponents:

Mass: $1 + a = 0$

Length: $1 - 2a + b = 0$

Time: $-2 - 2a = 0$

Solving simultaneously, we obtain $a = -1$ and $b = -3$

Substituting the values of a and b in Equation (D.10),

$$\pi_3 = \frac{V_m}{\gamma' D^3} \tag{D.11}$$

Fifth independent π:

$$\pi_4 = p_a \gamma'^a D^b \tag{D.12}$$

i.e.

$$\left\{M^{*0} L^{*0} T^0\right\} = \left\{\left(\frac{M^*}{L^{*1} T^2}\right)\left(\frac{M^*}{L^{*2} T^2}\right)^a \left(L^*\right)^b\right\}$$

Equating the exponents:

Mass: $1 + a = 0$

Length: $-1 - 2a + b = 0$

Time: $-2 - 2a = 0$

Solving simultaneously, we obtain $a = -1$ and $b = -1$

Substituting the values of a and b in Equation (D.12),

$$\pi_4 = \frac{p_a}{\gamma' D} \tag{D.13}$$

In dimensionless form, the vertical capacity of the bucket foundation can be expressed either by Equation (D.14) or Equation (D.15).

$$\frac{V_{load}}{\gamma' D^3} = f\left(\frac{w}{D}, \frac{V_m}{\gamma' D^3}, \frac{L}{D}, \frac{p_a}{\gamma' D}\right) \tag{D.14}$$

$$\frac{V_{load}}{\gamma' D L^2} = f\left(\frac{w}{D}, \frac{V_m}{\gamma' D^3}, \frac{L}{D}, \frac{p_a}{\gamma' D}\right) \tag{D.15}$$

The dimensionless parameters $\frac{V_{load}}{\gamma' D^3}$ and $\frac{L}{D}$ from the above equation (D.15) are plotted and the relation between them are given by curve fitting in Figure 4.19(a)-(b) in Chapter 4.

D.1.2 Lateral Response of Bucket Foundation

The lateral load response of bucket foundation depends on diameter (D) of the bucket foundation, skirt length (L), loading height (h) at which the lateral load is applied, superstructure load (V), lateral displacement at the bucket lid (w') and shear modulus of soil (G). The lateral load response can be expressed as a function of the parameters given above, as in Equation (D.16).

$$H = f(w', V, h, D, L, G) \tag{D.16}$$

Further, the shear modulus of the soil depends on atmospheric pressure and representative vertical stress, as given in Equation (D.2). Equation (D.16) can be re-written as:

$$H = f(w', V, h, D, L, p_a, \gamma') \tag{D.17}$$

The primary dimensions associated with the respective variables used in the study are listed in Table D.2.

Table D.2 List of dimensions of variables for lateral capacity

Symbol	Parameter	Dimension
D	Diameter of bucket foundation	L^*
G	Shear modulus	$M^*L^{*-1}T^{-2}$
H	Lateral load	$M^*L^*T^{-2}$
h	Loading height	L^*
L	Length of bucket foundation	L^*
p_a	Atmospheric pressure	$M^*L^{*-1}T^{-2}$
V	Superstructure load	$M^*L^*T^{-2}$
w'	Lateral displacement of bucket	L^*
γ'	Unit weight of soil	$M^*L^{*-2}T^{-2}$

Using Buckingham's theorem, the total number of parameters, n = 8. The number of repeating variables, j = 2. The expected number of π's, k = 8 – 2 = 5. D and γ' are chosen as the repeating variables.

First independent π:

$$\pi_1 = H\gamma'^a D^b \tag{D.18}$$

i.e.

$$\left\{M^{*0}L^{*0}T^0\right\} = \left\{\left(\frac{M^*L^*}{T^2}\right)\left(\frac{M^*}{L^{*2}T^2}\right)^a \left(L^*\right)^b\right\}$$

Equating the exponents:

Mass: $1 + a = 0$

Length: $1 - 2a + b = 0$

Time: $-2 - 2a = 0$

Solving simultaneously, we obtain a = -1 and b = -3

Substituting the values of a and b in Equation (D.18),

$$\pi_1 = \frac{H}{\gamma' D^3} \tag{D.19}$$

Second independent π:

$$\pi_2 = w' \gamma'^a D^b \tag{D.20}$$

i.e.

$$\left\{M^{*0} L^{*0} T^0\right\} = \left\{\left(L^*\right)\left(\frac{M^*}{L^{*2} T^2}\right)^a \left(L^*\right)^b\right\}$$

Equating the exponents:

Mass: a = 0

Length: 1 - 2a + b = 0

Time: -2a = 0

Solving simultaneously, we obtain a = 0 and b = -1

Substituting the values of a and b in Equation (D.20),

$$\pi_2 = \frac{w'}{D} \tag{D.21}$$

Third independent π:

$$\pi_3 = V \gamma'^a D^b \tag{D.22}$$

i.e.

$$\left\{M^{*0} L^{*0} T^0\right\} = \left\{\left(\frac{M^* L^*}{T^2}\right)\left(\frac{M^*}{L^{*2} T^2}\right)^a \left(L^*\right)^b\right\}$$

Equating the exponents:

Mass: 1 + a = 0

Length: 1 - 2a + b = 0

Time: -2 - 2a = 0

Solving simultaneously, we obtain a = -1 and b = -3

Substituting the values of a and b in Equation (D.22),

$$\pi_3 = \frac{V}{\gamma' D^3} \tag{D.23}$$

Fourth independent π:

$$\pi_4 = h\gamma'^a D^b \tag{D.24}$$

i.e.

$$\left\{M^{*0}L^{*0}T^0\right\} = \left\{\left(L^*\right)\left(\frac{M^*}{L^{*2}T^2}\right)^a \left(L^*\right)^b\right\}$$

Equating the exponents:

Mass: $a = 0$

Length: $1 - 2a + b = 0$

Time: $-2a = 0$

Solving simultaneously, we obtain $a = 0$ and $b = -1$

Substituting the values of a and b in Equation (D.24),

$$\pi_4 = \frac{h}{D} \tag{D.25}$$

Fifth independent π:

$$\pi_5 = L^*\gamma'^a D^b \tag{D.26}$$

i.e.

$$\left\{M^{*0}L^{*0}T^0\right\} = \left\{\left(L^*\right)\left(\frac{M^*}{L^{*2}T^2}\right)^a \left(L^*\right)^b\right\}$$

Equating the exponents:

Mass: $a = 0$

Length: $1 - 2a + b = 0$

Time: $-2a = 0$

Solving simultaneously, we obtain $a = 0$ and $b = -1$

Substituting the values of a and b in Equation (D.26),

$$\pi_5 = \frac{L^*}{D} \tag{D.27}$$

Sixth independent π:

$$\pi_5 = p_a \gamma'^a D^b \tag{D.28}$$

$$\left\{M^{*0} L^{*0} T^0\right\} = \left\{\left(\frac{M^*}{L^{*1} T^2}\right)\left(\frac{M^*}{L^{*2} T^2}\right)^a \left(L^*\right)^b\right\}$$

Equating the exponents:

Mass: $1 + a = 0$

Length: $-1 - 2a + b = 0$

Time: $-2 - 2a = 0$

Solving simultaneously, we obtain $a = -1$ and $b = -1$

Substituting the values of a and b in Equation (D.28),

$$\pi_5 = \frac{p_a}{\gamma' D} \tag{D.29}$$

In dimensionless form, the lateral capacity of the bucket foundation can be expressed either by Equation (D.30) or Equation (D.31):

$$\frac{H}{\gamma' D^3} = f\left(\frac{w'}{D}, \frac{V}{\gamma' D^3}, \frac{h}{D}, \frac{L}{D}, \frac{p_a}{\gamma' D}\right) \tag{D.30}$$

$$\frac{H}{\gamma' L D^2} = f\left(\frac{w'}{L}, \frac{V}{\gamma' L D^2}, \frac{h}{L}, \frac{L}{L}, \frac{p_a}{\gamma' L}\right) \tag{D.31}$$

From the above equation, the dimensionless parameters $\frac{H}{\gamma' D^3}$ and $\frac{h}{D}$ are plotted and the relationship between the two is determined by means of curve fitting in Figures 5.35 and 5.36 of Chapter 5.

REFERENCES

1. Abdel-Rahman, K., and Achmus, M. (2006). "Numerical investigation on the bearing capacity of bucket foundations under combined horizontal and moment loading." *International Symposium on Ultimate Limit State of Geotechnical Structures*, Paris, France, 6pp.
2. Achmus, M., Akdag, C., and Thieken, K. (2013). "Load-bearing behavior of suction bucket foundations in sand." *Applied Ocean Research*, 43(1), 157-165.
3. Ahmed, S. S., and Hawlader, B. (2016). "Numerical analysis of large-diameter monopiles in dense sand supporting offshore wind turbines." *International Journal of Geomechanics*, 16(5): 04016018.
4. Aubeny, C., Han, S. W., and Murff, J. D. (2003). "Suction caisson capacity in anisotropic, purely cohesive soil." *International Journal of Geomechanics*, 3(2), 225-235.
5. Bagheri, P., Son, S. W., and Kim, J. M. (2017). "Investigation of the load-bearing capacity of suction caissons used for offshore wind turbines." *Applied Ocean Research*, 67(1), 148-161.
6. Barari, A., and Ibsen, L. B. (2011). "Effect of embedment on the vertical bearing capacity of Bucket foundations in clay." *Proc. of 2011 Pan-Am CGS Geotechnical Conference*, Toronto, Canada, 7 pp.
7. Barari, A., and Ibsen, L. B. (2012). "Undrained response of bucket foundations to moment loading." *Applied Ocean Research*, 36(1), 12-21.
8. Barari, A., Ibsen, L. B., Taghavi Ghalesari, A., and Larsen, K. A. (2016). "Embedment effects on vertical bearing capacity of offshore bucket foundations on cohesionless soil." *International Journal of Geomechanics*, 17(4): 04016110.
9. Bhattacharya, S. (2014). "Challenges in design of foundations for offshore wind turbines." *Engineering & Technology Reference*, 9 pp., 10.1049/etr. 2014.004.1.

10. Bisoi, S., and Haldar, S. (2014). "Dynamic analysis of offshore wind turbine in clay considering soil–monopile–tower interaction." *Soil Dynamics and Earthquake Engineering*, 63(1), 19-35.
11. Bransby, F., and Randolph, M. F. (1999). "The effect of embedment depth on the undrained response of skirted foundations to combined loading." *Soils and Foundations*, 39(4), 19-33.
12. Bransby, M., and Yun, G. J. (2009). "The undrained capacity of skirted strip foundations under combined loading." *Géotechnique*, 59(2), 115-125.
13. Byrne, B., and Houlsby, G. (1999). "Drained behaviour of suction caisson foundations on very dense sand." Proc., *Offshore Technology Conference*, Houston, U.K., Paper No. OTC 10994.
14. Byrne, B., Villalobos, F., Houlsby, G., and Martin, C. (2001). "Laboratory Testing of Shallow Skirted Foundations in Sand." *Proc. British Geotechnical Association Int. Conf. on Foundations*, Dundee, Scotland, 161-173.
15. Byrne, B. W., and Houlsby, G. T. (2002). "Experimental investigations of response of suction caissons to transient vertical loading." *Journal of Geotechnical and Geoenvironmental Engineering*, 128(11), 926-939.
16. Byrne, B., and Houlsby, G. (2003). "Foundations for offshore wind turbines." *Philosophical Transactions of the Royal Society of London A: Mathematical, Physical and Engineering Sciences*, 361(1813), 2909-2930.
17. Byrne, B. W., and Houlsby, G. T. (2004). "Experimental investigations of the response of suction caissons to transient combined loading." *Journal of Geotechnical and Geoenvironmental Engineering*, 130(3), 240-253.
18. Cassidy, M., Randolph, M., and Byrne, B. (2006). "A plasticity model describing caisson behaviour in clay." *Applied Ocean Research*, 28(5), 345-358.

19. Cox, J. A., and Bhattacharya, S. (2016). "Serviceability of suction caisson founded offshore structures." *Proceedings of the Institution of Civil Engineers: Geotechnical Engineering*, 170(3), 273-284.
20. Dassault Systèmes (2010). Abaqus analysis users' manual, Simula Corp, Providence, RI, USA.
21. Ding, H., Liu, Y., Zhang, P., and Le, C. (2015). "Model tests on the bearing capacity of wide-shallow composite bucket foundations for offshore wind turbines in clay." *Ocean Engineering*, 103(1), 114-122.
22. DNV (2007). "Design of Offshore Wind Turbine Structure." Offshore Standard DNV-OS-J101.
23. Doherty, J. P., Deeks, A. J., and Houlsby, G. T. (2004). "Evaluation of foundation stiffness using the scaled boundary finite element method." *Computational Mechanics WCCM VI in Conjunction with APCOM*, 4(1), 5-10.
24. Doherty, J., Houlsby, G., and Deeks, A. (2005). "Stiffness of flexible caisson foundations embedded in nonhomogeneous elastic soil." *Journal of Geotechnical and Geoenvironmental Engineering*, 131(12), 1498-1508.
25. Duncan, J. M., and Chang, C. Y. (1970). "Nonlinear analysis of stress and strain in soils." *Journal of Soil Mech. and Found. Div.*, 96(5), 1629-1653.
26. EAU. (2004). "Recommendations of the committee for waterfront structures: Harbours and Waterways". Ernst & Sohn, Berlin, Germany.
27. Eid, H. T. (2013). "Bearing capacity and settlement of skirted shallow foundations on sand." *International Journal of Geomechanics*, 13(5), 645-652.
28. Foglia, A., Gottardi, G., Govoni, L., and Ibsen, L. B. (2015). "Modelling the drained response of bucket foundations for offshore wind turbines under general monotonic and cyclic loading." *Applied Ocean Research*, 52(1), 80-91.

29. Fu, D., Gaudin, C., Tian, Y., Cassidy, M. J., and Bienen, B. (2017). "Uniaxial capacities of skirted circular foundations in clay." *Journal of Geotechnical and Geoenvironmental Engineering*, 143(7): 04017022.
30. Geuss, M. (2016). "Get ready for 24-30% reduction in cost of wind power by 2030." [*https://arstechnica.com/science/2016/11/experts-forecast-giant-11mw-offshore-wind-turbines-by-2030/*] (accessed on March 21, 2018).
31. Ghaseminejad, V., Rowshanzamir, M. A., and Barari, A. (2018). "Predicting the drained capacity of skirted foundations under uniaxial loads." *Proc., GeoShanghai International Conference*, Sanghai, China, 718-725.
32. GWEC (2017). Global Wind 2016 Report [*www.gwec.net/wp-content/uploads/2017/05/Global-Offshore-2016-and-Beyond.pdf*] (accessed on March 21, 2018).
33. Golightly, C. (2014). "Tilting of monopiles long, heavy and stiff; pushed beyond their limits." Technical Note, *Ground Engineering*, 20–23.
34. Gourvenec, S., and Barnett, S. (2011). "Undrained failure envelope for skirted foundations under general loading." *Géotechnique*, 61(3), 263-270.
35. Gourvenec, S., and Mana, D. (2011). "Undrained vertical bearing capacity factors for shallow foundations." *Géotechnique Letters*, 1(4), 101-108.
36. Gourvenec, S., and Randolph, M. (2002). "Effect of strength non-homogeneity on the bearing capacity of circular skirted foundations subjected to combined loading." *Proc., The Twelfth International Offshore and Polar Engineering Conference*, Kitakyushu, country, 26-31.
37. Haddad, A., Amini, R., and Barari, A. (2018). "Effect of embedment on the vertical capacity of bucket foundation in loose saturated sand: Physical modeling." *Marine Georesources & Geotechnology*, 1-9. https://doi.org/10.1080/1064119X.2018.1443354.

38. Haiderali, A., Cilingir, U., and Madabhushi, G. (2013). "Lateral and axial capacity of monopiles for offshore wind turbines." *Indian Geotechnical Journal*, 43(3), 181-194.

39. Harte, M., Basu, B., and Nielsen, S. R. (2012). "Dynamic analysis of wind turbines including soil-structure interaction." *Engineering Structures*, 45, 509-518.

40. Houlsby, G. T., and Byrne, B. W. (2000). "Suction caisson foundations for offshore wind turbines and anemometer masts." *Wind Engineering*, 24(4), 249-255.

41. Houlsby, G., Kelly, R., Huxtable, J., and Byrne, B. (2005). "Field trials of suction caissons in clay for offshore wind turbine foundations." *Géotechnique*, 55(4), 287-296.

42. Houlsby, G., Kelly, R., Huxtable, J., and Byrne, B. (2006). "Field trials of suction caissons in sand for offshore wind turbine foundations." *Géotechnique*, 56(1), 3–10.

43. Hung, L. C., and Kim, S. R. (2012). "Evaluation of vertical and horizontal bearing capacities of bucket foundations in clay." *Ocean Engineering*, 52, 75-82.

44. Hung, L. C., and Kim, S. R. (2014). "Evaluation of undrained bearing capacities of bucket foundations under combined loads." *Marine Georesources & Geotechnology*, 32(1), 76-92.

45. Ibsen, L. B., Liingaard, S., and Nielsen, S. A. (2005). "Bucket Foundation, a status." *Proceedings of the Copenhagen Offshore Wind*, Copenhagen, Denmark, 1-15.

46. Ibsen, L. B., Barari, A., and Larsen, K. A. (2013). "Adaptive plasticity model for bucket foundations." *Journal of Engineering Mechanics*, 140(2), 361-373.

47. Ibsen, L., Larsen, K., and Barari, A. (2013). "Calibration of failure criteria for bucket foundations on drained sand under general loading." *Journal of Geotechnical and Geoenvironmental Engineering*, 140(7): 04014033.

48. Ibsen, L. B., Barari, A., and Larsen, K. A. (2015). "Effect of embedment on the plastic behavior of bucket foundations." *Journal of Waterway, Port, Coastal, and Ocean Engineering*, 141(6): 06015005.

49. Janbu, N. (1963). “Soil compressibility as determined by oedometer and triaxial tests.” *Proceedings of European Conference on Soil Mechanics and Foundation Engineering*, Wiesbaden, Germany, 19-25.

50. Kelly, R., Houlsby, G., and Byrne, B. (2006). “A comparison of field and laboratory tests of caisson foundations in sand and clay.” *Géotechnique*, 56(9), 617–626.

51. Kim, D.J., Choo, Y. W., Kim, J.H., Kim, S., and Kim, D.S. (2014). “Investigation of monotonic and cyclic behavior of tripod suction bucket foundations for offshore wind towers using centrifuge modeling.” *Journal of Geotechnical and Geoenvironmental Engineering*, 140(5): 04014008.

52. Kondner, R. L. (1963). “Hyperbolic stress-strain response: cohesive soils.” *Journal of the Soil Mechanics and Foundations Division*, 89(1), 115-144.

53. Kumar, N. D., and Rao, S. N. (2010). “Earth pressures on caissons in marine clay under lateral loads - A laboratory study.” *Applied Ocean Research*, 32(1), 58-70.

54. Kumar, N. D., and Rao, S. N. (2012). “Lateral load: deflection response of an embedded caisson in marine clay.” *Marine Georesources & Geotechnology*, 30(1), 1-31.

55. Kurian, V., Narayanan, S., and Ganapathy, C. (2009). “Towers for offshore wind turbines.” *Proc., AIP Conference Proceedings*, Kuala Lumpur, country, 475-487.

56. Larsen, K. A., Ibsen, L. B., and Barari, A. (2013). “Modified expression for the failure criterion of bucket foundations subjected to combined loading.” *Canadian Geotechnical Journal*, 50(12), 1250-1259.

57. LeBlanc, C., Houlsby, G., and Byrne, B. (2010). “Response of stiff piles in sand to long-term cyclic lateral loading.” *Géotechnique*, 60(2), 79-90.

58. Li, D., Feng, L., and Zhang, Y. (2014). “Model tests of modified suction caissons in marine sand under monotonic lateral combined loading.” *Applied Ocean Research*, 48(1), 137-147.

59. Li, D. Y., Zhang, Y. K., Feng, L. Y., and Guo, Y. X. (2014). "Response of skirted suction caissons to monotonic lateral loading in saturated medium sand." *China Ocean Engineering*, 28(4), 569-578.

60. Li, D., Zhang, Y., Feng, L., and Gao, Y. (2015). "Capacity of modified suction caissons in marine sand under static horizontal loading." *Ocean Engineering*, 102(1), 1-16.

61. Liu, M., Yang, M., and Wang, H. (2014). "Bearing behavior of wide-shallow bucket foundation for offshore wind turbines in drained silty sand." *Ocean Engineering*, 82(1), 169-179.

62. Malhotra, S. (2011). *Selection, design and construction of offshore wind turbine foundations*, Wind turbines, InTech.

63. Mana, D., Gourvenec, S., and Randolph, M. (2010). "A numerical study of the vertical bearing capacity of skirted foundations." *Proc. 2nd Int. Symp. Front. Off. Geotech.*, Perth, Australia, 433-438.

64. Mana, D. S., Gourvenec, S. M., Randolph, M. F., and Hossain, M. S. (2012). "Failure mechanisms of skirted foundations in uplift and compression." *International Journal of Physical Modelling in Geotechnics*, 12(2), 47-62.

65. Mana, D. S., Gourvenec, S., and Martin, C. M. (2013). "Critical skirt spacing for shallow foundations under general loading." *Journal of Geotechnical and Geoenvironmental Engineering*, 139(9), 1554-1566.

66. Mehravar, M., Harireche, O., and Faramarzi, A. (2016). "Evaluation of undrained failure envelopes of caisson foundations under combined loading." *Applied Ocean Research*, 59(1), 129-137.

67. Nguyen Sy, L., and Houlsby, G. T. (2005). "The theoretical modelling of a suction caisson foundation using hyperplasticity theory." *Frontiers in Offshore Geotechnics II*, Perth, Australia, 417-423.

68. Park, J. S., Park, D., Jang, H. S., and Yoon, S. W. (2015). "Numerical Modeling of Skirted Foundation in Alternating Layers of Sand and Clay." *Proc., The Twenty-fifth International Ocean and Polar Engineering Conference*, Hawaii, U.S.A., 658-661.

69. Park, J.S., Park, D., and Yoo, J.K. (2016). "Vertical bearing capacity of bucket foundations in sand." *Ocean Engineering*, 121(1), 453-461.

70. Potts, D. M., Zdravkovic, L., and Zdravković, L. (1999). *Finite element analysis in geotechnical engineering: theory (Vol. 1)*, Thomas Telford.

71. Sun, X., Luan, M., and Tang, X. (2010). "Study of horizontal bearing capacity of bucket foundation on saturated soft clay ground." *Rock and Soil Mechanics*, 31(2), 667-672.

72. Taiebat, H., and Carter, J. (2000). "Numerical studies of the bearing capacity of shallow foundations on cohesive soil subjected to combined loading." *Géotechnique*, 50(4), 409-418.

73. Tang, X., Zhang, X., Shao, Q., and Li, Z. (2016). "Rotation center and horizontal bearing capacity of the bucket foundation in soft ground." *Marine Georesources & Geotechnology*, 34(6), 594-601.

74. Vahdatirad, M., Diaz, A. T., Nielsen, S., Ibsen, L. B., Andersen, L. V., Firouzianbandpey, S., and Griffiths, D. (2016). "A load-displacement based approach to assess the bearing capacity and deformations of mono-bucket foundations." *Proceedings of the Sixth International Conference on Structural Engineering, Mechanics and Computation*, Cape Town, South Africa, 2105-2111.

75. Villalobos, F. (2007). "Bearing capacity of skirted foundations in sand." *Proc., VI Congreso Chileno de Geotecnia*, Valparaiso, Chile, 14 pp.

76. Villalobos, F. A., Byrne, B. W., and Houlsby, G. T. (2009). "An experimental study of the drained capacity of suction caisson foundations under monotonic loading for offshore applications." *Soils and Foundations*, 49(3), 477-488.

77. Wakil, A. Z. E. (2010). “Horizontal capacity of skirted circular shallow footings on sand.” *Alexandria Engineering Journal*, 49(4), 379-385.

78. Wakil, A. Z. E. (2013). “Bearing capacity of skirt circular footing on sand.” *Alexandria Engineering Journal*, 52(3), 359-364.

79. Walter, M., Beiter, P., Paul, S., Tian, T., Tyler, S., and Paul, S. (2016). *2016 Offshore Wind Technologies Market Report*, U.S. Department of Energy, Oak Ridge, TN.

80. Wang, X., Yang, X., and Zeng, X. (2017). “Centrifuge modeling of lateral bearing behavior of offshore wind turbine with suction bucket foundation in sand.” *Ocean Engineering*, 139(1), 140-151.

81. Yang, X., Wang, X., and Zeng, X. (2017). “Numerical simulation of the lateral loading capacity of a bucket foundation.” *Geotechnical Frontiers 2017*, Florida, U.S.A., 112-121.

82. Yun, G., and Bransby, M. (2007). “The undrained vertical bearing capacity of skirted foundations.” *Soils and Foundations*, 47(3), 493-505.

83. Zhang, J. H., Chen, Z. Y., and Li, F. (2010). “Three dimensional limit analysis of suction bucket foundations.” *Ocean Engineering*, 37(8-9), 790-799.

84. Zhang, Y. K., Gao, Y. F., Li, D. Y., and Mahfouz, A. H. (2016). “H-M bearing capacity of a modified suction caisson determined by using load-/displacement-controlled methods.” *China Ocean Engineering*, 30(6), 926-941.

85. Zhang, Y. K., Li, D., and Gao, Y. F. (2016). “Earth pressures on modified suction caisson in saturated sand under monotonic lateral loading.” *Journal of Renewable and Sustainable Energy*, 8(5): 053312.

86. Zhu, B., Kong, D. Q., Chen, R. P., Kong, L. G., and Chen, Y. M. (2011). “Installation and lateral loading tests of suction caissons in silt.” *Canadian Geotechnical Journal*, 48(7), 1070-1084.

87. Zhu, B., Byrne, B., and Houlsby, G. (2013). “Long-term lateral cyclic response of suction caisson foundations in sand.” *Journal of Geotechnical and Geoenvironmental Engineering*, 139(1), 73-83.

88. Zhu, B., Zhang, W. L., Ying, P. P., and Chen, Y. M. (2014). “Deflection-based bearing capacity of suction caisson foundations of offshore wind turbines.” *Journal of Geotechnical and Geoenvironmental Engineering*, 140(5), 04014013.

PUBLICATIONS

1. Deb, T. K., and Singh, B. (2018). "Response and capacity of monopod caisson foundation under eccentric lateral loads." *Marine Georesources & Geotechnology*, 36(4), 452-464.
2. Deb, T.K. and Singh, B. (2017). "Numerical modelling of bucket foundations in dense sand supporting offshore wind turbines." *Proceedings of 19th International Conference on Soil Mechanics and Geotechnical Engineering*, Seoul, pp. 2277-2280.
3. Deb, T.K. and Singh, B. (2017). "Numerical investigation of the vertical capacity of monopod bucket foundation embedded in sandy soil." *Proceedings of Indian Geotechnical Conference*, Guwahati, pp. 1-4.
4. Deb, T.K. and Singh, B. (2017). "Effect of lateral loading on the response of bucket foundation supporting offshore wind turbine in sandy seabed." *Proceedings of the National Conference on Sustainable Mechanical Engineering: Today and Beyond*, Tezpur University, pp. 1-4.
5. Deb, T.K. and Singh, B. (2016). "Influence of load eccentricity and aspect ratio on lateral load capacity of bucket foundation installed in medium dense sand." *Proceedings of International Conference on Soil and Environment*, Bangalore, India (CD-ROM), pp. 1-8.
6. Deb, T.K. and Singh, B. (2016). "Numerical analysis of bucket foundations under eccentric lateral loading in medium dense sand", *Proceedings of Internal Conference on Earth Sciences and Engineering*, Coimbatore, pp. 1-7.
7. Deb, T.K. and Singh, B. (2016). "Behaviour of bucket foundations in sandy bed subjected to eccentric lateral loading." *Proceedings of Indian Geotechnical Conference*, Chennai, pp. 1-4.
8. Deb, T.K. and Singh, B. (2015). "Horizontal load capacity of bucket foundation installed in sandy soil." *Proceedings of Indian Geotechnical Conference*, Pune, pp. 1-7.

9. Deb, T.K. and Singh, B. (2015). "Lateral load-deformation behaviour of bucket foundations in sandy soil." *Proceedings of Geo-Engineering and Climate Change Technologies for Sustainable Environmental Management*, Allahabad, pp. 1-6.
10. Deb, T.K. and Singh, B. (2014). "Behaviour of large diameter piles as foundation system for offshore wind turbine in sands." *Proceedings of Nort-East Students Geo-Congress on Advances in Geotechnical Engineering*, Guwahati, pp. 1-6.
11. Gupta, B.K., Deb, T.K. and Singh, B. (2013). "Lateral load carrying capacity of monopod bucket foundation in sand." *Proceedings of North-East Students Geo-Congress on Advances in Geotechnical Engineering*, Guwahati, pp. 129-138.
12. Deb, T.K. and Singh, B. (2018). "Numerical investigation and design of monopod bucket foundation embedded in sand." *Indian Geotechnical Conference*, Bengaluru. (Accepted).
13. Deb, T.K. and Singh, B. (2019). "Numerical investigation of the vertical response of bucket foundations supporting offshore wind turbines in sand." *International Symposium of International Association for computer methods and Advances in Geomechanics*, Gandhinagar. (Under review).